ASSESSMENT OF PRESSURE SWING ADSORPTION AS A CARBON DIOXIDE CAPTURE TECHNOLOGY IN NATURAL GAS COMBINED CYCLE POWER PLANTS

by

REBECA ANDREA AZPIRI SOLARES

Supervisors: Prof Joseph Wood, Dr Zhenyu Zhang

A Thesis Submitted to the University of Birmingham for the Degree of Engineering Doctorate (EngD)

Advanced Reaction and Catalysis Engineering Group

School of Chemical Engineering

College of Engineering and Physical Sciences

The University of Birmingham

December 2020

UNIVERSITY OF
BIRMINGHAM

University of Birmingham Research Archive

e-theses repository

This unpublished thesis/dissertation is copyright of the author and/or third parties. The intellectual property rights of the author or third parties in respect of this work are as defined by The Copyright Designs and Patents Act 1988 or as modified by any successor legislation.

Any use made of information contained in this thesis/dissertation must be in accordance with that legislation and must be properly acknowledged. Further distribution or reproduction in any format is prohibited without the permission of the copyright holder.

ABSTRACT

This project studied the technical and economic performance of pressure swing adsorption (PSA) as a carbon capture technology in natural gas combined cycle (NGCC) power plants. PSA is a well-established industrial process for obtaining gas products such as hydrogen, but the process implemented in industry does not achieve the carbon dioxide purity levels over 95% required for carbon capture. The NGCC power plant using PSA as a carbon capture technology also included a case study where hydrogen was co-produced in the power plant. Therefore, hydrogen purity levels above 99% were also required at the end of the PSA process.

NGCC power plants offer favourable conditions for using PSA as a carbon capture process, due to the process conditions and the composition of natural gas. The aim of this thesis was to discover how to optimise a plant for both carbon capture and hydrogen production, and the implications of this for product purities, recoveries, plant costs, and energy penalties. Numerical and process simulations were used in this project to assess the viability of the NGCC-PSA system.

Firstly, a laboratory-scale adsorption model was developed and the model results were validated against experimental data. Parameter estimation was used for the model validation, and the mass transfer coefficient was the variable calculated from this analysis. A sensitivity analysis of the PSA process variables was simulated using this model; the analysis studied the effects of several process conditions on the carbon capture performance indicators. The variable that produced the greatest effect on these indicators was the concentration of carbon dioxide in the feed; this highlighted the importance of

recycling carbon dioxide to the process to increase the purity of this product. The PSA process configuration developed at laboratory scale achieved hydrogen purities over 99%, required for the commercialization of this product.

Secondly, a pilot-scale PSA process was developed based on the results obtained from the laboratory-scale process. A rinse step that recycled the carbon dioxide at 1 bar proved essential for increasing the carbon dioxide purity. The purity and recovery of the carbon dioxide were further increased through the study of alternative variable values and process configurations. Carbon dioxide purity and recovery values over 95% and 90% were obtained, respectively, by decreasing the feed flow rate of the process steps at 1 bar and by the introduction of an assisted purge step that recycled the gas from a depressurizing bed to a process step at 1 bar. The recovery of hydrogen was improved to values near 95% with the introduction of three pressure equalization steps in the process.

Lastly, the pilot-scale PSA process configurations that improved the carbon capture performance parameters were integrated into a technical and cost analysis of an NGCC power plant. For that purpose, the effect of the process conditions of the plant on the energy penalty and levelized costs of electricity (LCOE) and carbon avoided (LCCA) were studied. The energy penalty of the plant was improved from 27% to 21% by decreasing the operating pressure of the water gas shift reactor.

The variables that had the greatest effect on the cost indicator values of the plant were the prices of the utilities and of the carbon tax. The LCCA of the power plant decreased by 42 \$/tonne CO_2 when the natural gas price decreased from 40 to 10 \$/MWh. Overall, the NGCC and PSA system showed promising results, with acceptable LCCA and LCOE values around 30 \$/tonne CO_2 and 90 \$/ MWh, respectively. These values would be

achievable under a number of future scenarios, such as with the implementation of a carbon tax of around 10 $/tonne CO_2.

ACKNOWLEDGEMENTS

First, I would like to express my gratitude to my supervisor Professor Joseph Wood for the guidance and support provided during my four years of research. I will always be grateful for the trust he placed in me and for the ideas he gave me that contributed to this project. Second, I would like to say thank you to Douglas Soares dos Santos, whose amazing research on new modified activated carbon materials was decisive in making this project possible. I also feel grateful to the people that surrounded me in the Advanced Reaction and Catalysis Engineering group, who supported my research and provided help when needed.

I want to say thank you to the community from the Centre for Doctoral Training in Carbon Capture and Storage and Cleaner Fossil Energy at The University of Nottingham, who gave me the opportunity to undertake this project. My thanks to the colleagues of the CDT based in Nottingham, Loughborough and Sheffield. I would also like to express my gratitude to Process Systems Enterprise (PSE) for believing in this project and providing a powerful simulation tool, ProcessBuilder.

I am grateful for the colleagues and the community at the University of Birmingham. Thank you to Argyris, Dimitris, Greg, Jana, Larry, Lucia, Stelios and Zoe. I will never forget our talks about science and trying to solve the world's problems. From the very first moment, the university felt like home; its research and work is amazing and will maintain and improve the quality of life of future generations.

Finally, I am grateful for the support from my family and friends. I dedicate the work done in this research to my grandmother, Mari, who provided me with the strength to

complete this project. Thank you to my brother, Joseba, for being a light unto others. Thank you to my parents, Jose Luis and Marisa. I would like to say a special thanks to my auntie Nekane and her friend Cynthia Grover. Both of them provided strong support during these four years, and they have been a great example and inspiration for me. Cynthia Grover also helped me by improving the language and spelling of this thesis, and ensuring consistency of the table formats, margins and page numbers. A big thank you to my friends back home who have also supported me in the difficult times.

TABLE OF CONTENTS

LIST OF TABLES

LIST OF FIGURES

LIST OF ABBREVIATIONS

Abbreviation	Full Term
A	Adsorption step
AC	Activated carbon
ATPC	Annual total production costs
ASU	Air separation unit
A-Pu	Assisted purge
CF	Capacity factor
CT	Carbon tax
CSS	Cyclic steady state
CCUS	Carbon capture utilization and storage
D/DEPRESS	Depressurization step
DOE	Department of Energy (United States)
DPC	Direct product cost
DSL	Dual-site Langmuir
EBTF	European Benchmarking Task Force
EOS	Equation of state
EP	Energy penalty
EPRI	Electric Power Research Institute
EPSRC	Engineering and Physical Sciences Research Council
EXP	Experimental
F	Feed
FC	Fixed costs
FTIR	Fourier transform infrared spectroscopy

GC	General costs
GE	General Electric
GHG	Greenhouse gas
HPVA	High pressure volumetric analyzer
HRSG	Heat recovery steam generator
HTS	High temperature shift
ID	Internal diameter
IEA	International Energy Agency
IGCC	Integrated gasification combined cycle
IPCC	Intergovernmental Panel on Climate Change
IUPAC	International Union of Pure and Applied Chemistry
LCCA	Levelized cost of carbon avoided
LCOE	Levelized cost of electricity
LDF	Linear driving force
LTS	Lower temperature shift
MC	Manufacturing costs
MDEA	Mono-di-ethanol-amine
MEA	Mono-ethanol-amine
MOF	Metal organic framework
MR	Marginal revenue
MSL	Multi-site Langmuir
NG	Natural gas
NGCC	Natural gas combined cycle
OD	Outer diameter
OECD	Organisation for Economic Co-operation and Development
OL	Operational loss
ORC	Organic Rankine cycle

P/PRESS	Pressurization step
PE	Pressure equalization step
PEC	Purchase equipment cost
POC	Plant overhead cost
Pr	Prandtl number
PSA	Pressure swing adsorption
PSE	Process systems enterprise
PU	Purge step
R	Rinse step
Re	Reynolds number
Sc	Schmidt number
SMR	Steam methane reformer
SRC	Steam Rankine cycle
SRK	Soave-Redlich-Kwong
SSR	Sum of the squared residuals
TCI	Total capital investment
TDC	Total direct costs
TEM	Transmission electron microscopy
TEPA	Tetra-ethylene-pent-amine
TGA	Thermogravimetric analysis
TIC	Total indirect costs
TRL	Technology readiness level
TSA	Temperature swing adsorption
TWC	Total working capital
VSA	Vacuum swing adsorption
WGS	Water gas shift [reactor]

LIST OF SYMBOLS

Symbol	Full Term and Unit
A	Area, m^2
b_i	Langmuir equilibrium constant of the i^{th} component, Pa^{-1}
C	Concentration in the gas phase, mol m^{-3}
$C_{p,\,g}$	Heat capacity of the components in the gas phase, J mol^{-1} K^{-1}
$C_{p,\,s}$	Heat capacity of the adsorbent, J kg^{-1} K^{-1}
D	Bed diameter, m
D_{AB}	Diffusion coefficient, m^2 s^{-1}
D_P	Particle diameter, m
D_x	Axial dispersion coefficient, m^2 s^{-1}
g	Gas phase symbol in equations
h_i	Heat transfer coefficient, J m^{-2} s^{-1} K^{-1}
$h_{r,i}$	Effective heat transfer coefficient, J m^{-3} s^{-1} K^{-1}
i=1…n	Number of components in equations
K	Effective mass transfer coefficient, s^{-1}
k	Thermal conductivity, J m^{-1} s^{-1} K^{-1}
k_D	Viscous force of the momentum balance, Pa m^{-1}
k_v	Kinetic force of the momentum balance, Pa m^{-1}
L	Length, m
Mw	Molecular weight, g mol^{-1}
n	Molar flow rate of gas, mol s^{-1}
P	Pressure, Pa

q	Volumetric flow rate, m^3s^{-1}
Q	Component concentration on the adsorbent, mol kg^{-1}
Q*	Equilibrium component concentration on the adsorbent, mol kg^{-1}
q_m	Maximum sorbent loading of the components, mol kg^{-1}
r	Radius, m
r_{in}	Inner radius of fixed-bed reactor, m
R	Ideal gas constant, J mol^{-1} K^{-1}
T	Temperature, K
v	Velocity, m s^{-1}
w	Fixed-bed wall symbol in equations
Y	Mole fraction of components in the gas phase, mol mol^{-1}
z	Position in the bed length discretization, m

Greek Symbols

Symbol	Full Term and Unit
ε_b	Bed voidage fraction, -
ε_t	Total voidage fraction, -
ε_p	Particle voidage fraction, -
λ	Heat axial dispersion coefficient, J s^{-1} m^{-1} K^{-1}
μ_g	Viscosity, Pa s
ρ	Density, kg m^{-3}
φ_i	Diffusion volume of i component, -

CHAPTER 1 – INTRODUCTION

1.1 Project Motivation

Carbon capture, utilization and storage (CCUS) is regarded as an essential technology for meeting the requirements established by the Paris Agreement to limit the rise in the earth's temperature to less than 2°C by 2050 (International Energy Agency, 2020). CCUS technology could play a key role in decarbonizing sectors where reaching zero carbon emissions is not technically or economically feasible (Heuberger et al., 2017). Additionally, the technology could generate revenues from the utilization of carbon dioxide and other compounds obtained from the capture process, such as the production of hydrogen or methanol (International Energy Agency, 2020). Therefore, research on CCUS should focus on technologies that show promising prospects in terms of the ease of the capture process and the economic revenue, since the cost of CCUS technologies has been shown to be the main drawback when implementing these processes at large scale (Gasworld, 2019).

Pressure swing adsorption (PSA) has been one of the main gas separation technologies applied for hydrogen production at industrial scale; it also shows potential for carbon dioxide capture (Abanades et al, 2015). Natural gas combined cycle (NGCC) power plants offer favourable conditions for using PSA as a carbon capture technology, since natural gas is the main source used for hydrogen production, as indicated by the U.S. department of energy (DOE, 2020).

Keeping this context in mind, the Engineering and Physical Sciences Research Council (EPSRC) Centre for Doctoral Training in Carbon Capture and Storage and Cleaner Fossil

Energy (The University of Nottingham) accepted project proposal EP/L016362/1, which involved studying the viability of PSA as a CCUS technology in NGCC power plants. This project was undertaken in the Catalysis and Reaction Engineering Research Group (School of Chemical Engineering) at The University of Birmingham, as part of the collaboration of the university with the doctoral centre. Numerical and process simulations were used to study the viability of PSA in NGCC power plants. The gPROMS® ProcessBuilder simulation package was provided in-kind by Process Systems Enterprise (PSE).

The simulation results were compared to laboratory data obtained by Douglas Soares dos Santos, who studied the performance of activated carbon adsorbents for carbon dioxide capture under various pressure and temperature conditions. All the experimental data presented in this thesis was provided by Douglas Soares dos Santos, and it is shown in Soares dos Santos (2019). All the simulation work was developed and performed and its results obtained by the author of this thesis.

1.2 Project Aims

The overall aim of this project was to assess the viability of pressure swing adsorption as a technology for capturing carbon dioxide prior to combustion in natural gas combined cycle power plants, in terms of the purity and recovery of the carbon dioxide captured and the hydrogen co-produced by the process. The purity and recovery of carbon dioxide are the indicators used to assess the performance of most carbon capture technologies.

Additionally, the viability of the NGCC-PSA system was assessed based on the energy efficiency and the economics of the power plant when it used the capture technology.

Numerical and process simulations were used for this project, since simulation is one of the main tools used to assess the viability of new carbon capture technologies at pilot and industrial scale (Abanades et al., 2015).

In order to analyze the viability of the system, the project was split into the following main tasks:

- A validation of the laboratory-scale adsorption model by using experimental data and a sensitivity analysis of the PSA process variables at laboratory scale (Chapter 4).
- A scale-up of the laboratory PSA process to pilot scale and improvement of the process by varying variable values and process configurations (Chapter 5).
- An assessment of the pilot-scale PSA process after integration into an NGCC power plant, in terms of the capture performance, energy efficiency and economics of the power plant (Chapter 6).

1.3 Thesis Outline

The outline of this thesis was developed based on the three main tasks above; the thesis comprises eight chapters. This chapter (Chapter 1) explains the project motivation, aims and the overall structure of the thesis.

The second chapter (Chapter 2) covers the gaps in the literature on which the project was built. The main carbon capture technologies are explained in that chapter, together with their main advantages and disadvantages. In-depth information about adsorption technology is provided, and the performance of adsorption with a view to carbon capture

is assessed based on the previous literature. Information about previous simulation work applied to PSA processes is provided, together with an assessment of power plants that have carbon capture technology. The future potential of PSA within an NGCC system, as it is developed in this project, is highlighted.

The methodology chapter (Chapter 3) explains the procedure used to link the PSA simulation results to the design of the power plant. It contains accurate information about the model used to simulate the PSA process and the criteria used to validate the laboratory scale model by using the experimental data. That chapter also explains the criteria used to scale up the PSA process and the procedure used to improve the process results. Last, it contains information about the design of the NGCC power plant and the indicators used to assess the performance of the power plant.

Chapter 4 presents the results of the validation of the laboratory-scale model by the experimental data under a number of process conditions. That chapter also presents the results of the sensitivity analysis of the PSA process variables. The PSA process was developed from the validated adsorption model. The results of that chapter made it possible to determine which process variables improved the capture performance indicator values; based on this information, the PSA process was scaled up.

The goal of assessing the performance of the PSA process at pilot scale, as shown in Chapter 5, was to enable the integration of the technology into an NGCC power plant. The performance of the scaled-up PSA process was improved by varying the process variable values and configurations. Several process configurations were selected to integrate the process into the power plant, based on their capture performance and predicted cost.

The last chapter (Chapter 6) assessed the viability of the NGCC-PSA system, in terms of the capture performance, energy efficiency and the economics of the plant. For that purpose, several conditions within the power plant were considered for implementation. Alternative plant arrangements were also studied, such as inclusion of hydrogen co-production in the power plant. The overall conclusions and recommendations for future studies are in Chapter 7, based on the thesis results.

CHAPTER 2 – LITERATURE SURVEY

2.1 Introduction

Climate change is one of the main challenges that the next generations will face in the following fifty years. Carbon capture use and storage is a technology able to decarbonize energy supplies that would otherwise generate carbon emissions (Heuberger et al., 2017). In fact, the implementation of the technology worldwide will be critical as a medium term solution, if fossil fuel reserves are still substantially in use by 2050 and if the targeted increase of no more than 2°C in the global temperature is to be met (Budinis et al., 2018).

The main technology that is at the most advanced stage of development and thus has already been introduced to scale up carbon capture projects is absorption via solvents in post-combustion conditions (Abanades et al., 2015). However, various alternative technologies are under study due to the variety of process conditions that are encountered in power generation and in industry. Pre-combustion carbon capture offers several advantages compared to this type of absorption technology, due to process conditions that include high pressures and high carbon dioxide concentrations before combustion. Pressure swing adsorption could be a potential technology to implement in these conditions, since it has been applied successfully in other industrial processes under similar conditions, such as the production of hydrogen (Ribeiro et al., 2008).

This chapter is a literature survey that describes the current state of the art of pressure swing adsorption processes and the main challenges to adapting these processes for carbon capture purposes, in terms of process conditions and adsorbent materials. First,

the future need and current state of carbon capture technology is reviewed. Then the advantages of pre-combustion capture technology are summarized.

After that, the potential of PSA in pre-combustion capture conditions is analyzed. Adsorbent materials, the techniques to measure their performance and their advantages and disadvantages are considered. Numerous process conditions from previously reported work on pre-combustion capture using PSA are compared here. The need to study alternative configurations comes out as a focus, due to the limited literature on obtaining carbon dioxide purities over 95% and on recovery up to 90%.

Finally, existing combined cycle power plants that use carbon capture are reported on in this chapter, and these power plants are compared based on their carbon capture performance and energy penalty. The chapter also reports where the gaps are in these combined cycle power plants in order to inform future study. The need for further study of the process design and the economics of these plants with carbon capture is highlighted. One of the main conclusions of this chapter is that natural gas combined cycle (NGCC) power plants that perform carbon capture using adsorption could yield promising results in terms of showing a better capture performance and lower energy penalty compared to coal fired power plants, due to the simpler composition of the natural gas compared to that of coal. Natural gas has a content of up to 98% carbon-based components, mostly hydrocarbons in the gas phase, whereas the content of carbon-based components in coal is of around 67%, with presence of volatile components and ash (IEA-GHG, 2009). The presence of these components affects the performance of the PSA process, blocking the pores on the adsorbent particles.

2.2 Carbon Capture Use and Storage

2.2.1 Carbon Emissions and Climate Change

Carbon dioxide emissions could be one of the major contributors to climate change. From the mid-1800s to 2012, measurements of atmospheric and ice-trapped air showed an increase of around 40% in the atmospheric carbon dioxide (The Royal Society and the National Academy of Sciences, 2014). The Intergovernmental Panel on Climate Change (IPCC) stated in 2014 that the annual greenhouse emissions grew on average by 1 gigaton of carbon dioxide equivalent ($GtCO_2eq$) per year between 2000 and 2010, whereas there was an average increase of 0.4 $GtCO_2eq$ per year from 1970 to 2000 (IPCC, 2014). Due to the increase in atmospheric carbon dioxide, the average temperature of the earth has increased by 0.8°C in the last 200 years, whereas the overall temperature of the earth has increased by 4–5°C over the last 7000 years (The Royal Society and the National Academy of Sciences, 2014). A report by the International Energy Agency (IEA) (2019d) revealed that a limited carbon dioxide storage scenario would require an additional 3325 gigawatts capacity of new power generation, compared to a scenario where carbon dioxide sequestration is widely used.

Fossil fuels and industrial processes are the major contributors to increasing atmospheric carbon dioxide levels. About 65% of this contribution is due to global greenhouse emissions, whereas about 11% of the contribution of carbon dioxide comes from forestry and land-use-based activities (IPCC, 2014). In this context, fossil fuels are the main sources of power generation worldwide. In 2018, power generation from fossil fuels accounted for 58.6% of the total gross electricity production in the countries belonging to the Organisation for Economic Co-operation and Development (OECD). That year,

natural gas as a power generation source surpassed the contribution by coal by 2.3 percentage points (International Energy Agency, 2019a). Natural gas is expected to become one of the sources of power generation with major prospects in the near future (Global CCS Institute, 2017; U.S. Energy Information Administration, 2019).

2.2.2 Future Energy Trends

The main scenarios for the future show an energy production system in which a mixture of technologies is implemented. Priority will be given to new renewable sources made of efficient materials and to low-carbon power generation produced from hydrogen. This last component is regarded as one of the main energy vectors in the near future (International Energy Agency, 2019c). However, a system that will depend heavily on renewables would require an effective and affordable energy storage network; this network will be not ready in the near future (Heuberger et al., 2017). The implementation of an energy network that depends purely on renewable energy is challenging for a system that depends heavily on fossil fuels. The International Energy Agency (2019a) showed that, in 2017, non-OECD countries obtained 46.8% of their gross electricity from coal and 19.8% from natural gas. Additionally, 70 Mt of hydrogen are produced annually, of which 76% comes from natural gas (International Energy Agency, 2019b)

In this scenario, the implementation of carbon capture use and storage (CCUS) will be imperative if fossil fuel reserves are still substantially in use by 2050 and the targeted increase of no more than 2°C in the global temperature is to be met (Budinis et al., 2018). The cost of climate change mitigation is predicted to increase by 138% if CCUS is not included as a mitigation option (IPCC, 2014). The use of the technology would be

required for a flexible power generation system (Mac Dowell and Staffell, 2016). Additionally, it is regarded as one of the main technologies for hydrogen production in the future (Grande, 2012).

On the one hand, a special report from the IPCC (2005) on CCUS stated that several carbon capture processes were ready for implementation at a large scale because gas separation processes operate successfully at an industrial scale. On the other hand, there is a need to adapt and optimize these systems to make them economically viable for CCUS (Abanades et al., 2015).

Therefore, research on how an economically viable and safe CCUS system can operate is required; this requires the analysis of the storage site, of the capture and of the utilization. For the capture site, the lack of regulations and of funding by governments for expensive capture technologies are the main issues noted by most authors. For the commercial operation of these technologies, substantial changes may be required, due to the alternative material, energy integration structures and components required by the process (Abanades et al., 2015). These new requirements increase the cost of the capture systems. In order to prove the suitability of these technologies, the energy balances and the type of material and equipment used in the plant can be indicators of the technical and economic viability of new processes.

2.2.3 Carbon Dioxide Capture Technology

There are three main technologies ready for the scaled-up implementation of carbon capture: post- and pre-combustion capture and oxy-fuel combustion. Post-combustion capture mainly uses absorption technology to separate the carbon dioxide from the

combustion fuel gases, using a liquid solvent. The fact that absorption is easy to retrofit in operating plants has made the process implementable on a large scale (Aaron and Tsouris, 2005). Pre-combustion capture uses either absorption or adsorption technology with a solid adsorbent to remove the carbon dioxide from the syngas before it has been combusted. It requires an upstream process to convert the fuel into syngas. These processes operate at high pressure and use carbon dioxide feed concentrations of around 40%, which is high compared to the carbon dioxide feed concentration used in post-combustion capture (Riboldi and Bolland, 2017). This technology can be applied in integrated gasification combined cycle (IGCC) or natural gas combined cycle power plants (Jansen et al., 2015).

Oxy-fuel combustion technology uses pure oxygen in the fuel combustion, resulting in a mixture of water and carbon dioxide ready to be stored using low temperature dehydration and desulphurization (Carpenter and Long, 2017). Figure 2.1 shows a flow diagram of the post-combustion, pre-combustion and oxy-combustion scenarios.

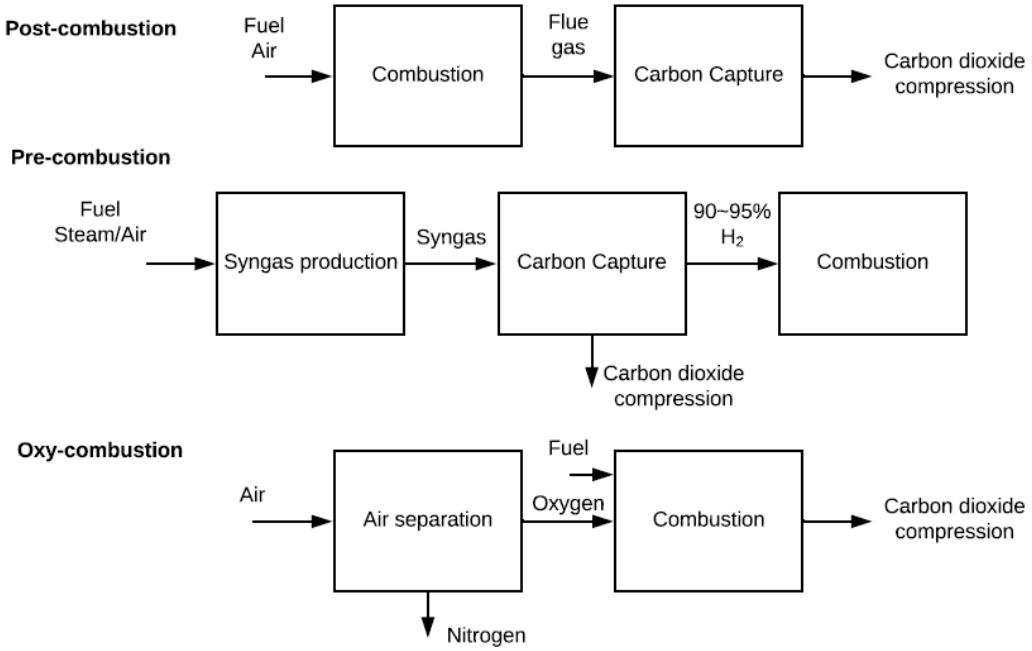

Figure 2.1. A flow diagram of post-, pre- and oxy-combustion capture technologies in operation

Abanades et al. (2015) compared these three main technologies in terms of their technology readiness level (TRL) in a review in an IPCC special report in 2005. Both post-combustion capture using absorption and pre-combustion capture using both absorption and adsorption had a TRL of 8. This means that the technologies are complete and qualified, ready for industrial scale implementation. Oxy-combustion was demonstrated for up to 30 MW and had a TRL of 6 in this case study. The technology has been demonstrated in industrially relevant environments.

Another study by Budinis et al. (2018) compared the energy penalties of coal-fired power plants and natural gas-fired power plants, in terms of the percentage of the energy applied to the process compared to that produced in the power plants. The energy penalty for the coal-fired power plants was in the range of 15–28%, whereas the energy penalty of gas-

fired power plants was in the range of 15–16%. The higher energy penalty of post-combustion capture using absorption is explained by the absorbent regeneration, which is energy-intensive. Another issue noted by most authors is the small concentration of carbon dioxide, of around 10–15% (volume-based), in the flue gases directed to the capture unit (Gibson et al., 2016; Yu et al., 2012).

The 2005 special report of the IPCC noted that, to address the required carbon dioxide emissions, a number of gas separation technologies would be required, depending on the conditions that hold in the capture process (IPCC, 2005). In this context, pre-combustion carbon capture applied to IGCC and NGCC power plants demonstrates high potential to reduce capture costs, due to the high pressures in the processes that decrease compression requirements and to the high carbon dioxide partial pressures that increase the success of the separation process (Lee et al., 2014).

2.3 Pre-Combustion Carbon Capture

Pre-combustion capture implies using air, oxygen or steam to convert the fuel into synthesis gas (syngas), which is formed mainly by carbon monoxide and hydrogen. The fuel can be biomass, coal or natural gas. Then, using a shift reactor, the syngas is converted to a mixture mainly formed of carbon dioxide and hydrogen. This mixture is fed to the capture unit (Jansen et al., 2015). Pre-combustion technology is mainly used for the production of fertilizers and hydrogen (Lee and Park, 2015).

Ultimately, it has been regarded as a potential capture technology to be applied in NGCC and IGCC power plants, due to the fact that these power plants operate with a gas turbine, which requires fuel gas at high pressures. In keeping with this, the main carbon capture

studies for these plants have considered pre-combustion technology (Casas et al., 2013a; Kunze and Spliethoff, 2012; Schell et al., 2009; Seyitoglu et al., 2016).

The main drawbacks noted by these authors are the addition to the original power generation system of units (the syngas production unit and a shift reactor unit) that have not been optimized for power generation purposes. These are expected to increase investment costs, and generate uncertainty about the profitability of the power plant (Abanades et al., 2015; Di Lorenzo et al., 2013; Kunze and Spliethoff, 2012).

2.3.1 State of the Art Technology

Numerous technologies apart from absorption have been studied for implementation in pre-combustion conditions. A study by Abanades et al. (2015) that presented the technology readiness levels (TRLs) for a number of capture processes gave a TRL of 8 for both absorption and adsorption in pre-combustion capture. Other capture technologies, such as calcium looping and membranes, produced TRLs of 2 and 3, respectively, for pre-combustion capture. TRLs 2 and 3 mean that the basic design and pilot testing of key components at small bench scale have been implemented for these technologies. However, the only pre-combustion capture plants that have been implemented at pilot scale are those that perform absorption using solvents such as methyl di-ethanol-amine (MDEA) and Selexol. These processes have been implemented in IGCC power plants. At the moment, there are no existing pilot-scale NGCC plants that perform carbon capture using pre-combustion capture (Jansen et al., 2015). There has been pilot-scale testing of post-combustion capture in NGCC power plants at the Technology Centre

Mongstad facility in Norway using absorption with several advanced solvent-based technologies (DOE, 2017).

Absorption uses liquid solvents to separate the carbon dioxide from the flue gases. It is a well-established technology that obtains high capture rates and that has been widely applied to processes involving syngas production and hydrogen manufacture (Sreenivasulu et al., 2015).

Absorption can be either chemical, using amine-based solvents such as mono-ethanol-amine (MEA) and MDEA, or physical, following Henry's law, using organic solvents such as Selexol or Rectisol. The most commonly used solvent for carbon capture processes has been MEA, due to the material's relatively cheap price and high capture rates (Van Der Zwaan and Smekens, 2007).

Absorption processes use the lean absorbent coming from a stripper column to absorb the carbon dioxide counter-currently. Once the carbon-dioxide-rich solvent flows out of the absorption column, it is fed to the top of a stripper for desorption and returned as carbon dioxide in the gas phase. Steam coming from a reboiler is used for this purpose (Yang et al., 2008). In pre-combustion capture, the steam requirements of the stripper are partially met with a heat integration system, taking a fraction of the steam produced from the gas turbine, decreasing the plant's overall energy efficiency (Di Lorenzo et al., 2013).

The main research on the improvement of the energy efficiency of absorbent plants focuses on the absorbent tower and stripper configurations and, especially, on the solvent materials. The main disadvantages of these materials noted by most authors are the degradation and corrosion of the solvent and the energy-intensive regeneration (Cormos, 2016; Yu et al., 2012).

The study by Jansen et al. (2015) compared several of the most recent IGCC power plants that perform pre-combustion capture. All of them used solvent-based absorption, such as the Duke Energy project in the USA, which produces 618 MW as energy output, or the Huaneng project in China, which produces 265 MW as energy output. The energy efficiency achieved by both plants was around 40%. However, another study showed that the energy penalties of these power plants could be between 4.9 and 20%, in terms of the amount of energy produced by the plant using carbon capture, compared to the plant without using capture. Heat integration was used in the power plant to lower the energy penalty values (Budinis et al., 2018). In an effort to improve the energy efficiency of pre-combustion capture, several technologies have been developed.

2.3.2 Technology Options

The main technologies suggested for carbon dioxide capture without using absorption in pre-combustion conditions are adsorption, membrane diffusion, calcium looping and chemical looping, based on the TRLs presented in the study by Abanades et al. (2015). These technologies have been demonstrated at pilot scale level. Table 2.1 presents the definition of each TRL value.

Table 2.1. The definition of each TRL as shown in Abanades et al. (2015)

TRL	Definition
1	Basic principles of technology observed
2	Technology concept formulated, basic process design
3	Pilot testing of key components at small bench scale
4	Continuous operated pilot plants at laboratory scale, less than 50 kW power output
5	Pilot plants operated at industrially relevant conditions at 0.05 to 1 MW
6	Steady state operation in industrially relevant environments, and pilot plants in the MWth range
7	Industrial pilot plants operating at over 10 MWth
8	System demonstration at industrial scale
9	Competitive manufacturing of the full system

Membrane technology, with a TRL 5 when applied to post-combustion capture, relies on the capacity of the material to selectively separate the carbon dioxide from the main flue gas and deposit it onto the other side of the membrane. It has been widely applied in some industrial applications, but its application to CCUS is in the early stages of research (Abanades et al., 2015). The main drawbacks of the technology are the properties of the membrane materials for carbon capture, such as their selectivity and permeability, and especially the cost of the membrane materials (Sreenivasulu et al., 2015).

Calcium and chemical looping are characterized by a TRL of 2, lower than that reported for membranes. The main drawbacks of these technologies are the high temperatures and pressures at which the sorbent regenerates and there are reportedly issues with conversion (Abanades et al., 2015; Sreenivasulu et al., 2015).

Overall, adsorption technology applied in combined cycle power plants under pre-combustion conditions has promising characteristics, namely, its low cost and success at separation, due to the conditions that hold in the separation process and due to the characteristics of the adsorbent materials suitable for those conditions. These are summarized in the next section.

2.3.3 Adsorption in Pre-Combustion Capture

Adsorption processes in pre-combustion capture have drawn attention in many research areas over the last 10 years (e.g., Casas et al., 2013a; Lee and Park, 2015; Schell et al., 2009). The lower cost of the capture technology would be one of the main advantages of adsorption-based capture systems compared to processes that use solvents. The lower costs are due to the ease of regenerating the adsorbents and to not needing to heat up large volumes of water during the recovery of the capture material (Liu et al., 2014). A study by Alhajaj et al. (2016) that analyzed a solvent-based capture system yielded costs per carbon dioxide unit captured of 70 to 90 $/tonne of CO_2 for the power plant, whereas a study by Ho et al. (2008) that analyzed the cost of an adsorbent-based capture system in a supercritical coal power plant yielded values of 30 to 46 $/tonne of CO_2 captured.

In carbon capture, the adsorbent selectively separates the carbon dioxide from the process gas, based on a gas-solid interaction. This process involves the cyclic adsorption and desorption of the carbon dioxide (Lee and Park, 2015). Industrial adsorption processes have been widely applied to purify gases such as hydrogen. These adsorption processes have yielded over 99% purity of the recovered light product, hydrogen. In fact, CCUS is

expected to be one of the main sources of hydrogen production in the future (Grande, 2012).

Additionally, hydrogen is regarded as one of the main energy vectors for decarbonizing several sectors, such as industrial heat and transport, as part of a zero-emissions future. The production of hydrogen is currently responsible for around 700 mtpa (million tonnes per annum) of carbon dioxide emissions, according to the International Energy Agency (Gasworld, 2019). Adsorption is the main technology used for hydrogen purification nowadays and is implemented under similar conditions to those that hold for pre-combustion capture at NGCC and IGCC power plants. The key challenge facing adsorption in pre-combustion capture lies in finding a process design that achieves a high purity and overall recovery of the heavy product, carbon dioxide; it may differ substantially from the conventional industrial design (Jansen et al., 2015).

For this purpose, both the material and the process engineering of adsorption must be considered. The main research on adsorbents focuses on the reactivity of adsorbents by modifying their surface area and on research on new synthetic materials. Each type of adsorbent has its specific surface area, pore structure and chemical groups on the surface. Therefore, the process that applies to them is very specific (Lee and Park, 2015).

The energy efficiency of the process could be increased through the demonstration of new cycle configurations. Therefore, there is a need to arrive at reference process designs for adsorption that could be implemented in pre-combustion capture; process simulations could be a tool to predict the suitability of these configurations (Abanades et al., 2015).

2.4 Adsorbents

Adsorption occurs when there is an interaction between a component in a fluid phase and the surface of an adsorbent. Adsorbents are the solids on which the adsorption occurs, and they enable the enrichment of one or more compounds in the interfacial layer between the fluid and the solid (Rouquerol et al., 2014). These compounds are called the adsorbates.

For application, adsorbents in the form of a dry powder of solid material of 1 mm or less in diameter are used and they are porous materials. This porosity gives adsorbents high specific surface areas, which increases the area for adsorption in a solid. Adsorbents also should preferably have high capacity, selectivity and stability in the process to which they will be applied (Abanades et al., 2015). Demonstrating these qualities within the process conditions where the adsorbents are applied is essential to the success of the separation process.

The most common adsorbents adopted for carbon capture using pressure swing adsorption have been zeolites or carbon-based materials, such as activated carbons and metal organic frameworks. Numerous surface treatments have been applied to these materials to improve their performance by injecting nitrogen groups into the surface via chemical impregnation (Hussin and Aroua, 2020). Sections 2.5.3 to 2.5.5 report further the main adsorbents and the surface treatments applied by using adsorbents for carbon capture, respectively.

2.4.1 Characterization of the Adsorbents

Numerous characterization methods exist for measuring the surface area of an adsorbent and its capacity and selectivity for a component in the fluid phase. Gas adsorption metrics measure the amount of the desired components that is adsorbed in the equilibrium phase onto the solid in a well-controlled environment. In order to execute the experimental procedure, it is essential to know what the aim of the work is, what technique and conditions are suitable for the adsorbent material, and the purpose of the application (Rouquerol et al., 2014). It is important to take these measurements before analyzing the dynamic capacity and kinetics of the adsorbent in a fixed-bed reactor unit (Gibson et al., 2016). Table 2.2 in Section 2.5.3 shows the measured parameters of previously studied adsorbent materials operating at high pressures.

One of the main techniques for measuring the amount of gas adsorbed is gas adsorption manometry, which measures the pressure of a gas at a constant volume and a fixed temperature. This method is mainly used to determine the specific surface area of an adsorbent and the pore size distribution.

Before determining the capacity of the adsorbent for the compound of interest, several techniques are used to assess the morphology of the surface area and thereby to judge the suitability of an adsorbent. One of these techniques is scanning electron microscopy (SEM), which enables one to observe the morphology of the surface of an adsorbent. Another technique is Fourier transform infrared spectroscopy (FTIR), which identifies the chemical bonds on the surface of an adsorbent. This technique can be used to see the surface interaction between the components to be adsorbed and the treatments applied to

the surface of an adsorbent. These treatments are performed to enhance the performance of the solid.

For instance, a study by Zhu et al. (2014) investigated a nitrogen-enriched activated carbon sphere for the uptake of carbon dioxide under post-combustion conditions. In this study, the SEM technique was used to compare the surface of the modified 1-mm carbon particles to that of polymer particles. The channel structure of the activated carbon was also studied. This study also used transmission electron microscopy (TEM) to assess the surface of the solid on a scale of 1 nm and the influence of the nitrogen treatment on the structure of carbon elements. Another study, by Rampe and Tiwow (2018), analyzed the structure of a charcoal-coconut-shell-based activated carbon before and after the chemical activation. The results from the microscopy showed that the charcoal had fewer impurities on the surface, and thus higher porosity, after the activation of the solid.

Dantas et al. (2012) analyzed a nitrogen-enriched carbon using the FTIR technique, in order to assess qualitatively the interaction of the functional groups on the adsorbent's surface. The results showed the bonding of the nitrogen element to the solid-surface-forming amide (carbon bonds with NH_2) groups on the solid surface. The study by Zhu et al. (2014) also used FTIR to find chemical groups on the adsorbents' surface after the chemical modification. They found several nitrile (a triple bond between carbon and nitrogen) and amide groups. Numerous chemical activations and surface modifications for adsorbents applied to carbon capture are discussed in Section 2.5.5.

Another technique that measures the suitability of an adsorbent for a given application is thermogravimetric analysis (TGA), which measures the mass of an adsorbent for a certain time under a change in temperature. This measurement reveals the thermal stability and

the amount of volatile material. High thermal stability can be important in applications where the adsorbent is exposed to high temperatures.

TGA combines with FTIR to obtain the change in the mass of the adsorbent and the identity of the compounds involved (Plaza et al., 2008). This study used this technique to analyze the stability of various amine groups on the surface of an alumina adsorbent. Another study by Fałtynowicz et al. (2015) measured the loss of mass on the adsorbent surface at temperatures between 50 and 200°C. In that study, the greatest loss of mass was due to moisture content. In the temperature range between 225 and 375°C, the greatest fraction of organic matter was lost due to working with activated carbons obtained from biomass (Mohamed et al., 2010).

2.4.2 Adsorption Theory

Adsorption can happen via physisorption or chemisorption, depending on the interaction forces between the adsorbent and the adsorbate. Physisorption is characterized by the condensation of gases and the formation of non-ideal gases with van-der-Waals/London-dispersion forces. Chemisorption is characterized by the formation of a chemical bond between the adsorbate and the adsorbent surface (Auroux, 2013).

Both physisorption and chemisorption can be beneficial in industrial processes; the adsorption performance varies for each of these phenomena under certain conditions. Therefore, it is important to determine which phenomenon is more suitable for a selected industrial application. Both processes are exothermic and the main feature that is used to distinguish these two phenomena in published work is the heat of adsorption, which is the heat released during the bonding process per unit of mass of the component adsorbed.

Physisorption bonding is characterized by low values for the heat of adsorption, in the range of 5 to 45 kJ/mol (Auroux, 2013). Thus, physisorption is favoured in pre-combustion capture conditions where temperatures are relatively low (Abanades et al., 2015). The weak bonding between the adsorbent and adsorbate requires little energy for regeneration overall (Ben-Mansour et al., 2016).

Abanades et al. (2015) studied various physisorption adsorbents, mostly zeolites and metal organic frameworks (MOFs) applied to post-combustion capture. The heat of adsorption of these adsorbents was in the range of 30–45 kJ/mol. Carbon-based and mesoporous physisorption adsorbents proved to be more suitable for pre-combustion applications due to their higher saturation capacities, as had been shown in previous work.

Overall, pore size has been shown to be important for physisorption. Previous work has shown that mesoporous materials, which are used for physisorption, have a high adsorption capacity for carbon dioxide. These adsorbents are mainly zeolites, MOFs, mesoporous silicas and activated carbons (Ben-Mansour et al., 2016).

The heat of adsorption of chemisorption processes is usually higher than in physisorption processes, around 90 kJ/mol, as reported by Abanades et al. (2015) for a number of amine-based chemisorption adsorbents, and it can reach values as high as 400 kJ/mol (Auroux, 2013). This is due to the chemical reaction and, thus, the stronger bonding between the adsorbent and the adsorbate; this in turn leads to new compounds forming on the surface of the adsorbent. Therefore, these adsorbents are more suitable for post-combustion conditions, where temperatures are higher than for pre-combustion. The regeneration of these adsorbents requires higher temperatures, which increases the overall cost of the carbon capture when these adsorbents are applied to the process (Ben-Mansour et al.,

2016). For instance, in a study by Zhu et al. (2014), nitrogen-enriched carbons were tested using a temperature swing between 25°C and 150°C for cyclic adsorption and desorption of CO_2. In pre-combustion capture, the performance of these adsorbents can be enhanced by increasing the process temperature (Ruthven, 1985).

In conclusion, depending on the mechanism of adsorption, the process conditions affect the performance of the adsorbent differently, and adsorbents should be selected accordingly. A further discussion of the performance of these adsorbents is included Section 2.5.3.

2.4.3 Adsorbent Equilibrium Measures

The adsorbent selected for the purpose of the application should have a high capacity for the adsorbate in the given process conditions. Particularly, most studies emphasize the importance of research for finding new adsorbents with a high capacity for use in carbon capture (Abanades et al., 2015; Ben-Mansour et al., 2016). The maximum capacity of an adsorbent for a gas component is found via equilibrium isotherms. These are obtained by measuring the amount of gas adsorbed by the adsorbent under equilibrium conditions at a fixed pressure and temperature. Figure 2.2 shows the adsorption isotherm types that can be obtained from the isotherm experiments (Gas Adsorption Technology, 2016).

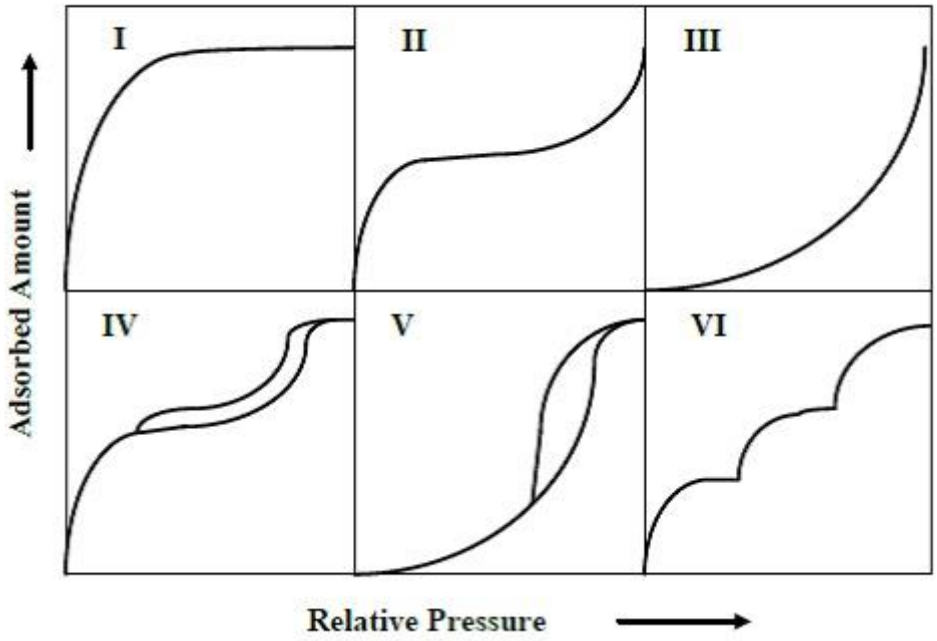

Figure 2.2. Adsorption isotherms based on the International Union of Pure and Applied Chemistry (IUPAC) classification (Gas Adsorption Technology, 2016)

The shapes of the adsorption isotherms vary based on the adsorbent, adsorbate and the interaction between them. They also enable the prediction of the type of pores located on the adsorbent surface. Type I isotherms are typical of microporous adsorbents, whereas Type II isotherms are typical of macroporous or non-porous adsorbents. Type III isotherms are also typical of macroporous or non-porous adsorbents, but the interaction between the adsorbate and the adsorbents is usually weak. Type IV isotherms are associated with mesoporous adsorbents. Type V isotherms are obtained when the interaction with the adsorbate is weak, both for microporous and mesoporous adsorbents. The existence of two values for the adsorbed amount at constant relative pressure in Type IV and V isotherms indicates the existence of capillary condensation when filling and

emptying the pores. Type VI is a rare form of isotherm that appears in adsorption by layers on highly uniform adsorbent surfaces (Rouquerol et al., 2014).

Isotherm experiments are executed at different relative pressures and at a constant temperature. High pressure volumetric analysis is one of the main experimental methods used to obtain isotherm curves; it enables one to determine the maximum capacity of an adsorbent in equilibrium. The maximum capacity of an adsorbent is calculated from a parameter estimation based on both the experimental data and the results obtained from the isotherm equation that best represents the laboratory data, by obtaining the smallest error, commonly defined as the sum of the squared residuals (Rouquerol et al., 2014). These isotherm models and their suitability for the selected type of adsorbent for this research project are studied in Section 2.6.4.

Several studies have measured the maximum capacity of the adsorbents for carbon dioxide (e.g., Lozinska et al., 2014; Mangano et al., 2013; Zhang et al., 2008; Zhu et al., 2014). These studies analyzed physisorption-based adsorbents, where the values of the capacity to adsorb carbon dioxide were between 2 and 4 mol/kg. A study by García et al. in 2013 produced maximum values as high as 10 mol/kg for the capacity of an activated carbon adsorbent for carbon dioxide at pressures up to 3000 kPa. Previous studies have shown that chemisorption-based adsorbents yield lower capacity values of around 1 mol/kg (Arenillas et al., 2005; Harlick and Sayari, 2006; Liu et al., 2013). The capacity values of these adsorbents were measured at between 25 and 100°C; at higher temperatures these values would be expected to be higher (Abanades et al., 2015). Therefore, there is a need for further research on chemisorption-based adsorbents to establish the process conditions under which their capacity can be maximized.

2.4.3 Fixed-Bed Reactor Experiments

Adsorbents must have a high operating adsorption capacity as well as selectivity for carbon dioxide. The operational capacity of the adsorbents is commonly measured by testing these materials in fixed-bed reactor experiments under fixed operational conditions. The working capacity of the adsorbents measured in these experiments is usually lower than those measured in isotherm experiments, due to the adsorption not achieving equilibrium. Additionally, fixed-bed reactor experiments are used to compare the affinity of an adsorbent for the components in the gas phase, referred to as selectivity.

In a study by Yuan et al. (2013) of a highly mesoporous adsorbent, a series of experiments showed that, although CO_2 selectivity values decreased gradually with the increasing mole fractions of CH_4 and N_2 in the gas phase, the values for selectivity were no lower than 2.5 and 8, respectively, at 45°C and 100 kPa, when the mole fraction of CH_4 and N_2 was 0.95. The study concluded that the selectivity for CO_2 was higher when the gas was mixed with N_2, due to the polarity of carbon dioxide, its affinity for the polar behaviour of the surface of the sorbent, and the non-polarity of N_2.

Fixed-bed reactor experiments are also used to measure the cyclic working capacity of an adsorbent. The adsorbent should be regenerated without losing its performance properties and original chemical composition. A recent study by Sun et al. (2015) analyzed the behaviour of a surface-modified spherical activated carbon material that operated under the conditions of 20 bar and 30°C. Results showed that after 20 cycles of adsorption and desorption, there were negligible changes in the uptake of carbon dioxide and the kinetics

were stable for both processes. The cyclic performance showed great promise for pre-combustion capture, according to the authors.

Another study, by Dinda (2013), presented an adsorption process that was carried out at 55°C with a concentration of 9% (volume-based) carbon dioxide that was regenerated at 120°C for the first three cycles and 130°C for the fourth one. The results showed that around 92% of the carbon dioxide was recovered for the first two cycles and around 88% for the third cycle.

Breakthrough experiments are also used to obtain the mass transfer coefficients for fixed-bed reactor models (Aguilera and Gutiérrez Ortiz, 2016; Knox et al., 2016). This is done by fitting the outcome of an adsorption model to the experimental data, by varying the mass transfer coefficient of one of the components. The mass transfer coefficient value is highly dependent on the adsorption kinetics for a given experiment in a fixed-bed reactor, during which the slope of the breakthrough increases with increasing values of the mass transfer coefficient. The relationship between the mass transfer coefficient and the breakthrough experiments is discussed further in Section 2.6.6.

2.5 Adsorption Applied to CCUS

Once the adsorption capacity and the selectivity of an adsorbent for a component in the gas phase are measured, the adsorption bed needs to be regenerated. This happens in industrial adsorption processes that operate in a cyclic mode, in order to operate continuously. The adsorbent bed is regenerated by changing the conditions of the fixed-bed reactor. These involve changes in the pressure, temperature and composition of the gases entering the fixed-bed reactor.

Changing the operating variable values in the fixed-bed reactor unit produces a series of steps that forms the adsorption-desorption cycle. Previous work focused on the arrangement and conditions of these steps in order to obtain high purity and recovery values of the non-adsorbed product. If adsorption processes are applied to carbon capture, attention should be paid to the conditions and steps of the regeneration process, since the adsorbed product (the heavy product) in this case has to fulfil the purity requirements for the purpose of storage.

2.5.1 The State of the Art of the Adsorbent Technology

The main strategies for recovering an adsorbent in an industrial process are recovery via the pressure differential and via the temperature differential (Yang, 1987). These regeneration strategies generate two industrial separation processes, called pressure swing adsorption and temperature swing adsorption (TSA). The adsorption capacity is given by the specific conditions of the pressure and temperature and of the gas composition. A change in one or more of these conditions changes the equilibrium between the solid and the gas phase (Grande, 2012).

TSA involves heating and cooling the adsorbent for regeneration purposes, which is very difficult to achieve in a short time and makes the overall cycle last for several hours (Webley, 2014). A study by Pirngruber et al. (2009) analyzed the performance of an amine-impregnated silica-based adsorbent in a fixed-bed reactor, using water vapour to increase the temperature during regeneration. The time required for desorption was longer than the adsorption time, implying that several columns would be required for the regeneration of the adsorbent. The use of water vapour to increase the temperature for

regeneration also consumed considerable energy in the process. Therefore, the increase in the temperature in the TSA process is expected to increase the energy penalty when the process is implemented in pre-combustion capture, due to the low operating temperatures.

The performance of TSA might potentially be more efficient in post-combustion capture, but adsorption processes applied to post-combustion could have disadvantages, due to the small amount of carbon dioxide in the flue-gas to be treated and the presence of sulphur and nitrogen monoxides, which would induce deactivation of the adsorbents and poison the adsorption surface (Aaron and Tsouris, 2005). Further research on adsorbent materials that can perform efficiently in such conditions is required.

PSA processes use high pressure and low pressure in a fixed-bed reactor for the cyclic adsorption and desorption of the heavy component, respectively. If the regeneration pressure goes below 1 bar, then the process is called vacuum swing adsorption (VSA). PSA has been shown to be the process of choice for pre-combustion capture, due to fast cycle times compared to those for TSA and due to being the main technology for hydrogen production (Abanades et al., 2015; Grande, 2012). The conditions used for hydrogen production are similar to those reported for pre-combustion capture (Casas et al., 2013a; Grande et al., 2017; Riboldi et al., 2014; Riboldi and Bolland, 2017).

PSA processes have commonly adopted steps to maximize the quality of the light product, aiming at over 95% purity values. They have been applied to industrial processes, such as ethanol dehydration, methane upgrading and purification of noble gases (Grande, 2012).

The performance of a PSA process is commonly measured by the purity obtained in the desired products, which is the amount of the gas component desired in the product stream divided by the amount of the product stream. In addition, the recovery of the product gas is another process performance indicator; it is calculated by dividing the amount of the gas component desired in the product stream by the amount of that same component in the feed stream.

These performance indicators depend on the selection and modification of the adsorbent material (the material engineering side) and the design of the PSA cycle (the process engineering side). These two sides of the design of a PSA unit must be effective and selective for the purpose of the process.

2.5.2 The Process Design for PSA

The first steps reported for a PSA process appeared in a study by Ruthven et al. in 1994, in which the four basic steps of a PSA process were shown. This process is called the Skarstrom cycle, and it was first designed to purify oxygen (Grande, 2012). Figure 2.3 is a diagram of the four steps in the PSA process.

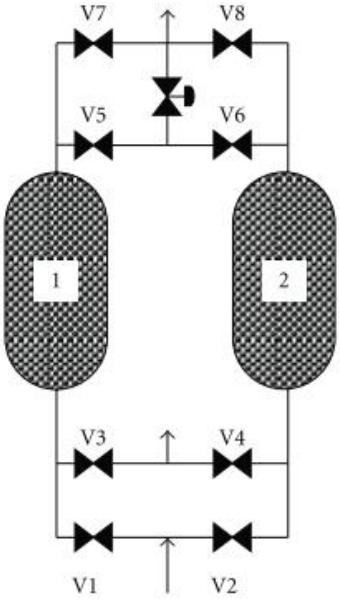

C1	Feed	Blow	Purge	Press
	V1, V7	V3	V5, V3	V1
C2	Purge	Press	Feed	Blow
	V6, V4	V2	V2, V8	V4

Figure 2.3. A schematic representation of the initial four-step Skarstrom cycle shown by Grande (2012)

The fixed-bed reactor is first pressurized with the feed gas until it reaches the adsorption pressure during the pressurization step, shown as “Press” in Figure 2.3. When the bed reaches the operating pressure, the product gas, the light product, is obtained at the end of the bed during the feed step, whereas the heavy components stay adsorbed in the fixed-bed reactor. Then the bed is depressurized during the blowdown step, shown as “Blow” in Figure 2.3., where the adsorbed gas starts desorbing near atmospheric pressures. Under these conditions and at constant pressure, a fraction of the light product is fed to the reactor to purge the remaining adsorbed gas out of the bed. Then the bed is again pressurized to repeat the cycle.

Following this reference study on this four-step process, there have been efforts by other authors to improve the quality of the light product by introducing additional steps into the PSA cycle. One of the main steps introduced in several patents and studies to improve the recovery of the light product is a step called pressure equalization (Lopes et al., 2011; Luberti et al., 2014b; Nikolaidis et al., 2015; Ribeiro et al., 2008). During this step, a depressurizing bed is connected to a pressurizing bed, saving on the total mechanical energy of the process. However, the introduction of pressure equalization steps needs additional fixed-bed reactors for the continuous operation of the process (Grande, 2012). Figure 2.4 shows the cycle configuration proposed by Ribeiro et al. (2008), where two pressure equalization steps are included.

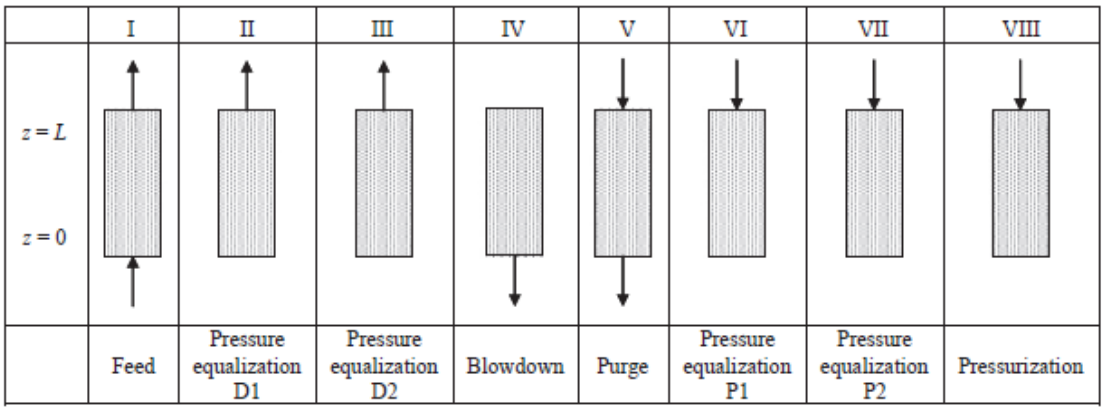

Figure 2.4. The PSA cycle configuration proposed by Ribeiro et al. (2008)

Another step introduced into PSA cycles has been the rinse step, in which a fraction of the heavy or light product is recycled after the adsorption step, from the purge step at 1 bar, in order to increase the recovery and the purity of the heavy or the light product,

respectively (Agarwal et al., 2010; Wang et al., 2015). This step has not been widely used in PSA, but the studies that have undertaken this step have demonstrated that it is essential when the heavy product must be produced at high purities beyond 95%, as in carbon capture. The PSA configurations that have been implemented for carbon capture processes are reported in Section 2.6.7.

The study by Luberti et al. (2014a) also introduced a providing purge (PP) step, which directs the outlet gas to a bed undergoing the purge (PU) step, as shown in Figure 2.5. This figure shows a flow diagram which is commonly used to represent the steps of a PSA process. These flow diagrams show the steps which only one fixed-bed reactor undertakes in the process, and they show the steps where the beds are interconnected. In the study by Luberty et al. (2014a) the beds were connected during the pressure equalization steps (DPE1, DPE2, PPE2 and PPE1), and during the PP and PU steps.

The table bellow the flow diagram in Figure 2.5 shows the sequence of the steps for each of the fixed-bed reactors of the process. Each of the rows of the table shows the steps of one fixed-bed reactor, as plotted by the author of the study (Luberti et al., 2014a).

This table also indicates which beds interact in each of the steps. For instance, the bed assigned to row 1 of the table, interacts with the bed of the second row during DPE1 and PPE1 steps. It also interacts with the bed in the third row during the PP and DPE2 steps, and with the bed in the fourth row during the PU and PPE2 steps. The interaction between the beds assigned to the rest of the rows is also determined the same way, by following the step interactions of the flow diagram, and determining which bed undergoes the complementary step in each moment of the process.

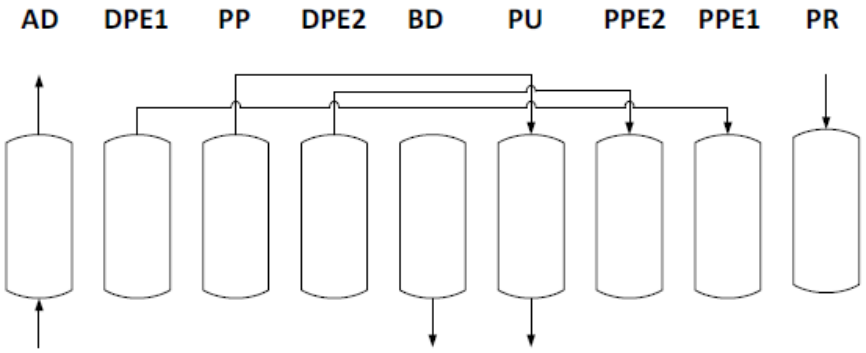

AD			DPE1	PP		DPE2	BD	PU	PPE2	PPE1	PR	
BD	PU	PPE2	PPE1	PR			AD			DPE1	PP	DPE2
DPE1	PP	DPE2	BD	PU		PPE2	PPE1	PR		AD		
PPE1	PR		AD				DPE1	PP	DPE2	BD	PU	PPE2

Figure 2.5. The PSA cycle configuration proposed by Luberti et al. (2014a)

2.5.3 Adsorbents for PSA

The properties of the adsorbent material are also important in determining the performance of a PSA process. When choosing a type of adsorbent for the process, several characteristics must be considered, such as the capacity, selectivity, chemical and thermal stability and the cost. The main adsorbents used in previous PSA processes were zeolites and carbon-based adsorbents, such as activated carbons and metal organic frameworks (Abanades et al., 2015). Table 2.2 shows some of the adsorbents analyzed in previous studies; their pore volume and carbon dioxide capacity at 10 kPa and temperatures are stated in the table.

Table 2.2. Comparison of adsorbents for carbon dioxide capture

Study	Adsorbent	Pore volume (cm^3/g)	CO_2 capacity (mol/kg)
Hao et al. (2013)	PAC	0.379	0.9 (298 K)
Harlick and Tezel (2004)	13X	0.506	2.6 (295 K)
Liu et al. (2012)	Ni-CPO-27	0.530	4.07 (298 K)
Lozinska et al. (2012)	Na-Rho	0.439	3.07 (298 K)
Yazaydin et al. (2009)	MOF-177	1.890	0.08 (298 K)
Zhang et al. (2008)	K-CHA	0.434	3.8 (303 K)

On the one hand, numerous studies highlight the advantages of zeolites as adsorbents. According to Hao et al. (2011), they exhibit microporous features and a high crystalline structure that gives a high chemical and thermal stability to the material. Samanta et al. (2012) concluded that zeolites have comparatively fast CO_2 adsorption kinetics and achieve equilibrium capacity in a few minutes.

On the other hand, the presence of water may greatly reduce the capacity of zeolites due to their chemical surface structure, lowering the adsorption area for carbon dioxide (Brandani and Ruthven, 2004). Surblé et al. (2006) claimed that, although zeolites are adequate for pressure swing adsorption processes, they need a large amount of heat to be regenerated, which increases the cost of the overall process.

Metal-organic-framework-based adsorbents are also promising for carbon dioxide removal purposes. Their regeneration energy is lower than that of zeolite adsorbents and their surface can be easily modified. They yield high capacity and selectivity values when the system operates at high pressures, due to the affinity of carbon dioxide to the surface area, compared to other gases such as carbon monoxide, hydrogen or nitrogen (Hao et al.,

2011). However, the lack of chemical and thermal stability makes MOFs difficult to implement in processes that require complex environments.

Although previous studies have analyzed the properties of these materials, activated carbons have been the main area of focus for the development of the adsorbents used in PSA (Abanades et al., 2015), and they are the adsorbents of choice for this study.

2.5.4 Activated Carbon Adsorbents

Numerous authors have outlined the advantages of activated carbon adsorbents (ACs), namely, their structural stability, relatively cheaper prices than those of other adsorbents, commercial availability, and recyclability (Di Biase and Sarkisov, 2015; Hao et al., 2011). Also, these adsorbents can be produced from waste materials, which decreases their cost (Chen et al., 2013). Moreover, they have fast adsorption kinetics, as the pore size distribution is usually wide in this material where macropores and mesopores enable diffusion of carbon dioxide to the micropores (Hao et al., 2011). Figure 2.6 shows the SEM images of the activated carbon studied by Sun et al. (2015), where the activated carbon particles and the surface structure can be observed at different microscope scales.

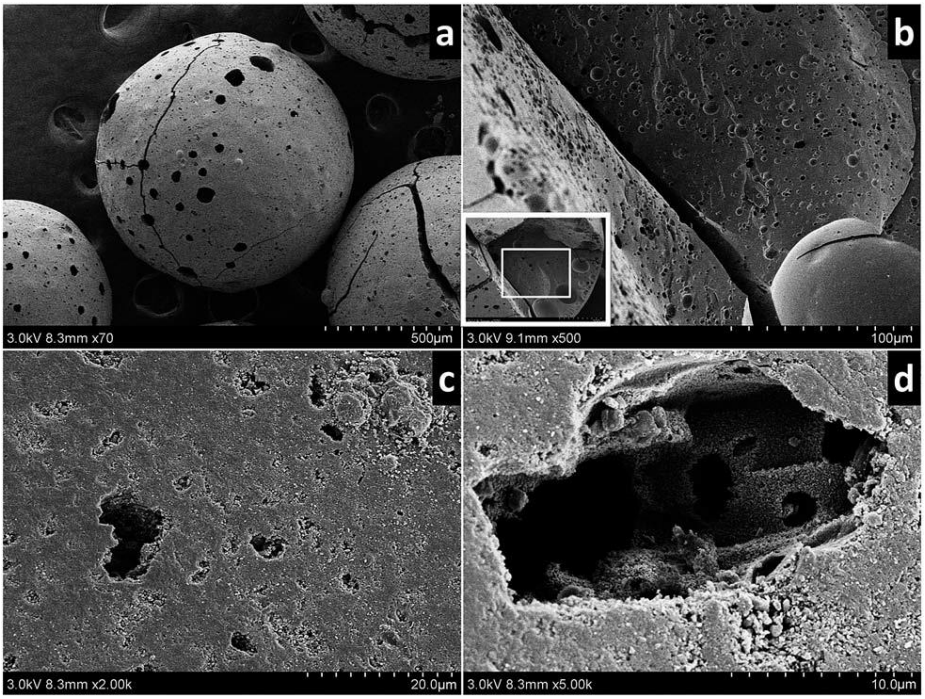

Figure 2.6. SEM images of the activated carbon at (a) 0.5 mm, (b) 0.1 mm, (c) 0.02 mm and (d) 0.01 mm microscope scale obtained by Sun et al. (2015)

ACs are stable under a broad range of temperatures and pressures and have a consistent adsorption behaviour. However, the selectivity and capacity for carbon dioxide could decrease when the process in which they are applied operates at low pressure, high temperatures and low carbon dioxide partial pressures (Choi et al., 2009; D'Alessandro et al., 2010; Di Biase and Sarkisov, 2015; Shafeeyan et al., 2015). Therefore, the performance of these adsorbents would decrease if the process operated under post-combustion conditions.

In contrast, several studies outline the fact that activated carbons with a high surface area and porosity show a high capacity and selectivity for carbon dioxide when the process operates under high pressure and at the relatively low temperatures of around 25°C to

85°C. This makes them suitable candidates for pre-combustion carbon dioxide capture via PSA (Himeno et al., 2005; Jordá-Beneyto et al., 2007).

2.5.5 Modifications to the Surface of the Adsorbents

In order to increase the selectivity and capacity of the adsorbent materials, the chemical impregnation of their surface has been broadly investigated (Plaza et al., 2008; Sun et al., 2015). The study by Hao et al. (2011) summarized some of the modifications carried out in metal organic frameworks, zeolites, silicas and activated carbons. The study revealed improved properties for most of the adsorbents when chemical groups were inserted onto their surface, so specifically improving their capacity for the adsorption of carbon dioxide.

Several studies have included the modification of activated carbon adsorbents via the insertion of amine groups into the surface (Chen et al., 2013; Shafeeyan et al., 2015; Sun et al., 2015; Wang et al., 2018; Zhu et al., 2014). Table 2.3 presents some of the studies that impregnated the surface with amine groups for the purpose of carbon dioxide adsorption.

Table 2.3. A comparison of various amine-modified adsorbents for carbon dioxide capture

Study	Adsorbent	Amine group	CO_2 capacity (mol/kg)
Ebner et al. (2011)	CARiACTG10	PEI	2.80 (353 K)
Franchi et al. (2005)	PE-MCM-41	DEA	2.85 (298 K)
Harlick and Sayari (2006)	PE-MCM-41	TRI	2.65 (298 K)
Knowles et al. (2005)	H5a-DT	AP	1.59 (298 K)
Liu et al. (2013)	MCM-41	TEPA	2.70 (298 K)
Zhang et al. (2014)	Silica	PEI	2.18 (343 K)

The insertion of amine groups onto the carbonaceous surface improved the chemical bonding between the surface and the carbon dioxide in the studies shown in Table 2.3. These studies used between 10 to 40 wt% of amines to substrate concentration. In these studies, the amine concentration on the adsorbent surface was related to the carbon dioxide adsorption performance. A study by Kamarudin and Alias (2013) used a maximum of 25 wt% of amine concentration on a silica adsorbent surface because the authors observed that the carbon dioxide adsorption capacity decreased at higher concentrations. A study by Zhao et al. (2010) reported that amine-rich carbons from glucose precursors showed high capacities for CO_2 (higher than 4.1 mmol/g) using oligo-amine concentrations on the surface between 5 to 10 wt%, although the authors stated that glucose-derived carbons had low specific surface areas and no microporosity. Figure 2.7 shows the experimental procedure followed by Zhu et al. (2014) to obtain nitrogen-enriched activated carbons. As shown in Figure 2.7, amine groups were used to impregnate the surface, before the activation of the adsorbent. In this study, the maximum carbon dioxide capacity registered was 3.8 mol/kg, at 1 bar and 25°C.

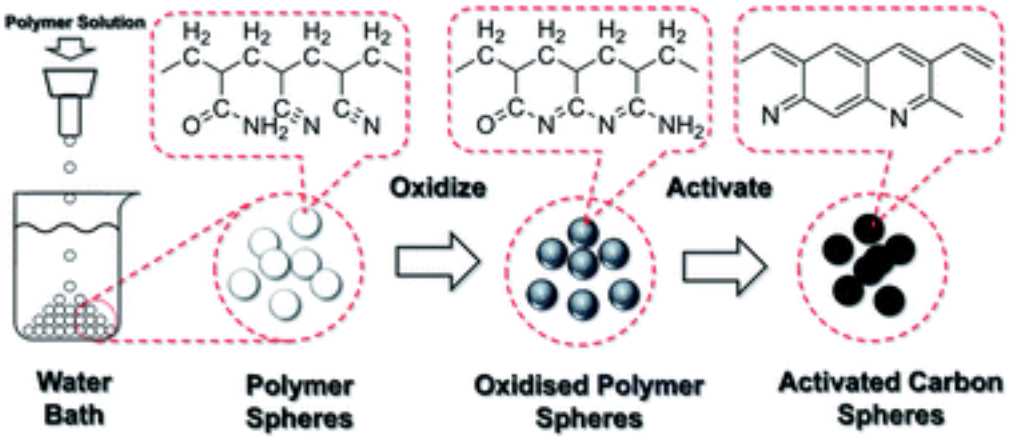

Figure 2.7. The experimental procedure developed by Zhu et al. (2014) to obtain nitrogen-enriched activated carbons

The studies in Table 2.3 together with the study by Zhu et al. (2014) show that carbons that have lower thermal activation temperatures but that have been modified using nitrogen groups show higher capacities, due to an optimum balance of nitrogen and micropores on the surface. The experiments to analyze the capacity of the adsorbents in these studies were carried out at 1 bar and temperatures up to 75°C.

Therefore, amine-modified adsorbents look promising for post-combustion capture, during which adsorption processes would operate at high temperatures and with lower partial pressures of carbon dioxide. However, there is a need for further research on the adsorption-desorption kinetics of amine-modified adsorbents in pre-combustion capture conditions (Abanades et al., 2015). Chemical impregnation could favour the adsorption-desorption performance of the adsorbent by pressure differential when the temperatures are relatively high, about 75 °C, under pre-combustion conditions.

2.6 Simulation Applied to PSA Processes

Once the adsorbent performance is tested for the purpose of the application, the properties of these adsorbents can be used to determine the process design. The modelling of pressure swing adsorption processes has been broadly used in the literature to analyze the separation performance in a fixed-bed reactor. Simulations using PSA processes have become a tool to predict and optimize the performance of the unit for new applications, in terms of cost, energy and product performance. This approach saves costs because an optimum design can be selected before the process is scaled up for commercial purposes. For carbon capture applications, the approach is viewed as an essential step before the implementation of the technology at large scale (Abanades et al., 2015).

The main variables that determine the performance of a fixed-bed reactor unit are the concentration of the components in the gas and solid phases, the temperature of the gas and the adsorbent and the pressure of the gas (Rase, 1990).

The values on these variables are calculated by solving a mass balance equation and energy balance equations applied to the reactor and by determining the pressure drop within the reactor. Modelling the PSA processes reveals their complexity; because of the number of calculation points and discontinuities due to flow reversals, numerous assumptions have been developed in previous studies; these are now well established and validated for this process (Tien, 2019).

Simulation applied to PSA processes has focused mainly on gas separation processes that obtain the light product, especially on hydrogen production (Moon et al., 2018; Ribeiro

et al., 2008). Therefore, the previously designed PSA processes targeted the obtention of high purity and recovery values for these products.

This study aims to achieve PSA configurations that achieve high purity and recovery values of both the light (hydrogen) and heavy (carbon dioxide) product. Achieving purity values over 95% in both products and recovery values over 90% in the light product is essential for the implementation of the process as a carbon capture technology. Additionally, this study aims to investigate the viability of the designed processes in terms of the energy usage and the cost of the process. Table 2.4 shows the common operational values and product requirement targets for PSA based on the main studies of PSA applied to hydrogen purification and carbon capture (Abanades et al., 2015; Moon et al., 2018; Ribeiro et al., 2008; Riboldi and Bolland, 2015b).

Table 2.4. Typical PSA process conditions and product performance indicator targets

Operational variable/ Performance indicator	Values/Target	Unit
Adsorbent capacity	2–3	mol/kg
Adsorption pressure	7–40	bar
Temperature	293–370	K
Carbon dioxide purity	95	%
Carbon dioxide recovery	> 90	%
Hydrogen recovery	> 90	%

2.6.1 The Overall Model

One of the main assumptions presented in previous work is that the unidimensional dispersed plug-flow model applies to PSA processes (Casas et al., 2013a; Moon et al., 2016; Nikolaidis et al., 2015; Riboldi and Bolland, 2016). This means that there are no radial variations in the pressure, temperature and concentration of the components in the gas and solid phase, especially in the large-scale industrial process (Ruthven et al., 1994). This assumption describes the diffusion of the gas phase through the reactor. The total gas concentration in the fixed-bed reactor is related to the total pressure by using an equation of state (EOS).

In terms of the mass transfer between the gas and the solid phase, the components go through three steps during adsorption. First, the components transfer from the gas phase to the film outside the surface of the particle. Then the components diffuse through the pores of the solid, and finally they become adsorbed onto the solid surface inside the pores (Unuabonah et al., 2019). The other main assumption adopted broadly in the literature pertains to the linear driving force (LDF). The LDF assumes that one of the mass transfer resistances is the controlling mechanism and that there is a constant gradient of the mass transfer rate of the components between the gas and the solid surface.

This assumption has been widely applied to PSA systems featuring activated carbons (Hao et al., 2018; Lopes et al., 2011; Moon et al., 2018; Ribeiro et al., 2008; Riboldi and Bolland, 2015b). The application of the LDF model to activated carbons that operate in fixed-bed reactors at high pressure is mainly supported by the study by Ribeiro et al. (2008).

This last study showed that this assumption is valid for PSA systems that feature natural gases and that use activated carbon adsorbents. In this work, a full model was compared with a simplified model that assumed that diffusion through micropores was the controlling step, as described by the Linear Driving Force Model. The simplified model predicted identical trends for the concentration of the components, compared to the full model, which considered all the steps of the mass transfer resistance. Figure 2.8 shows how the main equations are used in the model and the interaction between them. The equations are shown inside the rectangular shapes, while the obtained variables are shown inside the elliptical shapes. The cylindrical shapes contain the initial and output variables.

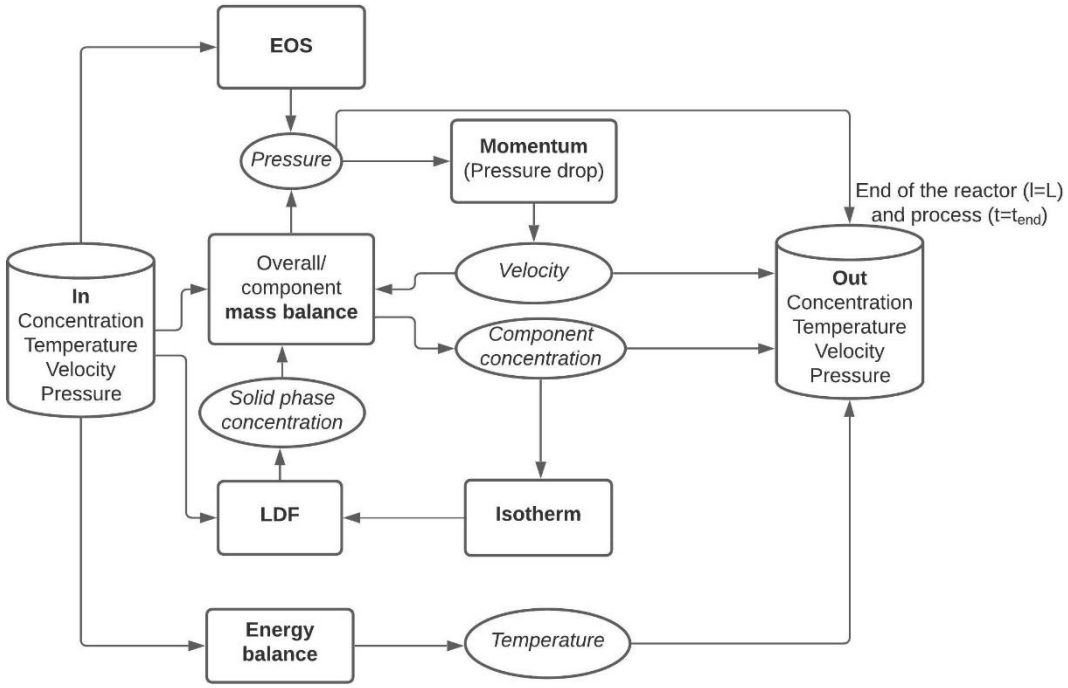

Figure 2.8. A flow diagram of the interaction between the main equations used in the axially-dispersed plug-flow model

2.6.2 The Gas Phase Equation of State

The thermodynamics of adsorption are defined by the Gibbs free energy, which is the chemical potential upon adsorption of a gas component, relative to the clean adsorbent. This is defined by the enthalpy and entropy of adsorption (Myers, 2003). These values are all negative because adsorption is an exothermic reaction. The values of G, H and S are dependent on both temperature and pressure. The enthalpy of adsorption, also called the heat of adsorption, is the amount of energy released to the ambient air by the adsorption process and is commonly measured by comparing the isotherm measurements at various temperatures. This variable is important for defining the affinity between the gas component adsorbed and the solid adsorbent.

The heat of adsorption is affected by the properties of the gas component to be adsorbed. These properties are related by the equation of state (EOS), which defines the relationship between the pressure, temperature and volume of the gas mixture. From these values, the density, viscosity and specific heat of the components in the gas phase are determined.

Defining an EOS for adsorption simulations is essential for establishing the relationship between these variables. Table 2.5 shows the EOS chosen by studies that feature the adsorption of gases at high pressures.

Table 2.5. Comparison of EOSs for gas-adsorption processes

Study	Application/ Process	Components	Conditions	Adsorbent	EOS
Casas et al., 2012	Breakthrough experiments	CO_2/H_2	T: 298 K P: 1–35 bar	AC	Peng-Robinson
Casas et al., 2013a	Carbon capture via PSA	CO_2/H_2	T: 473 K P: 1–25 bar	AC	Ideal gas
Casas et al., 2013b	Carbon capture via PSA	CO_2/H_2	T: 298 K P: 1–25 bar	MOF	Ideal gas
Khurana and Farooq, 2019	Carbon capture via VSA	CO_2/N_2	T: 298 K P: 0.05–1 bar	MOF/Zeolite	Ideal gas
Knox et al., 2016	Breakthrough experiments	CO_2/H_2O	T: 298 K P: 1-7 bar	Zeolite	Ideal gas
Luberti et al., 2014a	Carbon capture via PSA	$Ar/CO/CO_2/H_2/N_2$	T: 303 K P: 1–34 bar	Zeolite	Ideal gas
Moon et al., 2018	Carbon capture via PSA	$Ar/CO/CO_2/H_2/N_2$	T: 308 K P: 1–35 bar	AC/Zeolite	Soave-Redlich-Kwong
Ribeiro et al., 2008	Hydrogen production via PSA	$CO/CO_2/CH_4/H_2/N_2$	T: 303 K P: 1–7 bar	AC/Zeolite	Ideal gas
Riboldi and Bolland, 2015b	Carbon capture via PSA	$Ar/CO/CO_2/CH_4/H_2/N_2$	T: 337 K P: 1–38.8 bar	AC/Zeolite	Ideal gas

Table 2.5 shows that most of the studies used the ideal gas equation for gases at high pressures, although the deviation from the ideal state of the gas is higher at pressures above 1 bar. The most common non-ideal EOS models used in previous studies were the Peng-Robinson and Soave-Redlich-Kwong EOSs. However, these studies also used the ideal gas equation to describe the behaviour of the components in the gas phase.

For instance, in the work by Casas et al. (2012), the Peng-Robinson EOS was used to calculate the compressibility factor of the gas mixture to be studied, which is a variable that measures the deviation of the gas phase from ideal behaviour. The compressibility factor calculated in this study was between 0.9 and 1. Therefore, the hydrogen and carbon dioxide gas mixture studied was considered ideal for the given conditions of the process, featuring temperatures between 298 and 373 K and pressures between 1 and 35 bar.

2.6.3 The Mass and Energy Balance

In fixed-bed reactor models, the mass and energy balance equations are used to describe the evolution of the components' concentration and the temperature within the reactor. These equations are based on the previous assumption of the dispersed plug-flow model in the main PSA studies that cover fixed-bed reactor models (Casas et al., 2012; Moon et al., 2018; Luberti et al., 2014a; Riboldi and Bolland, 2015b). The variations of mass and temperature happen in the dimensions of space (length of the bed) and time, based on the previously mentioned assumption of dispersed plug-flow. These assumptions underpin the partial differential equations to describe the evolution of mass and temperature. These partial differential equations include the accumulation, dispersion, inlet and outlet, and reaction terms that hold for adsorption (Ruthven et al., 1994).

$$\frac{\partial C}{\partial t} = -\frac{\partial (Cv)}{\partial z} + D_x \frac{\partial^2 C}{\partial z^2} - \frac{(1-\varepsilon_t)}{\varepsilon_t} \frac{\partial Q}{\partial t} \qquad 2.1$$

Most of the studies undertaken previously on modelling PSA include the axial-dispersion term shown in Equation 2.1. However, some studies did not include this term in the plug-flow model (e.g., Agarwal et al., 2010; Dowling et al., 2012; Wang et al., 2015). Dowling

et al. (2012) did not include the dispersion term, because its value obtained after numerical integration was typically greater than the real value that obtained in industrial PSA processes. In other cases, the dispersion coefficient was not included in order to simplify the model, such as in Effendy et al. (2017).

Seader and Henley (2006) stated that axial dispersion can be neglected for extractors whose phase separation occurs between stages (for example, for mixer-settler cascade extractors or sieve-plate columns), but that it can be significant for packed columns. Another study, by Knox et al. (2016), stated that 1-D axial dispersion cannot be ignored in fixed-bed reactors, since it reduces capture efficiency.

When they include the axial dispersion term, most studies use empirical correlations, specifically, the Wakao and Funazkri correlation (Wakao and Funazkri, 1978) as do Lopes et al. (2011), Nikolaidis et al. (2015) and Nikolic et al. (2008). In other studies, the axial-dispersion coefficient is obtained using parameter estimation (Knox et al., 2016). Other studies have added complexity to the mass balance equation, by establishing a mass balance in the solid phase. A case in point is the study by Ribeiro et al. (2008), where the authors compared a model that included the mass balance in the solid phase to one that did not. The study concluded that the results after the addition of this complexity to the model did not deviate much from the results of the simplified model.

Heat dispersion is also included in the axially-dispersed plug-flow model to account for the energy balance; most of the studies infer that the gas and the solid phase are in thermal equilibrium (with and without wall effects) (Casas et al., 2013a; Moon et al., 2018; Luberti et al., 2014a; Ribeiro et al., 2008).

$$\varepsilon_t \frac{\partial(\rho c_{p,g} T)}{\partial t} + (1-\varepsilon_t)\frac{\partial(\rho_s c_{p,s} T)}{\partial t} = -\varepsilon_b \frac{\partial(\rho c_{p,g} T v)}{\partial z} + (1-\varepsilon_t)\rho_s \sum_{i=1}^{N_{comp}} \Delta H_{ads} \frac{\partial Q_i}{\partial t} + \varepsilon_b \lambda \frac{\partial^2 T}{\partial z^2} - \frac{2h_{wall}}{R_{in,bed}}(T - T_{wall}) \quad 2.2$$

The system has been considered by a few authors to be adiabatic (e.g., Riboldi and Bolland., 2015b) and it has been viewed as mostly non-isothermal with wall effects, as shown in Equation 2.2 (Agarwal et al., 2010; Casas et al., 2012; Dowling et al., 2012; Ribeiro et al., 2008; Schell et al., 2009; Wang et al., 2015). A study by Grande in 2012 stated that the heat generated in the adsorption step must be taken into consideration, as it can have consequences for the adsorption capacity. On the one hand, temperature variations may be important at laboratory scale, when the heat capacity of the wall should be included. On the other hand, the same author observed that large-scale PSA processes may behave adiabatically.

2.6.4 Isotherm Models

The implementation of an isotherm equation in a fixed-bed reactor model is necessary to describe the relationship between the gas and the solid phase. The parameters of an isotherm model describe the capacity of a material to adsorb a gas component; this capacity changes with pressure and temperature. The experimental data is recorded into a graph and then is used to validate or reject a number of isotherm models that describe this relationship; the shape of the isotherm can give important information about the pore structure and the isotherm model to apply (Rouquerol et al., 2014). The type of isotherm model depends on the equilibrium data extracted from laboratory HPVA (High Pressure Volumetric Analyzer) experiments; this data is specific for each type of adsorbent.

Several isotherm models have been used in past studies to obtain equilibrium data for carbon dioxide adsorption in fixed-bed reactors at high pressures. On the one hand, the Langmuir isotherm, given by Equation 2.3, has been widely used in the previous literature for carbon dioxide adsorption (Agarwal et al., 2010; García et al., 2013; Singh and Kumar, 2016; Yuan et al., 2013). For adsorption processes via the chemisorption mechanism, this is the common isotherm model, due to monolayer adsorption via a chemical bond (Rouquerol et al., 2014). This isotherm assumes that each site is covered by an adsorbed molecule and that the adsorption energy is equally distributed over all the sites. The amount of adsorbed gas is proportional to the surface available for the adsorbate (Ayawei et al., 2017).

$$q_i = \frac{q_{mi} b_{mi} P_i}{1+\sum_{j=1}^{n} b_{mj} P_j} \quad 2.3$$

$$Q^*_{(i,z)} = \frac{q^s_{1i} b_{1i} P_i}{1+\sum_{j=1}^{n} b_{1j} P_j} + \frac{q^s_{2i} b_{2i} P_i)}{1+\sum_{j=1}^{n} b_{2j} P_j} \quad 2.4$$

$$q_i = \frac{q_{mi} b_{mi} P_i^{\frac{1}{n_i}}}{1+\sum_{j=1}^{n} b_{mj} P_j^{\frac{1}{n_j}}} \quad 2.5$$

Several other isotherm models for the physisorption of carbon dioxide at high pressures are reported in the literature, the most common being the multi-site Langmuir (MSL, Equation 2.4), where numerous sites are covered by the adsorbate molecules. The Langmuir-Freudlich (LF, Equation 2.5) isotherm has also been implemented for a number of PSA systems; it describes the adsorption of the component under study onto a heterogeneous adsorbent surface and how the adsorption energy is distributed in the heterogeneous surface (Ayawei et al., 2017). Some other studies used the Sips isotherm, which is a combination of the Langmuir and the LF isotherm (Tzabar and ter Brake,

2016). Table 2.6 shows the isotherm models chosen by the main recent studies of PSA under pre-combustion conditions.

Table 2.6. A comparison of isotherm models for adsorption processes at high pressure

Study	Application/ Process	Components	Conditions	Adsorbent	Isotherm
Casas et al., 2012	Breakthrough experiments	CO_2/H_2	T: 298 K P: 1–35 bar	AC	Sips, Langmuir
Casas et al., 2013a	Carbon capture via PSA	CO_2/H_2	T: 473 K P: 1–25 bar	AC	Sips
Luberti et al., 2014a	Carbon capture via PSA	$Ar/CO/CO_2/H_2/N_2$	T: 303 K P: 1–34 bar	Zeolite	DSL
Moon et al., 2018	Carbon capture via PSA	$Ar/CO/CO_2/H_2/N_2$	T: 308 K P: 1–35 bar	AC/Zeolite	DSL
Ribeiro et al., 2008	Hydrogen production via PSA	$CO/CO_2/CH_4/H_2/N_2$	T: 303 K P: 1–7 bar	AC/Zeolite	MSL
Riboldi and Bolland, 2015b	Carbon capture via PSA	$Ar/CO/CO_2/CH_4/H_2/N_2$	T: 337 K P: 1–38 bar	AC/Zeolite	MSL

From Table 2.6 it is clear that many recent studies chose the DSL isotherm model for the adsorbents undergoing physisorption. A study by García et al. (2013), in which the isotherms for carbon dioxide, hydrogen and nitrogen were obtained for resin-based activated carbon at pressures ranging from 0 to 40 bar, also presented the DSL model as the best fit for the measured experimental CO_2 data.

From previous studies, it is clear that the isotherm models and parameters have to be determined and measured for the specific material and conditions that hold for the

process, because there is no overall agreement about which isotherm is the most suitable for adsorbent materials at high pressures.

2.6.5 Pressure Drop in a Fixed-Bed Reactor

Pressure drop is a phenomenon that must be included in any model of a fixed-bed reactor, due to the friction of the fluid against the catalysts and the reactor wall. Pressure drop is a variable that affects the velocity of the gas phase in the unit. It is a function of the density and the dynamic viscosity of the gas phase, of the particle diameter and of the fixed-bed reactor porosity (Casas et al., 2012). Pressure drop also affects the compression requirements of the gas, and thus, the energy requirements of the PSA process (Wang et al., 2015). Therefore, it is important to include this variable when determining the design and the amount of adsorbent in an industrial-scale unit (Worstell, 2014). The pressure drop of a fixed-bed reactor is commonly determined using a momentum balance equation that relates the fluid properties and the packing of the reactor to the drop in kinetic and mechanical energy.

The main correlation used in previous PSA studies for gas purification and carbon capture processes to determine the momentum balance is the Ergun equation (Casas et al., 2012; Moon et al., 2018; Ribeiro et al., 2008; Riboldi et al., 2014; Wang et al., 2015), given by Equation 2.6 (Shafeeyan et al., 2014). The momentum balance includes both the viscous (k_D) and the kinetic forces (k_v). However, if the Reynolds number is very low for the process (less than 5), the kinetic term can be neglected and the balance is determined by Darcy's equation (Ding and Alpay, 2000; Shafeeyan et al., 2014). Although the previously mentioned variables in the correlation can be empirically determined, most

studies of PSA as it applies to carbon capture used the terms determined by Ergun (1952), shown in Equations 2.7 and 2.8.

$$-\frac{\partial P(z)}{\partial Z} = k_D v_z + k_v v_z^2 \quad 2.6$$

$$k_D = 150 u_{g,z} \frac{(1-\varepsilon_b)^2}{D_p^2 \varepsilon_b^3} \quad 2.7$$

$$k_v = 1.75 \frac{(1-\varepsilon_b)\rho}{D_p \varepsilon_b^3} \quad 2.8$$

2.6.6 The Validation of PSA Models using Adsorption Experiments

The mass and energy balance, together with the mass transfer, equilibrium and the equation of state, describe the adsorption model that gives a breakthrough curve as a result. The suitability and working capacity of an adsorbent for a particular application under specific conditions can be measured from the plots of the breakthrough curves. With this method, certain authors were able to go further not only in studying the equilibrium behaviour of the adsorbent, but also in measuring its suitability when operating under process conditions at laboratory scale. Figure 2.9 shows an example breakthrough curve obtained in a fixed-bed reactor (Seader and Henley, 2006). The breakthrough point is indicated as t_b, when the solute concentration coming out the fixed-bed reactor (C_f) is 5% of the solute concentration in the feed (C_F).

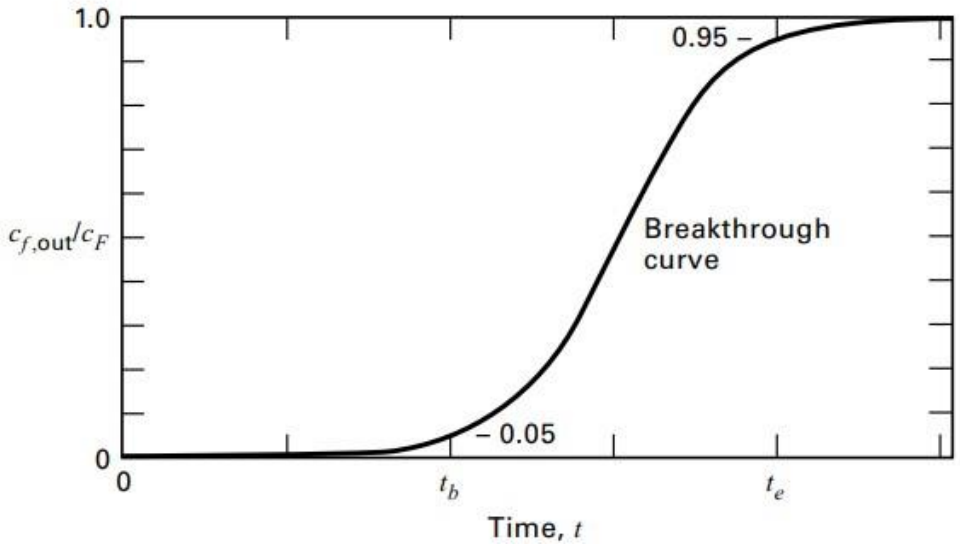

Figure 2.9. An example breakthrough curve illustrated by Seader and Henley (2006)

Aguilera and Gutiérrez Ortiz (2016) observed that the most influential variables for the linear driving force (LDF) model fell into two groups: (i) those obtained by comparing experimental data to a model or to correlations, such as the mass transfer and the axial dispersion coefficients, and (ii) those obtained from experimental conditions, such as the gas velocity, bed height and void fraction of the bed. The study showed that variations in the bed length and void fraction shifted the breakthrough curve considerably, over a range of between 1000 and 5000 s. Therefore, this study showed that defining the value of these variables is essential to determine the performance of the adsorption process.

Knox et al. (2016) also showed that the axial dispersion and mass transfer terms can be obtained by fitting the experimental data to the simulation results. They concluded that the LDF model was the preferable method for obtaining experimental mass transfer data for a one-dimensional axially-dispersed plug-flow model. On this point, a sensitivity analysis carried out by Aguilera and Gutiérrez Ortiz (2016) to see the effect of the above

variables found that when the mass transfer coefficient increased in the simulated LDF model, the slope of the breakthrough trend increased due to the decrease in mass transfer resistance.

In addition, they found that the axial dispersion coefficient also had a significant effect on the shape of the breakthrough curves at laboratory scale: with an increase in the axial dispersion coefficient from $3x10^{-4}$ to $7x10^{-4}$ m^2/s, the Peclet number decreased from 10.7 to 4.6. Therefore, axial dispersion must not be ignored when operating in a fixed bed at laboratory scale (Aguilera and Gutiérrez Ortiz, 2016; Knox et al., 2016).

The study by Knox et al. (2016) also analyzed the effect of estimating the mass transfer and dispersion coefficients simultaneously using parameter estimations based on a comparison of the experimental and model data, an approach used in several studies. The study concluded that one of the coefficients should be fixed to obtain accurate results and suggested that the dispersion of the bed should be measured before comparing the experimental data to the model.

The experimental determination of the adsorbent surface and fixed-bed reactor is important in determining the values of the model parameters, such as the mass transfer and axial dispersion coefficients. A study by Xiao et al. (2016) used an activated carbon and zeolite 5A. The pellet size and total void fractions of the system in the experiments that used activated carbon were 1.15 mm and 0.78, respectively, while the values of these parameters were 1.57 mm and 0.77 for the system using zeolite 5A. The mass transfer coefficient value in the experiments on activated carbon was fixed at 0.0355 s^{-1}, while the value of this parameter was fixed at 0.0135 s^{-1} for the experiments using zeolite 5A.

Few studies have analyzed the effects of adsorbent properties, the mass transfer coefficient and the dispersion coefficients on the shape of the breakthrough curves for activated carbon adsorbents in pre-combustion capture conditions. Sie et al. (2016) and Sun et al. (2015) studied the adsorption behaviour of the synthesized MOF for pre-combustion carbon dioxide capture, but did not show the effect that the synthesized inorganic framework and activated carbon adsorbents' surface properties had on the breakthrough curves.

Xiao et al. (2016) studied the effects of the flow rate and composition of the feed gas and of the axial dispersion coefficient for a mixture of hydrogen, carbon dioxide, carbon monoxide and methane in a fixed-bed reactor with zeolite 5A and activated carbon. However, the study did not analyze the effects on the breakthrough curves of the mass transfer coefficient and of adsorbent properties such as particle size, the bed void fraction and the void fraction of the adsorbent.

At this point, further study is needed to see the effects of the adsorbent and process variables on the breakthrough curves for carbon dioxide and hydrogen mixtures in pre-combustion capture conditions that feature activated carbons, because the breakthrough times can have a direct effect on the recovery and purity of the products and on the cost of the whole process.

2.6.7 The Process Steps of PSA Models Used to Capture Carbon Dioxide

In previous studies, the configurations of the steps in PSA were specifically designed for the purpose of the process. Up until now, most studies have produced cycle configurations for overall gas separation or for hydrogen purification. Few studies have reproduced step

configurations for hydrogen and carbon dioxide mixtures, in which both components must be obtained with high purity and recovery percentages (over 90%). The aim of this study was defined from this gap in literature, namely, that PSA configurations have been designed to maximize the purity and recovery of the hydrogen, instead of those of carbon dioxide. This project aimed to obtain reference PSA configurations for carbon dioxide capture in pre-combustion conditions, minimizing the energy penalty and the cost of the power plant where the technology would be implemented.

The study by Agarwal et al. (2010) introduced the carbon dioxide rinse step. This step has not been widely used in PSA, in which only the light component is the product of the process, but it is essential when the heavy product must be produced at high purities beyond 90%, as stated by Agarwal et al. (2010), Dowling et al. (2012), and Wang et al. (2015).

These studies designed a unidirectional PSA system that manipulated the steps by varying the control variables of the light (hydrogen) and heavy (carbon dioxide) refluxes. In this system, half of the process steps are on one bed and the other half on the other bed, with the same timeslots for the steps in each of the beds. Dowling et al. (2012) also introduced a check valve into the system, which ensured that the beds had a one-way flow.

It is worth noting that there are some limitations on varying the control variables in simulations. As Agarwal et al. (2010) stated, no more than two beds can interact simultaneously using this model. Therefore, further development of pressure equalization and of null steps cannot be carried out following the approach presented in these studies. These steps need more than a two-bed system to ensure continuous operation. Moreover,

the fact that only two beds interact in the model limits both further testing in multiple bed systems and optimizing the process when applied to carbon capture.

The studies by Riboldi et al. (2014) and Riboldi and Bolland (2016) integrated a seven-bed PSA process into an IGCC power plant using various pressure equalization steps. Riboldi and Bolland (2016) conducted a sensitivity analysis for a number of process variables (feed temperature and flash pressure) and steps (the rinse and the number of pressure equalization steps). However, the study did not include a sensitivity analysis of the number of beds used in the process. This variable has a direct effect on the purity and recovery of the components and on the cost of the plant.

Another recent study analyzed the effect of a number of variables for a four-bed and eight-bed pressure swing adsorption process on the final recovery and purity of hydrogen in IGCC power plants (Moon et al., 2018). Pressure equalization was used to reduce the amount of tail gas (the heavy product) in the hydrogen. Recycled hydrogen was used as a purging gas to increase the product recovery to 99%. However, the study did not yield a process arrangement that would give over 95% carbon dioxide purity, which is the requirement for carbon dioxide storage and utilization (Webley, 2014). The key challenge in obtaining carbon dioxide at such purity levels lies in finding a process step that effectively concentrates the carbon dioxide product (Abanades et al., 2015).

2.6.8 Calculating the Operating Points of PSA

Two of the main challenges of PSA lie in finding the optimal operating points to define the step change and in finding the optimal process conditions within each step. Agarwal et al. (2010) and Dowling et al. (2012) optimized for the energy efficiency and product

purity of the process, varying the heavy and light products' reflux fractions, adsorption and desorption pressures, bed length and time slots of the steps. This configuration included a vacuum generator to obtain pressures under atmospheric conditions for the desorption of carbon dioxide. However, they did not consider the possibility that the process might be more efficient without a vacuum generator.

The study by Riboldi et al. (2014) aimed to demonstrate the suitability of PSA in post-combustion and pre-combustion scenarios. However, an optimization of the energy efficiency in terms of the process variables and the number of beds was not carried out. The scenario was fixed as a 7-bed, 12-step pre-combustion set-up in an IGCC power plant.

In another study, by Lopes et al. (2011), a one-bed, ten-step vacuum PSA experiment was performed to validate the mathematical model that had been developed such that the boundary conditions changed at each step. However, the authors fixed the times for each step, and optimization in terms of the process variables (the adsorption pressure and the number of steps) was not carried out.

Admittedly, the optimization of the PSA process is a major task. The studies by Haghpanah et al. (2013), Hasan et al. (2012), and Wang et al. (2015) consider only a two-bed model, with a fixed cycle configuration and in which optimization is carried out only for the operational conditions. It is essential to find optimum values for the step schedule, for the duration of each step and for the number of bed units.

The selection of the process variables to optimize will play a key role in obtaining a valid interpretation of results. Agarwal et al. (2010) carried out a PSA optimization in two case studies. In the first, optimization was carried out to find the cycle step schedule and the

duration that gave maximum values for the concentration of carbon dioxide in the outlet of the reactor. In the second, they set the model to obtain the arrangement that gave minimum energy consumption values. The results of the second case study showed that 90% purity and 92% recovery of carbon dioxide and a minimum value of 0.1685 MJ/kg CO_2 for energy consumption could be obtained from this process, which makes the technology promising (Agarwal et al., 2010).

The purity of carbon dioxide (the first case study) should be part of the given specifications (input values) because the purity requirement for the transportation of carbon dioxide is set to 95% on a volumetric basis. In this case, energy consumption would be the performance indicator to minimize, as shown in the study of Wang et al. (2015).

2.7 The Application of Carbon Capture in Combined Cycle Power Plants

2.7.1 The Scale-up of Carbon Capture

Most work on scaling up carbon capture and on the associated adaptation of power plants has focused on post-combustion capture using liquid solvents (Adams and Mac Dowell, 2016; Alhajaj et al., 2016; Manaf et al., 2016; Reichl et al., 2014). A study by the International Energy Agency Greenhouse Gas Research and Development Programme (IEA-GHG, 2009) analyzed the implementation of an amine-solvent-based capture system in a supercritical pulverized coal power plant and a natural gas-fired combined cycle power plant. The study considered the technical challenges and operational risks of

the process. In addition, the effects of process variables such as the fuel type and capture percentage were studied. The authors concluded that the main challenges facing the technology were energy and water consumption, amine disposal and sulphur emission control.

Another study, by Manaf et al. (2016) analysed the viability of a post-combustion capture unit using absorption. They studied the implementation of amine absorption at pilot scale, by modelling a plant with an absorber, a heat exchanger and a desorber. A sensitivity analysis was carried out by introducing perturbations into the input data. The heat duty of the reboiler was the most influential variable in maximizing absorption efficiency. However, the effect of the process variables on cost was not studied, and this is the main issue when considering the development of carbon capture via solvent absorption.

Alhajaj et al. (2016) evaluated the cost and technical feasibility of a carbon capture unit based on amine absorption in a power plant modelled in gPROMS®. Optimization to minimize costs was carried out, featuring the area of heat exchangers, the applied power rates, the weight and volume of the packing beds and the utilization of flue gas. A sensitivity analysis was conducted by varying the input values, which helped to establish global minimum values instead of local minimum values by narrowing the range of initial values.

On the one hand, the authors noted several discrepancies relevant for the heat exchangers' design, due to assumptions about stream temperatures and heat transfer coefficients that had an effect on operating costs. On the other hand, a carbon tax was included to minimize the operating costs. These costs varied with the capture rate. This carbon tax implies a penalty on the earnings of the plant. It was concluded that at carbon prices higher than 60

$/tonne CO_2, a plant that can absorb 95% or more of the carbon dioxide would be profitable.

Lima et al. (2016) took a different approach in scaling up a carbon capture unit. The carbon dioxide removal was studied using a membrane reactor under pre-combustion capture conditions. The effects on the cost and the degree of capture were studied. The power output, the flow rate of streams and the surface area of the membrane were optimized. Although one of the final constraints was to obtain 95% purity of hydrogen, the degree of carbon capture was fixed at 90%. For the process to be promising, the degree of capture should be equal to or higher than 95%. In addition, the usage of water was not included in the cost optimization, and temperatures equal to or higher than 100°C would be essential for the steam entering the membrane reactor. Both variables translate into additional operating costs.

Overall, most of the studies on the scale-up of carbon capture for power plants have focused on absorption technology in post-combustion conditions. There is a need to study the performance of alternative technologies for the scale-up of carbon capture. A study by Riboldi et al. (2014) compared the performance of an absorption unit to that of a PSA unit in both post- and pre-combustion scenarios. The net electrical efficiency was 5% lower for the PSA unit than it was for the absorption unit under post-combustion conditions. However, the net electrical efficiency of the PSA unit was only 0.6% lower under pre-combustion conditions. The net electrical efficiency of the PSA unit could have been further improved in the study by testing alternative process conditions and PSA configurations.

2.7.2 The Integration of Carbon Capture into Combined Cycle Power Plants

Pre-combustion carbon capture has been implemented at a large scale using solvent-based absorption, such as at the ELCOGAS 335MW IGCC plant in Puertollano (Rackley, 2017). Such power plants could also offer the advantage of implementing a hybrid-power hydrogen production system (Li et al., 2012; Riboldi and Bolland, 2016; Seyitoglu et al., 2016). One of the main advantages noted by one of these studies was the ease of shifting between various power-to-hydrogen production ratios, with low energy penalties (Riboldi and Bolland, 2016). In fact, CCUS is regarded as one of the main technologies for future hydrogen production (Grande, 2012). For a zero-emissions future, hydrogen is seen as one of the main energy vectors for decarbonizing several sectors, such as industrial heat and transport. The production of hydrogen is currently responsible for around 700 mtpa of carbon dioxide emissions, according to the IEA (Gasworld, 2019).

Few studies have analyzed the implementation of pre-combustion carbon capture via solid sorbents on a large scale, especially applying PSA in integrated gasification combined cycle power plants. Even fewer studies have looked at pre-combustion capture in natural gas combined cycle power plants. This technology could offer advantageous costs of operating the plant and an acceptable success of the purification process, because of the lower amount of impurities in natural gas compared to the ones in the coal, such as ash.

Thus, three of the novelties of this thesis are the study of integrating a carbon capture technology other than absorption in a combined cycle power plant, the analysis of the energy penalty and economic performance of the process, and their comparison to results on these parameters from other technologies.

IGCC power plants use partial oxidation (gasification) of coal to obtain carbon monoxide, carbon dioxide and hydrogen at high pressures. Then, a water gas shift reactor (WGS) converts the remaining carbon monoxide into carbon dioxide. NGCC power plants use steam methane reforming (SMR) and a water gas shift process (WGS) to convert the natural gas to syngas. The energy penalty for the WGS applied to NGCC power plants is lower than that for the same process in IGCC power plants, due to the high carbon content in the syngas derived from coal, which leads to greater use of steam by the WGS and a greater loss in the heating value of the syngas (Jansen et al., 2015). Then the carbon dioxide and the hydrogen mixture are fed into a PSA capture system, where the concentration of carbon dioxide is around 30–50% at high pressures of 1500 kPa or higher (Agarwal et al., 2010). The concentration of carbon dioxide fed into a post-combustion capture unit is around 10–15% (Gibson et al., 2016; Samanta et al., 2012; Yuan et al., 2013), which makes the capture less selective for this component.

One of the most relevant works on integrating PSA into an IGCC plant is a study by Riboldi and Bolland (2015a), whose sensitivity analysis on process variables was carried out with a seven-bed, twelve-step PSA system. The effects on the energy and the CO_2 capture efficiency of the feed temperature, pressure equalization steps, regeneration pressure, flux pressure and heavy reflux step were studied. The authors also included carbon dioxide as a fuel for preparing the gas in the gasification process, instead of nitrogen. However, the effects of the number of PSA steps, cycles and number of beds were not studied with a view to improving the cost of the overall plant or the performance indicators for both carbon dioxide and the hydrogen products.

Another study by Seyitoglu et al. (2016) suggested integrating an innovative multi-generation system into an IGCC power plant; an energy and exergy analysis was

performed on different types of coal (lignite) using Aspen Plus software (Seyitoglu et al., 2016). The plant consisted mainly of a hydrogen production unit, a Fischer-Tropsch unit for diesel production and a power production unit, as shown in Figure 2.10. The PSA unit in this study was separated from the power production unit. Therefore, it was not used for carbon capture purposes, but the unit was essential for providing syngas in various carbon monoxide and hydrogen ratios to the Fischer-Tropsch unit.

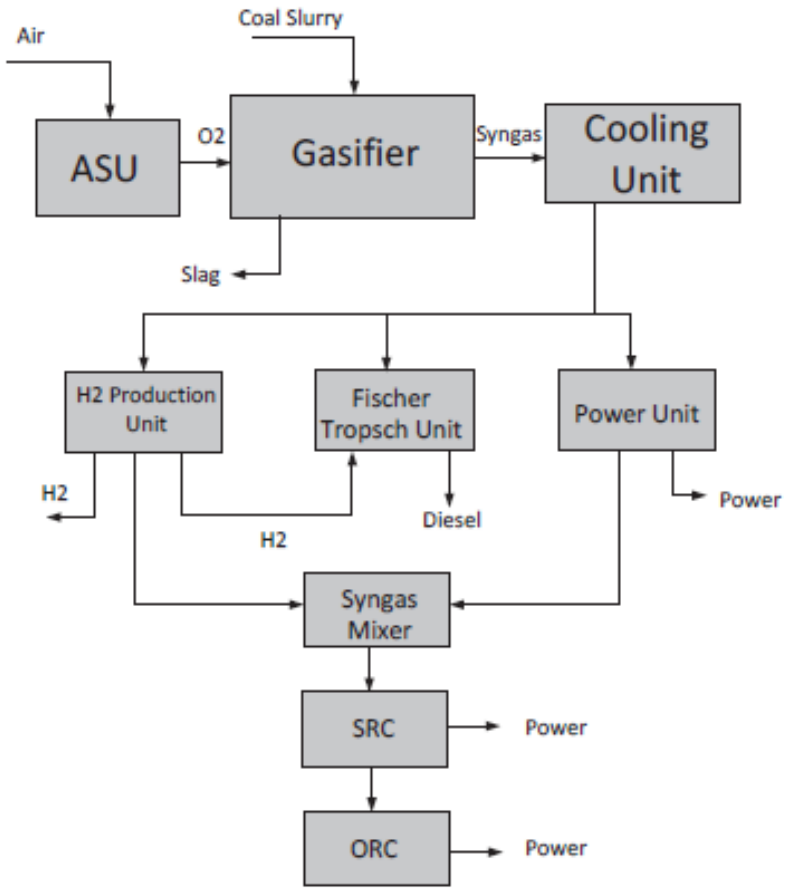

Figure 2.10. The schematic model of the multi-generation IGCC power plant proposed by Seyitoglu et al. (2016)

Although the energy efficiency analysis yielded promising results for future work, all the models for the units in the plant (including the PSA unit) were pre-defined by the software package, not custom-modelled, which, in the absence of careful consideration, can result in errors in real life implementation. The energy efficiency of this system was found to be as high as 53%; however, the authors did not consider the energy penalty of having a carbon capture unit.

Further refinement of the simulation is needed to establish more clearly what the effects of the process variables in PSA are on the cost and the carbon capture efficiency in an IGCC power plant. A variety of scenarios should be considered so as to obtain the optimum operating values of the plant. For instance, the selection of the adsorbent as well as the effect of the number of steps and beds on the operating costs should be studied. Research on types of PSA configurations valid for carbon capture and their effect on the cost is an objective of this thesis.

2.7.3 The Energy Efficiency and Cost Estimation of Combined Cycle Power Plants that Use Carbon Capture

In previous work, in the design of a combined cycle power plant with PSA as a carbon capture unit, the mass and energy balance information was derived from simulation-driven process flow diagrams (Luberti et al., 2014b; Riboldi and Bolland, 2017). From these calculations, the size and the energy penalty of the power plant models were determined.

The study by Riboldi and Bolland (2017) considered a number of sections in the design of an IGCC power plant, comprising mainly an air separation unit, a gasification and

syngas treatment section, a carbon dioxide separation unit using PSA and a set of compressors, and a power island section. In the work by Riboldi and Bolland (2017) the process variable values were obtained from the European Benchmarking Task Force (EBTF), in order to define a common framework (Anantharaman et al., 2011). Figure 2.11 shows the process flow chart of the IGCC power plant with pre-combustion PSA designed by Riboldi and Bolland (2017).

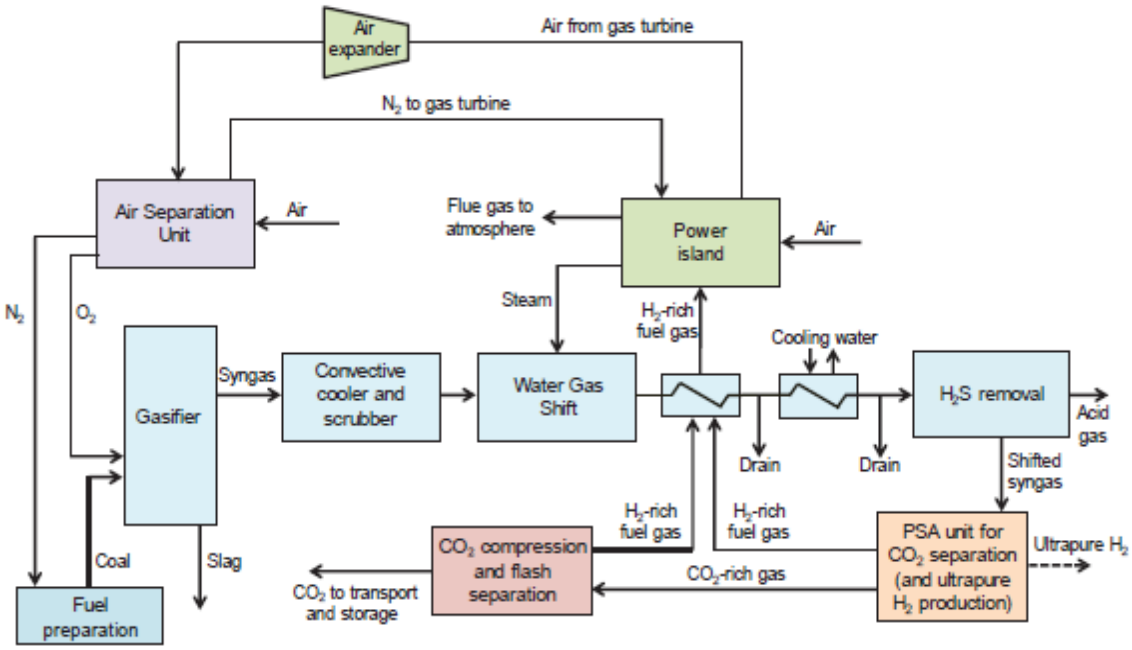

Figure 2.11. The flow chart of pre-combustion PSA integrated into an IGCC power plant proposed by Riboldi and Bolland (2017)

The energy penalty was calculated by estimating the power requirements for carbon dioxide storage, the compression work and heat provision in the process. The estimated energy efficiency was 35.8%, yielding a hydrogen product with a purity as high as 99.99%. However, the authors did not consider the requirements of a gas turbine for

operation under a hydrogen purity as high as this value, which can cause flame instability and high combustion temperatures (Cappelletti and Martelli, 2017; Ditaranto et al., 2015).

A study by Luberti et al. (2014b) used a similar approach to design an IGCC power plant, but a portion of the tail gas from the PSA unit was recycled to the shift reactor to improve the performance of the separation process. However, the authors calculated the energy penalty of only the tail gas compression for a number of PSA configurations; it was the lowest for the case containing four pressure equalization stages, yielding a value of 3.52 MW. The study focused on optimizing the hydrogen product performance values, which reached values of purity and recovery as high as 99.99% and 93%, respectively.

Most studies related the concept of the economic efficiency of the process to the energy efficiency of the process (Li et al., 2012; Riboldi et al., 2014; Riboldi and Bolland, 2015a; Seyitoglu et al., 2016). The main costs of the process were capital costs, operational costs and maintenance costs, as shown in previous work (Li et al., 2012) and the calculation method was mainly derived from National Energy Technology Laboratory studies. Table 2.7 shows the relationship between energy efficiency values and the carbon capture performance indicators from previous studies using carbon capture in combined cycle power plants.

Table 2.7. The relationship of energy efficiency to the capture performance of power plants

Study	Power plant	Capture type	Energy efficiency (%)	CO_2 purity (%)	CO_2 recovery (%)
Di Lorenzo et al. (2013)	IGCC	Pre-combustion Absorption	43.7	-	90
Di Lorenzo et al. (2013)	IRCC	Pre-combustion Absorption	37	-	90
Li et al. (2012)	IGCC	Pre-combustion Absorption H_2 co-production	18.51	-	95
Li et al. (2012)	IGFC	Pre-combustion Absorption H_2 co-production	31.63	-	97
Riboldi and Bolland (2016)	IGCC	Pre-combustion PSA H_2 co-production	31.54	98.8	84.7
Riboldi et al. (2014)	IGCC	Post-combustion Absorption	33.4	100	90
Riboldi et al. (2014)	IGCC	Post-combustion PSA	28.8	93	90.9
Riboldi et al. (2014)	IGCC	Pre-combustion Absorption	36.8	100	90.5
Riboldi et al. (2014)	IGCC	Pre-combustion PSA	36.2	98.9	85.4

The study by Di Lorenzo et al. (2013) shown in Table 2.7 conducted an economic analysis of an IGCC power plant in pre-combustion conditions using an absorption-based capture system and a defined capacity of 255 MW electrical output. The economic performance of this plant was compared to that of an integrated renewables combined cycle (IRCC) power plant where auto-thermal reforming was used to convert the natural gas to syngas.

The capital cost was estimated based on the scaling factor of the power plant and based on its capacity, a construction time of three years and a lifetime of 25 years. Also, an electricity value, a fuel value, and a discount rate of 10% were assumed to determine the maintenance and operational costs of the power plant. The study conducted a sensitivity analysis of factors that included the fuel price, carbon tax and discount rate. The study also estimated the energy efficiency for both scenarios, which yielded 43.7% for the IRCC case and 37% for the IGCC case.

2.7.4 The Carbon Dioxide Market

Previous studies considered storing the carbon dioxide when estimating the cost of a power plant with a carbon capture unit. However, this product could have several applications in the market, such as fertilizer manufacturing and the production of methanol and dimethyl ether (Matzen and Demirel, 2016).

When carbon dioxide is extracted from the power plant, it needs to be either stored or used as a reactant to manufacture other market products. The second option should be preferred, as environmental and safety issues are a drawback of the first option, for example, sudden carbon dioxide release. Also, carbon dioxide is typically stored under conditions of 20 bar and -30°C (McGillivray et al., 2014); achieving those conditions increases the overall cost of the plant.

Therefore, it would be preferable for carbon dioxide to be a precursor in the manufacture of market products; there are numerous applications that already use this component and that present clear advantages over the storage option (Aresta and Tommasi, 1997):

- Avoidance of the use of toxic chemicals.
- More direct synthesis procedures, saving energy and raw materials.
- Avoidance of extreme operating conditions.
- Energy savings by recycling carbon.

Urea production, an application that uses carbon dioxide as a prime material, is one of the most demanding processes in the agriculture industry and is used for manufacturing fertilizers. One of the advantages of the process is that the reaction takes place at high pressures, which is convenient for highly pressurized stored carbon dioxide entering the process, which in turn reduces energy requirements for compression. In addition, as 95% pure carbon dioxide comes from PSA, a shift reactor that produces carbon dioxide from carbon monoxide with an iron catalyst is not needed within the plant; neither is a separation process using solvents to purify carbon dioxide (Edrisi et al., 2016).

The manufacture of methanol and dimethyl ether is another application that uses carbon dioxide as a reactant. The plants use syngas coming from natural gas to manufacture methanol (Matzen and Demirel, 2016). Therefore, the cost of the process depends on natural gas prices. A report by The Global CO_2 Initiative (2016) concluded that the production of methanol synthetic fuel would have the greatest economic potential for the use of carbon dioxide. Another product with big market potential is carbon fibre, which could replace steel. Carbon fibres could be produced using 6% of the carbon dioxide emitted globally (The Global CO_2 Initiative, 2017). Other products derived from carbon dioxide with future potential are:

- Consumer products applied to health care.

- Polymers and chemical intermediates for the production of surfactants and alternative feedstock.
- Mineral carbonation applied to industries, such as the cement and concrete industry.

Catalysts applied to the production of carbon-derived products will play a key role in the success of the process implementation in the future. These industries use noble-metal-based catalysts, but recently, novel conditions have been applied to these industries, for instance, the introduction of the use of electrolysis and photocatalysis, with the use of polymer membranes and solid oxides in the synthesis of methanol (Styring, 2019).

Hydrogen and carbon dioxide both could come from a gasification power plant with pre-combustion PSA without needing an extra unit for syngas production in a methanol production plant. Power plants could sell these products and make the capture economically viable within the power plant. Although the power plant would need an investment to build a capture plant (so, capital costs), long term earnings could be higher than for current power plants if the plant is designed to deal with a number of scenarios. An economic analysis should be carried out in order to prove the economic viability of pressure swing adsorption in the markets for hydrogen and carbon dioxide. Chapter 6 presents the results of the economic performance for PSA integrated into an NGCC power plant.

2.8 Summary

Carbon capture use and storage is an essential technology if fossil-fuel-based power generation and carbon dioxide industrial emissions remain substantial over the next fifty

years. Absorption via amine solvents is the main technology implemented at large scale, but research in additional technologies is on-going and essential, due to the number of process conditions that hold in the power generation industry.

Pre-combustion capture is a promising approach due to high carbon dioxide concentrations and pressures before combustion. Pressure swing adsorption is a potential technology to implement in these conditions, because it has been successfully used in previous years for hydrogen purification and gas separation processes. However, using the technology for carbon capture purposes requires the adaptation of material and adaptation through process engineering.

Due to their capacity and selectivity, activated carbons and zeolites demonstrate the highest potential for PSA processes in the field of material science applied to adsorption processes for carbon capture. However, further research is required to optimize the performance of these adsorbents according to the process conditions. Specifically, there have been studies that analyzed the performance of amine-modified adsorbents in post-combustion studies, but there is hardly any literature on the application of these adsorbents in pre-combustion capture.

In terms of process engineering, the simulation of PSA processes is an essential step in analyzing the suitability of the technology and optimizing the process conditions before the scale-up of the process. However, there are few studies in the literature that have designed the PSA process to improve the performance indicators for the carbon dioxide product. There is a need to achieve reference conditions and process configurations to improve the economics of this process also.

Combined cycle power plants have demonstrated great suitability for applying PSA processes under pre-combustion conditions, due to the syngas concentration and the interest in hydrogen as an energy vector in the near future. Work in the literature has analyzed the performance of PSA units in an integrated gasification combined cycle power plant and calculated the cost of the process. However, the PSA configurations in these plants have not been designed to optimize the carbon dioxide product requirements and the cost of the process. Moreover, there is hardly any literature about the performance of PSA processes that have been integrated into natural gas combined cycle power plants. Further studies are required in this field, as PSA could offer several advantages in addition to that of its use in IGCC power plants, due to the composition of natural gas compared to that of coal.

CHAPTER 3 – METHODOLOGY

3.1 Introduction

This chapter explains the procedure used to obtain the results of the pressure swing adsorption and the natural gas combined cycle model. Section 3.2 explains how the different models in this thesis interact with each other and explains the software package (gPROMS® ProcessBuilder) environment in which the PSA custom model was developed. Section 3.3 describes the development of the axially-dispersed plug-flow model, including the variables and equations used. This model describes the adsorption of the carbon dioxide and hydrogen gas mixture in the fixed-bed reactor.

Section 3.4 explains how the axially-dispersed plug-flow model was compared to the laboratory data and how the PSA cycle was scheduled. The performance of the model was analyzed based on the indicators also shown in this section. The laboratory data was obtained by Douglas Soares dos Santos, as part of the collaboration with the author of this thesis, and the procedure to obtain the experimental data is shown in Soares dos Santos (2019). Section 3.5 explains the steps in scaling up the validated axially-dispersed plug-flow model and the PSA configurations developed to improve the values on the performance indicators of the model.

The procedure for the design and the units included in the NGCC power plant are explained in Section 3.6. Last, Section 3.7 explains the steps undertaken and the assumptions that held for the economic analysis of an NGCC power plant. This section also explains the performance indicators chosen to measure the economic viability of the power plant when using PSA.

3.2 The Outline of the Models

3.2.1 The Interaction between the PSA and the NGCC Power Plant Results

The PSA process was developed in gPROMS® ProcessBuilder. The process was built based on an axially-dispersed plug-flow model that described the adsorption process of the carbon dioxide and hydrogen components in the fixed-bed reactor. The parameter estimation capability within ProcessBuilder was also used to validate the axially-dispersed plug-flow model with laboratory data. The data used for the model validation was the carbon dioxide molar concentration exiting the fixed-bed reactor.

This model was linked to a schedule that changed the conditions of the fixed-bed reactor. The schedule enabled the definition of the variable values in each step; therefore, a PSA process could be obtained at both laboratory (Section 3.4) and pilot scale (Section 3.5). The PSA model developed in this work used a novel procedure for the validation of the axially-dispersed plug-flow model (Section 3.4.2) and for the cycle configurations developed in the PSA process for carbon capture (Sections 3.4.4 and 3.5.3).

The power plant model was developed based on a mass and energy balance made with the process upstream of the PSA unit using the model libraries of ProcessBuilder. The technical data from the gas turbine manufacturer was used to determine the heat and mass balance of the process downstream of the PSA unit. The power plant in this thesis was novel in that it integrated a PSA unit for pre-combustion capture in a natural gas combined cycle power plant (Section 3.6.1).

The natural gas and utilities requirements of the power plant were determined based on these mass and energy balances and on the sizing of the equipment. The steam and power requirements of the plant were determined by a pinch analysis (Section 3.6.4). Then the energy penalty was calculated. The cost of the power plant was also calculated based on the equipment cost and on the cost of the heat required and produced in the power plant. The cost analysis procedure is explained in detail in Section 3.7.

Figure 3.1 explains the data interaction between the models in this work. The blocks inside the rectangle show the processes developed in this work, while the cylinders show the data obtained and transmitted from each of the processes. The blocks outside the rectangle show the input and the output components of the plant.

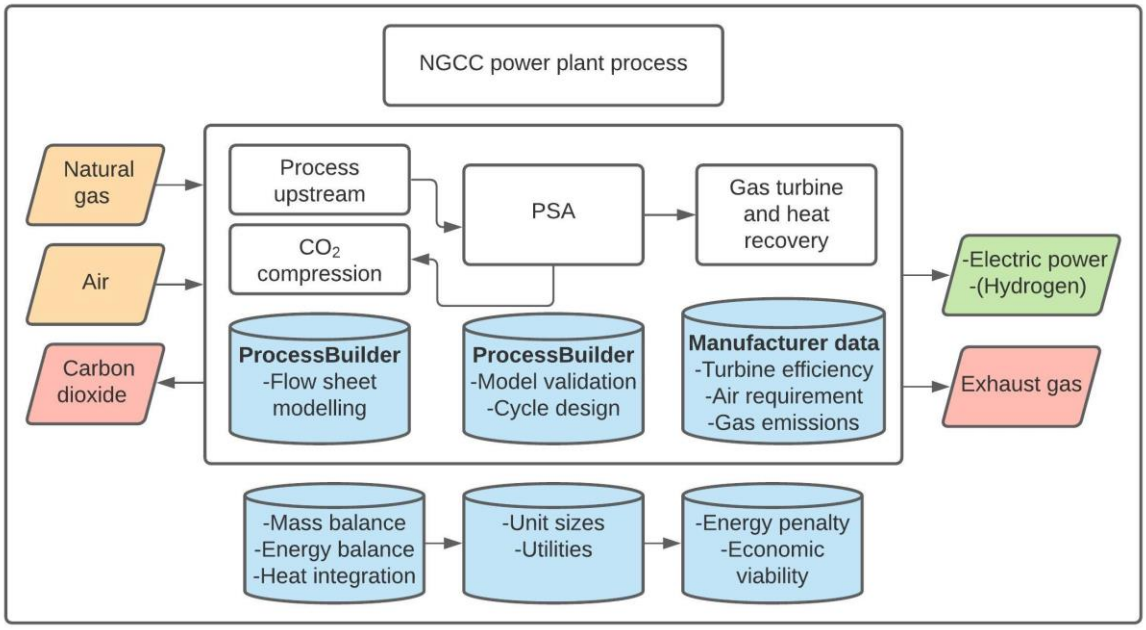

Figure 3.1. Block diagram describing the data interaction of the NGCC and PSA models studied in this thesis

3.2.2 The gPROMS® ProcessBuilder Environment

The simulations to analyze the results of the pressure swing adsorption model were carried out using the gPROMS® ProcessBuilder software developed by Process Systems Enterprise (PSE). This software was selected due to its advanced library models for separation processes and to its ability to integrate these with custom-defined models. The software also enables the development of flexible schedules, which is necessary when operating with dynamic processes, such as pressure swing adsorption. PSE was an in-kind sponsor of this project.

ProcessBuilder is a computer-aided chemical engineering software package that combines user-defined and pre-defined models for separation, heat exchange, flow transportation and instrumentation units for a range of reactions for a range of plants. These models can be included in a process flow, from which mass and energy balances can be determined at steady state or under dynamic conditions. The software also includes algorithms for the optimization of processes and parameter estimation using laboratory or real plant data.

The users can also develop custom models using an equation-oriented environment in ProcessBuilder and divide the models into various subtasks. First, there are several libraries for ‘variable types’ defined by the program, where the units and the boundary conditions of the variables to be used in the model, such as molar concentration, pressure and temperature, are defined. The selection of the boundary conditions of these variables is important for the convergence of the model. Second, a thermodynamic model for the created case file can be established, using the interface between ProcessBuilder and Multiflash (InfoChem). Multiflash is a physical properties package that calculates

thermodynamic variable values, such as density, viscosity, enthalpy and conductivity. The package determines these values based on the thermodynamic model selected for the mixture of components in a system. The implementation of the thermodynamic model for this process is further explained in Section 3.3.1.

The ‘model’ environment in the case file is used to create first-principles mathematical models that embody the physics, chemistry and chemical engineering relationships governing the units. Appendix C gives an example of the coding used in the axially-dispersed plug-flow model. The ‘model’ environment uses the ‘parameter’ and ‘variable’ sections to define the parameters and variables used in the model, relating them to ‘real’ or ‘array’ domains and to the ‘variable types’ section. A ‘distribution domain’ needs to be defined if differential equations are used in the model. In the ‘equation’ section, the mass, energy and momentum balances that govern the model are entered, using the previously defined variables and parameters.

The ‘task’ environment defines the time-related and conditional behaviour of the ‘model’ environment, using functions such as ‘if’, ‘while’ and ‘continue for’. It determines the schedule of the ‘process’ environment, where all the interfaces of the model are listed and the values of the parameters and variables are defined. If differential equations are used in the model, the discretization method and the number of points required must be defined in this environment, as well as the initial conditions. Figure 3.2 summarizes the main sections of the modelling environment explained here.

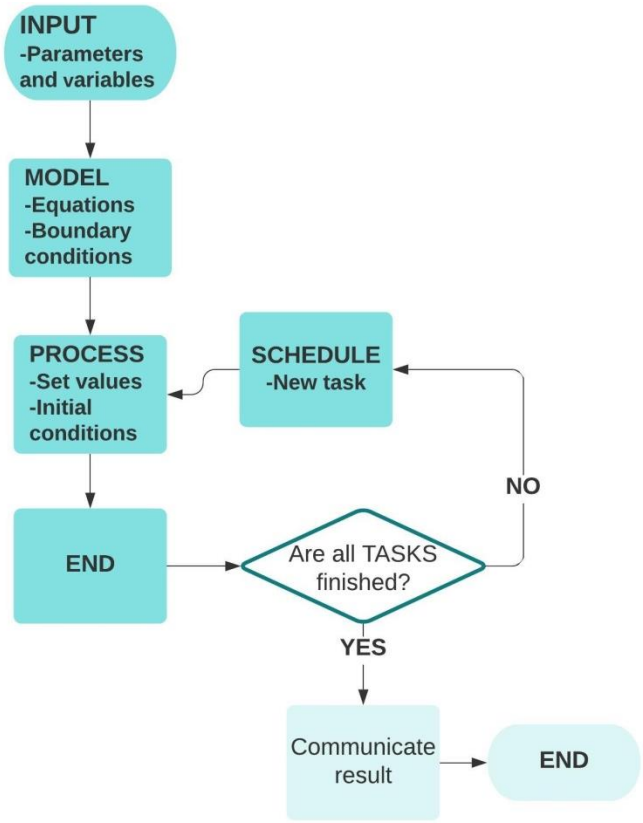

Figure 3.2. The process flow of the computational model of pressure swing adsorption

3.3 The Axially-dispersed Plug-flow Model

3.3.1 The Model Assumptions

The pressure swing adsorption process in the fixed-bed reactor was modelled on an axially-dispersed plug-flow model, based on the previous literature for fixed-bed separation processes at a high pressure over 10 bar (Ko et al., 2005; Moon et al., 2018; Ribeiro et al., 2008). An overall mass balance and a component mass balance in the axial direction of the bed described the evolution of the gas concentration in the bed. The

temperature of the gas in the fixed-bed reactor was described by an energy balance equation, and the pressure drop was accounted for by using a momentum balance equation. The concentrations of the component in the solid phase and in the gas phase were related using the linear driving force (LDF) mass transfer equation. The concentration of the component in the solid phase was determined using the isotherm model shown in Section 3.3.5.

Overall, the following points describe the main assumptions of the axially-dispersed plug-flow model developed in this work:

- The Soave-Redlich-Kwong equation of state was used to calculate the compressibility factor for this system when the value was over 0.9. Therefore, flowing gases were considered ideal.
- There were no radial variations in the pressure, temperature and concentration of the components in the gas and solid phases.
- The solid and gas phases were in thermal equilibrium and the bulk density of the solid remained constant.
- The adsorption kinetics are described by the linear driving force model, which assumes that diffusion through micropores is the limiting step.

The compressibility factor of the carbon dioxide and hydrogen gas mixture entering the fixed-bed reactors in this study was calculated by the Soave-Redlich-Kwong equation of state. This equation of state has been mainly applied to component mixtures in the vapour phase coming from natural gas, as in the work by Moon et al. (2018). The procedure for calculating the compressibility factor is shown in Appendix A, which shows that the calculated value of the compressibility factor was over 0.91 for the gas mixtures entering

the fixed-bed reactor in this work. Therefore, the ideal gas equation was used to relate the gas phase pressure and concentration. In the range of compressibility factor values between 0.9 and 1, the effect on the results of the deviation of the real gas from ideal gas has been considered insignificant in previous studies that used the ideal gas equation to simulate PSA systems, both in academia and in industry (Lopes et al., 2011; Moon et al., 2018; Ribeiro et al., 2008; Riboldi et al., 2014).

The assumption of a linear driving force is the assumption that diffusion through micropores is the controlling mechanism. This assumption has been widely applied for PSA systems that feature activated carbons (Hao et al., 2018; Riboldi et al., 2014). This simplification of the mass balance equations covers the limiting case in which one of the mass transfer mechanisms is the controlling step. This is supported by a previous study by Lopes et al. (2011) that reported that for the gases under study, micropore diffusion was the controlling mass transfer mechanism.

Ribeiro et al. (2008) also showed that this assumption is valid for PSA systems that operate on natural gases and that use activated carbons as adsorbents. A complete model was compared with a simplified model that assumed that diffusion through micropores was the controlling step. The model that included only micropore resistance, as described by the linear driving force model, and assumed thermal equilibrium between the gas and the adsorbent satisfactorily predicted the behaviour of the system.

3.3.2 Mass Balance

The overall mass balance described the evolution of the overall concentration of the gas phase in the fixed-bed reactor, and the component mass balance described the evolution

of each of the components in the axial direction of the fixed-bed reactor. The amount of gas entering and exiting the fixed-bed reactor was calculated by the mass balance equations; therefore, the amount of each component gas adsorbed in the fixed-bed reactor was known. The finite difference method was used to estimate the partial differential equations of the mass balance; it included partial derivatives in the bed length and time domains. This method divides these domains into a number of finite elements. The discretization method is further explained in Section 3.4.3.

The following terms were applied to develop both equations: the accumulation, the inlet and outlet terms, the dispersion term and the adsorption term for each finite element. The component fractions balance, Equation 3.2, combines the mass balance of the overall mass balance, Equation 3.1, and the component concentrations balance, following the method of Ko et al. (2005). Appendix B shows the derivation of the component mass balance. The overall concentration was related to the pressure of the gas phase using the ideal gas equation, shown in Equation 3.3. This equation was used because the compressibility factor values of the gas mixtures in this study were over 0.91, as explained in Section 3.3.1. The overall and component concentrations were related using the component molar fractions, as shown in Equation 3.4. The definitions of the main variables in the partial differential equations are also shown in Table 3.1.

Table 3.1. The equations of the model for determining the total and component concentrations and gas phase pressure

Overall	$\varepsilon_t \frac{\partial C(z)}{\partial t} = -\varepsilon_b \frac{\partial (C(z)v(z))}{\partial z} + \varepsilon_b D_x \frac{\partial^2 C(z)}{\partial z^2} - (1-\varepsilon_b)\rho_s \sum_{i=1}^{N_{comp}} \frac{\partial Q(i,z)}{\partial t}$ C = Concentration of the components in the gas phase Q = Concentration of the components in the solid phase v = Velocity of the gas phase	3.1
Component Fractions	$\varepsilon_t \frac{\partial Y(i,z)}{\partial t} = -\varepsilon_b v(z) \frac{\partial Y(i,z)}{\partial z} + \varepsilon_b D_x \left(\frac{\partial^2 Y(i,z)}{\partial z^2} + \frac{2}{C(z)} \frac{\partial Y(i,z)}{\partial z} \frac{\partial C(z)}{\partial z} \right) - \frac{(1-\varepsilon_b)\rho_s}{C(z)} \left(\frac{\partial Q(i,z)}{\partial t} - Y_{(i,z)} \sum_{i=1}^{N_{comp}} \frac{\partial Q(i,z)}{\partial t} \right)$ Y = Component molar fraction in the gas phase	3.2
The ideal gas law	$C(z) = \frac{P(z)}{R\,T(z)}$	3.3
The component concentration	$C(i,z) = C(z)\, y(i,z)$	3.4

3.3.3 The Energy Balance

The evolution of the temperature in the fixed-bed reactor was estimated using a non-isothermal energy balance equation. The balance was estimated based on the fact that the gas and the solid phases were in thermal equilibrium, following the approach in previous studies on modelling PSA (Casas et al., 2013a; Moon et al., 2018; Luberti et al., 2014a). This assumption is supported by a previous study by Ribeiro et al. (2008), in which a model that included the energy balance in the gas and in the solid phases showed identical

results to the model that assumed thermal equilibrium between both phases. In this study, the model that assumed thermal equilibrium yielded a product whose hydrogen purity deviated by 0.0003% from the product that the complete model yielded.

As was done for the mass balance in Section 3.3.2, the inlet and outlet terms of the convection heat flux, the heat accumulation, the heat generated due to adsorption and the axial dispersion of the heat were included. The axial dispersion of the heat and the heat transfer coefficient were estimated using the correlations shown in Sections 3.3.7 and 3.3.8. Equation 3.5 shows the non-isothermal energy balance with wall effects, applied to the fixed-bed reactor model at laboratory scale.

Table 3.2. The energy balance equation for determining the temperature evolution in the fixed-bed reactor

Gas	$\varepsilon_t \rho c_{p,g(z)} \frac{\partial T(z)}{\partial t} + \varepsilon_t \rho_s c_{p,s} \frac{\partial T(z)}{\partial t} = -\rho c_{p,g(z)} \frac{\partial \left(T(z) v(z)\right)}{\partial z} + (1-\varepsilon_b)\rho_s \sum_{i=1}^{N_{comp}} \Delta H_{ads(i)} \frac{\partial Q(_i,z)}{\partial t} - h_{r,i}(T(z) - T_{wall}) + \lambda \frac{\partial^2 T(z)}{\partial z^2}$	3.5

3.3.4 The Linear Driving Force Equation

The adsorption term in the overall and component mass balances (Equations 3.1 and 3.2) relates the component concentrations of the gas to those of the solid particles. The mass transfer from the gas phase to the adsorbent involves a number of steps: (i) the mass transfer from the gas to the adsorbent surface; (ii) the diffusion through macropores; and (iii) the diffusion through micropores.

Several studies, for example, Ribeiro et al. (2008), included all of the mechanisms when modelling PSA processes. However, the LDF approximation has been successfully implemented in PSA processes using activated carbon adsorbents at high pressures (Moon et al., 2018; Riboldi et al., 2014). This presumes that the rate of the component mass transfer from the gas phase to the adsorbent particle is proportional to the linear relationship between the average and equilibrium concentrations of the components in the adsorbent.

Equation 3.6 shows the equation for the mass transfer between the gas and the solid phases. The mass transfer coefficient represents the diffusion through micropores being the main resistance. The LDF assumption has yielded a decrease in computational time. Also, the results obtained with this assumption are valid for axially-dispersed plug-flow models at high pressure (Ribeiro et al., 2008). The mass transfer coefficient used in the LDF equation was obtained using parameter estimation by fitting the model to the laboratory data, and the procedure is explained in Section 3.4.2.

$$\frac{\partial Q_{(i,z)}}{\partial t} = K_{(i)}(Q^*_{(i,z)} - Q_{(i,z)}) \qquad 3.6$$

3.3.5 The Isotherm Model

The equilibrium concentration of the components in the solid phase required to estimate the mass transfer rate was initially calculated using the dual-site Langmuir (DSL) isotherm, Equation 3.7. The DSL isotherm showed a good fit to the experimental data generated by Douglas Soares dos Santos. It became apparent that one of the layers in the activated carbons applied in this study was dominant, because of the chemisorption

phenomena occurring between the gas phase and the amine-modified activated carbons (Soares dos Santos, 2019). Therefore, the Langmuir isotherm, shown in Equation 3.8, was used in the model for this study. The parameter values measured in the HPVA (High Pressure Volumetric Analyzer) data for the activated carbons were used in the simulations.

Table 3.3. Isotherm models for estimating the equilibrium concentration in the solid phase

DSL	$q_i^* = \frac{q_{m1i} b_{1i} P_{(z)} RT}{1+\sum_j b_{1j} C_j RT} + \frac{q_{2i}^S b_{2i} C_i RT}{1+\sum_j b_{2j} C_j RT}$	3.7
Langmuir	$Q_{(z)}^* = \frac{q_{mi} b_i P(z) RT(z)}{1+b_i P(z) RT(z)}$	3.8

3.3.6 The Pressure Drop Equation

The pressure drop in the fixed-bed reactor was calculated using the Ergun equation, Equation 3.9, and it was applied in all the steps of the dynamic model, as explained in Section 3.4.4. The pressure inside the fixed-bed reactor was related to the overall gas concentration using the ideal gas equation, Equation 3.3. It is also important to include the pressure drop because it affects the velocity of the gas phase.

$$-\frac{\partial P(z)}{\partial Z} = 150\, u_{g(z)} \frac{(1-\varepsilon_b)^2}{D_p^2 \varepsilon_b^3} v(z) + 1.75 \frac{(1-\varepsilon_b)\rho}{D_p \varepsilon_b^3} v(z)|v(z)| \qquad 3.9$$

3.3.7 Mass and Heat Transfer Coefficients

The mass and heat transfer coefficients yield the rates at which the components transfer from the gas phase to the solid phase and from the fixed-bed reactor system to the surroundings, respectively. These have commonly been calculated using correlations, such as that developed by Wakao and Funazkri (1978). Other studies determined these coefficients via parameter estimation using laboratory data.

A study by Knox et al. (2016) examined the accuracy of the parameter estimation by using data from breakthrough curves when varying both the mass transfer and dispersion coefficients. The results suggested that axial dispersion should be measured inside the bed because the experimental data exhibited concentration front sharpening at the outlet of the bed. Then the mass transfer coefficient was obtained via parameter estimation. Therefore, the axial dispersion coefficient of the laboratory fixed-bed reactor was determined using the procedure shown in Section 3.4.1, and the mass transfer coefficient for the adsorption of carbon dioxide onto the activated carbon was estimated using the parameter estimation technique explained in Section 3.4.2.

The heat transfer coefficient and mass transfer coefficients for hydrogen and nitrogen were calculated using the Wakao and Funazkri (1978) correlations. These correlations have been the ones most widely applied to PSA systems, such as in the work by Ribeiro et al. (2008). Equations 3.10 and 3.11 show the correlations for the estimation of these coefficients, respectively.

Table 3.4. The correlations for the estimation of the mass and heat transfer coefficients

Mass transfer	$K_i = \frac{D_{AB}}{D_p}(2 + 1.1\, Sc^{\frac{1}{3}} Re^{0.6})$	3.10
Heat transfer	$\frac{h_i L}{k_g} = \frac{0.67\, Re^{\frac{1}{4}}}{\left[1+\left(\frac{0.492}{Pr}\right)^{9/16}\right]^{\frac{4}{9}}}$; $h_{r,i} = \frac{2h_i}{r_{in,bed}}$	3.11

3.3.8 Mass and Heat Axial Dispersion Coefficients

The mass axial dispersion coefficient was measured inside the laboratory fixed-bed reactor using the procedure shown in Sections 3.4.1 and 3.4.2. However, scaling up the fixed bed would change the dispersion coefficients, so both the mass and heat axial dispersion coefficients were estimated using the Wakao and Funazkri (1978) correlations. The previous literature has shown that for industrial fixed-bed reactors, the scaled-up effect of the dispersion term is small compared to the convection and adsorption terms (Agarwal et al., 2010; Dowling et al., 2012; Ruthven et al., 1994). Equations 3.12 and 3.13 show the correlations for the mass and heat axial dispersion coefficients, respectively.

Table 3.5. The correlations for the estimation of the mass and heat axial dispersion coefficients

Axial dispersion of mass	$\frac{\varepsilon_b D_x}{D_{AB}} = 20 + 0.5\, Sc\, Re$	3.12
Axial dispersion of heat	$\frac{\lambda}{k_g} = 20 + 0.5\, Pr\, Re$	3.13

3.3.9 Auxiliary Equations

Several auxiliary equations in the model are required to estimate the values of the variables in the material and the heat balances, which describe the mass and heat transfer between the gas and the solid phase. The total void fraction of the reactor was calculated using the bed and the particle void fractions, as shown in Equation 3.14. These parameter values were determined from laboratory experiments and were included in the mass and energy balances, and they reveal the effective reaction area of the unit.

The diffusion coefficient of the gas was calculated using the Fuller et al. (1966) correlation for binary gas mixtures shown in Equation 3.15. This correlation has been widely applied to fixed-bed reactor systems at high pressure (Rase, 1990). Additional equations for the calculation of dimensionless numbers were required to estimate the correlations mentioned in the previous sections, as shown in Table 3.6.

Table 3.6. Auxiliary equations for the axially-dispersed plug-flow model

Total void	$\varepsilon_t = \varepsilon_b + \varepsilon_p(1-\varepsilon_b)$	3.14
Diffusion coefficient	$D_{AB,i} = \frac{10^{-3}\boldsymbol{T}^{1.75}\left[\sum_{i=1}^{n=2}\frac{1}{\boldsymbol{Mw_i}}\right]^{\frac{1}{2}}}{\frac{P}{101325}\left[\sum_{i=1}^{n=2}\varphi_i^{\frac{1}{3}}\right]^2}$	3.15
Dimensionless groups	$Re = \frac{\rho_g v d_p}{\mu_g}$; $\mathrm{Sc} = \frac{\mu_g}{\rho_g D_{AB,i}}$; $\mathrm{Pe} = \frac{v d_p}{\varepsilon_b D_x}$; $\mathrm{Pr} = \frac{\mu_g c_{p,g}}{k_g}$	3.16

3.3.10 Boundary Conditions

The boundary conditions applied to the system were those shown by Danckwerts (1953) assuming a plug-flow inside the fixed-bed reactor as well as convection and diffusion for the mass transfer in the gas phase. Due to the implementation of these boundary conditions, there is no radial variation in the concentration of the components and in the temperature in the gas phase at the inlet and outlet of the fixed-bed reactor.

The boundary conditions of the axially-dispersed plug-flow model are shown in Table 3.7, where the component and energy balance have the inlet and outlet boundary conditions specified by the second order partial derivatives in Equations 3.17 and 3.18. The pressure had only one boundary condition specified by the first order partial derivative in Equation 3.9. The value of the boundary conditions changed from step to step in the PSA model, due to the dynamic behaviour of the system. The conditions of each step are specified in Section 3.4.4.

The initial conditions of the process are also shown in Table 3.7. It was assumed that the bed was filled with inert gas at adsorption pressures of 25 bar at ambient temperature (298.15 K), and that no components were adsorbed onto the surface of the particles.

Table 3.7. The boundary and initial conditions of the axially-dispersed plug-flow model

Component concentration	$-\varepsilon_b D_x \frac{\partial C_i}{\partial z}_{z=0} = v_{z=0}(C_{i,feed} - C_{i,z=0});\ \frac{\partial C_i}{\partial z}_{z=L} = 0$	3.17
Temperature	$-\varepsilon_b \lambda \frac{\partial T}{\partial z}_{z=0} = v_{z=0} e c_{p,g,z=0}(T_{feed} - T_{z=0});\ \frac{\partial T}{\partial z}_{z=L} = 0$	3.18
Pressure	$P_{z=L} = P_{end}$	3.19
Velocity	$v_{z=0} = v_{feed};\ \frac{\partial v}{\partial z}_{z=L} = 0$	3.20
Initial conditions	$Y_{i,t=0} = Y_{inert}; T_{t=0} = T_{amb}; v_{t=0} = v_{feed};\ \frac{\partial Q_i}{\partial t}_{t=0} = 0$	3.21

3.4 The Pressure Swing Adsorption Model at Laboratory Scale

First, a laboratory-scale pressure swing adsorption model was developed, with the aim of validating the results of the dispersed plug-flow model. This model was validated with data obtained in a laboratory fixed-bed reactor. The procedure used to obtain this data is shown in Soares dos Santos (2019). He measured the adsorption of carbon dioxide in a fixed bed reactor using a number of activated carbon adsorbents. The aim of his work was to measure the suitability of these activated carbons in post- and pre-combustion capture technology conditions and to select the optimal adsorbents and fixed-bed reactor conditions for these technologies.

The fixed-bed reactor experimental data selected to validate this model was that obtained using (i) tetra-ethylene-pent-amine (TEPA) and (ii) a blend of mono-ethanol-amine-mono-di-ethanol-amine (MEA-MDEA) modified activated carbons. These two types of activated carbons were selected due to their optimal performance in pre-combustion

conditions. The experimental work also obtained the isotherm model data for these adsorbents and the fixed-bed reactor parameters (Soares dos Santos, 2019). The model was validated using this data and by obtaining the mass transfer coefficient used in Equation 3.6. Once the model was validated, a number of PSA process conditions and configurations were studied to analyze their effect on the carbon capture performance.

3.4.1 The System Surrounding the Fixed-Bed Reactor

In order to compare the results from the laboratory experiments on the fixed-bed reactor to the axially-dispersed plug-flow model, a dispersion model was developed to simulate the response of the piping around the fixed-bed reactor. The experimental work with the fixed-bed reactor and the surrounding system is shown in detail in Soares dos Santos (2019). Figure 3.3 shows a flow diagram of the experimental set-up of the fixed-bed reactor. Additional information about the procedure used in the fixed-bed reactor experiments is reported in Azpiri Solares et al. (2019).

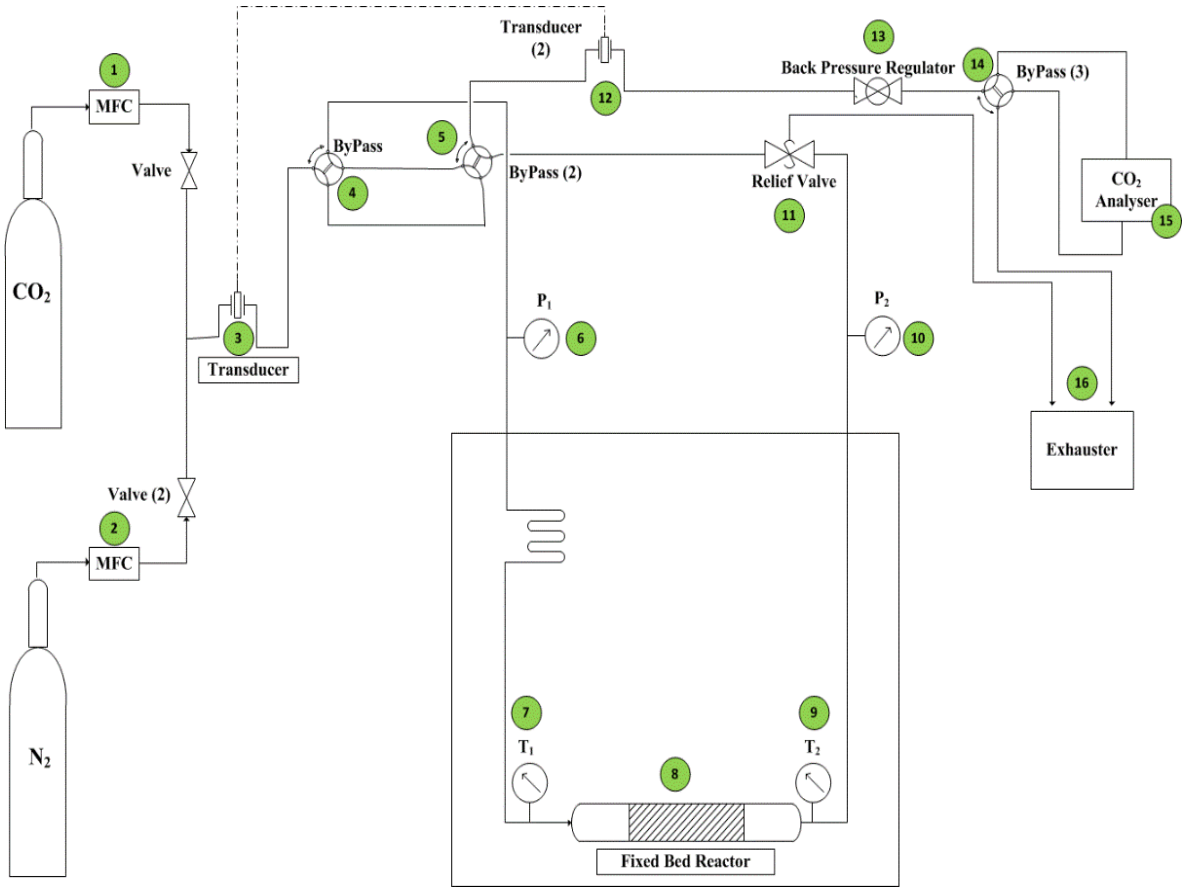

Figure 3.3. A flow diagram of the fixed-bed reactor experiments designed by Douglas Soares dos Santos (Azpiri Solares et al., 2019)

A dispersion model was added to the fixed-bed reactor model in the system shown in Figure 3.3 in order to account for the delay in the components' response in the analyzer. This model included the pipe that connected the CO_2 and N_2 feed vessels to the fixed-bed reactor (ID = $1x10^{-3}$ m, L = 0.5 m) and it included the outlet pipe that connected the reactor to the CO_2 analyzer (ID = $1x10^{-3}$ m, L = 0.1 m). Nitrogen was used instead of hydrogen in the fixed-bed reactor experiments because the use of hydrogen involved higher risks in the experimental work. The use of hydrogen instead of nitrogen would not worsen the adsorption results of carbon dioxide, as explained in Section 4.3.1. Equation

3.22 shows the equation for the component mass balance used in the inlet and outlet fittings of the fixed-bed reactor. The inlet wall of the tubes of the system surrounding the fixed-bed reactor was thermally isolated, so there was no heat exchange with the air outside the tubes and the temperature of the gas inside the tubes remained constant. The temperature of the gas entering and exiting the fixed-bed reactor was monitored using two thermocouples. The velocity of the gas was assumed to be constant in the surrounding system, and it was monitored by mass flow controllers. The pressure of the fixed-bed reactor was controlled by a back-pressure regulator by regulating the outlet flow if the pressure went above the value entered in the control system.

$$\frac{\partial Y(z)}{\partial t} = -v\frac{\partial\left(Y(i,z)\right)}{\partial z} + D_x\frac{\partial^2 Y(i,z)}{\partial z^2} \qquad 3.22$$

3.4.2 The Comparison of the Model to the Experimental Data

The dispersion and mass transfer coefficients of the laboratory scale PSA model were determined using a maximum likelihood parameter estimation algorithm developed by Process Systems Enterprise that minimizes the standard deviation between the model's results and the experimental data using an optimization problem. The algorithm varies the variable value to be estimated until the sum of the squared residuals (SSR) (Equation 3.23) between the experimental result and the model's value for N given data points is equal to or smaller than the tolerance established in the problem set-up. The conditions given in the adsorption step of the PSA model were used to estimate dispersion and the mass transfer coefficients, at 25 bar and 298.15 K. These conditions were also used in the experiments on the activated carbons and the axially-dispersed plug-flow model applied to the fixed-bed reactor.

In order to start the simulation, the initial values and the boundary conditions must be established for the variables that will be estimated. These values were selected based on previous studies that simulated fixed-bed reactor experiments at high pressures (Moon et al., 2018; Ribeiro et al., 2008).

$$SSR = \left[\frac{\sum_{n=1}^{n=N}\left(Y_{exp}-Y_{PSA}\right)^2}{N-1}\right]^{0.5} \quad 3.23$$

The mass axial dispersion coefficient was determined using glass beads inside the fixed-bed reactor. Activated carbon was used inside the fixed-bed reactor for the adsorption of carbon dioxide; therefore, adsorption occurred together with dispersion. However, to measure only dispersion without adsorption, the glass beads replaced the activated carbon.

Therefore, as adsorption did not occur when using the glass beads, the mass balance for the components followed the mechanism shown in Equation 3.22, similarly to the surrounding system. The temperature was assumed to be constant in the model because adsorption did not occur in the glass beads. However, the pressure drop, Equation 3.9, was still included in the fixed-bed reactor, due to the friction between the gas and the glass beads.

The mass transfer coefficient (k_{CO_2}) for the adsorption of carbon dioxide was determined by the parameter estimation method using the component molar fractions obtained in the axially-dispersed plug-flow model and the component molar fractions from the fixed-bed reactor experiments using the activated carbon adsorbents. The mass axial dispersion coefficient was set to the value determined in the parameter estimation that used the glass beads. This procedure was followed to obtain the mass transfer coefficient values with

experiments using (i) tetra-ethylene-pent-amine and (ii) a blend of mono-ethanol-amine and mono-di-ethanol-amine-modified activated carbons, using nitrogen and carbon dioxide mixtures. The methodology followed to obtain the modified activated carbons is reported in Azpiri Solares et al. (2019) and Soares dos Santos (2019).

3.4.3 Discretization Method

The default method of lines from the simulation package was used to solve the partial differential equations of the axially-dispersed plug-flow model. The equations are discretized in the axial domain, reducing the model to a set of one-domain differential equations. The backward finite difference method was used to discretize the variables for the component and overall concentrations, velocity and temperature. The direction of the discretization scheme was selected to go against the flow, due to the diffusion phenomena. However, the pressure was discretized using the forward finite difference method, because the pressure was specified in the outlet of the bed. Fifty discretization intervals were selected for the laboratory-based axially-dispersed plug-flow model. Because more numerical dispersion may be introduced with the discretization method, grid independence was achieved by varying the discretization order from one to two, and the number of discretization points from fifty to one hundred.

3.4.4 The Pressure Swing Adsorption Steps

After the parameter estimation using the axially-dispersed plug-flow model's values and the laboratory data, a seven-step pressure swing adsorption model was developed that

included a mixture of carbon dioxide and hydrogen entering the fixed-bed reactor. The conditions that held in each step of the pressure swing adsorption model are explained in Chapter 4, where the results of the laboratory-scale PSA model are presented. This process simulated the conditions of a pre-combustion PSA process in an integrated gasification combined cycle power plant. Table 3.8 shows the steps adopted in the model, which used Equations 3.1 to 3.16 and the boundary and initial conditions shown in Equations 3.17 to 3.21 to obtain the simulation results. Figure 3.4 is a flow diagram of the seven-step pressure swing adsorption (PSA) model.

Table 3.8. The steps in the reference laboratory PSA model

Steps	Description
Pressurization (P)	The fixed bed is pressurized to the adsorption pressure with feed gas
Adsorption (A)	Adsorption of carbon dioxide onto the surface of the adsorbent. Hydrogen is obtained as a product
Pressure equalization-depressurization (PE-D)	The bed pressure is decreased to the midpoint between the adsorption and the purge pressures, when the depressurizing bed is connected to a pressurizing bed
Depressurization (D)	The bed pressure is further decreased to atmospheric pressure. The product gas goes to a purging bed
Rinse (R)	Carbon dioxide enters the bed at a constant pressure and is obtained as a product at the same time
Purge (Pu)	Hydrogen enters the bed at a constant pressure, coming from the depressurization step, and carbon dioxide is obtained as a product
Pressure equalization-pressurization (PE-P)	The bed pressure is increased to the midpoint between the purge and the adsorption pressures, when the pressurizing bed is connected to a depressurizing bed

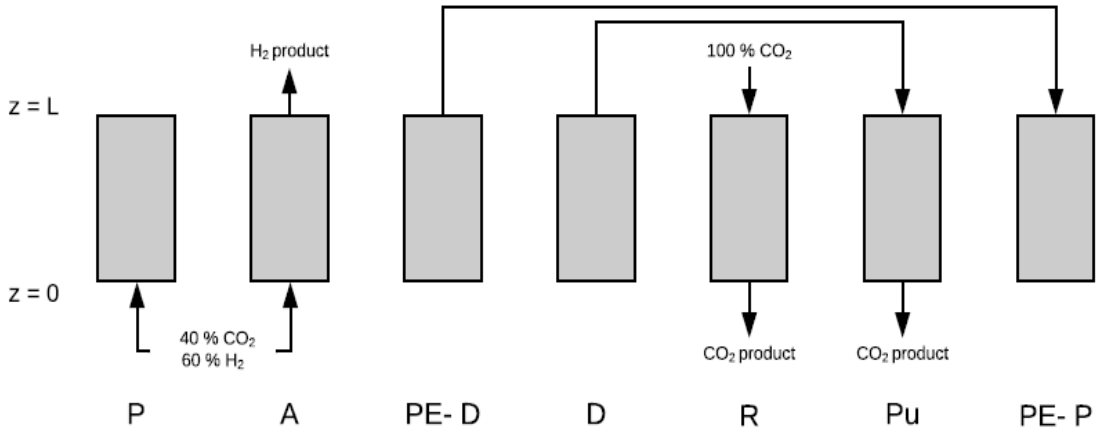

Figure 3.4. The flow diagram of the seven-step PSA laboratory model

The boundary conditions of the axially-dispersed plug-flow model were changed in order to develop the dynamic simulation. The inlet boundary conditions for the molar fraction (Y_i) of the components and the temperature (T) variables were changed for each step of the PSA model. These were introduced using the set of Equations in 3.21.

The outlet boundary condition of the pressure (P) was kept constant for the adsorption, purge and rinse steps. However, for the pressurization, depressurization and pressure equalization steps, the outlet boundary condition of the pressure was described by the transition equations 3.24 to 3.26. The transition equations changed the reactor pressure between the adsorption, pressure equalization and purge steps. The changes were described by linear equations that modelled a linear valve.

$$\frac{\partial P_{press}}{\partial t}_{z=L} = \left(\frac{P_{ads} - P_{atm}}{t_{pressurization}}\right) \quad 3.24$$

$$\frac{\partial P_{depress}}{\partial t}_{z=L} = \left(-\frac{P_{eq} - P_{atm}}{t_{depressurization}}\right) \quad 3.25$$

$$\frac{\partial P_{equal}}{\partial t}_{z=L} = \left(- \frac{P_{ads} - P_{eq}}{t_{equalization}} \right) \quad 3.26$$

3.4.5 Performance Indicators

The performance indicators selected to represent the degree of success of the separation process at laboratory scale were the purity and recovery of the hydrogen and carbon dioxide product streams. Their values were calculated by including the amount of the components in the inlet and the outlet streams of the fixed-bed reactor during each unit of time and by integrating these amounts during the duration of the steps in which these components were obtained as a product.

Equations 3.27 to 3.30 show the calculation of these performance indicator values. The purity of a component was calculated by dividing the amount of the product of interest in the outlet stream by the total amount of the component in that outlet stream. The recovery of a component was calculated by dividing the amount of the product of interest in the outlet stream by the amount of that product in the inlet stream.

We changed several process variables and process configurations from those of the basic conditions explained in Section 3.4.4 to see the effect of these variations on the process performance.

$$CO_2\ Purity = \frac{\int_{t=t_D}^{t=t_{Pu}} C_{CO_2,z=L} v_{z=L} dt}{\sum_{i=1}^{n} \int_{t=t_D}^{t=t_{Pu}} C_{i_{z=L}} v_{z=L} dt} \quad 3.27$$

$$H_2\ Purity = \frac{\int_{t=0}^{t=t_A} C_{H_2,z=L} v_{z=L} dt}{\sum_{i=1}^{n} \int_{t=0}^{t=t_A} C_{i_{z=L}} v_{z=L} dt} \quad 3.28$$

$$H_2\ Recovery\ =\ \frac{\int_{t=0}^{t=t_A} C_{H_2,z=L} v_{z=L} dt - \int_{t=t_R}^{t=t_{Pu}} C_{H_2,z=0} v_{z=0} dt}{\int_{t=0}^{t=t_A} C_{H_2,z=0} v_{z=0} dt + \int_{t=t_{Pu}}^{t=t_P} C_{H_2,z=0} v_{z=0} dt} \quad 3.29$$

$$CO_2\ Recovery\ =\ \frac{\int_{t=D}^{t=t_{Pu}} C_{CO_2,z=L} v_{z=L} dt}{\int_{t=0}^{t=t_A} C_{CO_2,z=0} v_{z=0} dt + \int_{t=t_{Pu}}^{t=t_P} C_{CO_2,z=0} v_{z=0} dt} \quad 3.30$$

3.5 The Pilot-Scale Pressure Swing Adsorption Model

The laboratory-scale PSA model of Section 3.4 was scaled up to analyze the performance of the technology at pilot scale, as simulation is used as an initial tool to predict the viability of a carbon capture technology at bench scale (Abanades et al., 2015). The scale-up of the fixed-bed reactor model was also necessary in order to study the viability of the technology in a pilot-scale power plant in terms of the energy efficiency and the economics of the plant.

3.5.1 Defining the Capacity of the Pilot-Scale Power Plant and Its Variables

The previously reported fixed-bed reactor model at laboratory scale was scaled up using a number of cycle designs and was based on 293.2 mol/s gas being fed into the PSA system. This flow rate was estimated based on the requirements of a GE-10 gas turbine that can operate on over 95% hydrogen purity (Goldmeer, 2018). The aim of scaling up the PSA model was to analyze the effect of the design and of the process variables on the product performance indicators at plant scale. The rate of the flow fed into the gas turbine determined the sizing of the PSA process. The feed composition, pressure and temperature of the PSA unit were determined by the process upstream, which was a water gas shift unit.

The volumetric flow rate (m^3/s) was derived using the ideal gas equation, Equation 3.3, which included the feed pressure and the temperature of the reactor. The feed conditions of the PSA unit were established based on the outlet stream of the water gas shift reactor described by Anantharaman et al. (2011), with values of 36.7 bar and 523 K. The temperature of the gas at the WGS reactor outlet was decreased to 338 K to enter the PSA unit, as reported in a previous study (Riboldi and Bolland, 2015b).

The volumetric flow rate at a feed pressure of 36.7 bar was 0.225 m^3/s. The adsorption time was established as 300 s, based on the feed pressure and the breakthrough capacity of the adsorbent (Jain et al., 2003). The superficial velocity of a pilot-scale or industrial fixed-bed reactor is typically between 0.01 and 0.05 m/s, which is a compromise between the productivity of the unit and avoiding fluidization inside the reactor (Wiheeb et al., 2016). With a superficial velocity of 0.04 m/s, the diameter of the reactor was 2.57 m.

The length of the reactor was determined using a length-to-diameter ratio (L/D) of 1.51, based on the number of carbon dioxide moles to treat during the adsorption step. This ratio was established to obtain a breakthrough time of the carbon dioxide at 600 s, which allowed the total cycle time to be around 1000 s. Cycle times much higher than that are predicted to decrease the carbon dioxide recovery (Abanades et al., 2015). The wall thickness of the fixed-bed reactor should be between 1 mm and 10 mm, as stated in Rase (1990), and it was used to calculate the heat transfer through the walls. For this system, a value of 7 mm was chosen, because a high value of wall thickness is required when there is severe pressure inside the fixed-bed reactor. The particle diameter was 1 mm, the same as at laboratory scale.

3.5.2 Design Variations in the Pilot-Scale Model

The choice of several process variables for scaling up the PSA process has an effect on the separation process and, thus, on the composition of the outlet streams in each of the process steps shown in Figure 3.3. The capacity of an NGCC plant is determined as the number of moles of hydrogen gas required to produce a certain power. This logically also determines the number of moles that must enter the PSA separation process. The molar flowrate was established with a constant value of 293.2 mol/s, at 36.7 bar and at 338 K from the process upstream, a water gas shift reactor, and a cooler, as mentioned in Section 3.5.1.

Once the feed's molar flow rate, pressure and temperature were established, the main operational variables were the length-to-diameter ratio of the bed, the purge-to-feed flow rate ratio, and the superficial velocity of the gas, which depended on the bed diameter. Figure 3.5 is a flow diagram of the various design choices for the PSA process explained here.

The effect of the PSA decision variables was analyzed using the Global System Analysis (GSA) capability in gPROMS®. This capability enables users to explore the behaviour of a system, based on a set of input variables. Several model simulations are simultaneously performed for a selected range of decision variables. A parametric study was executed by inserting a range of the input values shown in Figure 3.5 and obtaining the purity values of hydrogen and carbon dioxide, with the requirement of achieving over 85% recovery of hydrogen in each of the case studies. The range of the variable values for this study was chosen based on the conditions shown in previous PSA studies that separated carbon dioxide from hydrogen (Moon et al., 2018; Ribeiro et al., 2008; Riboldi et al., 2014).

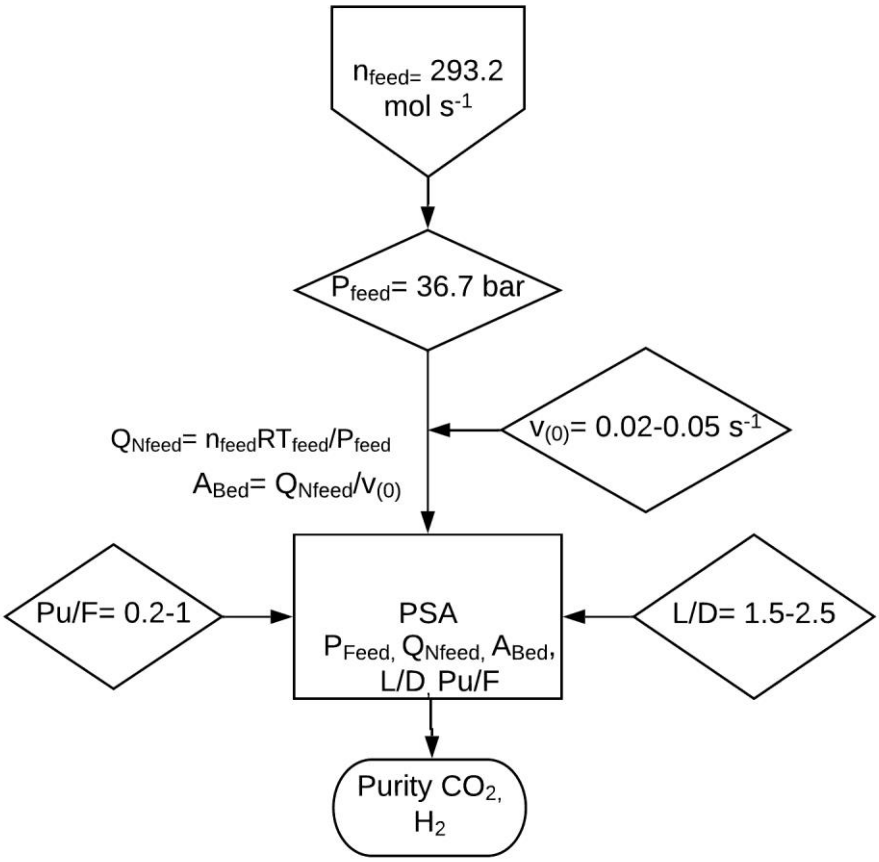

Figure 3.5. A flow diagram of the design choices for the scaled-up PSA model

3.5.3 Alternative Configurations and Numbers of Units

Once the operational conditions were established using the parametric study explained in Section 3.5.2, additional configurations and beds were included in the model. The number of beds is one of the variables that dictates the number and types of steps in a PSA model. The goal of the alternative configurations was to increase the carbon dioxide purity, in view of the fact that the target of 99% purity of the hydrogen had been obtained with the previous case studies using GSA. Additional configurations were based on the four-bed

base case, adding one (a five-bed model) and two (a six-bed model) reactors. Cases beyond a six-bed PSA model were not studied here, as more beds would critically raise the capital costs of an NGCC power plant (Casas et al., 2013a).

Additional configurations within the four-bed model were investigated. The mass and energy balances between the process steps were maintained by storing the simulation results of the gas concentration, flowrate, temperature and pressure at the end of each of the steps. The following process steps were added to the initial configuration:

1. The depressurization step was replaced by an assisted purge step (A-Pu). The outlet gas of the A-Pu step was to feed the fixed-bed reactor undergoing the purge step. The sequence of the steps for this configuration is shown in detail in Figure 5.10 (Section 5.4.1).The A-Pu step replaced the final depressurization step of the initial configuration. The assisted purge step was placed after the pressure equalization-depressurization step, in order to direct the hydrogen exiting the bed to the purge step, where hydrogen was required.

2. The effect of including a rinse step (R1) was also studied, feeding the carbon dioxide product into the fixed-bed reactor after the adsorption and pressure equalization steps. The durations of the assisted purge step and the rinse step were the same, in order to synchronize the beds.

The effects of introducing an assisted purge step (A-Pu) and a rinse step (R1) were also tested on the five-and six-bed models. These models offered the introduction of additional pressure equalization steps; the five-bed model had two pressure equalization steps and the six-bed model had three pressure equalization steps. It has been reported that the addition of pressure equalization steps increases the carbon dioxide purity and the

hydrogen recovery (Casas et al., 2013a). The insertion of additional pressure equalization steps also allows the process to include the rinse step between the first and second pressure equalization steps (in the five-bed model) and between the second and third equalization steps (in the six-bed model). The feed gas for these rinse steps (in the five- and six-bed models) required less compression work, as the gas was pressurized at lower pressures than the adsorption pressure.

3.6 The NGCC Power Plant Model

3.6.1 The Overall Design

The scaled-up pressure swing adsorption process was integrated into a natural gas combined cycle power plant model. Combined cycle power plants offer favourable conditions for the implementation of carbon capture using PSA, due to the processes operating at pressures as high as 37 bar before the gas fuel enters the gas turbine (Riboldi and Bolland, 2017). These operating conditions reduce the gas compression requirements of the power plant, increasing its overall energy efficiency. Additionally, operation with natural gas as a fuel favours the separation process using PSA, due to the composition of natural gas compared to that of coal. These power plants also offer the advantage of implementing a hybrid power generation system that produces hydrogen (Riboldi and Bolland, 2016; Seyitoglu et al., 2016).

The power plant was initially designed to operate with a GE-10 gas turbine, which can be fuelled with up to 95% pure hydrogen gas (Goldmeer, 2018). The gas turbine produces a net power output of 11.44 MWe, with a net output efficiency of 31.1%.

The aim of this section of the study is to examine the impact of operating a carbon capture unit using PSA on the power output of a reference plant that does not capture carbon. The model that integrated the carbon capture unit included components for hydrogen production, such as steam methane reforming and water gas shift reactors, and components from combined cycle power plants that use gas turbines for power production. The components of the model are described further in Section 3.6.2. Figure 3.6 presents the overall flow diagram of the power plant model.

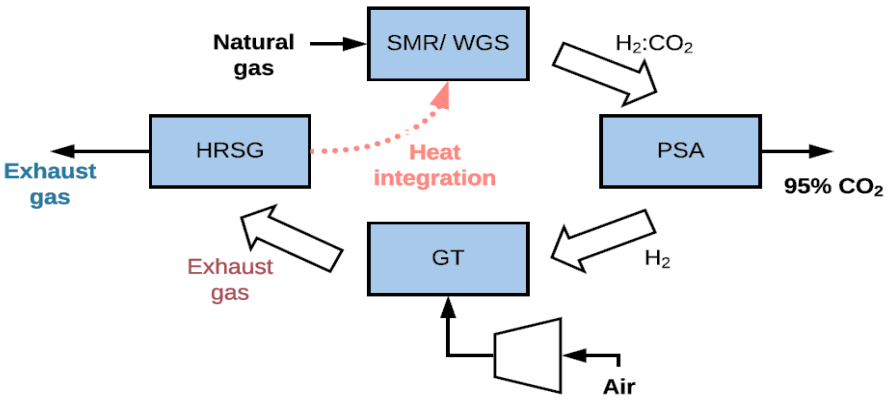

Figure 3.6. The overall flow diagram of the NGCC power plant model using the PSA process

The power plant was divided into the main following units:

- A syngas production unit, described in Section 3.6.2.
- A unit for carbon capture via PSA, described in Section 3.5.
- A unit that compressed carbon dioxide, described in Section 3.6.3.
- A power production unit, described in Section 3.6.4.

A heat integration analysis was carried out to maximize the energy efficiency of the power plant, as described in Section 3.6.4. The technical data and the properties of the natural gas used in the power plant were based on a study by the International Energy Agency Greenhouse Gas R&D Programme (IEA-GHG, 2009), which analyzed the integration of an amine-absorption-based carbon capture technology in coal- and gas-fired power plants. The technical data for the natural gas is shown in Appendix D.

3.6.2 Syngas Production

The aim of having a process upstream of the PSA unit was to produce the syngas to efficiently capture the carbon dioxide before it enters the gas turbine. The main units of the syngas production unit were the steam methane reforming reactor and the water gas shift reactor. Figure 3.7 shows the units used to simulate the syngas production section in gPROMS® ProcessBuilder. The natural gas was fed into the process via a pipeline, following the guidelines in the European Benchmarking Task Force report (Anantharaman et al., 2011), with a flow rate of 114.44 mol/s in order to operate the plant at 100% capacity. Saturated steam also entered into the reactor in a steam-to-methane ratio in excess of 2.7 coming from the heat recovery unit of the gas turbine (Section 3.6.4) to obtain a conversion of over 90% in the steam methane reforming reaction (Sharma et al., 2019).

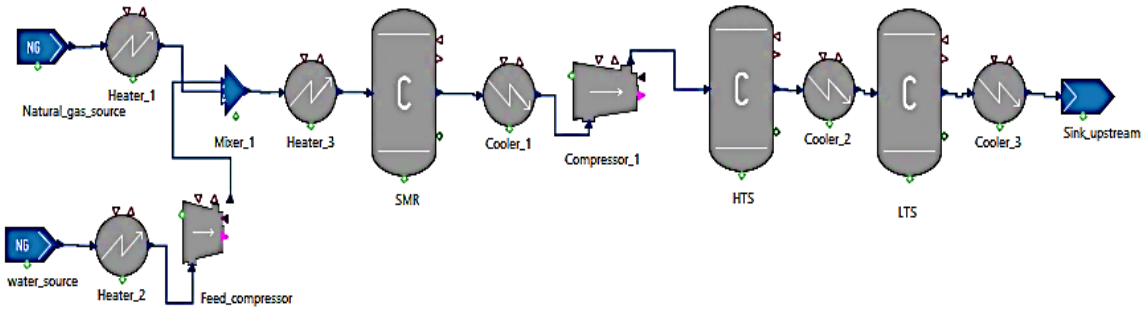

Figure 3.7. The syngas production section as simulated in gPROMS® ProcessBuilder

After both inlet streams were heated to a reaction temperature of 1073.2 K, they entered the reactor at 26 bar. The heating requirements of the reactor were calculated based on the process simulation results. In addition to the main steam reforming reaction, shown by Equation 3.31, a secondary reforming reaction, Equation 3.32, and a water gas shift reaction, Equation 3.33, happened inside the SMR unit, achieving an overall methane conversion of 99.90%.

$$CH_4 + H_2O \leftrightarrow CO + 3H_2 \quad 3.31$$

$$CH_4 + 2H_2O \leftrightarrow CO + 4H_2 \quad 3.32$$

$$CO + H_2O \leftrightarrow CO_2 + H_2 \quad 3.33$$

An outlet stream of 62% hydrogen, 20% steam, 10% carbon monoxide and 7% carbon dioxide and less than 1% methane (molar basis) was obtained using process simulation. These component concentration results are in line with the steam methane reforming reactions performing in industry (U.S. Energy Information Administration, 2020). The dimensions of the unit were established based on the previous conditions and the flow

rates of the inlet streams. The outlet stream of the SMR was cooled to 680 K and further compressed to 36.7 bar to meet the inlet conditions for the water gas shift reaction.

The water gas shift process was performed using two intercooled adiabatic fixed-bed reactors, a high temperature shift (HTS) reactor that operates at 680 K, and a low temperature shift (LTS) reactor that operates at 473.15 K. These two stages were selected as a compromise between obtaining a WGS conversion of over 95%, the capital costs of the plant (the number of units), and the conditions based on a report by the European Benchmarking Task Force (Anantharaman et al., 2011). The first reactor (HTS) obtained a carbon monoxide conversion of 75%, and there was a water-quench cooling process between the HTS and LTS reactors that lowered the gas stream temperature to 473.15 K for the second stage of the WGS reaction. The LTS reactor obtained a 98% conversion of carbon monoxide with the variable values chosen. The design variables of the SMR and WGS processes are further specified in Appendix D.

The outlet stream of the LTS unit was further cooled down to 338 K to enter the pressure swing adsorption process, and concentrations of 59% hydrogen and 40% carbon dioxide were achieved, yielding a concentration lower than 1% carbon monoxide in the outlet stream. The feed pressure of the PSA unit was set to the outlet pressure of the WGS unit with a value of 36.7 bar, to minimize compression costs.

3.6.3 Carbon Dioxide Compression

The carbon dioxide captured in the PSA process was compressed from 1 bar to 110 bar, and cooled down below 303.15 K, to fulfil the requirements for storage. This compression section was designed following the guidelines given in the European Benchmarking Task

Force report (Anantharaman et al., 2011). The process involved three compression stages that used intercooling with water. Figure 3.8 shows the carbon dioxide compression process implemented in gPROMS® ProcessBuilder.

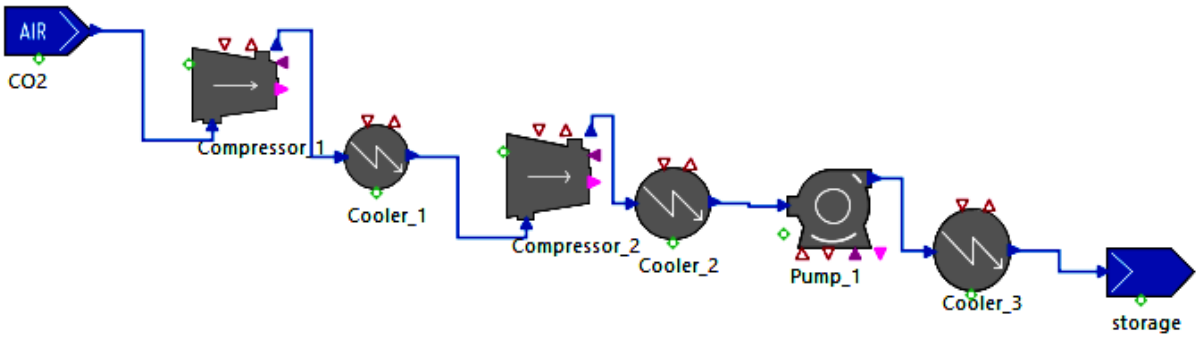

Figure 3.8. The carbon dioxide compression section as simulated in gPROMS® ProcessBuilder

The carbon dioxide coming from the PSA unit was compressed to 40 bar in an initial compression stage and to 80 bar in the second stage. The coolers between the first and third compression stages lowered the carbon dioxide temperature to 301.15 K, to counteract the gas's rise in temperature due to compression. Centrifugal compressors were used to model the process, setting a polytropic efficiency of 85% in the compressor model. In the third stage, dense carbon dioxide was pumped to 110 bar using a pump with a polytropic efficiency of 85% and cooled down to a temperature of 298.15 K for storage. The calculation of the energy losses of this section included the power required for the three stages of the compression.

3.6.4 Power Production and Heat Integration

The hydrogen leaving the PSA unit was directed to a GE-10 gas turbine for the production of electricity. This type of gas turbine was selected based on the hydrogen purity obtained in the PSA process, because it can operate on up to 99% pure hydrogen (Goldmeer, 2018). The design features of the turbine are given by the manufacturer and are in Appendix D.

The package provided by the manufacturer includes a single open-cycle gas turbine, with an eleven-stage axial low compressor and a single slot-cooled combustion chamber designed for low NO_x emissions. The turbine also includes an air-cooled electric generator and an inlet module with air filters, a silencer and a ventilation system. The power output of a single gas turbine is 11.25 MWe, with a net turbine efficiency of 31.1%. This efficiency also includes the power losses due to the compression of air within the turbine. The exhaust gas from the gas turbine is formed by up to 90% steam, with a flow rate of 47.5 kg/s and a temperature of 763.15 K. The exhaust gas is cooled down to 288 K in a steam generator using a waste heat boiler, mainly to meet the heat requirements of the SMR process.

A pinch analysis was conducted to maximize the energy efficiency of the power plant. This analysis was developed following the procedure shown in Kemp (2011). The analysis was based on the heat requirements of the units in the process flow modelled in ProcessBuilder and on the heat released from the exhaust gas of the turbine. Appendix E shows the hot and cold streams of the units covered in the analysis, the problem table and the pinch point. The process streams that required cooling were called hot streams, whereas the cold streams were those that required heating, as defined in Kemp (2011). A minimum temperature difference of 10 degrees was assumed between the hot and cold

streams. The hot streams went from a maximum temperature of 1164.46 K to a minimum temperature of 300 K, and the cold streams went from a maximum temperature of 1173.15 K to a minimum temperature of 283 K. The maximum temperature of the hot stream was lower than that of the cold stream because the stream entering the steam methane reforming (SMR) reactor required more heating than any other stream in the power plant. Therefore, external heating was provided to this stream, as shown in Appendix E. The temperature ranges of the process streams were divided into sections to calculate the additional power requirements for the power plant and the power remaining for heating purposes within the plant. A steam turbine was not installed in this power plant, due to the high steam demand of 4.82 kg/s of the SMR process in this power plant.

3.7 The Economic Analysis

The economic analysis of the designed NGCC power plant was carried out by following the procedure of Peters et al. (2003). The standard costing methodology for chemical engineers to design plants was adopted from this work. The defence of the economic aspects of the model are beyond the scope of a chemical engineering thesis. However, planning the costs of a technology is key to successfully implementing it, so an economic analysis was done.

The preliminary economic assessment was carried out to assess the viability of the capture technology presented in this work, compared to the viability presented in previous studies. For that purpose, the technical parameters of the plant, such as the plant location and the fuel specification data were obtained from a study by the International Energy Agency Greenhouse Gas R&D Programme (IEA-GHG, 2009). The programme is supported by

fifteen countries, the European Commission, the Organization of the Petroleum Exporting Countries (OPEC) and sixteen international sponsors.

The performance of a reference NGCC power plant without capture was compared to that of a plant with carbon capture using the PSA process developed in this work. For each of the cases, the total capital investment (Section 3.7.1) and the total annual product cost (Section 3.7.2) were calculated. Then the economic performance of the two power plants was compared using the indicators shown in Section 3.7.3.

The technical specifications of the power plant, on which the economic analysis is based, are shown in Appendix D. The technical specifications include the plant location, ambient conditions, the provision of a cooling water system, and product and raw material delivery. These specifications were obtained from the work by the IEA-GHG Programme (2009), in which a power plant with carbon capture was assessed. The power plant was located on the coast of the Netherlands.

The date specification for the economic analysis was the second quarter of 2020. The currency selected for the economic analysis was the US dollar, based on previous work that analyzed the implementation of carbon capture technologies in power plants (Alhajaj et al., 2016; Li et al., 2012; Riboldi and Bolland, 2017). This study assumes constant money values and no inflation, based on previous studies by IEA-GHG and the Electric Power Research Institute, EPRI (IEA-GHG, 2009).

3.7.1 Estimation of the Total Capital Investment

The amount of the total capital investment (TCI) for the power plant was estimated based on the capital necessary to buy and install the process equipment, with the equipment

auxiliary units to enable plant operation, and the construction costs of the equipment. It also included plant sections that are not directly related to production, such as the cost of land, buildings, yard improvements and the construction of a utilities supply system, all of which have an effect on the overall cost that depends on the location of the plant (Peters et al., 2003). The estimation of the total capital investment was categorized into estimated direct costs, indirect costs and working capital costs.

The total direct capital cost (TDC) was the major contributor to the total capital investment; this includes the material and labour required to install the power plant and enable the operation of the plant. The material and energy balances of the steam methane reformer and water gas shift reactor units were used to determine the requirements for the size of these utilities, and so to calculate their cost. The mass and energy balances of these units were calculated by process flow modelling in ProcessBuilder. The gas turbine size and power produced were obtained from the manufacturer, and the size of the PSA unit was determined from the scale-up process explained in Section 3.5.

The equipment purchase cost for each unit was estimated using cost indicators based on the Marshall and Swift equipment cost indexes (Peters et al., 2003). The price of the gas turbine was obtained from the manufacturer. The total equipment purchase cost was calculated summing up the values of individual process equipment, and it is shown as PEC in Table 3.9. A 10% contingency was considered for the main process equipment and the heat exchangers, and a 21% contingency for pumps, fans and compressors (U.S. Department of Energy, 2010).

The installation cost of the units was calculated as a percentage of the equipment purchase cost of each unit, based on the percentages proposed by Guthrie (1974). The percentages

for the installation costs for the power plant units are shown in Table 3.9. The installation costs of the units were determined following the structure shown in Equation 3.34. The cost item values obtained for the equipment purchase costs and installation costs are shown in Appendix F.

$$Cost\ item\ value = \frac{Contribution\ percentage}{100} \times Reference\ item\ value \qquad 3.34$$

The other variables in the direct cost of the power plant were piping, electrical installation, building construction, yard improvements, utilities supply auxiliaries, land, and instrumentation and control equipment and their installation service. The costs of these were also estimated using Equation 3.34, with the percentage values shown in Table 3.9.

The total indirect costs (TIC) of the plant included the engineering and supervision costs, the construction expenses, the contractors' fees, and the start-up expenses. These cost items were calculated using percentage factors provided by Peters et al. (2003), shown in Table 3.9, and using Equation 3.34. The last contributor to the total capital investment was the total working capital (TWC), which was assumed to be 15% of the total capital investment (TCI). Finally, the TCI was estimated by summing the TDC, TIC and TWC components.

Table 3.9. The percentages for the cost items that contributed to the total capital investment

Main cost items	Cost item	Contribution percentage (%)	Reference item	Source
Total direct cost (TDC)	Equipment purchase cost (PEC)	27	TCI	Calculated based on cost indexes (Peters et al., 2003)
	Equipment installation costs	Fixed beds: 70 Gas turbine: 50 Compressor: 40 Heater/cooler: 30	PEC	Guthrie (1974)
	Insulation	9	PEC	Peters et al. (2003)
	Instrumentation	20	PEC	Peters et al. (2003)
	Piping	60	PEC	Peters et al. (2003)
	Electrical installation	13	PEC	Peters et al. (2003)
	Plant buildings	45	PEC	Peters et al. (2003)
	Yard improvement	15	PEC	Peters et al. (2003)
	Utilities supply	55	PEC	Peters et al. (2003)
	Land	1	TDC+TIC	Peters et al. (2003)

Total indirect cost (TIC)	Engineering and supervision	30	PEC	Peters et al. (2003)
	Construction	10	TDC	Peters et al. (2003)
	Contractors' fees	5	TDC	Peters et al. (2003)
	Start-up expense	8	TIC	Peters et al. (2003)
Total working capital (TWC)	Working capital	15	TCI	Peters et al. (2003)

3.7.2 Estimation of the Total Annual Product Cost

The annual product cost (ATPC) was estimated as the sum of the manufacturing costs (MC) and general expenses (GC) per year. The manufacturing cost covered all costs related to the operation of the plant, and it was calculated using the direct product costs (DPC), fixed costs (FC) and plant overhead costs (POC), as shown in Equation 3.35 (Peters et al., 2003).

In the case study where hydrogen co-production was included in the plant, the annual product cost ($ATPC_{H2}$) was calculated using Equation 3.36, where the earnings from the hydrogen sales were included in the equation, following the production cost calculations in power plants with co-generation (Li et al., 2012).

$$ATPC = MC + GC = DPC + FC + POC + GC \quad 3.35$$

$$ATPC_{H2} = ATPC - Annual\ Earnings\ from\ Hydrogen\ Sales \quad 3.36$$

The direct product costs covered the price of the raw materials for the power plant, which are natural gas and process water, based on the market price on the date of the estimation

(the 27th of March 2020). The operating labour cost and supervisory work cost were estimated based on the size of the plant and assumed three work shifts per day. The annual maintenance and repair costs were 5% and the operating supplies cost was 15% of the direct and indirect costs. Table 3.10 shows the components of the direct production costs and their contribution as a percentage of the cost.

For the estimation of the fixed costs, an annual depreciation rate of 10% of the sum of the direct and indirect capital costs was assumed for the equipment, and of 3% for the buildings, assuming a plant life of 30 years. The plant overhead costs were 60% of the operating labour and maintenance costs. Table 3.10 shows the components of this cost and their percentages.

The estimation of general expenses included the administrative, distribution and marketing expenses. For the distribution expenses, 5% of the total product cost was assumed, due to the ease of transferring the produced bulk electricity to the grid. The administrative expense was established as 25% of the operating labour cost. In addition, an interest rate of 5% was assumed in the general yearly expenses of the power plant, to compensate for repayments of the capital investment borrowed from a bank or another financial entity (Peters et al., 2003). Table 3.10 shows the components and their percentages that contribute to the total annual product cost.

Table 3.10. The percentages for the cost items that contribute to the total annual production cost

Main cost items	Cost item	Contribution percentage (%)	Cost category	Source
Direct production costs (DPC)	Raw materials	37	ATPC	Calculated based on the natural gas and process water price in the chosen location at the time of estimation
	Operating labour (OL)	7	ATPC	Calculated based on the number of workers and shifts recommended by Peters et al. (2003)
	Maintenance and repairs (MR)	5	TDC+TIC	Peters et al. (2003)
	Operating supplies	20	MR	Peters et al. (2003)
	Laboratory charges	10	OL	Peters et al. (2003)
Fixed charges (FC)	Depreciation	Process equipment: 10 Buildings: 3	TDC+TIC	Peters et al. (2003)
	Local taxes	2	TDC+TIC	Peters et al. (2003)
	Insurance	1	TDC+TIC	Peters et al. (2003)
Plant overhead (PO)	General plant upkeep Payroll overhead Safety equipment Storage facilities	60	OL+MR	Peters et al. (2003)

General expenses (GC)	Administrative costs	25	OL	Peters et al. (2003)
	Distribution and selling costs	5	ATPC	Peters et al. (2003)
	Yearly interest	5	TCI	Peters et al. (2003)

3.7.3 The Economic Performance Indicators of the Power Plant

To compare the costs of the designed power plant to the costs of those in previous work, the levelized cost of electricity (LCOE) and the cost of carbon avoidance (LCCA) were calculated. These performance indicators were selected in the study by the IEA-GHG (2009) in order to compare the carbon capture technologies analyzed in that work.

The LCOE was calculated using Equation 3.37, for the power plants with and without carbon capture. Then the cost of a power plant that used carbon capture was compared to the one without capture, based on the amount of electricity that was produced in the power plant. The unit used to compare both plants was $/MWh. The LCCA (Equation 3.38) represents the extra cost per tonne of carbon dioxide sequestered by the plant that had the carbon capture technology compared to the cost of the reference plant, and the results were given in $/tonne of CO_2 captured.

$$LCOE = \frac{Cost\ of\ electricity\ production_{plant}}{Electricity\ Produced_{plant}} \quad 3.37$$

$$LCCA = \frac{LCOE_{plant\_CCS} - LCOE_{plant\_ref}}{Emissions_{plant\_ref} - Emissions_{plant\_CCS}} \quad 3.38$$

CHAPTER 4 – THE MODEL VALIDATION AND THE LABORATORY-SCALE PSA PROCESS

4.1 Introduction

This chapter reports the results of the parameter estimation that were calculated by fitting the axially-dispersed plug-flow model to the experimental fixed-bed reactor data. The chapter also reports the results of the pressure swing adsorption model that was developed at laboratory scale and a sensitivity analysis of the PSA process variables that analyzed their effect on the purity and recovery of the products. The results of this chapter are published in Azpiri Solares et al. (2019).

The first step in validating the axially-dispersed plug-flow model was to compare the output of the simulation to the data from a laboratory-scale fixed-bed reactor, as shown in Section 4.2. This was important for determining whether the model assumptions and equations represented the experimental fixed-bed reactor rig under the same process conditions, such as temperature and pressure. The validation of the model also enabled the estimation of the input model values that could not be measured in the laboratory experiments.

The axially-dispersed plug-flow model explained in Section 3.3 was validated against experimental fixed-bed reactor data shown in Soares dos Santos (2019). The model was validated using experimental data that featured a maximum likelihood parameter estimation method within gPROMS® ProcessBuilder that minimizes the standard

deviation between the computational and experimental results for the carbon dioxide concentration at the outlet.

The procedure for the parameter estimation is described in Section 3.4.2. This estimation was carried out by varying the value of the mass transfer coefficient of the carbon dioxide. The parameter estimation algorithm changed the mass transfer coefficient value to minimize the difference between the simulated and experimental data.

Amine-modified activated carbon adsorbents were developed to increase the affinity of carbon dioxide for the activated carbon surface (Soares dos Santos, 2019). The parameter estimations were developed using tetra-ethylene-pent-amine and a novel blend of mono-ethanol-amine and mono-di-ethanol-amine-modified activated carbon adsorbents data. These adsorbents are also referred to as AC-TEPA and AC-MEA-MDEA, respectively, in this chapter.

Before determining the mass transfer coefficient from the fixed-bed reactor data using the activated carbons, the mass dispersion coefficient was determined via parameter estimation using the axially-dispersed plug-flow model and the data from the experimental fixed-bed reactor rig; glass beads were used inside the fixed-bed reactor instead of the activated carbons. This enabled the determination of the dispersion of the bed independently from the mass transfer coefficient, as adsorption did not occur in the glass beads.

Once the mass dispersion and mass transfer coefficient were determined, a seven-step PSA model was developed, as explained in Section 3.4.4. The results of the PSA laboratory process are shown in Section 4.3. These results are used later as the core model to scale up the process and to study the carbon capture plant configurations, the number

of beds, the cycle design and the plant optimization, as reported in Chapter 5. Seven steps were required in the PSA model to obtain purity and recovery values over 90%.

The model was simulated using the experimental conditions and the adsorbent parameters obtained from the MEA-MDEA-modified activated carbons, as these adsorbents showed the most promise for the implementation of PSA under pre-combustion conditions. For the process explained in Section 3.4.4., the adsorbent parameter and process variable values were varied, such as the feed gas composition, pressure and fixed-bed reactor size. These sensitivity analyses were carried out to study the effect of these variables on the PSA performance indicators shown in Section 3.4.5 and to select the variables that gave the best output in order to scale up the PSA process.

4.2 The Validation of the Axially-dispersed Plug-Flow Model

4.2.1 The Validation of the Fixed-Bed Reactor Rig

The dispersion coefficient required in the mass balance Equations 3.1 and 3.2 was first obtained by fitting a dispersed plug-flow model to data from a fixed-bed reactor experiment that used glass beads. After the axial dispersion coefficient value was fixed, the mass transfer coefficient could be determined independently with the experiments using the activated carbons.

The fixed-bed reactor model was developed in view of the fact that adsorption of the gas components does not occur in glass beads, and consequently, the dispersion coefficient of the gas mixture in the fixed-bed reactor can be determined using Equation 3.22, following the procedure explained in Section 3.4.2. The temperature, pressure and feed

gas composition in the fixed-bed reactor experiment using glass beads were the same as in the experiments using amine-modified adsorbents.

Table 4.1 shows the conditions of the fixed-bed reactor experiment using glass beads. These parameters were included in the axially-dispersed plug-flow model to determine the dispersion coefficient. The wall of the reactor and the inlet diameter of the tubes were thermally isolated, so the system was isothermal. The gas phase flow rate was set to a value of 200 Nml min^{-1} to match the value in the laboratory experiments. The experiments were carried out in these conditions so as to be similar to an adsorption step at a pressure of 25 bar in the PSA processes used in pre-combustion capture. Therefore, the aim of the parameter estimation was to determine the mass transfer coefficient during the adsorption step, because the feed step mostly determines the light product quality and the amount of carbon dioxide that is adsorbed in the fixed-bed reactor.

Table 4.1. The conditions for the fixed-bed reactor experiment using glass beads

Composition CO_2, mol basis (%)	40	Bed length (m)	0.069
Composition N_2, mol basis (%)	60	Bed diameter (m)	0.025
Gas feed pressure (bar)	25	Gas feed temperature (K)	298

Figure 4.1 shows the mol fractions for the carbon dioxide component in the outlet of the fixed-bed reactor rig for the plug-flow model and the laboratory experiments using glass beads. Initially, there was only nitrogen in the fixed-bed reactor at 25 bar, at ambient temperatures of 298.15 K. As shown in Figure 4.1, the gas entered the fixed-bed reactor rig initially with the component fractions listed in Table 4.1, and no carbon dioxide was detected by the analyzer until around 300 s from the start of the experiment. The shape of

the experimental breakthrough curve, with a steep s-shaped section, showed that the dispersion of the operated gas mixture that occurred in the system was quite low.

This was confirmed by the value of the dispersion coefficient obtained from the model results which best fit the experimental data. The value of the dispersion coefficient in this case was $5 \times 10^{-6}\ m^2\ s^{-1}$ with an excellent value of the sum of the squared residuals of 0.1%. The value obtained for the axial dispersion coefficient is in agreement with previously reported values for fixed-bed reactors operating with gases at high pressure, between the orders of 10^{-5} and $10^{-7}\ m^2\ s^{-1}$ (Seader and Henley, 2006).

The dispersion coefficient was then fixed at the value derived using the glass beads, in order to increase the accuracy of the parameter estimation using the data of the experiments with the amine-modified activated carbons, following a procedure of Knox et al., (2016). The mass transfer coefficient for the carbon dioxide gas component was the parameter estimated from this fit.

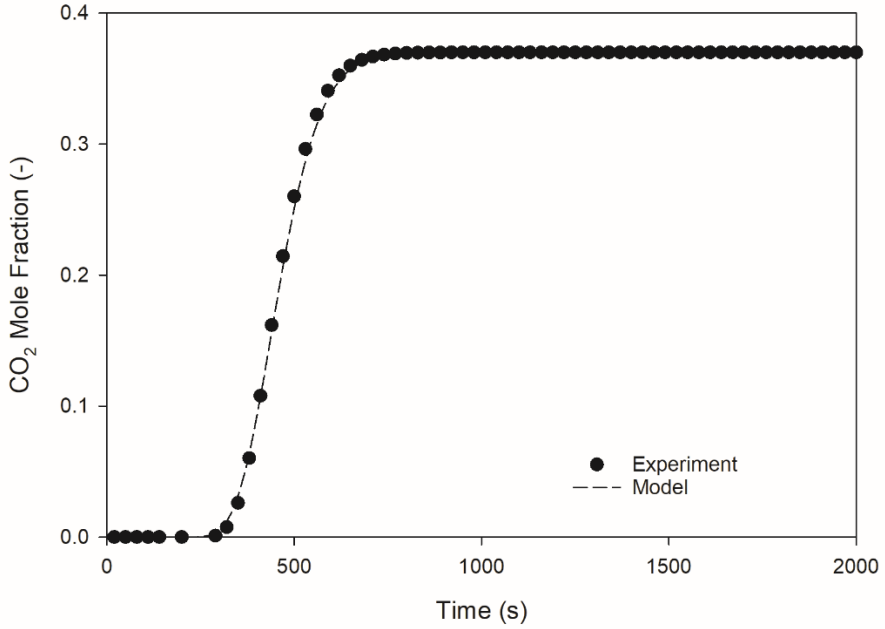

Figure 4.1. Dispersed plug-flow model fit to the experimental data using glass beads at 25 bar

4.2.2 Parameter Estimation Comparing the Axially-dispersed Plug-flow Model to the Data from the Experiments Using the Amine-Modified Activated Carbon Adsorbents

Once the dispersion coefficient was determined, the mass transfer coefficients from the experiments with MEA-MDEA- and TEPA-modified activated carbons were obtained using the parameter estimation procedure explained in Section 3.4.2. The aim of the parameter estimation using the breakthrough curves under the adsorption step conditions of a PSA process was to measure the adsorption performance of the activated carbons during that step. Additionally, the estimation of the mass transfer coefficient enabled the determination of a simulation variable value that could not readily be directly measured

in the laboratory and which is necessary to achieve accurate results in simulation processes applied to adsorption (Knox et al., 2016).

For this purpose, the results of the axially-dispersed plug-flow model explained in Section 3.3 were fitted to the outlet concentrations of carbon dioxide from the experiments for both types of amine-modified activated carbons, by varying the mass transfer coefficient. These amine-modified activated carbons showed better adsorbent capacity and carbon dioxide selectivity than did the unmodified activated carbons. The unmodified activated carbons displayed a capacity of 9.6 mmol g^{-1}, whereas the modified activated carbons had a capacity of 10.6 mmol g^{-1}. Therefore, the parameter estimation was carried out using the experimental data obtained from the modified activated carbons, because they showed a greater capacity to adsorb carbon dioxide.

The procedure for modifying the adsorbent surface and the experimental set-up of the fixed-bed reactor rig are reported in Azpiri Solares et al. (2019). For each of the experiments, 10 g of adsorbent was placed inside the fixed-bed reactor, based on the maximum capacity of the reactor.

Table 4.2 shows the parameters used in the model. The adsorbent surface modifications, the isotherm and the fixed-bed reactor experiments' methodology and results are shown in Soares dos Santos (2019). The experiments were all carried out at a constant flow rate of 200 Nml min^{-1}, at 25 bar and a feed temperature of 298.15 K, as also reported in Azpiri Solares et al. (2019).

These isotherm parameters were obtained using a high-pressure volumetric analyzer that measured the total gas volume adsorbed at equilibrium pressure, and that changed the gas phase pressure from 0 to 40 bar. The Langmuir model (Equation 3.8, Section 3.3.5) was

selected to represent the data obtained from the HPVA measurements. The model was used to calculate the amount of components adsorbed at equilibrium upon the solid surface and used in the linear driving force equation (Equation 3.6, Section 3.3.4). The isotherm parameter values for the adsorption of nitrogen are the values reported by Ribeiro et al. (2008), since experimental isotherm parameter values were not obtained using nitrogen gas for the amine-modified adsorbents, as nitrogen is weakly adsorbed onto the adsorbent surface and carbon dioxide is the component of interest.

The effective heat transfer coefficient and the axial heat dispersion coefficient were obtained using the Wakao and Funazkri (1978) correlations, as described in Sections 3.3.7 and 3.3.8. These correlations have previously been used in modelling studies of fixed-bed reactors that operate at high pressure (Lopes et al. 2009 and 2011).

Table 4.2. Adsorbent and reactor parameters and their values for modelling fixed-bed reactor experiments using amine-modified activated carbons

Particle density, e_s (kg m^{-3})	262	Bed length, L (m)	0.069
Particle void fraction, ε_p	0.74	Bed void fraction, ε_b	0.48
Particle diameter, d_p (m)	0.001	Bed diameter, D (m)	0.025
Sorbent specific heat, cp_s (kJ kg^{-1} K^{-1})	1	Wall specific heat, cp_w (kJ kg^{-1} K^{-1})	0.46
Adsorption heat CO_2, ΔH (kJ mol^{-1})	24.8	Wall thickness, L_w (m)	0.002
Adsorption heat N_2, ΔH (kJ mol^{-1})	8.4	Wall density, e_w (kg m^{-3})	7700
Maximum monolayer coverage capacity for CO_2, $q_{m,CO2}$ (mol kg^{-1})	9.2	Langmuir equilibrium constant for CO_2, b_{CO2} (Pa^{-1})	$3x10^{-6}$
Maximum monolayer coverage capacity for N_2, $q_{m,N2}$ (mol kg^{-1})	5.89	Langmuir equilibrium constant for N_2, b_{N2} (Pa^{-1})	$2x10^{-10}$
Effective heat transfer coefficient, h_i (kW m^{-2} K^{-1})	500	Axial heat dispersion coefficient, λ (W m^{-1} K^{-1})	1.5

Figures 4.2 and 4.3 show the breakthrough curves obtained from the parameter estimation based on the model and the MEA-MDEA- and TEPA-modified activated carbon experiments, respectively. The parameter estimation was carried out using the results of the experiments on 40%–60% and 30%–70% CO_2-H_2 nominal molar fractions, respectively, to ensure that the results of the mass transfer coefficient were kept constant when varying the molar feed fraction of carbon dioxide in the feed gas. The terms labelled as 'PSA' show the results of the experiments, while the 'parameter estimation' labels show the model results. A good visual fit was achieved between the experiments and the model for both of the adsorbents, with sums of the squared residuals (SSR) of 0.1% and

0.3%, which is less than a deviation of 10%, which is within the limit considered acceptable for engineering purposes using parameter estimation.

The model accurately predicted the breakthrough curves for the experiments using 30% and 40% CO_2 feed fractions with AC-MEA-MDEA and a 30% feed fraction with AC-TEPA. The model results using a 40% CO_2 feed fraction showed a steeper breakthrough curve than the one showed by the experiment with the AC-TEPA, due to the chemisorption effects that may have been introduced by the amine groups on the activated carbon surface.

The results for the mass transfer coefficient of the AC-MEA-MDEA and the AC-TEPA were 0.046 s^{-1} and 0.074 s^{-1}, respectively; these are consistent with previously reported mass transfer coefficient values for activated carbons under PSA conditions. These were the values of the mass transfer coefficient that gave the breakthrough curves shown in Figure 4.2, with the AC-MEA-MDEA, and Figure 4.3, with the AC-TEPA. These mass transfer coefficient values gave the computational carbon dioxide molar fraction values that fitted the experimental molar values in Figures 4.2 and 4.3, using Equation 3.23 (Section 3.4.2).

The value for the mass transfer coefficient reported for the MEA-MDEA-modified activated carbon was similar to that reported for the PSA model by Moon et al. (2018). In this study, the value of the mass transfer coefficient in the LDF model was 0.036 s^{-1}. The experiments with the activated carbons in the study by Moon et al. (2018) were performed at 35 bar, but the aim of this study was to obtain high purity and recovery values of hydrogen over 95%. The estimation of the mass transfer coefficient is also important for determining the carbon dioxide performance indicators in PSA processes,

as is shown in Section 4.3 for the laboratory scale and in Chapter 5 for a scaled-up PSA model.

The mass transfer coefficient value for the TEPA-modified activated carbon was 0.074 s^{-1}, which is between the value shown by Moon et al. (2018) and the value of 0.15 s^{-1} for the activated carbon reported by Casas et al. (2013b). The mass transfer coefficient values obtained in this project for both activated carbons are quite low. Therefore, the adsorption process with the reported amine-modified activated carbons under these conditions was equilibrium-driven, following previous adsorption studies on activated carbons at high pressure, where the mass transfer coefficient value was below 0.1 s^{-1} (Moon et al., 2018; Ribeiro et al., 2008).

Although the AC-TEPA showed a greater mass transfer value and, thus, a steeper breakthrough curve, the AC-MEA-MDEA showed a later breakpoint, with around 3–4 minutes lag for both CO_2 feed fractions, due to the high capacity obtained from the experimental work, as high as 10.6 mol kg^{-1} (Azpiri Solares et al., 2019). The high capacity of the modified activated carbon compared to the single-amine-group-modified adsorbents reported in Abanades et al. (2015) can be explained by the insertion of a two-amine-group solution (MEA and MDEA) into the pores in this project. In contrast to the 10.6 mol kg^{-1} adsorption capacity reported in here, Abanades et al. (2015) reported the maximum capacity of the activated carbons to be between 2 and 6 mol carbon dioxide per kg adsorbent.

Therefore, the mass transfer coefficient obtained and the isotherm parameter values measured for the MEA-MDEA-modified activated carbon were accepted for use in the PSA simulations reported in this study in Section 4.3 and Chapters 5 and 6.

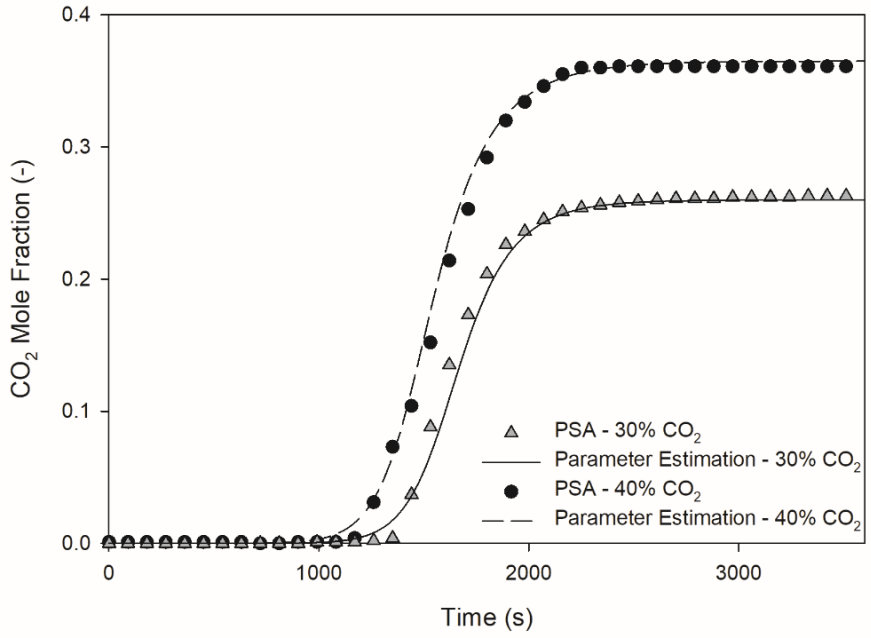

Figure 4.2. Parameter estimation fit of the model to the experimental data for nominal 30% and 40% CO_2 feed fractions using AC-MEA-MDEA

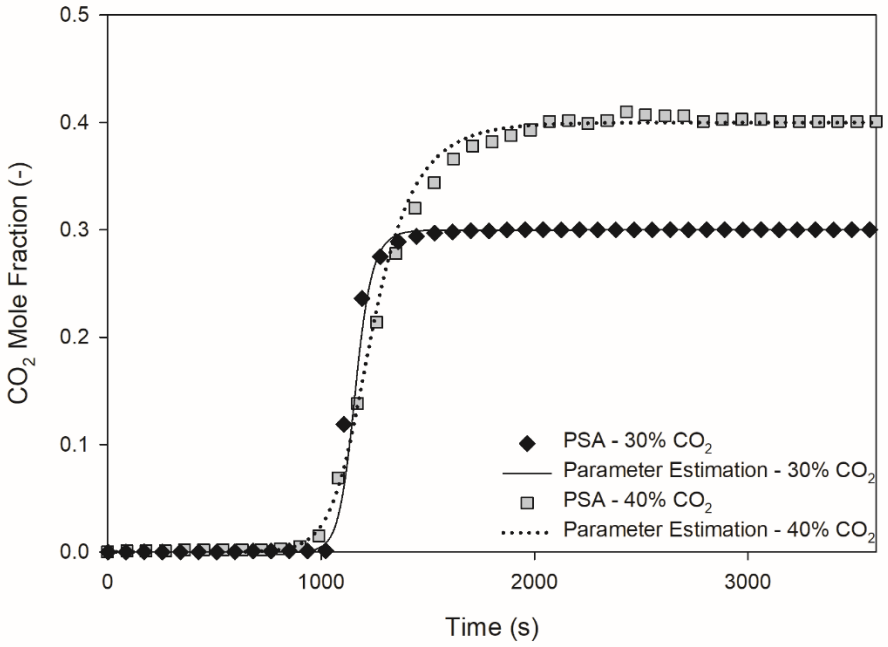

Figure 4.3. Parameter estimation fit of the model to the experimental data for 30% and 40% CO_2 feed fractions using AC-TEPA

4.3 The Effect of the Model Parameters and Variables on the Overall Purity of the Components

After the model verification, a seven-step PSA model was developed that included a mixture of 40% carbon dioxide and 60% hydrogen entering the fixed-bed reactor during the adsorption step. This process simulated the conditions of a pre-combustion PSA process in a combined cycle power plant. The steps adopted are shown in Table 3.8 (Section 3.4.4). In each of the process steps, Equations 3.1 to 3.6 and Equations 3.8 to 3.16 of the axially-dispersed plug-flow model (Section 3.3) were used to obtain the simulation outputs. The boundary conditions changed from step to step following the

procedure explained in Section 3.4.4, for which Figure 3.3 shows the cycle sequence used in the PSA simulations.

The process conditions used in the simulation were the same as those in the laboratory experiments at ambient temperatures of 298.15 K and a feed pressure of 25 bar during the adsorption step, and of 1 bar during the purge and rinse steps. The only variables that changed from step to step were the fixed-bed reactor pressure and the component flow rates and concentrations entering the system. During the adsorption and pressurization steps, a 40% CO_2 and 60% H_2 (mol basis) gas mixture entered the fixed-bed reactor, whereas during the purge and rinse steps, 100% H_2 and 100% CO_2 gas entered the fixed-bed reactor. During the pressure equalization steps, the gas exiting the depressurizing bed entered the pressurizing bed. These steps were simulated by assigning the concentration, pressure and temperature values of the gas exiting the depressurizing bed to the gas entering the pressurizing bed. All the pressure equalization steps are explained in the following sections. The experiments described in other chapters followed the same procedure.

The performance indicators of the PSA simulations were calculated using Equations 3.27 to 3.30 (Section 3.4.5) in order to analyze the results for the carbon dioxide and hydrogen product purity and for hydrogen recovery. The recovery of the carbon dioxide was not calculated at this stage, due to the facts that carbon dioxide is not a valuable product of the power plant and that the requirements for carbon dioxide storage specify a purity of 95% at 110 bar and 303.15 K (Anantharaman et al., 2011). Therefore, the aims in carrying out the PSA simulations shown in Sections 4.3.2 and 4.3.3 and in Chapters 5 and 6 were to maximize the recovery of hydrogen to over 90%, while obtaining a carbon dioxide and hydrogen product purity over 95%. For this purpose, a number of adsorbent parameters

(Section 4.3.2) and process variables (Section 4.3.3) were studied, so as to analyze their effect on the performance indicators and optimize the PSA process conditions.

4.3.1 The PSA Cycle with Hydrogen Gas instead of Nitrogen Gas

The simulations of the PSA process were carried out using hydrogen gas instead of nitrogen gas entering the fixed-bed reactor system with the carbon dioxide. Nitrogen was used instead of hydrogen in the experimental procedure shown in Section 4.2 to test the adsorption behaviour of the adsorbents in pre-combustion capture conditions, due to safety concerns and due to the fact that the performance of the CO_2-H_2 mixture was expected to be far more efficient than that of the CO_2-N_2 mixture. This expectation is due to the light weight of hydrogen gas compared to nitrogen. A study by García et al. (2013) on AP3-60 activated carbons showed that the fraction of carbon dioxide captured for a CO_2-N_2 mixture was 82% of the total volume of gas captured, whereas it was 92% for a CO_2-H_2 mixture. Operations with CO_2-H_2 and CO_2-N_2 gas mixtures were compared using the adsorption capacity values from previous studies that measured the capacity of the activated carbons for these mixtures. In the studies that compared the adsorbent capacities of CO_2-H_2 gas mixtures, the capacity of the activated carbons to adsorb hydrogen varied between 0.04 and 0.06 mol kg^{-1} and between 9 and 10 mol kg^{-1} for the adsorption of carbon dioxide (Hao et al., 2018; Lopes et al., 2009; Ribeiro et al. 2008). The study by Lopes et al. (2009) measured the capacity of the activated carbon for nitrogen gas as 0.14 mol kg^{-1}, which was similar to the activated carbons' capacity to adsorb hydrogen shown by the previous studies.

The heat of adsorption of the activated carbons was the other parameter chosen for the comparison of CO_2-N_2 gas adsorption to CO_2-H_2 gas adsorption. The values for the heat of adsorption that featured activated carbons at high pressure ranged between 21 and 30 kJ mol^{-1} for carbon dioxide in previous PSA studies, and between 8 and 18 kJ mol^{-1} for nitrogen (Lopes et al., 2011; Ribeiro et al., 2008). The heat of adsorption for hydrogen gas in these studies varied between 6 and 13 kJ mol^{-1}.

The similar capacities to adsorb hydrogen and nitrogen and the reported heat of adsorption for the activated carbons imply that carbon dioxide and hydrogen systems will perform similarly to carbon dioxide and nitrogen systems. Considering the reported numbers, an increase of 10% in the amount of carbon dioxide adsorbed was estimated when operating with CO_2-H_2 mixtures, compared to the amount adsorbed in the experiments using CO_2-N_2 mixtures.

4.3.2 The Effect of the Adsorbent Properties on the Overall Purity of H_2 and CO_2

The effect of varying the values of the adsorbent parameters was studied in the designed PSA system. These were independently varied to see the effect of each parameter. The selected adsorbent parameters for the study were the mass transfer coefficient, particle diameter and the particle and bed void fraction.

First, the results of the mass transfer coefficient sensitivity analysis were obtained; these are illustrated in Figure 4.4. This figure shows the evolution of the molar fraction of carbon dioxide at the end of the fixed-bed reactor for the simulations of the seven-step pressure swing adsorption model when varying the mass transfer coefficient.

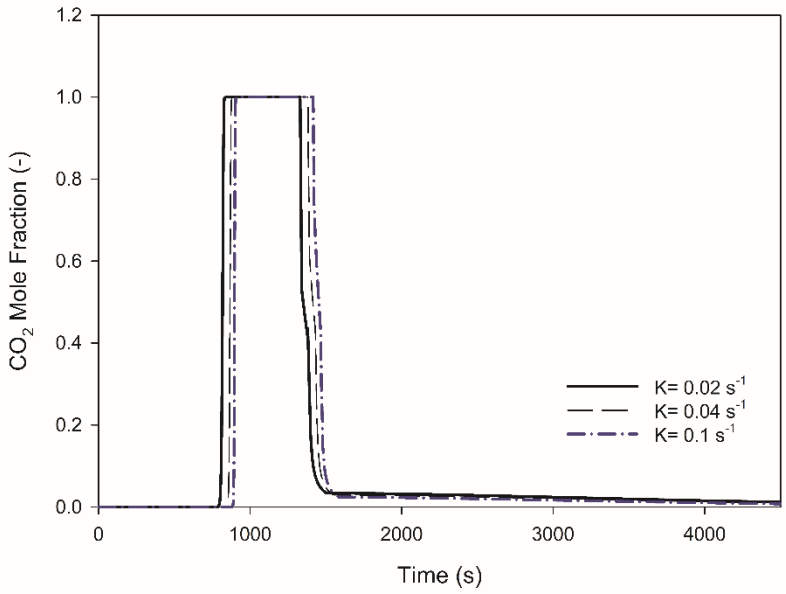

Figure 4.4. The effect of the mass transfer coefficient value on the outlet molar fractions of carbon dioxide for a seven-step PSA process

The breakpoint of the feed step does seem to be affected by variations in the mass transfer coefficient value. With an increase from 0.02 s^{-1} to 0.1 s^{-1} in the mass transfer coefficient, the breakpoint occurs around 120 s later. The breakthrough time increases by 12% and the increase in the hydrogen purity is not significant, with an increase of 0.3 percentage points. However, the purity of carbon dioxide increases from 71.9% to 90.3%, which demonstrates the importance of the breakthrough time in increasing the purity of this product. The increase in the purity of carbon dioxide can be explained by the duration of this component's adsorption in the fixed-bed reactor, which is 120 s longer with the 0.1 s^{-1} mass transfer coefficient value, as shown in Figure 4.4.

The slope between the adsorption and the purge and rinse steps remains constant, due to the depressurization of the bed before the breakpoint caused by the adsorbents' saturation.

This step decreases the pressure in the bed and creates a pressure gradient between the inlet and the outlet of the bed. Carbon dioxide is not desorbed until the end of the bed reaches pressures of around 1 bar.

Second, the results for the sensitivity analysis using the rest of the adsorbent properties are shown in Table 4.3, together with the carbon dioxide and hydrogen purity values obtained for each parameter value. The laboratory (default) values for those properties are shown with an asterisk in the table.

For the particle diameter, the sensitivity analysis was simulated with a deviation of 25% from the original size. Smaller particles may cause pressure drop issues. For the particle and bed void fractions and for the mass transfer coefficient, values were selected based on the values used previously for activated carbon adsorbents (Shafeeyan et al., 2015; Zhu et al., 2014).

Table 4.3. Calculated purity values (%) for the H_2 and CO_2 product streams for a number of adsorbent properties

Particle diameter(m)	Purity H_2/CO_2 (%)	Particle void fraction (-)	Purity H_2/CO_2(%)
0.75×10^{-3}	99.5/82.1	0.55	99.4/82.7
1×10^{-3}*	99.4/81.9	0.74*	99.4/81.9
1.25×10^{-3}	99.3/81.6	0.85	99.4/81.6
Bed void fraction(-)	**Purity H_2/CO_2 (%)**	**MT coefficient(s^{-1})**	**Purity H_2/CO_2(%)**
0.48*	99.4/81.9	0.02	99.2/71.9
0.6	99.4/81.0	0.04*	99.4/81.9
0.7	99.5/80.8	0.1	99.5/90.3

*Reference laboratory value

Table 4.3 shows that the mass transfer coefficient is the variable that had the greatest effect on the overall purities of CO_2. The purities of hydrogen did not deviate from 99% when changing this variable. The values of the breakthrough capacity for carbon dioxide remain constant when varying the mass transfer coefficient. The same was observed for the rest of the adsorbent properties.

The most common correlation that has been used to calculate the mass transfer coefficient is that of Farooq and Ruthven (1990), which sums the micro-, meso- and macropore mass transfer resistances. This variable can also be calculated using the Peclet number (the dimensionless number shown in Equation 3.16, Section 3.3.9), as calculated by Wang et al. (2015). These correlations have been shown to be uncertain due to dispersion effects in the bed (Knox et al., 2016). In this study the mass transfer coefficient was varied independently and the results were that with high mass transfer coefficient values using carbon dioxide (around 0.1 s^{-1}) a product purity value of around 90% could be obtained, whereas the purity of carbon dioxide was around 71% with a mass transfer coefficient value of 0.04 s^{-1}. The mass transfer coefficient affects the breakpoint, as shown in Figure 4.4. Therefore, this coefficient affects the amount of carbon dioxide adsorbed and the purity of the CO_2 product stream in the rinse and purge steps (between 1100 and 1700 s).

The properties of the particle and bed void fractions and the particle diameter do not seem to affect the purity of hydrogen; it remains constant at 99%, with a marginal error of ± 0.1%. A plausible explanation for this is that if the adsorbent properties are in an acceptable range for the adsorption of carbon dioxide, the outcome of the hydrogen product stream will be highly pure (over 99%), due to the lightness of the hydrogen gas and the high affinity of the carbonaceous surface for the carbon dioxide gas in binary mixtures.

The purity of carbon dioxide gas is more sensitive to the properties of the adsorbent applied in the given process conditions and is about 20%–30% lower than the purity of hydrogen, as reported for most industrial processes where the light product (hydrogen) is the desired product (Ribeiro et al., 2008). Decreasing the particle diameter favourably increases the purity of the CO_2 stream, due to the greater external surface areas for adsorption in the fixed-bed reactor. It also favours the plug-flow in the bed, because the ratio of the bed-to-particle diameter increases (Knox et al., 2016).

The recovery of the hydrogen and carbon dioxide products remained practically constant when varying the adsorbent properties in this sensitivity analysis. The recovery of carbon dioxide was around 52% for this process, whereas it was around 75% for the hydrogen product. The recovery of these products decreased, due to recycling hydrogen and carbon dioxide during the process, compared to in previous studies, where the recovery of carbon dioxide was over 80% (Casas et al., 2013a; Riboldi and Bolland, 2015a).

4.3.3 The Effect of the PSA Process Variables on the Overall Purity of H_2 and CO_2

The selected process variables for the sensitivity analysis in the designed seven-step PSA cycle were the gas components' feed fractions and feed and purge pressures and the reactor's length-to-diameter ratio. These variables were varied independently, following the same procedure as for the adsorbent properties. The adsorbent properties in the model were set to be the same as the AC-MEA-MDEA properties (shown in Table 4.2) with a mass transfer coefficient value of 0.046 s^{-1}. The results for the process variables that had

the greatest effect on the breakthrough curves are illustrated in Figures 4.5 and 4.6. These variables were the gas components' feed fractions and the feed pressure.

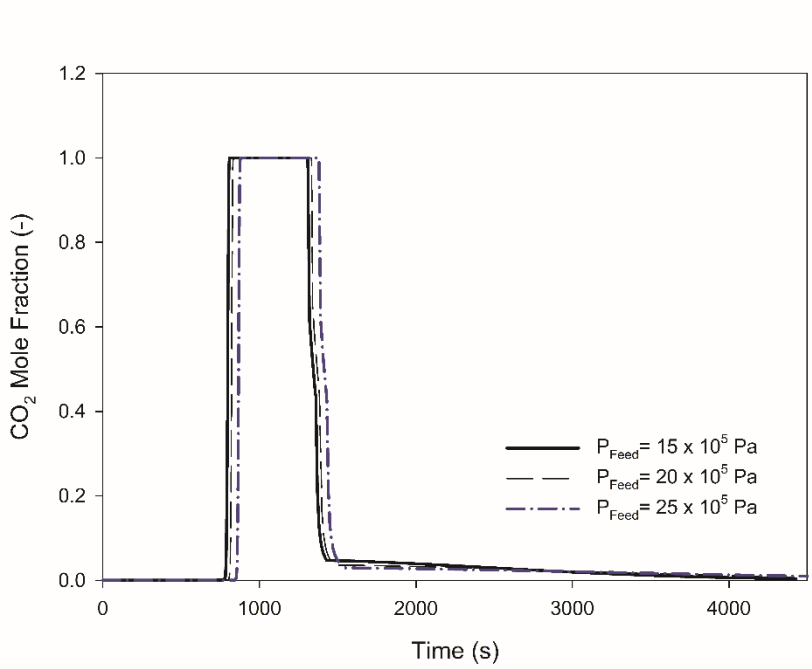

Figure 4.5. The effect of feed pressure on the outlet molar fractions of CO_2 for a seven-step PSA process

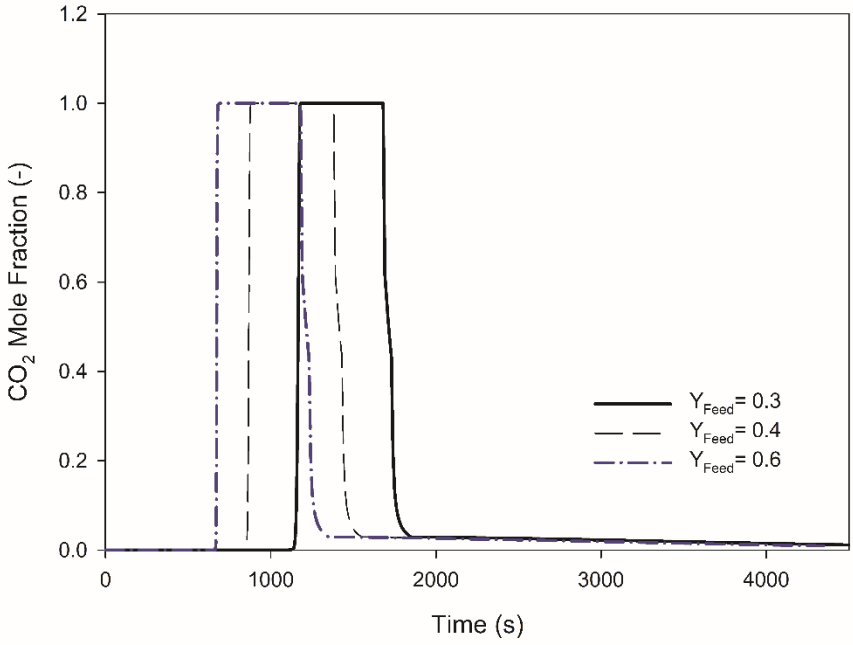

Figure 4.6. The effect of feed molar fractions on the outlet molar fractions of CO_2 for a seven-step PSA process

For the sake of consistency, one process variable value at a time was changed from the original laboratory process value. The results for the rest of the process variables are shown in Table 4.4, together with the carbon dioxide and hydrogen purity and recovery values obtained from the sensitivity analysis.

Table 4.4. Calculated purity and recovery (%) values for the H_2 and CO_2 product streams for a number of PSA process variables

Feed pressure (Pa)	Purity H_2/CO_2 (%)	Recovery H_2/CO_2 (%)	Purge pressure (Pa)	Purity H_2/CO_2 (%)	Recovery H_2/CO_2 (%)
15×10^5 (P_{ratio}**=15)	99.4/74.8	74.7/51.5	0.5×10^5 (P_{ratio}=50)	99.4/96.4	75.4/52.3
20×10^5 (P_{ratio}=20)	99.4/79.2	74.9/51.8	1×10^5* (P_{ratio}=25)	99.4/81.9	75.4/52.1
25×10^5* (P_{ratio}=25)	99.4/81.9	75.4/52.1	1.5×10^5 (P_{ratio}=16.7)	99.4/77.0	75.4/51.8
CO_2 feed fraction (-)	Purity H_2/CO_2 (%)	Recovery H_2/CO_2 (%)	Reactor length-to-diameter ratio (-)	Purity H_2/CO_2 (%)	Recovery H_2/CO_2 (%)
0.3	99.3/73	75.5/51.8	2.5	99.5/84.7	77.1/52.7
0.4*	99.4/81.9	75.4/52.1	2.76*	99.4/81.9	75.4/52.1
0.6	99.5/91.6	75.2/52.4	3.5	99.1/79.5	73.7/51.6

*Reference laboratory value, **$P_{ratio} = \frac{P_{feed\ step}}{P_{purge\ step}}$

The laboratory (default) values for variables are shown with an asterisk in Table 4.4. The rest of the values of the table were selected based on previous conditions given in PSA process studies (Riboldi and Bolland, 2015b). The molar feed fraction of carbon dioxide was varied from 0.3 to 0.6 in order to study the effect of the feed concentration of CO_2 in the adsorption step, with a view to future work on a recycle stream of carbon dioxide product featuring a compressor. Input purge pressures were decreased to less than the atmospheric pressures in order to investigate the need for a vacuum swing adsorption process. The reactor's length-to-diameter ratios did not deviate more than 50% from the original value, due to the design standards of process engineering.

Figures 4.5 and 4.6 show that the selected process variables had a greater effect than the adsorbent properties on the overall CO_2 purities. On the one hand, the carbon dioxide molar fraction after the breakthrough curve remained constant, with a value of 1, same as with the adsorbent properties' results. On the other hand, the breakthrough point of the feed step was greatly affected by variations in these variables. The breakthrough point is the time when the carbon dioxide concentration coming out the fixed-bed reactor is 5% of the carbon dioxide concentration in the feed, as explained in Section 2.6.6.

The feed pressure affected only the overall purity of the carbon dioxide at high pressures over 15 bar. This could be due to the increase in the pressure ratio (P_{ratio} in Table 4.4) between the adsorption and purge steps, which increased the CO_2 partial pressure in the pressure equalization and depressurization steps. Although the purity of hydrogen was not affected, an increase of 5 bar in the feed pressure delayed the breakpoint by 2 min, as shown in Figure 4.5. This explains why the overall purity of carbon dioxide was higher in the purge step. The total uptake of CO_2 increased due to a longer adsorption time, given that all PSA processes had the same duration.

The purge pressure variations had a greater effect than the feed pressure on the total purity of carbon dioxide, as shown in Table 4.4. This is because of the larger pressure ratio, indicated as P_{ratio} in Table 4.4, between the adsorption and the purge step when the fixed-bed reactor pressure decreased to vacuum values bellow 1 bar. Then, the carbon dioxide product was obtained in the purge and rinse steps. The increase in the pressure ratio caused higher depressurization rates, which enabled a purer carbon dioxide stream of about 96.4% at vacuum pressures of 0.5 bar. The carbon dioxide purity values in this analysis showed a linear increase with increasing pressure ratio values. Therefore,

increasing the pressure ratio between the feed and purge step would be one of the key parameters to increase the carbon dioxide purity in the pressure swing adsorption process.

The feed fraction of carbon dioxide in the adsorption step had a greater effect on the breakpoint than did the purge or the feed pressures, as shown in Figure 4.6. With an increase from 0.4 to 0.6 carbon dioxide feed fractions, the purity of the carbon dioxide increased by 10 percentage points. This enhanced the mass transfer between the gas and the adsorbent surface, because the carbon dioxide concentration gradient increases between the gas and the solid phase (Seader and Henley, 2006).

The increase of the carbon dioxide purity with higher inlet concentrations is supported by previous studies, where increasing the carbon dioxide concentrations in the inlet of the reactor would be a key parameter to achieve over 95% carbon dioxide purity values using PSA as a carbon capture technology (Riboldi and Bolland, 2015a).

This demonstrated that it could be useful, with a view towards future work, to introduce a recycle stream from the depressurization to the adsorption step, which would increase the carbon dioxide partial pressure in the inlet of the reactor. This step is supported by a previous study on the implementation of PSA in an IGCC power plant (Riboldi and Bolland, 2015b). This step would require a compressor in the recycle stream.

In terms of the reactor design, smaller length-to-diameter ratios yielded a higher purity of carbon dioxide product, as shown in Table 4.4. When the ratio was about 10% smaller than that of the standard laboratory reactor, the purity of carbon dioxide was 3% higher. A plausible explanation for this could be the decreasing carbon dioxide partial pressure as the feed gas passed through the reactor, which decreased the mass transfer driving force between the gas and the solid surface. Greater diameters would enable higher adsorbent

densities in the inlet of the bed, increasing the adsorption capacity of the fixed-bed reactor in the inlet, where the carbon dioxide concentration is at feed concentrations as high as 60% (molar basis).

Overall, this section shows that deviant values on PSA process variables had a greater effect on the final purity of carbon dioxide than did values of the adsorbent properties shown in Section 4.3.2. The PSA process variables, specifically, the feed fractions and the pressure ratio between the feed and the purge step, seem to have had a greater effect on the final CO_2 purity, with variations of ± 10–20% in the final purity values. Carbon dioxide concentrations of around 60% at 25 bar are preferred in the feed during the adsorption step, and at 0.5 bar pressures in the purge and rinse steps.

The overall recovery of the hydrogen and carbon dioxide products was less sensitive to varying these process conditions than was the purity of these products. The recovery values obtained with the standard case (conditions shown with an asterisk in Table 4.4), were 52.1% and 75.4% for carbon dioxide and hydrogen, respectively. These recovery values varied no more than 2% when the process conditions were varied.

The amount of the components that entered the fixed-bed reactor did not vary during the PSA process, and the PSA configuration presented in Figure 3.3 (Section 3.4.4) was not varied, which lead to have small variations of the recovery of the gas components. The low values obtained for the components is explained by the inclusion of only one pressure equalization step in the process, and using recycled carbon dioxide during the rinse step. The hydrogen gas product which was not recovered was used during the pressurization steps, or lost in the carbon dioxide product stream. Therefore, the study of additional PSA

process configurations to increase the recovery of the products was required, which are shown in Chapter 5.

This sensitivity analysis shows that over 90% pure carbon dioxide cannot be obtained in the basic case, but, by varying the PSA process conditions, such as increasing the carbon dioxide concentration in the feed, purities over 90% were achieved. These results could be useful and further analyzed at a larger scale. Chapter 5 reports the simulations of the PSA process at pilot scale.

In the case of operation under higher feed pressures over 25 bar, the higher compression requirements would lead to a significant increase in the energy penalty and plant cost. The advantages in terms of separation performance would thus need to be weighed against the disadvantages in terms of the energy efficiency and the cost of the process. Chapter 6 presents the effects of the PSA variables, such as the feed pressure, on the energy penalty and cost within a natural gas combined cycle power plant.

4.4 Conclusion

An experimental adsorption step under pre-combustion PSA conditions of 25 bar and 298.15 K was fitted to an axially-dispersed plug-flow model, using activated carbons modified with TEPA and a novel blend of MEA-MDEA solutions. Initially, the activated carbon modified with MEA-MDEA has shown promising results compared to the unmodified activated carbon, in terms of the carbon dioxide adsorbed (around 10% higher) and the selectivity during adsorption experiments in a fixed-bed reactor.

A parameter estimation using an experimental PSA adsorption step with TEPA- and MEA-MDEA-modified adsorbents, and an axial-dispersed plug-flow model set to the same conditions, showed a good fit between the breakthrough curves of both results, with an SSR of less than 10%. Although the TEPA-modified activated carbon showed a greater mass transfer coefficient, namely, a value of 0.074 s^{-1}, the more promising result for pre-combustion carbon capture using pressure swing adsorption was the delayed breakpoint of around 200 s in the experiment with the MEA-MDEA-modified activated carbon.

A sensitivity analysis of the effect of the adsorbent properties showed that these parameters had a greater effect on the purity of carbon dioxide than on the purity of the hydrogen in the product stream. The properties of the amine-modified adsorbents were demonstrated to be important in obtaining highly purified products, specifically, 99.4% for hydrogen and 81.9% for carbon dioxide, in the hydrogen product stream obtained from the adsorption step.

A sensitivity analysis of the process variables of PSA showed that modifications in these variables could yield higher purities of the carbon dioxide product stream, namely over 90%. The results of the sensitivity analysis showed that purities of carbon dioxide and hydrogen as high as 91.6% and 96.4%, respectively, could be achieved by increasing the carbon dioxide feed fraction by 50% and decreasing the purge pressure by 50%, which doubled the pressure ratio compared to the initial case. For these cases, the additional capital and operational costs should be investigated, as there would be a need for a compressor for the recycle stream and for a vacuum generator to obtain pressures under atmospheric conditions. However, increasing the pressure ratio between the adsorption and purge steps by increasing the feed pressure would be an alternative to increase the carbon dioxide purity and avoid using vacuum pressures.

Additionally, the use of a vacuum generator is out of the scope of this study, as this would imply the use of conditions below atmospheric pressure, turning the process into vacuum swing adsorption. Therefore, the effect of including a compressor was only analyzed for the cost and energy penalty of the plant; this is presented in Chapter 6.

The recovery of these products did not seem greatly affected by variations of the adsorbent properties and process variables, with a maximum of 2% variation when varying the PSA process variables. The recovery of both products was low compared to previous PSA studies, with values below 80% (Ribeiro et al., 2008; Riboldi and Bolland, 2015b). The low recovery values were due to not using multiple pressure equalization steps, and a fraction of the feed gas lost in the depressurization step. Therefore, alternative cycle configurations were required when scaling up fixed-bed reactors for carbon capture using PSA.

CHAPTER 5 – THE PILOT-SCALE PSA PROCESS

5.1 Introduction

In this chapter the scale-up of the laboratory-based axially-dispersed plug-flow model that was validated in Chapter 4 is reported. The results of this chapter are published in Azpiri Solares and Wood (2020) (see Appendix G). In order to scale up the fixed-bed reactor simulations of Chapter 4, the procedure explained in Section 3.5.1 was followed to define the capacity of the pressure swing adsorption process and scale up the variables. The capacity of the PSA process was defined based on the flow rate requirements for hydrogen of the GE-10 gas turbine selected for the power plant. The results for the product performance indicators for the laboratory and scaled-up PSA models were compared (Section 5.2.3), simulating the process using the conditions and initial PSA cycle configuration explained in Section 5.2.1. The results of the laboratory and scaled-up models were obtained when the PSA processes achieved a cyclic steady state (CSS), as shown in Section 5.2.2.

After comparing quantitatively the evolution of the molar fractions of carbon dioxide at the end of the laboratory and scaled-up PSA models, the effects of a number of process variables (Section 5.3) and cycle configurations (Section 5.4) on the product performance indicators were studied using the scaled-up PSA process. The performance indicators chosen were the purity and recovery of the carbon dioxide and hydrogen products.

The process variables chosen for the analysis were the velocity of the feed gas, which was adjusted by varying the diameter (Section 5.3.1) and the length of the bed, by varying the length-to-diameter ratio (Section 5.3.2) and the feed-to-purge flow rate ratio (Section

5.3.3). The pressure and temperature of the process were fixed based on the conditions reported for NGCC power plants (Anantharaman et al., 2011), and the adsorbent parameters from the laboratory model were maintained. The adsorbent parameter values selected for the scaled-up model were those obtained with the MEA-MDEA modified activated carbon. The properties of this activated carbon are shown in Table 4.2, Section 4.2.2.

A number of cycle configurations were studied for the scaled-up fixed-bed reactor, such as the inclusion of an assisted purge step, explained in Section 5.4.1, and additional pressure equalization steps after adding a number of fixed-bed reactors (Section 5.4.2). The inclusion of a rinse step with carbon dioxide at pressures higher than 1 bar was also studied in Section 5.4.3. The additional PSA conditions were studied in order to improve on the product performance indicator values from the base scaled-up cycle (Section 5.2), so that the process could be integrated into an NGCC power plant. Then the process was analyzed in terms of the overall economics of the plant and energy efficiency, as shown in Chapter 6.

5.2 Comparison between the Laboratory- and Pilot-Scale PSA Models

5.2.1 The Conditions and Initial Cycle Configuration for the Comparison of the Models

The aim of scaling up the PSA model was to analyze the effects of the process variables at a pilot-scale plant and choose those that would give over 95% purity of the carbon dioxide product, while maximizing hydrogen recovery. The purity established for the

carbon dioxide product is that used as the minimum benchmark value to store this product effectively (Webley, 2014).

The pilot-scale operation in this work was defined based on the technology readiness level explained in Section 2.3.2, where the viability of several carbon capture technologies was analyzed based on their operation environment and capacity (Abanades et al., 2015). The TRL classification method was applied to the pilot-scale operation of power plants with carbon capture in the order of 1 to 10 MW of power production. Therefore, the PSA unit was designed based on the flow rate requirements for hydrogen of a GE-10 gas turbine that operates for the production of 10 MW power generation. The scale-up of the PSA laboratory model shown in Chapter 4 also enabled the study of the energy efficiency and the cost of an NGCC power plant when integrating the designed PSA cycles for carbon capture, and a comparison to the efficiency and cost of an NGCC power plant without carbon capture.

The performance indicators for recovery and purity were calculated using Equations 3.27 to 3.30 (Chapter 3, Section 3.4.5), and the evolution of the product mole fractions at the outlet of the bed was quantitatively compared for the laboratory and the scaled-up PSA models. The molar fractions of the carbon dioxide at the end of the bed had an effect on the product purity and recovery, as shown in the product performance Equations 3.27 to 3.30 (Section 3.4.5). The PSA cycle used for this comparison is shown in Figure 5.1, which adds a carbon dioxide rinse step followed by a purge step to the previously reported PSA cycles (Moon et al., 2018; Ribeiro et al., 2008). The PSA cycle had a depressurization step in which the exhaust gas was emitted to the carbon dioxide product. Initially this configuration was selected, as it had not been determined for the scaled-up process whether the stream of the depressurizing bed would have pure enough hydrogen

(up to 99.99%) to enter the purge step, as implemented for the laboratory-scale process shown in Figure 3.4 (Section 3.4.4). In contrast to the laboratory-scale process (Figure 3.4), where the depressurization product was used as a purge gas, in the pilot-scale process (Figure 5.1), the depressurization product was assumed to be mostly carbon dioxide, so a separate flow of pure hydrogen was required as a purge gas.

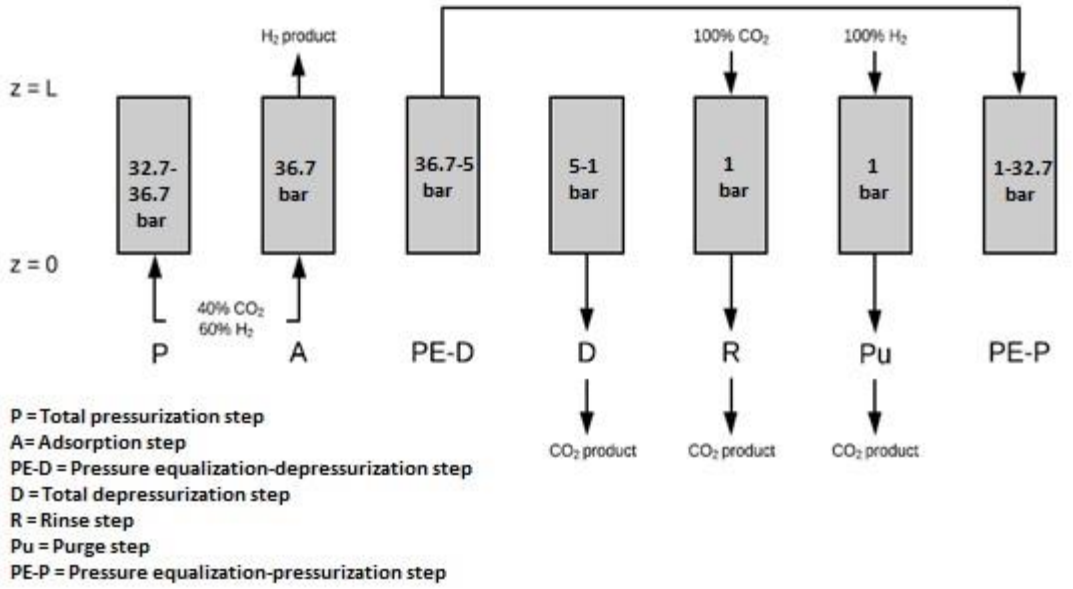

Figure 5.1. The flow diagram for the comparison of the laboratory-based to the scaled-up PSA model

The following conditions were applied for the comparison of the PSA models: (i) an adsorption step at 36.7 bar, with 40% CO_2 and 60% H_2 molar fractions; (ii) a depressurization-pressure equalization step, in which the outlet stream of the depressurizing bed was connected to a pressurizing bed, until the depressurizing bed reached 5 bar; (iii) a total depressurization step down to 1 bar, in which the outlet gas

went to the carbon dioxide product; (iv) a rinse step at 1 bar and with a 100% CO_2 feed molar fraction coming from a carbon dioxide storage tank; (v) a purge step, with a 100% H_2 feed molar fraction coming from the adsorption step; (vi) a pressurization-pressure equalization step, with the same duration as the pressure equalization step during the depressurization; and (vii) a total feed pressurization step up to 36.7 bar. The rinse step was similar to the purge step, but instead of feeding up to 99% pure hydrogen gas into the fixed bed at 1 bar, a stream containing up to 99% pure carbon dioxide was entered into the fixed-bed reactor. This step increased the carbon dioxide product purity before the purge step. There were no waste streams in this configuration, but a fraction of carbon dioxide and hydrogen product was not recovered, because it was recycled to the process during the purge (Pu) and rinse (R) steps.

The depressurization and pressurization of the bed were set to a rate that matched the adsorption time, for the sake of synchronizing the beds. The rinse and purge durations were of 5/6 and 1/6 of the adsorption step, respectively, to purge the remaining carbon dioxide gas out of the bed and to maximize hydrogen recovery. The durations of the rinse and purge steps were determined based on the minimum purge time required to clear out all the carbon dioxide from the fixed bed, in order to start a new cycle.

On the one hand, the PSA configuration shown in Figure 5.1 includes depressurization and pressurization steps commonly reported in the literature, since the inclusion of a pressure equalization step was regarded as necessary to improve the recovery of hydrogen (Moon et al., 2018). On the other hand, a rinse step with carbon dioxide at 1 bar was necessarily added to the cycle to increase the purity of the carbon dioxide. This step has not commonly been implemented in previous PSA studies because carbon dioxide has not been the product of interest.

Table 5.1 shows the parameters of the adsorbent and the fixed-bed reactor used in the scaled-up PSA model. The scaled-up variable values of the fixed-bed reactor model were determined based on the flow rate requirements of the GE-10 gas turbine of the power plant and on the procedure explained in Sections 3.5.1 and 3.5.2. This procedure followed the steps required to scale up fixed-bed reactors from laboratory- to pilot-scale (Rase, 1990). The variable values of the laboratory-scale PSA model are those shown in Table 4.2, Section 4.2.2. For both scale processes, the parameters of the MEA-MDEA-modified activated carbon were used in the simulation. The isotherm parameters and the coefficient for the mass transfer of the carbon dioxide to the activated carbon were calculated from the laboratory data and from the parameter estimation reported in Chapter 4. The mass transfer coefficient for the hydrogen, as well as the axial mass and heat dispersion coefficients, were calculated using the Wakao and Funazkri (1978) correlation. The isotherm parameters of hydrogen were the values reported by Riboldi et al. (2014) for the activated carbon.

Table 5.1. The fixed-bed reactor and adsorbent parameters for the scaled-up PSA simulations

Particle density, ρ_s (kg m^{-3})	262	Bed diameter, D (m)	2.57
Particle void fraction, ε_p	0.74	Bed void fraction, ε_b	0.48
Particle diameter, d_p (m)	0.001	Bed length, L (m)	3.88
Heat transfer coefficient, h_i (kW m^{-2} K^{-1})	500	Wall specific heat, cp_w (kJ kg^{-1} K^{-1})	0.46
Effective mass transfer coefficient, K_i (s^{-1})	CO_2: 0.046 H_2: 0.092	Wall thickness, L_w (m)	0.007
Axial mass dispersion coefficient, D_x (m^2 s^{-1})	9.3 x 10^{-5}	Wall density, ρ_w (kg m^{-3})	7700
Axial heat dispersion coefficient, λ (W m^{-1} K^{-1})	1.5		
Maximum monolayer coverage capacity for CO_2, $q_{m,CO2}$ (mol kg^{-1})	9.2	Langmuir equilibrium constant for CO_2, b_{CO2} (Pa^{-1})	3 x 10^{-6}
Maximum monolayer coverage capacity for H_2, $q_{m,H2}$ (mol kg^{-1})	23.57	Langmuir equilibrium constant for H_2, b_{H2} (Pa^{-1})	7.69 x 10^{-11}

5.2.2 The Criteria for Obtaining a Cyclic Steady State (CSS)

The laboratory and the scaled-up PSA cycles were simulated until a cyclic steady state (CSS) was achieved. When a PSA process achieves a cyclic steady state, the component concentration and temperature profiles remain constant when each of the cycles finishes in a constant position in the bed. When the CSS was achieved for the PSA models, the drop in the product performance indicators was of the order of 0.0005% for purity, and 0.008% for recovery, relative to the first cycle. CSS was achieved after 497 cycles at both scales, when the temperature profiles were stable in the gas phase for 10 consecutive cycles. The number of cycles was the same because the size and the amount of adsorbent

in the fixed-bed reactor were proportional to the amount of gas treated in both the laboratory-scale and the scaled-up reactors. Figures 5.2 and 5.3 show the temperature profile at the inlet of the laboratory and at the scaled-up fixed-bed reactors until CSS, respectively.

The figure of 497 cycles obtained at CSS in this work is consistent with previous PSA studies, such as Ribeiro et al. (2008), in which the purity of the hydrogen product declined from 99.9997% in the first cycle to 99.9994% in CSS after 500 consecutive cycles. The recovery of hydrogen increased by around one percentage point from the first cycle until CSS in the study by Ribeiro et al. (2008), from 51% to 52%. These recovery values show that the 1 percentage point change in the recovery value is not significant and that it would be worth it to achieve CSS if the performance indicator values changed by over 5 percentage points from the first cycle.

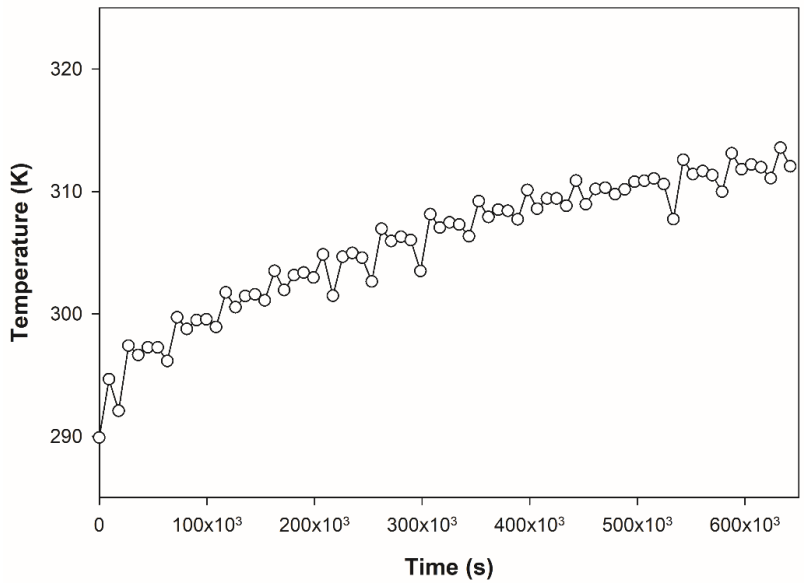

Figure 5.2. The evolution of the gas phase temperature at the inlet of the fixed-bed reactor until CSS for the four-bed laboratory-scale PSA process

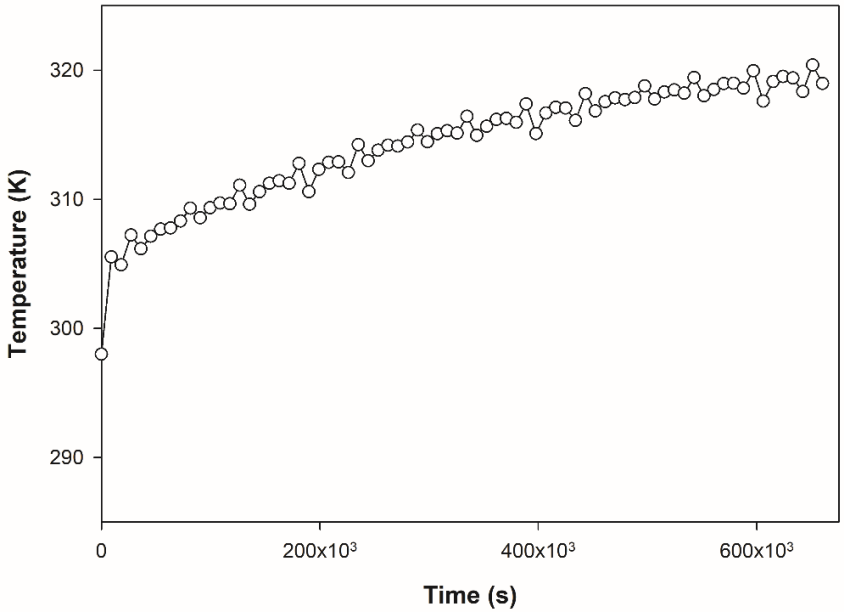

Figure 5.3. The evolution of the gas phase temperature at the inlet of the fixed-bed reactor until CSS for the four-bed scaled-up PSA process

After reaching CSS for the initial PSA cycle design, the simulations in Sections 5.3 and 5.4 were carried out for a couple of cycles due to the irrelevant change in the component fractions front at the end of the bed at cyclic steady state. Therefore, it is not necessary to achieve CSS to analyze the viability of the PSA process in terms of the product performance indicators for purity and recovery. If the process is optimized in terms of the product performance indicators for the first cycles, then it is optimum at CSS, due to the small change of around 0.001 percentage points in the product performance indicators; this conclusion is also supported by previous studies (Ribeiro et al. 2008; Riboldi and Bolland, 2015a).

5.2.3 The Comparison Between the Laboratory- and Pilot-Scale PSA Processes on Their Carbon Dioxide Concentration Profiles and Their Performance Indicators

The process shown in Figure 5.1 and explained in Section 5.2.1 was simulated to compare the laboratory and scaled-up PSA models. Figures 5.4 and 5.5 show the molar hydrogen and carbon dioxide component fractions at the outlet of the bed for the laboratory and scaled-up PSA cycles, respectively. During the adsorption time (300 s), hydrogen gas that was around 99.99% pure came out of the bed and the carbon dioxide remained adsorbed in the activated carbon inside the bed at 36.7 bar. The depressurization-pressure equalization step lasted for 250 s (up to 5 bar) and carbon dioxide remained adsorbed in the bed until the end of this step. The 99.99% pure hydrogen stream coming from the depressurization-pressure equalization bed was used to pressurize another bed.

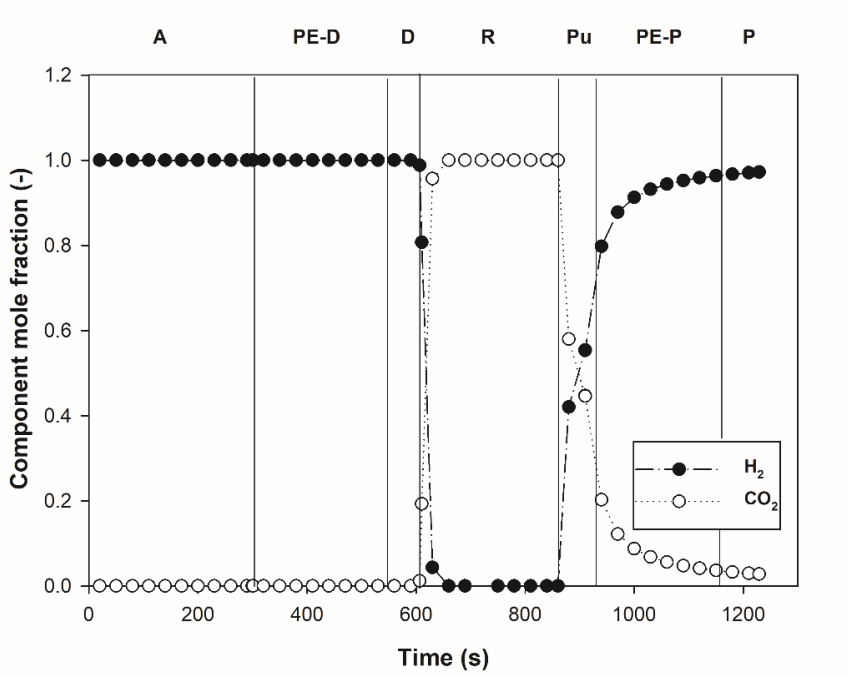

Figure 5.4. The components' concentration profiles at the end of the bed for the seven-step four-bed PSA model at laboratory scale

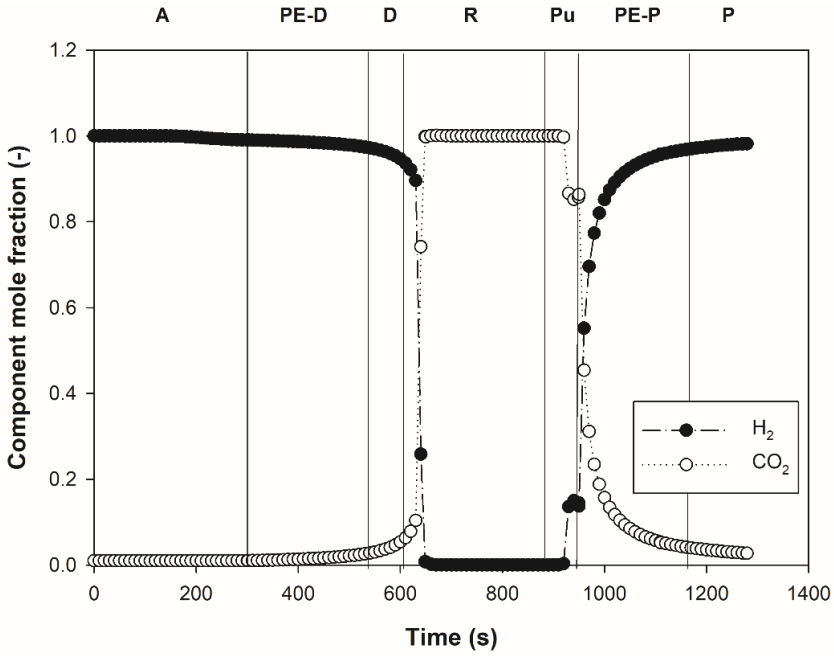

Figure 5.5. The components' concentration profiles at the end of the bed for the seven-step four-bed PSA scaled-up model

The carbon dioxide product was obtained as soon as the depressurization step started and during the rinse (250 s) and purge steps (50 s). It took the last seconds of the depressurization step and the initial seconds of the rinse step to reach around 99.99% pure carbon dioxide exiting the bed and purity remained at that level until the rinse step finished for both PSA processes.

There was a slight difference between the laboratory and the scaled-up process when the hydrogen purge was fed at 1 bar into the system: the carbon dioxide concentration decreased rapidly during those 50 s in the laboratory process to 43% purity, but decreased to 84% purity for the scaled-up process. The slower decrease of the carbon dioxide concentration during the scaled-up process can be explained by the greater length of the reactor and the longer residence time: the response to a component entering the system occurs later.

The purity of hydrogen obtained for both processes was 99.99%. The purity of carbon dioxide was 84.7% in the laboratory set-up and 86.4% in the scaled-up process. Hydrogen recovery was 87.6 % in both systems, and the recovery of carbon dioxide was lower than 85%.

The temperature evolution in the fixed-bed reactor at both scales was accounted for by using the energy balance shown in Equation 3.5 (Section 3.3.3). Figure 5.6 shows the temperature profile for the four-bed scaled-up model, where there is a temperature variation of 15°C before the depressurization step starts. This rise in temperature happens during the adsorption step at the end of the bed and then is compensated for by the desorption, purge and rinse steps.

The temperature proves to be variable in a PSA process under approximately ambient conditions and the heating of the adsorbent during the adsorption step is compensated for by the cooling of the bed during the desorption step. The rise in temperature of the fixed-bed reactor is mainly due to the heat of adsorption. Similar rising trends in temperature were shown in the studies by Ribeiro et al. (2008) and Knox et al. (2016), where the reported temperature rises were of around 15°C and 20°C, respectively. Temperature greater than these values could hamper the adsorbent performance. The PSA configurations for the scaled-up PSA model shown in Sections 5.3 and 5.4 revealed identical trends to each other in the temperature inside the fixed-bed reactor. This can be explained by the duration of the adsorption step, which remained constant for all models. This step is the one that releases heat in the fixed-bed reactor, due to the exothermic nature of the adsorption process. The design conditions that changed in the PSA processes shown in Sections 5.3 and 5.4 were the gas velocity, the length-to-diameter ratio, the purge-to-feed flow rate ratio and the cycle design.

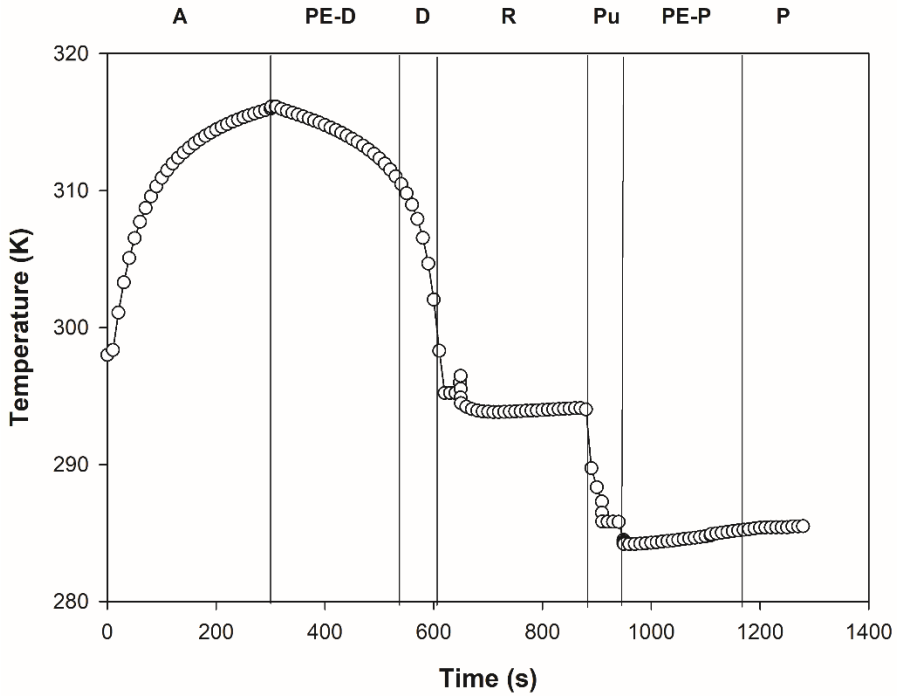

Figure 5.6. The evolution of the gas phase temperature at the end of the fixed-bed reactor in each of the steps of the four-bed scaled-up process

5.3 The Parametric Study of the Pilot-Scale Process Variables

5.3.1 The Effect of the Superficial Gas Velocity due to Varying the Bed Diameter

The effect of the superficial gas velocity was investigated using the process shown in Figure 5.1. For this purpose, the superficial gas velocity was varied by changing the bed diameter at a constant molar flow rate of 293.2 mol s^{-1} and a pressure of 36.7 bar, following the procedure shown in Figure 3.4 (Section 3.5.2). The length of the bed was constant and was set at the value of the basic case study presented previously (3.88 m). Therefore, as the bed diameter was varied, different bed length-to-diameter ratios were

used in each of the studied cases. The flow rate was kept constant, because of the requirements of the gas turbine in the power plant.

The parametric study simulated by the Global Systems Analysis was applied to determine the effects of the superficial velocity and diameter of the reactor on the product performance indicators. GSA performs various simulations using a number of values of a variable selected within a range, as explained in Section 3.5.2. In this case, the bed diameter was the selected variable. A quasi-random sampling method was applied that executed the analysis by distributing the variable values uniformly across the sampling range selected, yielding eight different estimated values for both the carbon dioxide and hydrogen product purity.

The sampling range selected for the superficial velocity was between 0.02 m s^{-1} (lower bound) and 0.05 m s^{-1} (upper bound). This sampling space was selected to avoid pressure drop and fluidization issues inside the fixed-bed reactor. At superficial velocities lower than 0.02 m s^{-1}, pilot-scale fixed-bed reactors could cause pressure drop issues, whereas a 0.05 m s^{-1} superficial velocity establishes the limit by using the minimum fluidization velocity (Wiheeb et al., 2016).

The purity of hydrogen remained over 99.99% for all the cases studied using GSA. These purity values were obtained with the process steps shown in Figure 5.1. The hydrogen was obtained during the adsorption step, which lasted for 300 s. This adsorption time was established as a compromise to maximize the purity of the hydrogen and to guarantee the cyclic recovery of the activated carbon based on the dynamic capacity of the material tested at laboratory scale. The carbon dioxide was obtained after the pressure equalization

step, during the depressurization step (from 5 bar to 1 bar) and during the rinse (250 s) and purge (50 s) steps (at 1 bar).

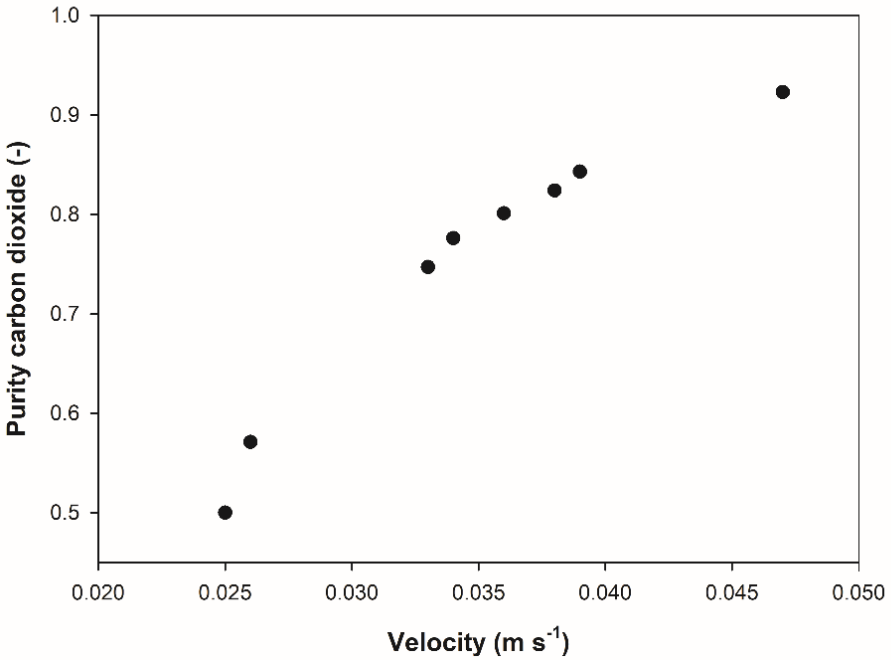

Figure 5.7. The results for carbon dioxide purity from the GSA analysis that varied the superficial velocity

The hydrogen purity was not sensitive to the superficial velocity of the gas, nor to varying the diameter of the bed, which had a maximum variation of 0.0001% when operating at superficial velocities between 0.02 m s^{-1} and 0.05 m s^{-1}. This insensitivity can be explained by the affinity of the carbon dioxide at 36.7 bar for the adsorbent surface compared to the affinity of the hydrogen for the range of superficial velocities chosen.

Figure 5.7 shows the results of the GSA using the superficial gas velocity as the decision variable. The figure relates the value on the decision variable to the purity of the carbon dioxide product. The carbon dioxide purity was more sensitive to the superficial velocity

of the gas, which varied by approximately 42% around the selected velocity values. The purity of the carbon dioxide reached 92.93% when the superficial velocity was at the maximum limit of 0.048 m s^{-1}, as shown in Figure 5.7. This behaviour showed that, at higher velocities, the mass transfer of carbon dioxide between the gas and the solid phase increased, within the range of velocities selected.

In order to study this behaviour, the concentration front of the carbon dioxide at the end of the bed during the PSA process was investigated for three runs in the sampling space of the GSA. Table 5.2 shows the values of the bed diameter for those runs. At a velocity of 0.048 m s^{-1}, the value of the bed diameter was 2.38 m, which is among the smallest diameter values for the sampling space selected. This result gives a higher length-to-diameter ratio of 1.63, compared to the result obtained with the simulation in Section 5.2.3, which had a bed diameter of 2.57 m.

Table 5.2. The values on the PSA product performance indicators for three runs of the GSA when varying the superficial velocity (v)

Run	v (m s^{-1})	D (m)	Recovery H_2 (%)	Recovery CO_2 (%)	Purity H_2 (%)	Purity CO_2 (%)
1	0.036	2.75	87.56	83.57	99.999	80.02
2	0.039	2.64	86.45	83.72	99.999	84.67
3	0.048	2.38	84.56	84.13	99.994	92.93

The recovery of hydrogen varied by about 2% over the three selected runs and by 1% for the carbon dioxide product. The recovery of hydrogen decreased mainly due to the purge step and the inclusion of only one pressure equalization step in the four-bed PSA model. The hydrogen was used as a purging gas; therefore, the amount of hydrogen obtained as

a product decreased. Additionally, after one pressure equalization step, the fixed-bed reactor was pressurized further with the feed gas containing a 60% hydrogen molar fraction. Run 3 yielded the lowest recovery value, 84.57%, because the hydrogen product entered the purge step at the highest velocity in the sampling range.

5.3.2 The Effect of the Reactor Length due to Varying the Bed Length-to-Diameter Ratio

The effect of the fixed-bed reactor length was studied by considering a number of length-to-diameter ratios at a constant diameter of 2.38 m. This fixed diameter was selected because it gave the best performance in terms of the overall product quality values, as explained in Section 5.3.1. The length of the bed was discretized by the finite difference method in the PSA model. Therefore, the analysis could not be executed using GSA, since the bed length needed to be a parameter with a fixed value for the discretization in the model, but GSA requires a variable for the simulations using the Monte Carlo method. Instead, several runs varied the length-to-diameter ratio; then the trends of the component molar fractions at the end of the reactor and the product performance indicators were analyzed.

Table 5.3 shows the PSA performance indicator values for three runs that varied the length of the reactor and the corresponding length-to-diameter ratios for each of the runs. Figure 5.8 shows the carbon dioxide molar fractions in the outlet of the reactor from the adsorption until the purge step, when the carbon dioxide and hydrogen products were obtained. The highest product purity values were obtained with a length-to-diameter ratio of 1.68, as shown in Table 5.3.

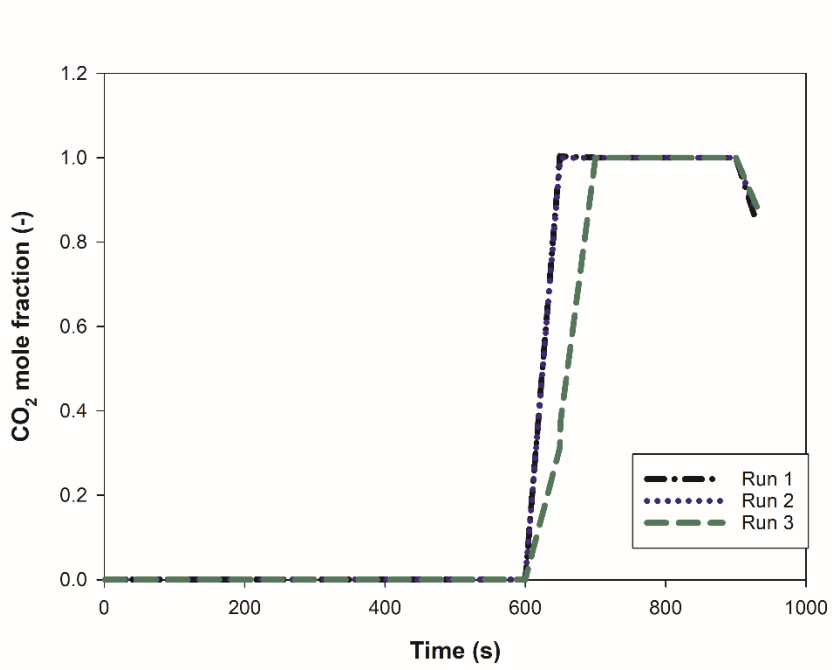

Figure 5.8. The carbon dioxide concentration profiles at the end of the bed for a number of bed length-to-diameter ratios

Table 5.3. The values on the PSA product performance indicators for the analysis that varied the bed length (L)

Run	L (m)	L/D	Recovery H_2 (%)	Recovery CO_2 (%)	Purity H_2 (%)	Purity CO_2 (%)
1	4	1.68	83.76	83.45	99.991	93.12
2	4.76	2	84.56	84.13	99.994	92.65
3	5.72	2.4	85.67	84.69	99.999	90.67

The three runs yielded a hydrogen purity of 99.99%. Figure 5.8 shows that with a length-to-diameter ratio of 1.6 (Run 1) and 2.0 (Run 2), the carbon dioxide started desorbing at the end of the depressurization step (t = 600 s), which obtained carbon dioxide purities as

high as 93.12%. The slope of the desorbing carbon dioxide concentration front was slower when a length-to-diameter ratio of 2.4 was used, decreasing the carbon dioxide purity to 90.67%. The desorption rate is related to the pressure gradient in the reactor, thus the slower desorbing rate of the carbon dioxide in a longer bed can be explained by the smaller pressure gradient in the fixed-bed reactor compared to that in a shorter reactor.

The hydrogen and carbon dioxide recovery values decreased with smaller length-to-diameter ratios, with a total decrease of 2% over all the simulations studied, but still did not achieve the value of 90%, due to the amount of hydrogen used in the purge and rinse steps, as well as in the pressurization steps.

5.3.3 The Effect of the Purge-to-Feed Flow Rate Ratio

The effect of the purge-to-feed flow rate (Pu/F) was studied using GSA following the methodology explained for the superficial velocity. The purge flow rate was selected as a variable for the parametric analysis, which yielded a number of purge-to-feed ratios. The purge flow rate was the flow rate at entry into the PSA reactor during the rinse and purge steps. Afterwards, the flow rate was increased for the pressurization step until it reached the adsorption flow rate. The range of purge-to-feed flow rate ratios selected was based on previous PSA studies in which values ranged from 0.1 to 1.0 (Luberti et al., 2014a; Moon et al., 2018; Ribeiro et al., 2008; Riboldi and Bolland, 2015a).

The carbon dioxide purity values from the GSA analysis are shown in Figure 5.9. The purity values for hydrogen were constant for this analysis, because hydrogen was obtained during the adsorption step and the only flow rate that varied during the analysis was the flow rate during the rinse and the purge steps. Figure 5.9 shows that the purity of

carbon dioxide decreased in a linear trend with the increasing gas flow rate during the rinse and the purge steps. The PSA product performance indicators for three runs of the GSA sampling space are shown in Table 5.4.

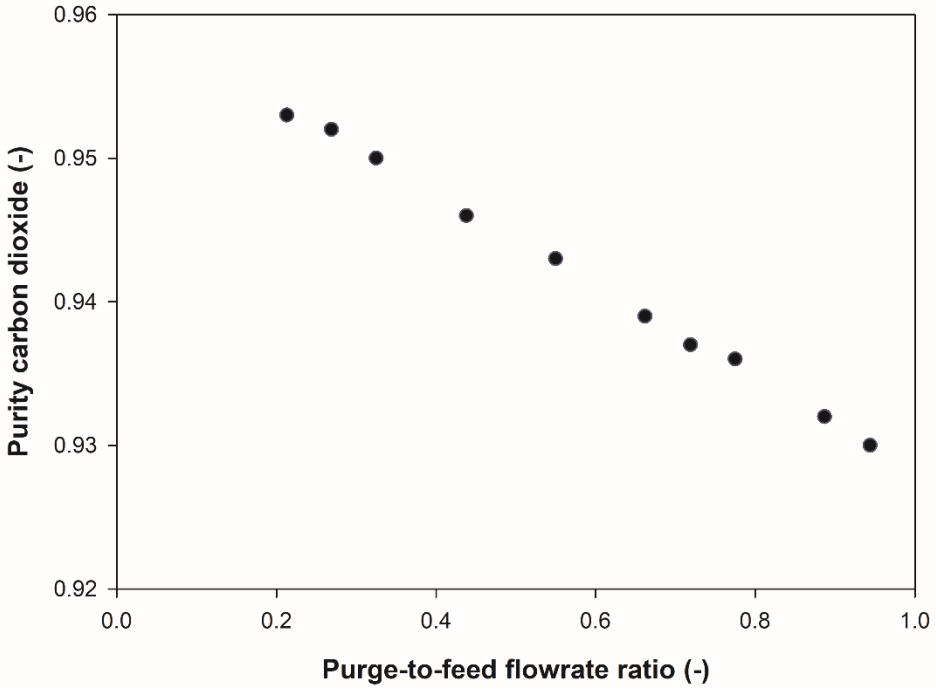

Figure 5.9. The results for carbon dioxide purity from the GSA analysis due to varying the purge-to-feed flow rate ratio

Of the three simulation runs, Run 1 gave the highest carbon dioxide purity. Although the flow rate of the carbon dioxide in the feed decreased during the rinse step, the overall purity of the carbon dioxide increased due to the smaller hydrogen flow rate during the 50 s purge.

Table 5.4. The values on the PSA product performance indicators for three runs of the GSA while varying the purge-to-feed (Pu/F) flow rate ratio

Run	Q_{Pu} (m^3 s^{-1})	Pu/F (-)	Recovery H_2 (%)	Recovery CO_2 (%)	Purity H_2 (%)	Purity CO_2 (%)
1	0.066	0.22	92.27	90.11	99.994	95.37
2	0.165	0.55	89.13	89.77	99.994	94.36
3	0.267	0.89	87.59	87.65	99.994	93.22

The decrease in the flow rate of the carbon dioxide entering the rinse step from Run 3 to Run 1 did not have an effect on the purity of hydrogen during that step and it was constant for all three runs. However, the overall purity of the carbon dioxide did increase at smaller purge-to-feed flow rate ratios, because less hydrogen entered the fixed-bed reactor during the purge step when carbon dioxide was obtained as a product. The recovery of carbon dioxide increased at smaller feed-to-purge ratios, but this was not analyzed in this study, because carbon dioxide is not a valuable product. A part of the carbon dioxide product was used in this study to increase the carbon dioxide purity during the rinse step by using a storage tank at 1 bar in the product end. This performed as a carbon dioxide 'make-up' tank to recycle the carbon dioxide product in the PSA process.

The purge-to-feed flow rate had a greater effect on the hydrogen recovery than did either the superficial gas velocity and the bed length, with overall deviations in recovery of about 5% in the simulated runs. The deviations in recovery with the bed diameter and length were of maximum 3% and 2%, respectively.

The purge-to-feed flow rate ratio had the biggest effect on the hydrogen recovery, because the amount of hydrogen product recycled to the purge step determines the recovery of the light product and the amount of hydrogen product obtained in the adsorption step.

Therefore, smaller purge flow rates than the feed flow rate in the adsorption step here were used in previous works using PSA for carbon capture (e.g., Ribeiro et al., 2008). Run 1 gave the best result for this performance indicator, because less hydrogen was recycled to the purge. The recovery of hydrogen for this run was above 90%, which is in the acceptable range for an NGCC power plant.

5.4 Additional Configurations of the Pilot-Scale PSA Model

The PSA process shown in Figure 5.1 obtained a maximum purity of hydrogen of 99.994% and a recovery of 92.27%, by varying the scaled-up variables. The maximum purity obtained for carbon dioxide was 95.37%, which meets the accepted limit value of 95% purity for storing carbon dioxide (Webley, 2014). Additional configurations were tested in order to improve the hydrogen recovery and the purity of carbon dioxide.

5.4.1 The Addition of an Assisted Purge Step

The overall purity of the carbon dioxide in the four-bed PSA model decreased mainly due to the light fractions of hydrogen entering the bed during the depressurization step. In order to increase the overall purity of the carbon dioxide, an assisted purge step was added to the four-bed PSA model. An assisted purge step sends the outlet gas of a fixed bed that undergoes the last step of depressurization into a fixed bed that undergoes the purge step. Figure 5.10 shows the flow chart for the four-bed PSA model with an assisted purge step (A-Pu), where the outlet gas of this step goes to the fixed-bed with the purge (Pu) step.

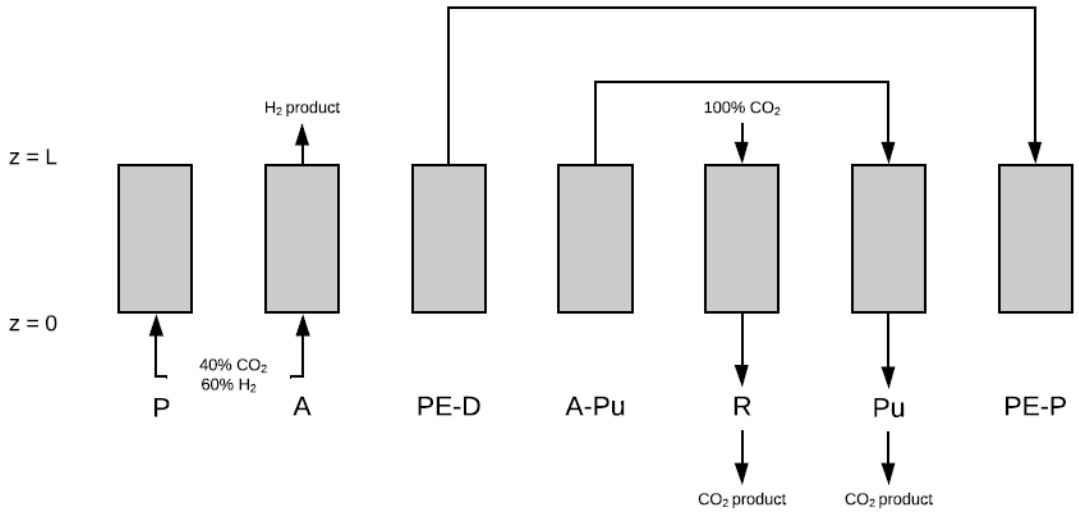

Figure 5.10. A schematic figure of the four-bed PSA model, adding an assisted purge step

The assisted purge step shown in Figure 5.10 enabled the obtention of all the hydrogen as a product in the adsorption step, instead of using a fraction of the product as a purging gas. The assisted purge step also enabled the recycling of the hydrogen product at the outlet of the depressurization step, because carbon dioxide started desorbing around 1 bar (t = 600 s), as shown in Figure 5.8. Figure 5.11 shows the concentration fronts of the products for the four-bed PSA model with an assisted purge.

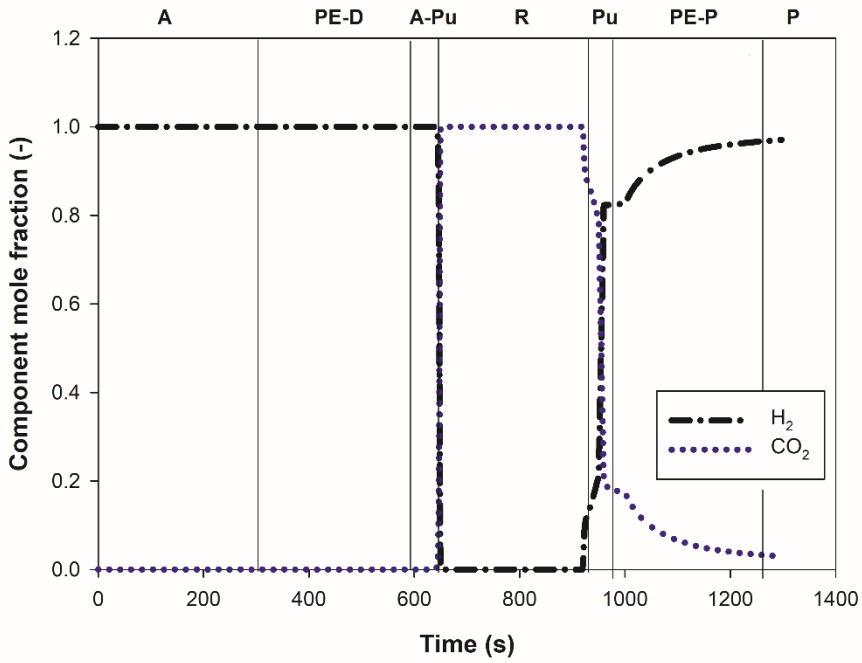

Figure 5.11. Component concentration profiles at the end of the bed for the four-bed PSA model adding an assisted purge step

In Figure 5.11, the concentration fronts of the components for the adsorption, depressurization, purge and rinse steps did not change much, compared to those from the four-bed model without an assisted purge, shown in Figure 5.5. The concentration fronts did change slightly during the 50 s of the purge step and pressurization step due to the components coming from the depressurization step instead of the hydrogen. The purity of the hydrogen remained constant for this configuration, at 99.994%, compared to the purity from the four-bed reference model. However, the recovery of hydrogen increased to 94.35%, due to not using hydrogen as a feed for the purge step. The hydrogen that was not directed to the purge stream formed part of the hydrogen product during the adsorption step. There was a slight increase in the carbon dioxide recovery to a value of 90.56%, due to having a less pure stream of hydrogen in the inlet of the purge step.

The carbon dioxide purity increased to 96.12% due to not obtaining the light component fractions during the depressurization step. This step enables the obtention of a purity of over 95% for carbon dioxide, without the addition of more than four beds. A previous study reported a purity of 98% for carbon dioxide after a PSA and a flash separation, but the separation process included seven fixed-bed reactors (Riboldi et al., 2014).

5.4.2 The Addition of Pressure Equalization Steps

Industrial PSA reactors usually have more than one pressure equalization step; this requires additional beds. Additional pressure equalization steps have been used in industrial PSA reactors to improve the light product recovery (Moon et al., 2018; Ribeiro et al., 2008). A maximum of three pressure equalization steps were included in this work; there would be additional capital costs if there were more than six fixed-bed reactors in a power plant. Therefore, one and two beds were added to the process in two case studies mainly to improve the recovery of the light product (hydrogen). The total duration of the pressure equalization step was kept constant for the synchronization of the steps. For the five-bed model each of the pressure equalization steps lasted 125 s, and for the six-bed model each of the steps lasted 83.3 s. The length of the pressure equalization steps was decided based on the model calculations of the time required for the pressure to equalize. Tables 5.5 and 5.6 show the configuration of the steps for the five- and six-bed models, with two and three pressure equalization steps, respectively. Figure 5.12 shows the process flow for the five-bed PSA model with two pressure equalization steps.

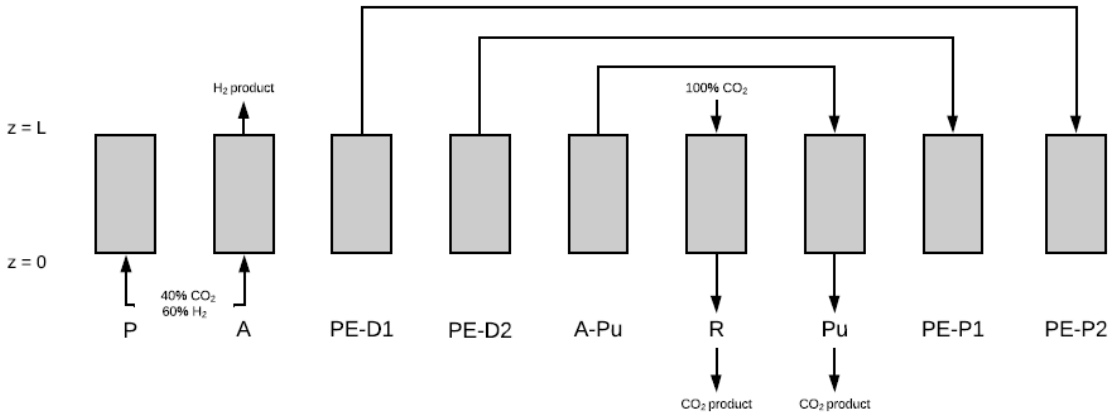

Figure 5.12. A schematic figure of the five-bed PSA model with two pressure equalization steps

Table 5.5. The step configuration for the five-bed PSA model with two pressure equalization steps and an assisted purge step

Steps	1	2	3	4	5	6	7	8	9	10
Bed 1	A		D1	D2	A-Pu	R	Pu	P1	P2	P
Bed 2	P2	P	A		D1	D2	A-Pu	R	Pu	P1
Bed 3	Pu	P1	P2	P	A		D1	D2	A-Pu	R
Bed 4	A-Pu	R	Pu	P1	P2	P	A		D1	D2
Bed 5	D1	D2	A-Pu	R	Pu	P1	P2	P	A	

Table 5.6. The step configuration for the six-bed PSA model with three pressure equalization steps and an assisted purge step

Steps	1	2	3	4	5	6	7	8	9	10	11	12
Bed 1	A		D1	D2	D3	A-Pu	R	Pu	P1	P2	P3	P
Bed 2	P3	P	A		D1	D2	D3	A-Pu	R	Pu	P1	P2
Bed 3	P1	P2	P3	P	A		D1	D2	D3	A-Pu	R	Pu
Bed 4	R	Pu	P1	P2	P3	P	A		D1	D2	D3	A-Pu
Bed 5	D3	A-Pu	R	Pu	P1	P2	P3	P	A		D1	D2
Bed 6	D1	D2	D3	A-Pu	R	Pu	P1	P2	P3	P	A	

The first pressure equalization-depressurization step (D1) had the lightest fractions of all the pressure equalization steps. This step was used in the third pressure equalization-pressurization step to clean the bed for the six-bed model, based on the component fractions profile in the outlet of the reactor for the four-bed model. Because the assisted purge step was also used for the five- and six-bed models, the purity of carbon dioxide was expected to be over 95%, with the previously mentioned requirement of over 90% hydrogen recovery. Table 5.7 shows the product performance indicators for the stated bed configurations when varying the number of pressure equalization steps.

Table 5.7. The PSA product performance indicator values and variable values for the bed configurations using an assisted purge step

Number of beds	Number of PEs	Recovery H_2 (%)	Recovery CO_2 (%)	Purity H_2 (%)	Purity CO_2 (%)
4	1	94.35	90.56	99.994	96.12
5	2	95.61	90.42	99.994	97.18
6	3	96.87	90.37	99.994	97.39

Table 5.7 demonstrates that, although the purity of hydrogen remained constant over a varying number of pressure equalization steps, the recovery of this component increased by more than 2 percentage points from a four-bed to a six-bed PSA model. There was a slight decrease in the recovery of the carbon dioxide to a value of 90.37% with three pressure equalization steps. The purity of carbon dioxide increased by 1 percentage point from the four- to the five-bed model. However, it increased by only 0.2 percentage points from the five- to the six-bed model. Previous work has not reported the effect of pressure equalization steps on the carbon dioxide purity, but did show an increase in the recovery of the hydrogen product by 2 percentage points (Luberti et al., 2014a).

5.4.3 The Addition of a Rinse Step after the Feed or Pressure Equalization Steps

The effect on the PSA product performance indicators of adding a rinse step after the feed step was investigated for the four-bed PSA model and across the various pressure equalization steps for the five- and six-bed models. This step was studied after the feed and after each step of the pressure equalization steps. For the five-bed model, the rinse

was applied after the first pressure equalization step (D1) and after the second pressure equalization step (D2) for the six-bed PSA model. Table 5.8 shows the product performance indicators for the configurations using the rinse step.

Table 5.8. The product performance indicator values and variable values for a number of bed configurations using the assisted purge step and the rinse step

Number of beds	Number of PEs	Rinse position	Recovery H_2 (%)	Recovery CO_2 (%)	Purity H_2 (%)	Purity CO_2 (%)
4	1	A-PE1	95.48	90.76	99.991	98.28
5	2	PE1-PE2	96.07	90.57	99.994	98.56
6	3	PE2-PE3	97.02	90.49	99.994	98.74

As shown in Table 5.8, the purity of hydrogen decreased insignificantly by 0.003 percentage points in the four-bed PSA model with a rinse step after the feed step (A-PE1) compared to the model without this step. The small decrease was due to the rinse that the carbon dioxide feed adsorbed inside the reactor at 37.6 bar. This is further clarified in Figure 5.13, where the carbon dioxide did not come out of the bed until it finished the depressurization step. The recovery of hydrogen did slightly increase by 1 percentage point due to not feeding gas during the rinse step. The recovery of carbon dioxide also increased slightly, due to recycling the carbon dioxide at high pressures and then obtaining the product at atmospheric pressures. The purity of carbon dioxide increased by between 1 and 2 percentage points when adding the rinse step to the various PSA configurations with pressure equalization.

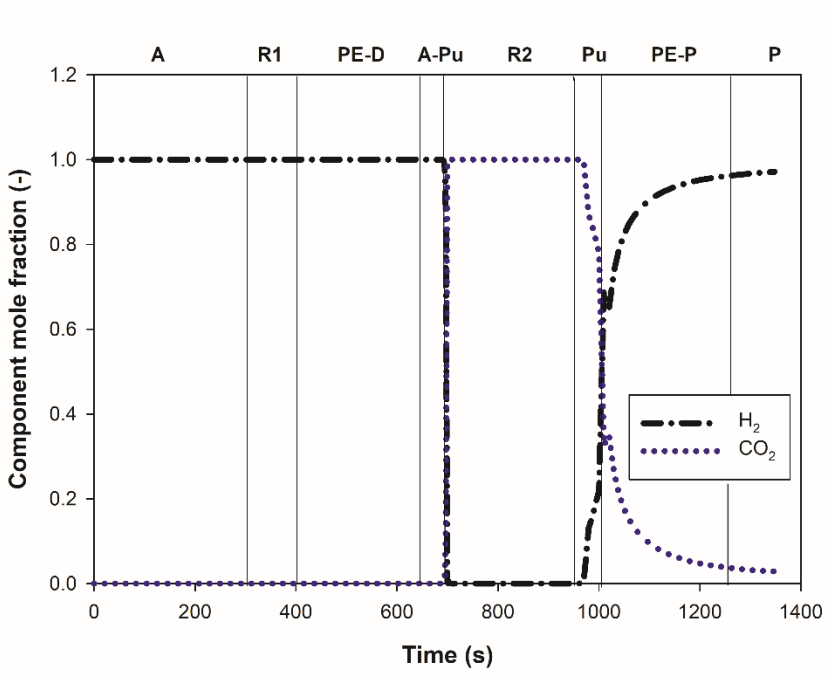

Figure 5.13. The component concentration profiles at the end of the bed for the four-bed PSA model after adding a rinse step

The effect of the rinse step at pressures higher than 1 bar has not been previously reported for pressure swing adsorption processes applied to hydrogen purification and carbon capture in combined cycle power plants, for example in Riboldi and Bolland (2017).

A similar step has been previously reported where the outlet gas of the purge step is recycled to the adsorption step to obtain a carbon dioxide purity over 95% (Wang et al., 2015). This step also shows an improvement on the overall hydrogen recovery, due to the lower amount of hydrogen fed into the adsorption step when the carbon dioxide is recycled at pressures higher than 1 bar. However, the introduction of a rinse step at pressures higher than 1 bar requires the use of a compressor; therefore, the obtained improvements of between 1 and 2 percentage points on the recovery of hydrogen from the four- to the six-fixed-bed reactor models are not significant compared to the impact on the cost when including additional compression requirements in the plant. Therefore,

a four-fixed-bed model with a rinse step at higher than 1 bar would be a sensible choice for the power plant.

5.5 Conclusion

A laboratory four-bed and seven-step PSA model was scaled up to operate in an NGCC power plant and the results from the scaled-up and laboratory models were compared. The aim of scaling up the fixed-bed reactor was to analyze the performance of the PSA process at pilot scale for an NGCC power plant. Both processes yielded the same purity and recovery values of 99.99% and 87.6% for hydrogen, respectively. Carbon dioxide yielded a purity of 86.4% in the scaled-up model, 2% higher than in the laboratory model, and a recovery lower than 85% for both cases. The four-bed PSA model included a rinse step at 1 bar that proved to be essential to increase the carbon dioxide purity.

The effects of the process variables in the scaled-up model, such as the bed diameter and purge-to-feed flow rate ratio, were investigated by using a global system analysis to maximize the values on the product performance indicators. At high velocities, such as 0.048 m s^{-1}, and at a bed diameter of 2.38 m, a carbon dioxide purity of 92.93% was obtained. This can be explained by the increase in the mass transfer between the gas and the solid phase. The carbon dioxide purity increased further to 95.37% with a bed length of 4 m and a purge-to-feed flow rate ratio of 0.22. The purity of hydrogen remained nearly constant with a value of 99.99% for all the GSA cases. The recovery of hydrogen decreased to 84.56% at gas velocities of 0.048 m s^{-1}, but it increased to 92.27% using a purge-to-feed flow rate ratio of 0.22. The recovery of carbon dioxide yielded a value of 90.11% in this case.

Additional PSA configurations were studied to improve the carbon dioxide purity and the hydrogen recovery. These configurations included an assisted purge step, which increased the hydrogen recovery to 94.35%. This assisted purge step also proved to be essential to obtain carbon dioxide purities over 96%. These purities increased slightly (by one percentage point) upon the introduction of two (the five-bed model) and three (the six-bed model) pressure equalization steps. The main performance indicator that increased with the number of pressure equalization steps was hydrogen recovery, by 2 percentage points, by including three pressure equalization steps. The recovery of carbon dioxide changed by less than one percentage point after the introduction of pressure equalization steps.

The number of pressure equalization steps increases with the number of beds, which increases the CAPEX of the plant. The use of a rinse step after the feed or pressure equalization step increased the carbon dioxide purity by around 2 percentage points, obtaining a maximum purity of 98.74% for the six-bed model. This model included the rinse step after a second pressure equalization step. A compressor is required for this rinse step, which also increases the CAPEX of the plant.

Overall, the four-bed model with an assisted purge step and a rinse step at higher than 1 bar showed promising results, due to the lower capital costs expected for a power plant with a lower number of fixed-bed units, and based on the cyclic capacity required to operate the gas turbine. The CAPEX and the OPEX of the designed PSA process integrated into an NGCC power plant were studied in Chapter 6. The cycle configurations that were expected to be the most successful in terms of the performance indicators of the products and of the economics of the process were integrated within the plant.

CHAPTER 6 – THE PERFORMANCE OF THE NGCC POWER PLANT WITH PSA

6.1 Introduction

This chapter reports the economic viability of the developed pressure swing adsorption process configurations in a natural gas combined cycle power plant. PSA was selected as a suitable process for pre-combustion carbon capture due to the high pressures above 20 bar before the gas stream enters the gas turbine, and because of the composition of the natural gas compared to that of coal (Anantharaman et al., 2011). Natural gas has a content of up to 98% carbon-based components, mostly hydrocarbons in the gas phase. These gases are converted to syngas (carbon dioxide and hydrogen) with steam methane reforming technology. The content of carbon-based components in coal is of around 67%, and processes such as gasification are required to obtain syngas before SMR. In addition, the content of ash in coal is around 15% (IEA-GHG, 2009). This component could affect the performance of the PSA process, blocking the pores on the adsorbent surface.

Additionally, integrating a PSA process in a power plant with pre-combustion capture gives the opportunity to co-produce hydrogen (Seyitoglu et al., 2016). Hydrogen has a high potential to be one of the main energy vectors in the near future (Gasworld, 2019). In this context, natural gas processed by SMR and PSA has already been used to obtain up to 95% of the commercial hydrogen worldwide (The Fourth Generation, 2020). Therefore, NGCC power plants with pre-combustion PSA are expected to be a potential technology for the upcoming decades.

The performance indicators chosen to study the viability of PSA technology in the NGCC power plant were the percentage of the energy penalty (EP) of the power plant with PSA compared to the plant without PSA, and the economic performance indicators, specifically, the levelized cost of electricity and the levelized cost of carbon avoided. These economic indicators have been used to measure the viability of carbon capture technologies in coal- and gas-fired power plants. The LCOE is an estimate of the cost of the power plant per unit of power produced. The LCCA is an estimate of the extra cost of the power plant with capture compared to the cost of the power plant without capture, based on the unit of mass of carbon dioxide captured. Appendix F shows the costing of the different units included in the power plant.

First, the effect of the power plant operation sequence and the conditions on the performance indicators was studied, as shown in Section 6.2. The operational sequences chosen for study in the power plant were the PSA configuration, such as the number of pressure equalization steps and the inclusion of a rinse step. These results are discussed in Section 6.2.1. The other condition chosen in the power plant was the operating pressure of the water gas shift reactor, in Section 6.2.2, which determines the feed pressure of the PSA process. The operating pressure of the WGS was maintained constant for entry into the PSA unit, in order to lower the compression requirements. The effect of the inclusion of hydrogen co-production in the NGCC power plant is reported in Section 6.2.3 of this chapter. For that purpose, the capacity of the power plant was doubled and half of the hydrogen product of the PSA unit was directed to a hydrogen storage tank, whence it could be sold as a by-product of the electricity generation to supplement plant income.

Second, the effects of the technical specifications of the power plant were studied. Those were the capacity factor (Section 6.3.1) of the power plant and the plant life (Section

6.3.2). The capacity factor indicates the percentage of the capacity at which the plant operates compared to that of a reference plant that operates at maximum capacity during the whole year, based on the capacity of the gas turbine (Anantharaman et al., 2011). In this study the maximum operational capacity of the gas turbine was 11.25 MW.

The capacity factor of the power plant is an important variable for the flexible electricity supply in the near future and for an energy system that integrates renewable electricity sources. The plant life is a specification that also has an effect on the operational and maintenance costs of the power plant. The effects of economics of scale were also studied, as shown in Section 6.3.3, by doubling the capacity of the plant.

Last, the effects of the market price of natural gas (Section 6.4.1) and the carbon tax (Section 6.4.2) were studied. The natural gas price has been highly variable with big fluctuations during the last two decades. Therefore, it is important to estimate the effect of this variable on the cost of NGCC power plants. The other factor considered was the carbon tax, which is predicted to increase during the following three decades with the introduction of decentralized and renewable power production technologies at bench scale (International Energy Agency, 2019c).

6.2 The Effect of the Variations in the Process Design on the Energy Efficiency and Economics of the Plant

The effect of the plant design upon the energy efficiency and economics of the plant was analyzed by varying the design of the PSA unit and the operating pressure of the water gas shift unit, which comprises a high temperature shift reactor and a lower temperature shift reactor. A cooler between the LTS and the PSA unit lowered the gas temperature

from 473.15 K to 338 K. The operating pressure of the WGS reactor has an effect on the capture performance of the PSA unit, as the WGS process establishes the operating pressure of PSA in order to decrease the compression costs (Riboldi and Bolland, 2017).

Hydrogen co-production was also considered in the design choices of the power plant, following plant configurations such as those of Seyitoglu et al. (2016), which integrate a gasification combined cycle power plant with a Fischer-Tropsch unit for the production of diesel and gasoline. This chapter studies the effect of integrating hydrogen co-production in an NGCC power plant with the designed PSA processes.

A parametric study is reported in this section, where the effect of the design choices on the energy penalty of the NGCC power plant is analyzed for PSA for pre-combustion carbon capture, and the EP values are compared to those obtained in a reference plant without PSA. The levelized cost of electricity and the cost of carbon dioxide avoided, estimated by Equations 3.37 and 3.38 (Section 3.7.3), respectively, were also used to compare the economic performance of the two plants.

6.2.1 The Effect of the PSA Process Configurations

In order to study the effect of the PSA design choices on the energy efficiency and economics of the plant, the PSA configurations of Chapter 5 that yielded a purity above 95% for the CO_2 and H_2 products and above 90% recovery were selected (Webley, 2014). The purity of hydrogen was not studied here, as it was over 99% for all the configurations studied in Chapter 5. The configurations that included one to three pressure equalization (PE) steps with an assisted purge step and a rinse step higher than 1 bar produced the values directly above. Therefore, these configurations were selected to study the

performance indicators of the power plant when including PSA for carbon capture. The capital cost of the power plant included the additional fixed-bed units, valves and compressors that are required when pressure equalization steps and a rinse step higher than 1 bar are included in the process. The capital cost of these units is shown in Appendix F. The additional energy penalty of the compression requirements for the rinse step was calculated using gPROMS® ProcessBuilder by specifying the inlet and outlet conditions of the pressure in the streams.

Tables 6.1 and 6.2 show the results for the PSA configurations, without and with the rinse step, respectively, and the values obtained for the EP, LCOE and LCCA of the power plant. Table 6.1 also shows the purity and recovery values obtained with the PSA configurations studied in Chapter 5. The aim of adding equalization steps was to analyze the effect of an additional operational step in the sequence on the performance indicator values from the power plant. The rinse pressure for each of the PE-step configurations in Table 6.2 is explained in Chapter 5.

Table 6.1. The performance indicator values for the PSA configurations without a rinse step above 1 bar

PE Steps	LCCA ($/tonne)	LCOE ($/MWh)	EP (%)	Recovery CO_2 (%)	Recovery H_2 (%)	Purity CO_2 (%)
1	39.52	92.65	22.88	90.56	94.35	96.12
2	39.94	92.71	22.88	90.42	95.61	97.18
3	40.36	93.18	22.88	90.37	96.87	97.39

Table 6.2. The performance indicator values for the PSA configurations with a rinse step above 1 bar

PE Steps	LCCA ($/tonne)	LCOE ($/MWh)	EP (%)	Recovery CO_2 (%)	Recovery H_2 (%)	Purity CO_2 (%)
1	41.58	93.84	28.67	90.76	95.48	98.28
2	40.83	93.32	27.21	90.57	96.07	98.56
3	40.85	93.33	26.42	90.49	97.02	98.74

Table 6.1 shows that the additional pressure equalization steps do not have a significant effect on the LCOE and LCCA of the power plant, just increasing these indicators by one percentage point. The energy efficiency of the plant did not vary due to increasing pressure equalization steps, as the instruments in the additional beds (i.e., valves) did not change this value, and the energy losses were compensated by the smaller loss of momentum due to the pressure equalization steps. However, the addition of from one to three pressure equalization steps did increase the hydrogen recovery by around 2 percentage points, increasing the LCCA and LCOE of the plant by less than one percentage point.

The inclusion of a rinse step did decrease the energy efficiency of the plant, as shown in Table 6.2. The increase in the energy penalty by 6 percentage points for one pressure equalization step with a rinse step was due to the inclusion of a centrifugal compressor that recycled the carbon dioxide exiting the rinse and purge steps at 1 bar into a rinse step at 18 bar, as explained in Section 3.6.3. The energy penalty and the cost indicator values for the plant decreased with the addition of pressure equalization steps. The energy penalty decreased by 2 percentage points when using one to three pressure equalization steps, due to the decrease in the compression requirement of 9 bar. The LCCA and LCOE

decreased slightly, by less than one percentage point, due to the compression requirements having a more significant impact on the cost than did the number of fixed-bed reactor units.

Overall, the inclusion of a rinse step had a greater effect on the energy penalty than on the LCCA and LCOE cost indicators because the contribution of the cost of the compressor required for the rinse step had a small impact on the capital cost of the plant compared to the cost of the gas turbine. The gas turbine was the greatest contributor to the capital costs for the plant. However, the energy efficiency of the plant was affected by the operation of this compressor, increasing the energy penalty by 4 to 6 percentage points.

The hydrogen recovery was the capture performance indicator most affected by the inclusion of pressure equalization steps, as shown in Tables 6.1 and 6.2. Figure 6.1 relates the hydrogen recovery values to the energy penalty of the plant. The variable changed in these configurations was the number of pressure equalization (PE) steps. When the rinse step was included, the energy penalty decreased by 2 percentage points with the increasing number of pressure equalization steps. However, the energy efficiency was not affected when the rinse step was not included in these configurations because there were no compression requirements for these configurations. The recovery of hydrogen using three PE steps was around 97%, similar to the recovery for the three-PE-steps configuration without a rinse step.

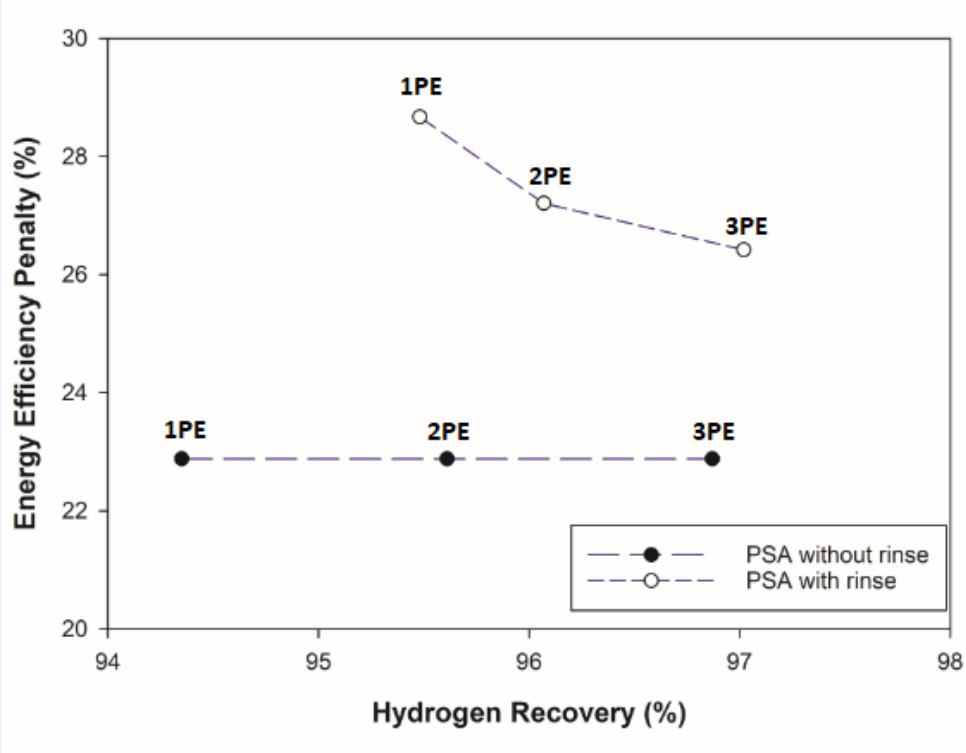

Figure 6.1. The relationship between the energy efficiency of the plant and the hydrogen recovery with an increasing number of pressure equalization (PE) steps in the PSA configurations

6.2.2 The Effect of the Water Gas Shift Unit Operating Pressure

The other input condition of the PSA unit studied here was the feed pressure coming from the water gas shift unit. This value was established by a previous study as 36.7 bar (Anantharaman et al., 2011). Taking the above value as a reference, the feed pressure of the PSA unit was decreased to 34 bar, 30 bar and 28 bar, to see the impact of this variable on the cost indicators, energy efficiency and capture performance of the plant. Pressures below 28 bar were not considered in this study, because the purity and recovery of the products dropped to under 80% in the simulations at pressures below this value. Tables 6.3 and 6.4 show the values of the performance indicators when varying the PSA feed

pressure, for the PSA configuration with one pressure equalization (1 PE) and an assisted purge step, and 3 PEs with a rinse step, respectively.

Table 6.3. The performance indicator values for several WGS operating pressures, for the PSA configuration with 1 PE

WGS Pressure (bar)	LCCA ($/tonne)	LCOE ($/MWh)	EP (%)	Recovery CO_2 (%)	Recovery H_2 (%)	Purity CO_2 (%)
34	38.84	91.92	19.43	90.37	93.89	95.93
30	38.23	91.49	13.87	90.06	93.16	95.12
28	37.93	91.27	10.96	89.75	92.84	94.76

Table 6.4. Performance indicator values for several WGS operating pressures, for the PSA configuration with 3 PEs and a rinse step above 1 bar

WGS Pressure (bar)	LCCA ($/tonne)	LCOE ($/MWh)	EP (%)	Recovery CO_2 (%)	Recovery H_2 (%)	Purity CO_2 (%)
34	40.44	93.04	22.79	90.41	96.77	97.65
30	39.83	92.61	17.32	90.12	96.43	96.79
28	39.52	92.41	14.4	89.67	96.08	96.13

As shown in Tables 6.3 and 6.4, the performance indicator most affected by the decrease of the WGS reactor operating pressure is the energy efficiency penalty, which decreases by 9 and 8 percentage points for the configurations shown, respectively. This is due to the decreasing requirements for compression between the steam methane reformer and the water gas shift reactor, which also lowers the LCCA and LCOE of the plants in both

configurations by one percentage point. The lower requirement for compression naturally brings about an associated reduction in the requirement for electricity.

Figure 6.2 relates the efficiency penalty to the cost of carbon dioxide avoided. The intercept of the configuration with three pressure equalization steps and with a rinse step was different to the one with one pressure equalization step, due to the increase on the capital cost when adding a compressor and two fixed-bed reactors.

The variable value that changed from point to point was the WGS pressure for the PSA configurations displayed in Figure 6.2. Both performance indicator values decreased with decreasing WGS operating pressures. This trend is due to the decrease in the requirements for compression between the WGS and the PSA process, which had a linear relationship with the energy efficiency of the plant. However, the recovery of carbon dioxide was affected by decreasing WGS pressures; it had a value below 90% for both configurations at 28 bar, shown in Tables 6.3 and 6.4, so, outside of the specified range.

The energy penalty of the power plant decreased by around 8 percentage points, whereas the decrease in the carbon dioxide recovery was of around 3 percentage points for the WGS pressure range studied. A trade-off thus exists between the cost of CO_2 avoided and the purity of the CO_2 stream, with only pressures over 30 bar giving the required purity. Therefore, the analysis found that the WGS pressure must be set over 30 bar to obtain a carbon dioxide recovery over 90%.

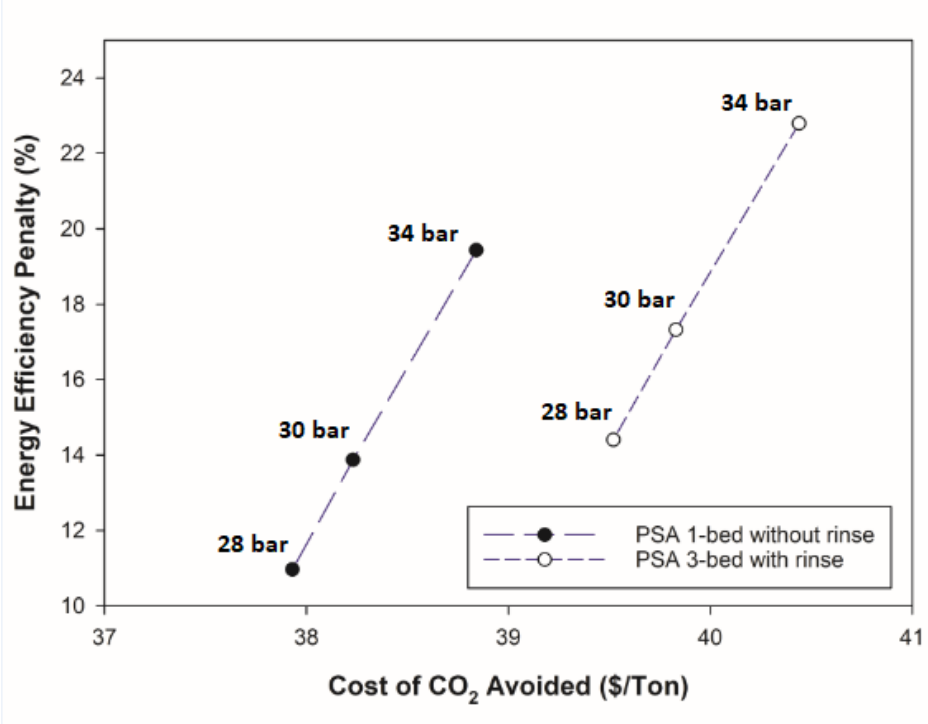

Figure 6.2. The relationship between the energy efficiency of the plant and the LCCA under increasing WGS operating pressures in the studied PSA configurations

6.2.3 Hydrogen Co-Production in the Power Plant

The effect on the plant costs of including hydrogen co-production was studied, since the PSA process obtained up to 99.99% hydrogen purity with the designed configurations in Chapter 5. This is the minimum purity value for hydrogen gas commercialization (Ribeiro et al., 2008). For this purpose, the capacity of the pressure swing adsorption unit was doubled for this case study relative to the case without hydrogen co-production.

This approach enabled the maintenance of the same power production as in the previous sections and enabled the comparison of the plant performance at constant capacity, directing half of the hydrogen production to the gas turbine for power generation, and the other half of the hydrogen production to storage for selling purposes. This hydrogen co-

production unit is in line with the interest in multi-generation systems, where electricity, steam, hydrogen and fuels are produced in the same plant (Ozturk and Dincer, 2013; Seyitoglu et al., 2016).

For the purpose of energy and hydrogen co-generation in the plant, the capacity of the plant was doubled to treat 3.5 kg s^{-1} natural gas. The reference plant treated 1.75 kg s^{-1} of natural gas. This increase in the capacity of the plant was considered as a reference value for the study of hydrogen co-production. The integration of hydrogen production was developed following co-generation unit design structures such as the one in Seyitoglu et al. (2016).

The size of the NGCC power plant units was adjusted to operate under 3.5 kg s^{-1} natural gas mass flow. Half of the hydrogen product was directed to the GE-10 gas turbine, while the other half of the hydrogen product was directed to a hydrogen storage tank. The design of these units of the power plant was carried out following the procedure described in Section 3.6. The storage tank was added to the capital cost of the power plant, as shown in Appendix F.

The earnings from the hydrogen production were included in the calculation of the annual total product cost indicator (ATPC). Therefore, the income obtained from the hydrogen commercialization was reflected in the LCOE and the LCCA of the plant. Previous studies have also included the earnings of the co-products from the plant in the calculation of these indicators, such as the earnings from heat supply in Hu et al. (2018).

Table 6.5 shows the results for the economic performance indicators under varying hydrogen market prices when including the co-production unit. The additional economic indicator studied here with the change in hydrogen market prices was the total annual

production cost of the plant. The $ATPC_{H2}$ is a net cost indicator in this case study, which includes an offset for the sale of the hydrogen produced, as shown in Equation 3.36 (Section 3.7.2). The $ATPC_{H2}$ also included the annual payment of the total capital investment at an interest rate of 5% (Peters et al., 2003). The values for the $ATPC_{H2}$ are shown in Table 6.5 to explain the variations in the LCCA and LCOE indicators when including hydrogen co-production in the plant.

The PSA configuration chosen for this analysis was the configuration with one pressure equalization step without a rinse step; this is the reference PSA configuration. The results of the other configurations would have followed the same trend when doing this analysis, as the PSA process was not modified when co-producing hydrogen in the plant.

On the one hand, the energy efficiency penalty of the power plant did not change with the introduction of the co-production unit; it was constant at a value of 22.88%. The hydrogen product was stored at a high pressure of 36.7 bar coming from the adsorption step of the PSA process; therefore, saving on the compression requirements for this product. On the other hand, the LCCA and the LCOE economic indicator values changed with the addition of hydrogen co-production in the plant, as shown in Table 6.5. These indicators varied due to the effect of the hydrogen market price on the $ATPC_{H2}$ of the plant.

Table 6.5. The values on the economic performance indicators for several hydrogen market prices and the co-generation plant

Hydrogen Price($/tonne)	LCCA ($/tonne)	LCOE ($/MWh)	$ATPC_{H2}$ ($/year)
13,000	85.83	104.22	13,195,344.68
14,000	55.51	99.12	12,406,947.24
15,000	48.26	94.01	11,618,549.80
16,000	41.01	88.91	10,830,152.35

The values in Table 6.5 show that the market price of hydrogen, when it includes a co-production unit, has a greater effect on the economic performance indicators of the power plant, than the type of the PSA configuration used and the water gas shift operating pressure. The LCOE of the plant increased from 88.91 to 104.22 $/MWh, when the market price of hydrogen decreased from 16,000 to 13,000 $/tonne H_2. The varying market prices had a greater effect on the LCCA than on the LCOE of the plant; the LCCA decreased by over 50% when the hydrogen market value increased from 13,000 to 16,000 $/tonne.

Figure 6.3 shows the values of the LCCA with varying hydrogen market prices. At hydrogen market prices of around 13,000 $/tonne H_2, the LCCA of the plant was 85.83 $/tonne CO_2, which is 45 $/tonne CO_2 higher than the LCCA values obtained for the power plant without hydrogen co-production. The LCCA value for the power plant decreased less than 20 $/tonne CO_2 when the hydrogen market price increased from 14,000 to 16,000 $/tonne H_2.

The lowest LCCA value obtained by adding a hydrogen co-production unit was 41 $/tonne CO_2, at hydrogen market prices of 16000 $/tonne H_2, which is similar to the

LCCA values between 37 and 42 $/tonne CO_2 obtained with the power plant designs without hydrogen co-production. The inclusion of the hydrogen co-production unit yielded an improvement in the LCOE of the plant, with a value of 88.91 $/MWh when the hydrogen market price was 16,000$/tonne H_2. The LCOE of the power plant configurations without hydrogen co-production was between 91 and 94 $/MWh.

Market prices as high as 16,000 $/tonne H_2 could be achieved during the next three decades with the increase in hydrogen demand. For this case, the inclusion of hydrogen co-production in these plants shows promising results. Hydrogen is predicted to be a necessary energy vector for an affordable and sustainable energy supply in the near future (Mac Dowell and Staffell, 2016). The inclusion of the hydrogen co-production unit and the increase in the hydrogen prices also reveals advantages in terms of the decrease in the ATPC from around 13 $m/year to 11 $m/year. The ATPC values obtained for the power plant in this study are in line with the values obtained by Anantharaman et al. (2011), which were of around 10.5 $m/year. This study analyzed the cost of an IGCC power plant with solvent-based capture.

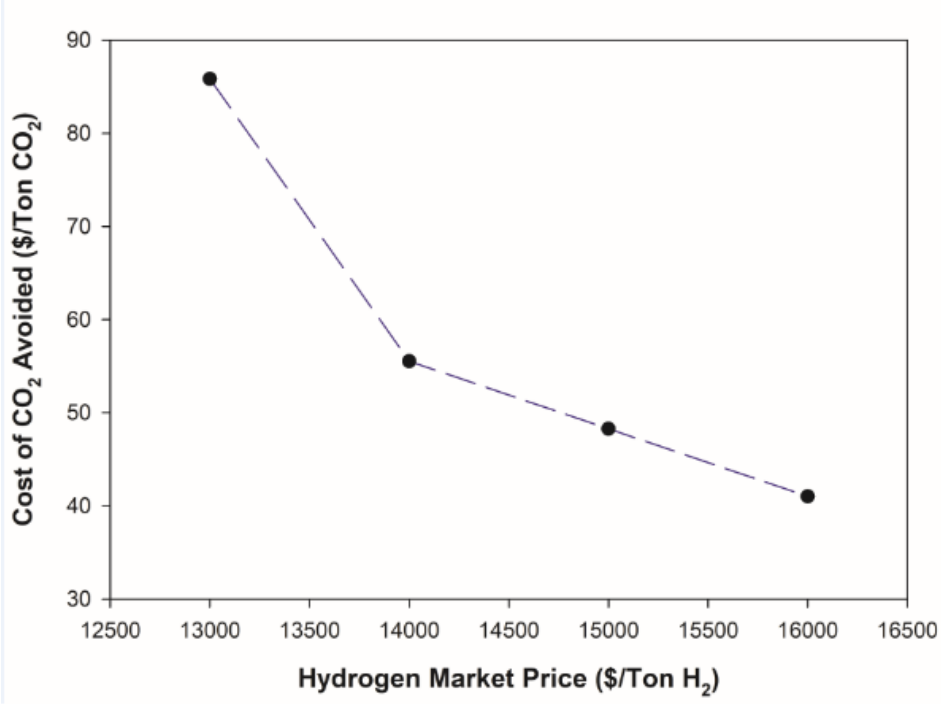

Figure 6.3. The relationship between the LCCA for the power plant and the hydrogen market price, with a hydrogen co-production system

6.3 The Effect of the Technical Specifications on the Energy Efficiency and Economics of the Plant

6.3.1 The Plant Capacity Factor

The maximum plant capacity factor (CF) for NGCC power plants had been established in the previous cases as 95%, since this type of plant requires less downtime for maintenance purposes compared to IGCC power plants operating with coal. This maximum value of the capacity factor was chosen based on previous studies on combined cycle power plants with carbon capture. These studies considered a capacity factor of 80–90% for IGCC power plants (Di Lorenzo et al., 2013), and 85–90% for NGCC power plants (Anantharaman et al., 2011). However, the effect of a number of capacity factor

values was studied to analyze the effect of the plant's operational capacity on the economic performance indicators.

For this study, with a PSA unit integrated into an NGCC power plant, a maximum capacity factor of 95% was chosen for the initial study because of the smaller size of the power plant compared to those in the other previous studies and because of the use of adsorption technology instead of amine scrubbing, which could reduce the downtime of the power plant. As a reference, a plant that operates at 100% capacity factor operates the whole year 24 hours per day.

The power plant capacity was reduced in stages to study the effect on the economic indicators, as electricity demand is likely to be flexible in future generations, and the electricity production from renewable sources would be integrated into the grid (Heuberger et al., 2017). Thus NGCC power plants may need to accept a higher turndown ratio in order to accommodate the fluctuations expected from renewable energy, e.g., wind and solar. The capacity factor of the power plant was studied in the range between the initial value of 95% to a value of 40%, based on the previous capacity given in combined cycle power plant studies (Alhajaj et al., 2016; Anantharaman et al., 2011; IEA-GHG, 2009). Table 6.6 relates the capacity factors (CF) applied to the reference power plant studied in Section 6.2 to the LCCA, LCOE and the ATPC of the power plant.

Table 6.6. The values on the economic performance indicators for plants with different capacity factor values

CF (%)	LCCA ($/tonne)	LCOE ($/MWh)	ATPC ($/year)
85	44.18	101.80	11,852,471.68
75	48.32	109.97	11,224,753.76
50	65.91	144.73	9,655,458.98
40	79.10	170.79	9,027,741.05

As shown in Table 6.6, overall, the value of the levelized cost of electricity and of carbon avoided decreases when the power plant operates at higher capacity. Operating the plant at higher capacity is desirable in terms of the economic performance indicator values. The LCOE increased by around 70% when the capacity factor of the plant decreased from 85% to 40%. Although the total annual product cost decreases with decreasing capacity factor values, the economic performance indicators of the LCCA and LCOE do not reflect this trend, as in the case of including hydrogen co-production (Section 6.2.3), because the earnings from electricity production were not included in the calculation of the LCCA and LCOE variables.

Figure 6.4 shows the capacity factors plotted against the LCCA results. The trend shows that operating the designed plant at a capacity of over 75% would obtain a reasonable value on the LCCA. At a capacity of 50%, the LCCA increases to 65.91 $/tonne, which is not very attractive for the implementation of the technology. Additionally, power plants without carbon capture can vary their capacity and be turned down more easily. Gas-fired power plants with carbon capture could vary their capacity faster compared to coal fired power plants, due to the fuel treatment and the processes before the gas turbine.

The LCCA value of 48.32 $/tonne CO_2 obtained for this case study when the plant operated at 75% capacity is similar to the value obtained by the study of the European Benchmarking Task Force. In this study an 830MW NGCC power plant with carbon capture showed a LCCA value of 48 $/tonne CO_2, but the capacity was fixed at 65% for the first year, and 85% for the rest of the years (Anantharaman et al., 2011). The LCCA of the NGCC power plant in this study was 44.18 $/tonne CO_2 captured when operating at 85% capacity, which is a promising result for the designed PSA technology when integrated into an NGCC power plant. Another study, by Hu et al. (2018), which integrated an MEA-based-amine scrubbing capture technology into an NGCC power plant, obtained an LCCA value of 70.39 $/tonne CO_2 operating at 85% constant capacity, which is around 25 $/tonne CO_2 higher than the value obtained in this study. The increase in the LCCA value in Hu et al. (2018) over that in the reference plant without carbon capture was mainly due to the inclusion of a boiler to recover the amine-based solvent.

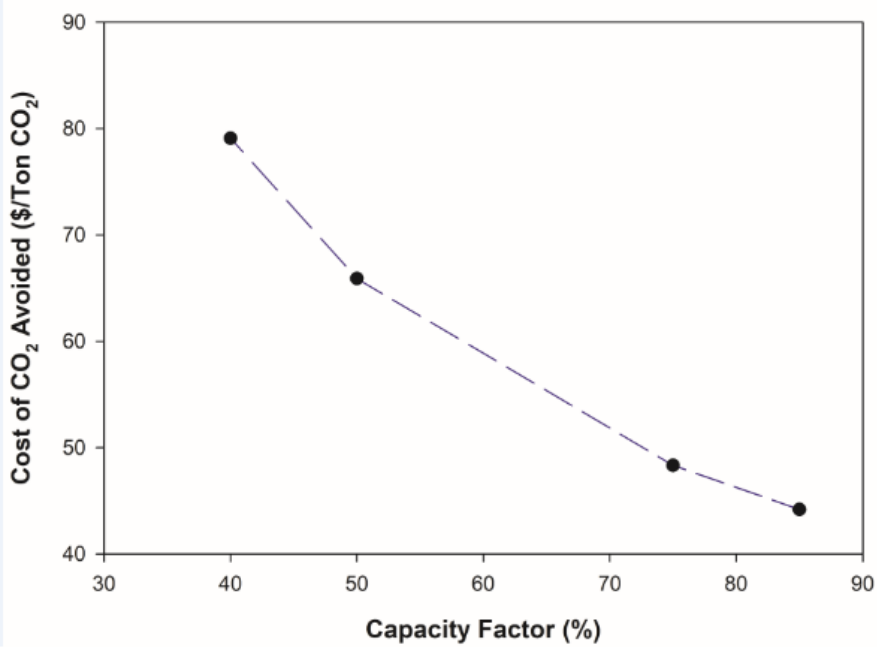

Figure 6.4. The relationship between the LCCA of the power plant and the operating capacity

6.3.2 Plant Life

The effect of the plant life on the economic performance indicators was studied for a range of 25 to 40 operating years. These values are based on previous studies with combined cycle power plants, where a plant life of 20 to 30 years is a common approach, e.g. Hu et al. (2018). The upper range of the sensitivity analysis was defined as the value of 40 years, since natural gas combined cycle power plants can reach this lifespan (Anantharaman et al., 2011). For this study, the operating life of the reference plant was assumed to be 30 years, due to the size and the conditions given in the plant. The plant life has an effect on the return on the capital investment of the plant and the interests, therefore it has an effect on the economic performance indicators of the power plant.

Table 6.7 relates the LCCA and LCOE to a set of values for the life of a plant designed with PSA. The plant life (PL) does not have as much effect as the operating capacity of the power plant. The LCCA of the power plant decreased from 40.61 to 38.17 $/tonne CO_2 when the power plant operation increased by 15 years, whereas the LCOE decreased from 94.71 to 89.96 $/MWh in that same lifespan. This is due to the distribution of the capital cost over the plant life, although the annual cost includes a yearly depreciation rate of 10% for the power plant equipment. Dividing the capital cost over 40 years produced a substantially lower annual cost than discounting the capital cost over 25 years.

In the study by Hu et al. (2018), which analyzed an MEA-solvent-based capture technology integrated into an NGCC power plant, a 30-year lifespan was considered and an LCCA value of 70.39 $/tonne CO_2 was obtained, whereas for the power plant in this study the LCCA was between 38 and 40 $/tonne CO_2. Therefore, the power plant in this study that integrated PSA showed a decrease in capture costs due to the lower compression costs and heat requirements compared to the MEA-solvent-based capture technology. This configuration yields an attractive LCCA value lower than 50 $/tonne CO_2. The lower LCCA of this study is due to lower additional capital costs of the power plant with the carbon capture unit, compared to the additional costs of the carbon capture unit in Hu et al. (2018).

However, the LCOE value of the power plant in Hu et al. (2018) was 80.11 $/MWh, which is around 10 to 15 $/MWh less than the LCOE value obtained in this study. The lower LCOE value of the plant is due to a lower capital cost of the reference plant in this study. The reference plant in Hu et al. (2018) included a gas turbine with a heat recovery system, but a syngas production unit was not required in the original design because the carbon dioxide was captured at post combustion conditions. However, this configuration

could not include co-production units, such as the one studied in Section 6.2.3, due to not having a syngas unit.

Table 6.7. The values on the cost performance indicators with different operating durations (PL) of the designed plant

PL (Years)	LCCA ($/tonne)	LCOE ($/MWh)
25	40.61	94.71
35	38.75	91.08
40	38.17	89.96

6.3.3 Economies of Scale

The effect of the economy of the scale on the power plant was studied using the operation of two GE-10 gas turbines in the designed power plant. Therefore, the capacity of the plant was doubled as in the case study that included hydrogen co-production, but in this case all the hydrogen produced in the PSA unit was directed to the two gas turbines. The aim of having two turbines in the power plant was to analyze whether the increased capacity of the plant and the production of electricity would improve the energy efficiency and the cost performance indicator values for the power plant that could capture carbon.

The capture performance was also studied in this case, as the size of the PSA unit was doubled. The PSA configurations studied for the power plant that had two gas turbines were the four-bed system without a rinse step and the six-bed with a rinse step. The first configuration had one pressure equalization step, while the second one had three pressure

equalization steps. These configurations were selected based on the results obtained for the performance indicators in Section 6.2.

Table 6.8 shows the energy efficiency values and the cost indicator values for the power plant that had two turbines and the PSA configurations featuring one pressure equalization step without a rinse step (PE1-No rinse) and three pressure equalization steps with a rinse (PE3-Rinse). Table 6.9 shows the carbon capture performance indicator values for the designed power plant with the stated PSA configurations.

Table 6.8. The energy efficiency penalty and economic performance indicator values for the plant with the operation of two gas turbines

PSA	EP (%)	LCCA ($/tonne)	LCOE ($/MWh)
PE1-No rinse	22.97	33.39	83.53
PE3-Rinse	24.70	35.50	85.02

Table 6.9. The values for the carbon capture performance indicators for the plant with the operation of two gas turbines

PSA	Recovery CO_2 (%)	Recovery H_2 (%)	Purity CO_2 (%)
PE1-No rinse	90.23	92.13	95.61
PE3-Rinse	90.12	94.76	98.15

The values in Tables 6.8 and 6.9 were compared to those obtained for the reference plant (Section 6.1), where various PSA configurations were analyzed. Table 6.8 shows that the efficiency penalty was almost constant for the configuration with one pressure equalization step, with a value of 22.97%, whereas this value was 22.88% for the

reference plant. However, the efficiency penalty decreased by around 2 percentage points compared to the penalty for the reference plant for the configuration with three pressure equalization steps and a rinse step, from a value of 26.42% to a value of 24.70%. Therefore, the decrease in the energy penalty was not significant when the plant capacity doubled.

The LCCA decreased by around 5 \$/tonne CO_2 for both configurations studied in this section, as shown in Table 6.8, compared to the reference plant where the LCCA values were 39.52 \$/tonne CO_2 with one pressure equalization step and 40.85 \$/tonne CO_2 with three pressure equalization steps. The LCOE of the plant also decreased for both configurations, by 9 and 8 \$/MWh, compared to the reference plant with LCOE values of 92.61 \$/MWh and 93.33 \$/MWh, respectively. The decrease in the cost indicator values can be explained by the smaller cost ratio between the reference plant and the plant with CCS, when operating at greater scale. The LCOE values obtained in this section are rather similar to those obtained by Hu et al. (2018), which were 86.35 \$/MWh without heat integration and 80.11 \$/MWh with heat integration in the power plant.

The overall decrease on the cost indicator values of the power plant explains why the combined cycle plants are built based on power capacities as high as 500 MW, which is the average generation capacity for NGCC power plants (U.S. Energy Information Administration, 2019). However, power plants are predicted to operate with varying capacities in the near future, and power plants with smaller capacities would have a cost advantage in adapting to the energy demand of the grid.

As shown in Table 6.9, the performance indicator values for carbon capture decreased slightly when the capacity of the plant doubled, but the decrease in the carbon dioxide

purity and recovery were of less than one percentage point. The hydrogen recovery values were of around 95% for the reference plant and they also decreased by around 3 percentage points when doubling plant capacity, as shown in Table 6.9. The hydrogen recovery was affected because the capacity of the PSA unit was doubled in order to operate the plant with two gas turbines. The change in the hydrogen recovery was not significant, but it could be a factor to take into account in plants with higher capacities.

6.4 The Effect of the Natural Gas price and the Carbon Tax on the Economics of the Plant

6.4.1 The Natural Gas Price

The effect of the natural gas price on the performance indicator values of the reference plant with one gas turbine was studied. When designing, the values on the variables studied in the previous section can be selected before the design and the construction of the power plant. However, the fluctuating market prices for the raw materials of the plant are external disturbances that cannot be neglected and they have an effect on the cost indicator values for the power plant. The fuel price has been regarded by the previous literature as one of the most influential variables on the LCOE of combined cycle power plants (Anantharaman et al., 2011).

For the analysis in this section, the PSA process with one pressure equalization step and without a rinse step was selected as the reference configuration. The other configurations with an increasing number of pressure equalization steps and with a rinse step would follow the same trend as in this analysis.

The natural gas prices selected for this sensitivity analysis were obtained based on the historical trends of the prices of this raw material, in a range between 10 and 50 $/MWh. The analyses in the previous sections considered the gas market value during the period when the analysis reported in this chapter was carried out (April 2020), so a value of 5.87 $/MWh, which is amongst the lowest values seen since 1987. The cost of natural gas has usually varied between 10 and 40 $/MWh. Table 6.10 presents the values on the cost performance indicators of the power plant for a range of natural gas market prices.

Table 6.10. The values on the economic performance indicators for the carbon capture plant for a number of natural gas market prices

NG Price ($/MWh)	LCCA ($/tonne)	LCOE ($/MWh)
10	45.33	113
20	59.38	161
30	73.44	209
40	87.49	257
50	101.54	305

The values in Table 6.10 show that the NG price had a greater effect on the cost indicator values than did the variables selected in previous sections, such as the capacity, plant life and the economies of scale. The LCOE of the power plant increased from 113 to 305 $/MWh when the market price of natural gas increased from 10 to 50 $/MWh. Figure 6.5 shows that the LCCA increased at a constant rate from a value of 45.33 to 101.54 $/tonne CO_2 in the natural gas price range selected.

The trend is that the LCCA is linearly related to the fuel cost. The fuel cost is a variable that is related to the operational costs and affects both the plants with and without carbon capture and is required to calculate the LCCA, as shown in Equation 3.38, Section 3.7.3. The variables analyzed in Section 6.2 affected the NGCC power plant that had a PSA unit, because they affected the design of the carbon capture plant. These were the design of the PSA process, the water gas shift reactor pressure and the design of the hydrogen co-production unit. The variables analyzed in Section 6.3, such as the capacity and the plant life, affected the operational costs and earnings of both the reference and the carbon capture plants. Therefore, the relationship of the LCCA to these variables was not linear.

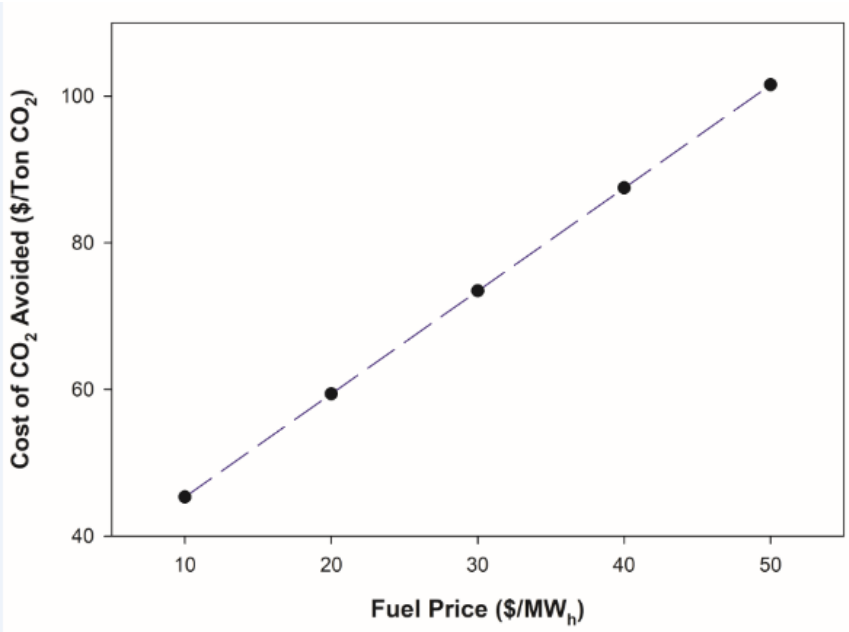

Figure 6.5. The relationship of the fuel price from the sensitivity analysis to the LCCA

6.4.2 The Carbon Tax

The previous sections of this study did not consider a carbon tax in costing the power plant. In this section, the carbon tax is introduced into the analysis; this is a penalty established by a governmental body on the profit of the power plant, calculated per carbon dioxide unit emitted into the atmosphere. The values selected for the carbon tax in this study were between 5 and 20 \$/tonne CO_2. The range of the carbon tax was selected based on previous studies and on the increasing carbon taxes that are expected from governments worldwide before 2050 (ICIS, 2019). Table 6.11 shows the values of the LCCA when including the carbon tax (CT) penalty for the reference plant without carbon capture and comparing it to the tax on the plant that had the PSA unit. The carbon tax had an effect on the LCCA of the power plant because a cost penalty would be applied to the reference power plant without the carbon capture unit, increasing the LCOE of the reference power plant. Therefore, the LCCA cost indicator would decrease, following Equation 3.38 (Section 3.7.3).

Table 6.11. Several carbon taxes and the corresponding costs of carbon dioxide avoided

CT (\$/tonne)	LCCA (\$/tonne)
5	34.53
10	29.52
20	19.52

The values in Table 6.11 show that if a carbon tax of 5 \$/tonne CO_2 is imposed, the LCCA of the power plant with the PSA unit without a rinse step (Table 6.1) decreases from 39.52

to 34.53 $/tonne CO_2. Additionally, if the carbon tax is increased further in the future to 20 $/tonne CO_2, the LCCA of the plant with capture would be reduced to 19.52 $/tonne CO_2. This analysis demonstrates the importance of including carbon tax regulations from governmental bodies before implementing zero emissions power plant in the near future.

The LCCA value obtained with the NGCC power plant in this study, including 5 $/tonne CO_2 carbon tax, is around 25 $/tonne CO_2: lower than the best scenario value obtained in the study by Hu et al. (2018) of 70.39 $/tonne CO_2. However, that study did not state whether a carbon tax was included. The study by Anantharaman et al. (2011) included a carbon tax and a sensitivity analysis was carried out for an NGCC power plant that integrated absorption technology, which gave a minimum value of LCCA of around 47 $/tonne CO_2. The comparison of the values shows that lower LCCA values were obtained in those studies that included the carbon tax.

6.5 Conclusions

A number of design choices were studied in an NGCC power plant using PSA in a carbon capture unit. A sensitivity analysis of the technical specifications of the plant and the external disturbances was carried out, in order to analyze the effect of the market prices on the cost indicators of the plant and choose optimal specifications for the plant. The indicators studied were the capture performance, energy efficiency, LCCA and LCOE of the plant.

The PSA configurations chosen for the study were the configurations with one, two and three pressure equalization steps, with and without a rinse, based on the capture performance using these configurations in Chapter 5. The PSA configurations with no

rinse step did not have an effect on the energy efficiency penalty of the plant, which was constant at a value of 22.88%. However, this indicator value decreased from 28.67% to 26.42% with the introduction of pressure equalization steps when there was a rinse step above 1 bar. The LCCA and LCOE of the plant varied by only by 1 percentage point over the range of the configurations chosen. The results for the energy efficiency penalty showed that the PSA configuration with three pressure equalization steps and a rinse step produced the best results, with a penalty of 26.42%. Additionally, when the WGS pressure decreased from 36.7 to 30 bar, the efficiency penalty for the configurations decreased by around 5 percentage points. Operation at WGS pressures below 30 bar did not produce promising results in terms of the capture performance: the carbon dioxide recovery was below 90% in this case. The addition of a hydrogen co-production unit increased the LCCA of the plant by 8 \$/tonne CO_2; this is a promising result if the market price for hydrogen is around 16000 \$/tonne H_2.

Varying the operating capacity of the power plant had a greater effect on the LCCA and LCOE of the plant with carbon capture, with increases of 35 \$/tonne CO_2 and 70 \$/MWh in the cost, respectively, when the capacity decreased from 85 to 40%. The plant life had a smaller effect on these indicators, with values around 2 \$/tonne CO_2 to 4 \$/MWh for the electricity produced, when changing the plant life by 15 years. Using a plant with double the capacity improved these indicator values by 5 \$/tonne CO_2 and 8 \$/MWh for the configurations studied, compared to those for the reference plant. The scale-up of the power plant yielded a promising output, but a pilot-scale implementation is necessary to verify the simulation results.

The fluctuations in the natural gas market price had the greatest effect on the cost indicator values of the plant: the LCCA and LCOE of the plant increased by 42 \$/tonne CO_2 and

145 $/MWh, respectively, when the natural gas price increased from 10 to 40 $/MWh. The inclusion of a carbon tax effectively decreased the LCCA in power plants to 29.52 $/tonne CO_2 when the penalty was 10 $ per tonne of emitted carbon dioxide, similar to previous studies where the introduction of a carbon tax reduced effectively the LCOE and LCCA values of the power plant with carbon capture Anantharaman et al. (2011). Therefore, the introduction and increase on the carbon tax prices would be determinant to ease the transition to power production with carbon capture.

CHAPTER 7 – CONCLUSIONS AND FUTURE WORK

7.1 Overall Conclusions

This project aimed to study the viability of pressure swing adsorption as a carbon capture technology in natural gas combined cycle power plants using simulation. The following indicators were used to assess the viability of PSA in the NGCC system:

- The carbon dioxide capture performance indicators. These were the purity and the recovery of the carbon dioxide and the hydrogen products obtained in the processes studied in this project. First, these indicators were used to study the viability of the process at laboratory scale with a validated model and to identify the process variables that had the biggest effect on the performance indicator values (Section 7.1.1). Second, the process was scaled up to pilot scale, so that the viability of PSA in the NGCC system could be estimated, based on the capture performance indicator values. Additionally, a number of PSA configurations were studied at this scale to improve performance by optimizing the performance indicator values (Section 7.1.2).
- The energy efficiency and the economic performance of the system. The energy efficiency was measured by estimating the energy penalty of the NGCC power plant when using PSA for pre-combustion carbon capture. The economic performance of the power plant was measured using the levelized cost of electricity (LCOE) and carbon avoided (LCCA) as economic indicators (Section 7.1.3).

7.1.1 The Model Validation and Laboratory-Scale PSA Process Performance

The axially-dispersed plug-flow model that simulated the PSA process was validated against experimental data obtained from a fixed-bed reactor adsorption process. The conditions given in the fixed-bed reactor experiments were applied in the simulations. The model was validated using experimental data obtained from adsorption processes that used TEPA- and MEA-MDEA-modified activated carbons. A maximum likelihood parameter estimation algorithm was used to fit the model to the experimental data by varying the mass transfer coefficient in each of the processes using the modified adsorbents. The model validation led to the following main conclusions:

- The axially-dispersed plug-flow model showed a good fit to the experimental data on amine-modified activated carbon by producing a sum of the squared residuals of less than 10 % in all parameter estimation cases.
- The value of the mass transfer coefficient obtained from the experiments with TEPA- modified activated carbons was 0.074 s^{-1}, which was greater than the value of 0.046 s^{-1} obtained in the experiments on MEA-MDEA activated carbon. Therefore, the experiments with the TEPA-modified activated carbons showed a steeper breakthrough curve.
- The MEA-MDEA-modified activated carbons showed a higher carbon dioxide capacity with a value of 10.6 mmol g^{-1}. Therefore, the isotherm and mass transfer coefficient parameters obtained with these adsorbents were used in the PSA simulations of this project.

Once the model was validated, a sensitivity analysis was carried out using the laboratory-scale PSA process variables. The sensitivity analysis enabled the estimation of the variable values that had the greatest effect on the capture performance parameters. The following main conclusions arose from these simulations:

- The purity of hydrogen achieved for all the sensitivity analyses was over 99%. The variations in the PSA process variable values had the greatest effect on the carbon dioxide purity, which achieved purities over 90% by increasing the carbon dioxide feed molar fractions from 0.4 to 0.5 and by decreasing the purge pressure. These results highlighted the need to increase the concentration of the feed carbon dioxide in the process steps above 1 bar and to study alternative PSA configurations to achieve purities over 95%.
- The recovery of the carbon dioxide and hydrogen products was not greatly affected by variations in the selected PSA process variable values, and the maximum deviation registered was of around 2%. The recovery of the products did not vary as much as the purity because the process steps were not modified. The importance of studying alternative process configurations to increase the recovery of the products to over 80% is highlighted.

7.1.2 Pilot-Scale PSA Process Performance

The validated laboratory-scale PSA model was scaled up to meet the flow rate requirements of the gas turbine in the NGCC power plant. After comparing the two models' carbon dioxide concentration at the outlet, the capture performance indicator values of the pilot-scale model were improved by varying a number of process variables

and changing the process configurations. The following conclusions were reached from this study:

- The laboratory and scaled-up PSA models yielded similar results on the capture performance indicators. The hydrogen purity and recovery remained constant from the laboratory to the scaled-up model, with values of 99.99% and 87.6%, respectively. The purity of carbon dioxide obtained with the scaled-up model was 86.4%, an increase by 2 percentage points on the laboratory value. The PSA process configuration used to compare the laboratory and scaled-up model included a carbon dioxide rinse step at 1 bar that proved to be essential to obtain carbon dioxide purities over 85%. The recovery of carbon dioxide was less than 85% for both cases; therefore, the study of alternative process conditions and configurations was required.
- The PSA process conditions studied in the pilot-scale PSA model were the gas velocity, the bed length and the feed flow rate in the process steps at a purge pressure of 1 bar. The purity of hydrogen remained constant within these case studies, with a value of 99.9%. The carbon dioxide purity improved to a value of 95.37% by increasing the superficial gas velocity to 0.048 m s^{-1}, increasing the bed length from 3.88 to 4.00 m and decreasing the purge-to-feed flow rate ratio to 0.22. The recovery of hydrogen and carbon dioxide obtained under these conditions was 92.27% and 90.11%, respectively.
- The PSA process configurations studied were the addition of an assisted purge step at 1 bar, pressure equalization steps and rinse steps over 1 bar. The introduction of the assisted purge step proved to be essential to increase the carbon dioxide purity to over 96% and the hydrogen recovery to 94.35%. The

experiments on configurations that included additional pressure equalization steps showed that the addition of pressure equalization steps most improved the hydrogen recovery, by 2 percentage points, whereas the performance parameter values for carbon dioxide varied by less than one percentage point. The use of rinse steps above 1 bar improved the carbon dioxide purity by 2 percentage points. This step required recycling carbon dioxide from 1 bar to higher pressures and, therefore, the need for a compressor. The economic analysis of these configurations in a power plant was required to take an overall decision about the optimum PSA cycle for carbon capture.

7.1.3 The Performance of the NGCC Power Plant and the PSA System

The performance of the NGCC and the PSA system was measured by estimating the energy penalty and the cost of the power plant, based on the cost of an NGCC power plant operating at the same capacity without carbon capture. For that purpose, the levelized cost of electricity (LCOE) and the carbon dioxide avoided (LCCA) economic indicators were calculated.

A number of design variations were made in the PSA cycle configuration, and water gas shift (WGS) pressure and hydrogen co-production were also studied. Alternative technical specifications, such as plant capacity, years of operation and economies of scale were studied to reduce the energy penalty and improve the values of the economic performance indicators for the plant. The effects of the fuel price and the carbon tax on the economics of the plant were studied, as these variables' values are likely to increase

in the next few decades. The following points summarize the main conclusions of this analysis:

- The LCCA and LCOE economic performance indicators varied by only one percentage point when the studied PSA configurations were modified. The PSA process with three pressure equalization steps and a rinse step produced the best results in terms of the energy penalty, with a value of 26.42%. The energy penalty of the plant with carbon capture decreased further by 5 percentage points when the WGS pressure decreased from the reference value of 36.7 bar to 30 bar. The WGS pressure did not show promising results at pressures below 30 bar, because the carbon dioxide recovery dropped below 90%.
- At hydrogen market prices as high as 16000 $/tonne, the inclusion of a hydrogen co-production unit showed promising results on the economic cost indicators. Specifically, the LCOE for the plant decreased from a reference plant value of around 91 to 88.91 $/MWh. These high hydrogen market prices are likely to arrive in the next few decades, when the demand for hydrogen is expected to grow considerably (Mac Dowell and Staffell, 2016).
- Plant capacity was the factor that had the greatest effect on the LCCA and LCOE indicators within the technical specifications of the plant. These indicators' values increased by 35 $/tonne CO_2 and 70 $/MWh, respectively, when the capacity decreased from 85 to 40%. The analysis of the economies of scale showed that a plant with the doubled capacity improved the cost indicator values by 5 $/tonne CO_2 and 8 $/MWh. Therefore, plants with higher capacities show promising results for the implementation of the NGCC and PSA system, but pilot-scale processing is necessary to verify the simulation results, following the technology

readiness level procedure shown in Abanades et al. (2015), and explained in Section 2.3.2.

- The sensitivity analysis with the natural gas prices and the carbon tax revealed that the natural gas price had the greatest effect on the cost indicator values amongst all the variables studied in this analysis. The LCCA and LCOE of the plant increased by 42 \$/tonne CO_2 and 145 \$/MWh, respectively, with an increase in the natural gas price from 10 to 40 \$/MWh. The introduction of a carbon tax into the analysis showed promising results, decreasing the LCCA of the plant from 39.52 to 29.52 \$/tonne CO_2, when the carbon tax was 10 \$/tonne CO_2 emitted. The proposed carbon tax values are likely to be realized in the next few decades to ease the introduction of sustainable energy policies and renewable energy development.

7.2 Future Prospects

This project demonstrated the potential of the NGCC power plant and PSA system for carbon capture, using the cycle configurations with an assisted purge step and three pressure equalization steps to improve the recovery of the hydrogen. These PSA cycle designs specifically optimize the carbon capture performance in an NGCC power plant under pre-combustion conditions.

The technology also looks promising under various future scenarios, such as under scenarios where there is an increase in the carbon tax and the hydrogen price. These future scenarios depend on the energy policies adopted in the next decade. Therefore, several

areas related to this project need further attention so as to implement the technology in the next few decades.

7.2.1 Advanced Adsorbent Materials

New adsorbent materials that demonstrate high capacity and stability under pre-combustion conditions are essential to improve the carbon capture performance and the cost of the PSA process for carbon capture. The amine-modified adsorbents in this study proved suitable for the process, but research on advanced adsorbents that demonstrate higher cyclic capacities and stability is essential to reduce the cost of the technology. This point is also stressed in the work by Abanades et al. (2015), which emphasizes the study of new sustainable materials and surface modifications for the development of adsorption technology applied to carbon capture.

7.2.2 Pilot-Scale Data Analysis

The NGCC and PSA system investigated in this work requires further validation with pilot-scale data, following the technology readiness level criteria described in Section 2.3.2. This work provides a preliminary assessment of the technology at pilot scale, from which variable values could be used as a guide for pilot-scale plant operation. The next step would be to obtain experimental data and optimize the process accordingly at that scale. The data analysis and model validation at that scale are essential before an industrial scale implementation, in order to identify plant operation issues such as heat

accumulation in the fixed-bed reactors and the degree of conversion of the water gas shift reactors.

7.2.3 The Outlook for a Future Energy System

The future energy network and policy areas require extensive research in order to judge which carbon capture technologies deserve further research on the process materials and engineering sides. This study has shown that external disturbances, such as market prices, have the greatest effects on the economics of the plants with CCS, in line with what previous studies have shown (International Energy Agency, 2019a).

At present, the NGCC and PSA system studied in this work offers a promising outcome, due to predictions based on a hydrogen-based economy scenario, such as the one published by the International Energy Agency (2020). However, the introduction of new and more efficient energy storage batteries for renewable energy technologies would decrease the amount of power production from fossil fuels by prioritizing cleaner technologies in the future. Additionally, the evolution of the carbon tax will be decisive for the implementation of technologies that produce zero carbon dioxide emissions. This tax depends mainly on the energy policies adopted in the next decade.

All these factors would have an effect on the economics and technical specifications of the carbon capture plants, which depend highly on plant location. Therefore, development of energy policies and simulation models that predict efficient local energy systems would be a key area of research in the next few decades.

APPENDIX A – CALCULATION OF THE COMPRESSIBILITY FACTOR

The Soave-Redlich-Kwong (SRK) equation of state was used to calculate the compressibility factor for this system. This equation of state was selected due to its suitability demonstrated in the study by Moon et al. (2018), where a PSA model was developed in gPROMS® for a system similar to the one developed in this study, which operated with an adsorption pressure and a temperature of 35 bar and 308.15 K, respectively. Equation A.1 shows the overall expression of the SRK EOS, a derivation of the equation developed by Redlich and Kwong (1949). Equation A.2 enabled the calculation of the compressibility factor value from this EOS (Soave, 1972).

$$P = \frac{RT}{V_m - b} - \frac{a\propto}{V_m(V_m + b)} \tag{A.1}$$

$$Z = \frac{1}{1-h} - \frac{{A_T}^2}{B_T} \tag{A.2}$$

Equations A.3 to A.9 were used to calculate the variable values used in Equation A.2, for the calculation of the compressibility factor.

$$a = 0.42747 \frac{R^2 T_c^2}{P_c} \tag{A.3}$$

$$b = 0.08664 \frac{RT_c}{P_c} \tag{A.4}$$

$$\propto = \left[1 + (0.48508 + 1.55171\omega - 0.17613\omega^2)\left(1 - \sqrt{T_r}\right)\right]^2 \tag{A.5}$$

$$T_r = \frac{T}{T_c} \tag{A.6}$$

$$A^2 = \frac{a}{R^2 T^{5/2}} \quad \text{(A.7)}$$

$$\text{B} = \frac{b}{RT} \quad \text{(A.8)}$$

$$\text{h} = \frac{b_T}{V_m} \quad \text{(A.9)}$$

The variables A_T, B_T, and b_T (used in Equation A.9) were calculated by Equations A.10 to A.12. These variables are used to calculate the compressibility factor values of gas mixtures.

$$A_T = \sum_i^n Y_i A_i \quad \text{(A.10)}$$

$$B_T = \sum_i^n Y_i B_i \quad \text{(A.11)}$$

$$b_T = \sum_i^n Y_i b_i \quad \text{(A.12)}$$

Table A.1 shows the values of the variables used in the calculation of the compressibility factor values and the result for the compressibility factor obtained for the conditions given in this study. Table A.2 shows the definition of the nomenclature used in Appendix A.

Table A.1. The carbon dioxide and hydrogen values for the variables used to calculate the compressibility factor

	Carbon dioxide	Hydrogen
Tc (K)	304.1	33.2
P_c (bar)	73.8	13.03
T (K)	298.15	298.15
P (bar)	25	25
Y_i	0.4	0.6
V_m (m^3)	$0.908x10^{-3}$	
Z	0.91	

Table A.2. Definitions of the nomenclature used in Appendix A

A, a	SRK constants that correct for the attractive potential of molecules for each component in the mixture
A_T	An SRK constant that corrects for the attractive potential of molecules of the mixture
B, b	SRK constants that correct for the volume for each component in the mixture
B_T	An SRK constant that corrects for volume of the mixture
h	An SRK constant
T	Temperature
T_c	Critical temperature
T_r	Relative temperature
P	Pressure
P_c	Critical pressure
R	Gas constant
V_m	The molar volume of the gas mixture
Y	The molar fraction of the component in the gas phase
Z	The compressibility factor
$\propto$	An SRK constant
ω	Acentric factor

APPENDIX B – THE DEVELOPMENT OF THE COMPONENT MASS BALANCE

The following procedure was used to obtain the component mass balance based on these variables. On the one hand, the carbon dioxide and hydrogen components' concentrations were calculated using the following equation:

$$C_i = C\ Y_i \tag{B.1}$$

Equation B.1 was replaced in the component mass balance equation (B.2), to give Equation B.3. Then, Equation B.3 was further developed to give Equation B.4.

$$\varepsilon_t \frac{\partial C_i(i,z)}{\partial t} = -\varepsilon_b \frac{\partial\left(C_i(i,z)v(z)\right)}{\partial z} + \varepsilon_b D_x \frac{\partial^2 C_i(i,z)}{\partial z^2} - (1-\varepsilon_b)\frac{\partial Q(i,z)}{\partial t} \tag{B.2}$$

$$\varepsilon_t \frac{\partial (C(z)Y(i,z))}{\partial t} = -\varepsilon_b \frac{\partial\left(C(z)Y(i,z)v(z)\right)}{\partial z} + \varepsilon_b D_x \frac{\partial^2\left(C(z)Y(i,z)\right)}{\partial z^2} - (1-\varepsilon_b)\frac{\partial Q(i,z)}{\partial t} \tag{B.3}$$

$$\varepsilon_t \left(Y(i,z)\frac{\partial C(z)}{\partial t} + C(z)\frac{\partial Y(i,z)}{\partial t}\right) = -\varepsilon_b \left(Y(i,z)\frac{\partial\left(C(z)v(z)\right)}{\partial z} + C(z)v(z)\frac{\partial Y(i,z)}{\partial z}\right) + \varepsilon_b D_x \left(Y(i,z)\frac{\partial^2 C(z)}{\partial z} + C(z)\frac{\partial^2 Y(i,z)}{\partial z} + 2\frac{\partial C(z)}{\partial z}\frac{\partial Y(i,z)}{\partial z}\right) - (1-\varepsilon_b)\frac{\partial Q(i,z)}{\partial t} \tag{B.4}$$

On the other hand, the overall mass balance was expressed using Equation B.5. This equation was multiplied by the component fraction ($Y_{(i,z)}$) to give Equation B.6.

$$\varepsilon_t \frac{\partial C(z)}{\partial t} = -\varepsilon_b \frac{\partial\left(C(z)v(z)\right)}{\partial z} + \varepsilon_b D_x \frac{\partial^2 C(z)}{\partial z^2} - (1-\varepsilon_b)\sum_{i=1}^{N_{comp}} \frac{\partial Q(i,z)}{\partial t} \tag{B.5}$$

$$\varepsilon_t Y(i,z)\frac{\partial C(z)}{\partial t} = -\varepsilon_b Y(i,z)\frac{\partial\left(C(z)v(z)\right)}{\partial z} + \varepsilon_b D_x Y(i,z)\frac{\partial^2 C(z)}{\partial z^2}$$

$$-(1-\ \varepsilon_b)\ Y(i,z)\sum_{i=1}^{N_{comp}}\frac{\partial Q(i,z)}{\partial t} \qquad \text{(B.6)}$$

Then, some terms of Equation B.4 were cancelled out using Equations B.4 to B.6, to give Equation B.7. Then this equation was divided by the overall concentration $(C(z))$ to give the component mass balance (Equation B.8), which appears as Equation 3.2, Section 3.3.2.

$$\varepsilon_t\ C(z)\frac{\partial Y(i,z)}{\partial t} = -\varepsilon_b C(z)v(z)\frac{\partial Y(i,z)}{\partial z} +\ \ \varepsilon_b D_x\left(C(z)\frac{\partial^2 Y(i,z)}{\partial z} + 2\frac{\partial C(z)}{\partial z}\frac{\partial Y(i,z)}{\partial z}\right)$$

$$-\ (1-\varepsilon_b)\left(\frac{\partial Q(i,z)}{\partial t} - Y(i,z)\sum_{i=1}^{N_{comp}}\frac{\partial Q(i,z)}{\partial t}\right) \qquad \text{(B.7)}$$

$$\varepsilon_t\ \frac{\partial Y(i,z)}{\partial t} = -\varepsilon_b v(z)\frac{\partial Y(i,z)}{\partial z} +\ \ \varepsilon_b D_x\left(\frac{\partial^2 Y(i,z)}{\partial z} + \frac{2}{C(z)}\frac{\partial C(z)}{\partial z}\frac{\partial Y(i,z)}{\partial z}\right)$$

$$-(1-\varepsilon_b)\left(\frac{\partial Q(i,z)}{\partial t} - Y(i,z)\sum_{i=1}^{N_{comp}}\frac{\partial Q(i,z)}{\partial t}\right) \qquad \text{(B.8)}$$

APPENDIX C – PSA PROCESS CODING IN GPROMS®

The pressure swing adsorption process explained in the Methodology chapter (Chapter 3) was developed and simulated in gPROMS® ProcessBuilder, in the *Custom modelling* section. The computational work was divided into the *Model* and *Task* domains, and then it was simulated in the *Process* domain, which gathered all the variables, equations and time-based tasks of the simulation. The *Model* domain enabled the definition of the variable types and the equations of the process. The *Task* domain enabled the initialization, schedule and finalization of the process.

Section C.1 includes the axially-dispersed plug-flow model that describes the process inside the fixed-bed reactor (C.1.1) and the dispersion model surrounding the system (C.1.2). Section C.2 shows the *Task* section simulating the laboratory-based PSA model explained in Chapter 3.

C.1 The Model Domain Coding

C.1.1 The Axially-Dispersed Plug-Flow Model

```
PARAMETER
# Number of components
   N_comp  AS INTEGER
# Bed Properties
   Bed_length  AS REAL
   Bed_diameter AS REAL
   Bed_area AS REAL
   Bed_density AS REAL
   wall_th AS REAL
   Bed_in_diameter AS REAL
   Bed_cross AS REAL
   Cpw AS REAL
```

```
    Wall_density AS REAL  #Stainless_Steel
 #Diffusion parameters
    M_mass  AS ARRAY(N_comp) OF REAL
    M_AB AS REAL
   Diff_vol AS ARRAY(N_comp) OF REAL
   Takahashi_f  AS REAL
 # Ideal gas constant and Pi
    R AS REAL
    Pi AS REAL
# Isotherm Parameters
   q1 AS ARRAY(N_comp) OF REAL
   B1 AS ARRAY(N_comp) OF REAL
#Phisical properties package
   Multiflash   AS FOREIGN_OBJECT
#Tortuosity
   Tortuosity AS REAL
#Atmospheric pressure
   P_atm AS REAL
# Heat transfer coefficients
    Cps AS REAL
    dH AS ARRAY(N_comp) OF REAL
    Tw_in AS REAL
    HeatTranStag AS REAL
    alphaw AS REAL
# Flow control Parameters
    P_ads AS REAL
    Feed_ads AS REAL
    Feed_blow1 AS REAL
    Feed_purge AS REAL
    End_blow_mol AS REAL
    Y_ads AS ARRAY(N_comp) OF REAL
    Y_purge AS ARRAY(N_comp) OF REAL
    Ads_t AS REAL
    Purge_t AS REAL
    Blow_t AS REAL
    Depress_rate_int AS REAL
    Reflow_rate_int AS REAL
    Deflow_rate_int AS REAL
    Error_prop AS REAL
    Error_int AS REAL

DISTRIBUTION_DOMAIN
    L AS [ 0 : Bed_length ]
    LP AS [ 0 : Bed_length ]

VARIABLE
#Bed/Particle variables
   Bed_void AS No_Type
   Particle_D AS No_Type
   Particle_void AS No_Type
```

```
  Total_void  AS No_Type
# Assigned Variables
# Feed conditions
   P_feed AS Pressure
   T_feed AS Temperature
   Y_feed AS ARRAY(N_comp) OF MoleFraction
   Q_vol  AS Volumetric_Flowrate
   Feed_norm AS Volumetric_Flowrate
   Y_inert AS ARRAY(N_comp) OF MoleFraction
#Calculated variables
   # Mole fraction
   Y AS DISTRIBUTION(N_comp,L) OF MoleFraction
   Y_out AS MoleFraction
   # Solid phase concentrations
   Q AS DISTRIBUTION(N_comp,L) OF Solid_Concentration
   # Equilibrium solid phase concentrations
   Qeq AS DISTRIBUTION(N_comp,L) OF Solid_Concentration
   # Superficial gas velocity
   v AS DISTRIBUTION(L) OF Velocity
   # Pressure
   P AS DISTRIBUTION(LP) OF Pressure
   # Temperature
   T AS DISTRIBUTION(L) OF Temperature
   # Concentration
   C  AS DISTRIBUTION(L) OF No_Type
   Ci AS DISTRIBUTION(N_comp,L) OF No_Type
   Flow AS DISTRIBUTION(L) OF Volumetric_Flowrate
#Heat transfer coefficient calculation and wall temperature
  Pr AS No_Type
  Landa AS No_Type
  Hi AS No_Type
  Tw AS DISTRIBUTION(L) OF  Temperature
# Dispersion and mass transfer coefficient calculation
   Dispersion AS No_Type
   Dm AS Diffusivity
   Dm_phigh AS Diffusivity
   Dm_eff AS Diffusivity
   Re AS No_Type
   Sc AS No_Type
   Pe AS No_Type
   k AS ARRAY(N_Comp) OF Mass_Coefficient_gML
# Isotherm variables
   qeq AS DISTRIBUTION(N_comp,L) OF Solid_Concentration
#Flow change
   Depress_rate AS No_Type
   Reflow_rate AS No_Type
   Deflow_rate AS No_Type
   Error AS No_Type
   End_mol AS Volumetric_Flowrate
```

```
BOUNDARY #boundary conditions
# At l=0
#Component mole fraction
        For i := 1 to N_comp DO
          -Dispersion *PARTIAL(Y(i,0),L) = v(0) * (Y_feed(i) - Y(i,0)) ;
         END
         #Velocity
          v(0) =( Q_vol / Bed_area / Bed_void)
         #Temperature
         -Landa*PARTIAL(T(0),L)=Multiflash.VapourDensity(T_feed,P_feed,Y_feed)*
Multiflash.VapourHeatCapacity(T_feed,P_feed, Y_feed) /1000 * v(0) * (T_feed - T(0)) ;
 # At l=L the end of the bed
         #Temperature
          PARTIAL(T(Bed_length), L) = 0  ;
         #Component concentration
          PARTIAL(Ci(,Bed_length),L) = 0 ;
         #Velocity
          PARTIAL(v(Bed_length),L)  = 0  ;
        #Pressure
         P(Bed_length)=P_feed;

EQUATION
   # Normalised Flowrate/ flowrate
   Q_vol = Feed_norm*(1e5*T_feed/(P_feed*273))/1e6/60 ;
    Flow(Bed_length) = End_mol ;
   # Total voidage fraction
   Total_void = Bed_void + Particle_void *(1- Bed_void) ;
  # Overall mass balance
   FOR z := 0|+ TO Bed_length|- DO
     Total_void*$C(z)=Bed_void*Dispersion*PARTIAL(C(z),L,L)-Bed_void*
     PARTIAL(v(z)*C(z),L)  -(1-Total_void)* SIGMA($Q(,z)) ;
    End
  # Component mass balance
   FOR i := 1 TO N_comp DO
      FOR z := 0|+ TO Bed_length|- DO
          C(z)* Total_void*$Y(i,z) = -C(z)*Bed_void*v(z)*PARTIAL(Y(i,z), L)
          + Bed_void* Dispersion  * ( C(z)*PARTIAL(Y(i,z),L , L) + 2 * PARTIAL(Y(i,z),L) *
           PARTIAL(C(z), L)-(1-Total_void)*  ($Q(i,z) - Y(i,z) * SIGMA($Q(,z))
      END
   END
 #Ideal gas equation
   FOR z := 0 TO Bed_length DO
    P(z) = C(z) * R * T(z) ;
    END
 #Component concentration
   FOR i := 1 TO N_comp DO
      FOR z := 0 TO Bed_length DO
         Ci(i,z)=C(z)*Y(i,z) ;
      END
   END
```

```
 # Adsorption rate equation
 FOR i := 1 TO N_comp DO
    FOR z := 0 TO Bed_length DO
       $Q(i,z) = k(i) * ( (qeq(i,z)) - Q(i,z) ) ;
    END
 END

 # Langmuir Isotherm
 FOR z := 0 TO Bed_length DO
    FOR i := 1 TO N_comp DO
   qeq(i,z)*(1 + SIGMA(b1()*P(z)*Y(,z)))= Bed_density* (q1(i)*b1(i)*P(z)*Y(i,z))  ;
    END
 END
 # Ergun Equation
 FOR z:= 0 TO Bed_length|-  DO
 -PARTIAL(P(z),LP)=(150*Multiflash.VapourViscosity(T(z),P(z),Y(,z))*
 (((1-Total_void)^2)/((Particle_D^2)*(Total_void^3)))*v(z))+((1.75/Particle_D)*
 ((1-Total_void)/(Total_void^3))*v(z)*ABS(v(z)* Multiflash.VapourDensity(T(z), P(z), Y(,z))));
 END
 # Volumetric Flowrate calculation inside the bed
 FOR z := 0 TO Bed_length DO
    Flow(z) = Bed_area * v(z) ;
 END
#Diffusion and Dispersion
((P(0)/101325)* (M_AB^0.5)*(((Diff_vol(1)^(1/3))+(Diff_vol(2)^(1/3)))^2))* (1000*Dm)=
 0.00143*  (T(0)^1.75);
#Takahashi correction for high pressures (only for high pressures)
P(0)* Dm_phigh= Dm*1e5* Takahashi_f; #P_atm=1e5
 #Effective diffusivity (Advanced thermodinamics for engineers, 1997)
 Tortuosity* Dm_eff= Dm_phigh*Total_void;
 #Via Wakao and Funazkri
 #Dispersion=(Dm_phigh(0)*(20+(0.5*Sc(0)*Re(0))))/ Bed_void;
 #Adimensional numbers
  #Reynolds
   Multiflash.VapourViscosity(T_feed,P_feed,Y(,0))*Re=
   ABS(Multiflash.VapourDensity(T_feed,P_feed,Y(,0)) *ABS( v(0)) *Particle_D) ;
  #Schmidt
  Dm_eff*Multiflash.VapourDensity(T_feed,P_feed,Y(,0))*Sc=
  ABS(Multiflash.VapourViscosity(T_feed,P_feed,Y(,0)))  ;
  #Peclet
  (0.328*(1+0.59)+3.33*((Re*Sc)^2))*Pe =Re *Sc *(1+0.59);
  #Prandtl
   Multiflash.VapourThermalConductivity(T_feed,P_feed,Y(,0))*Pr=
   Multiflash.VapourHeatCapacity(T_feed,P_feed,Y(,0))*
   Multiflash.VapourViscosity(T_feed,P_feed,Y(,0));
 # HT , Wakao & Funazkry
   Hi = HeatTranStag + alphaw * Multiflash.VapourHeatCapacity(T_feed,P_feed,Y(,0))/1000*
    Multiflash.VapourDensity(T_feed,P_feed,Y(,0)) * v(0) ;
  #Axial thermal dispersion coefficient
    Landa = Multiflash.VapourThermalConductivity(T_feed,P_feed,Y(,0))*(7+0.5*Pr*Re)/1000;
```

```
   # Non-IsothermalGas phase energy balance
    FOR z := 0|+ TO Bed_length|- DO
     (Total_void*Multiflash.VapourDensity(T(z),P(z),Y(,z))*
     Multiflash.VapourHeatCapacity(T(z),P(z),Y(,z))/1000 + Bed_density * Cps) * $T(z) +
     Multiflash.VapourDensity(T(z),P(z),Y(,z)) * Multiflash.VapourHeatCapacity(T(z),P(z),Y(,z))/1000
    * PARTIAL(T(z) *v(z),L) - Landa * PARTIAL(T(z),L,L)-(1-Total_void)*SIGMA(dH()*$Q(,z))
    +4 * Hi / Bed_diameter * (T(z) - Tw(z))=0 ;
 END
 #Outlet component fractions
 Y_out= Y(2,Bed_length);
```

C.1.2 The Model of Dispersion around the Fixed-Bed Reactor

```
PARAMETER
# Number of components
  N_comp AS INTEGER
 # Pipe dimensions
   Pipe_length AS REAL
   Pipe_D AS REAL
   Pipe_area AS REAL
 # Ideal gas constant and Pi
   R AS REAL
   Pi AS REAL

DISTRIBUTION_DOMAIN
   L AS [ 0 : Pipe_length ]

VARIABLE
   # Mole Fractions
   Y AS DISTRIBUTION(N_comp,L) OF MoleFraction
   Y_outp AS DISTRIBUTION(N_comp) OF No_Type
   # Gas velocity
   v AS DISTRIBUTION(L) OF Velocity
   # Volumetric Flow
   Q AS DISTRIBUTION(L) OF Volumetric_Flowrate
   # Pressure
   P AS DISTRIBUTION(L) OF Pressure
   # Temperature
   T AS DISTRIBUTION(L) OF Temperature
   # Feed conditions
   P_feed AS Pressure
   T_feed AS Temperature
   Y_feed AS ARRAY(N_comp) OF No_Type
   v_inlet AS Velocity
   # Dispersion Coefficient
   Dispersion AS Diffusivity

EQUATION
```

```
# Boundary conditions
#l=0 System inlet
FOR i := 1 TO N_comp DO
   Y(i,0) = Y_feed(i) ;
END # For
P(0) = P_feed ;
T(0) = T_feed ;
v(0) = v_inlet ;
# At l=L System Exit
PARTIAL(y(,Pipe_length),L) = 0 ;
PARTIAL(v(Pipe_length),L) = 0 ;
# Component mass balance
FOR i := 1 TO N_comp DO
   FOR z := 0|+ TO Pipe_length|- DO
      $Y(i,z) = -v(z) * PARTIAL(Y(i,z) , L)
      + Dispersion * PARTIAL(Y(i,z) , L , L);
   END
END
# Overall mass balance
FOR z := 0|+ TO Pipe_length|- DO
   PARTIAL(v(z) , L) = 0 ;
END

# Outlet mole fraction
FOR i := 1 to N_comp DO
   Y(i,Pipe_length) = Y_outp(i) ;
END
#Temperature and Pressure
FOR z := 0|+ TO Pipe_length DO
   T(z) = T_feed ;
   P(z) = P_feed ;
END
# Volumetric Flow
FOR z := 0 TO Pipe_length DO
   Q(z) = v(z) * Pipe_area  ;
END
```

C.2 The Task Domain Coding of the Laboratory-Scale PSA Model with One Pressure Equalization Step

```
SEQUENCE

   CONTINUE FOR 300
   SWITCH
      Bed.Mode := Bed.Deflow ;
   END
```

```
    CONTINUE UNTIL Bed.Feed_norm <= Bed.Feed_blow1
    REASSIGN
         Bed.Y_feed:= Bed.Y_rinse;
     END
     SWITCH
       Bed.Mode := Bed.BD;
      END
      REASSIGN
        Bed.Stage:= 2;
      END
      CONTINUE UNTIL Bed.P_feed<= Bed.P_low
       END
SEQUENCE
REASSIGN
        Bed.Stage:= 3;
 END
SWITCH
         Bed.Mode := Bed.Reflow ;
END
       CONTINUE UNTIL Bed.Feed_norm >= Bed.Feed_ads
SWITCH
         Bed.Mode := Bed.Purge ;
 END
       CONTINUE FOR 250
SEQUENCE
       REASSIGN
          Bed.Stage:= 4;
          Bed.Y_feed:= Bed.Y_purge;
       END
CONTINUE FOR 50
REASSIGN
        Bed.Stage:= 5;
END
SWITCH
         Bed.Mode := Bed.Press ;
END
CONTINUE UNTIL Bed.P_feed >= Bed.P_ads
 END
 REASSIGN
       Bed.Y_feed:= Bed.Y_ads;
 END
 SWITCH
       Bed.Mode := Bed.Ads ;
END
```

APPENDIX D – THE DATA FOR THE NGCC POWER PLANT DESIGN

The design of the NGCC power plant was divided into three tasks: (i) the design of the process upstream of the PSA unit, which was done using flowsheet modelling in gPROMS® ProcessBuilder, (ii) the PSA process design, using the custom modelling capability in gPROMS® ProcessBuilder, and (iii) the gas turbine selection downstream of the PSA unit, which was based on the hydrogen purity obtained from the PSA process, which was up to 99%.

Section D.1 of this appendix presents the technical specifications of the NGCC power plant, based on the study by the International Energy Agency Greenhouse Gas R&D Programme (IEA-GHG, 2009), which established a framework for assessing carbon capture technologies in coal and gas-fired power plants. Section D.2 presents the process data obtained from gPROMS® ProcessBuilder for the steam methane reforming and water gas shift reactor units. Section D.3 shows the manufacturer's specifications for the GE-10 gas turbine.

D.1 Power Plant Technical Data

Table D.1. The power plant location, ambient conditions, raw material and cooling water delivery data (IEA-GHG, 2009)

Location	
Country	Netherlands
Plant site	Coastal
Site conditions	Clear, level, no special civil works
Seismic risk	Negligible
Ambient conditions	
Average temperature (K)	282.15
Maximum Temperature (K)	303.15
Minimum Temperature (K)	263.15
Average Humidity (%)	60
Average Pressure (bar)	1
Raw material delivery and process cooling water	
Natural gas delivery	Pipeline
Cooling type	Once-through sea water cooling
Sea water inlet temperature (K)	285.15

Table D.2. Natural gas composition and technical data (IEA-GHG, 2009)

Composition (%)	
Methane	89
Ethane	7
Propane	1
Butane	0.1
Pentane	0.01
Carbon dioxide	2
Nitrogen	0.89
Pressure (bar)	
Pipeline	70
Heating value (MJ/kg)	
High (HHV)	303.15
Low (LHV)	263.15

D.2 Process Data for the Steam Methane Reformer and Water Gas Shift Reactors

Table D.3. Steam Methane Reformer (SMR) flowsheet simulation and design data

Inlet stream	
Natural gas molar flowrate (mol/s)	114.44
Steam to methane ratio (mol/mol)	2.7
Temperature (K)	1073.15
Pressure (bar)	27
Operation	
Temperature (K)	1173.15
Pressure (bar)	27
Methane molar conversion (%)	90
Design	
Diameter (m)	0.1
Length (m)	10
Number of channels	49
Superficial velocity of gas (m/s)	0.04
Outlet stream composition (mol/mol)	
Hydrogen	0.62
Steam	0.2
Carbon dioxide	0.08
Carbon monoxide	0.2

Table D.4. The flowsheet simulation and design data for the water gas shift reactors

From the inlet stream to the high temperature shift (HTS) reactor	
Syngas gas molar flow rate (mol/s)	594.6
Steam to methane ratio (mol/mol)	2.5
Temperature (K)	753.77
Pressure (bar)	36.7
From the inlet stream to the low temperature shift (LTS) reactor	
Temperature (K)	473.15
Pressure (bar)	36.7
Design	
Diameter (m)	2.38
Length (m)	4.76
Superficial velocity of gas (m/s)	0.04
Outlet stream conditions	
Temperature (K)	503.2
Pressure (bar)	36.7
Outlet stream composition (mol/mol)	
Hydrogen	0.58
Carbon dioxide	0.41
Carbon monoxide	0.01

D.3 The Manufacturer's Technical Data on the Gas Turbine

Table D.5. GE-10 gas turbine technical data provided by the manufacturer (Goldmeer, 2018)

Model: GE-10 single shaft gas turbine	
Power output (Mwe)	11.25
Value ($)	5,500,000 (includes all components)
Dimensions	
Length (m)	9
Width (m)	2.5
Height (m)	6
Weight (kg)	34,000
Performance	
Pressure ratio	15.5:1
Turbine speed (rpm)	11000
Exhaust gas flowrate (kg/s)	47.5
Exhaust gas temperature (K)	763.15
Efficiency (%)	32
Components	
Inlet module	Includes an air filter, silencer and a ventilation system
Compressor	An eleven-stage axial flow compressor
Combustion chamber	A single-slot cooled combustion chamber, designed for low nitrogen oxide emissions
Turbine/expander	Three reaction stages, with the first two stages cooled down
Exhaust module	Includes a silencer

APPENDIX E – PINCH ANALYSIS

The pinch analysis for the heat integration of the power plant was carried out following the procedure described in Kemp (2011). In order to estimate the heating requirements of the power plant, the hot and cold streams of the power plant were identified, based on the cooling and heating requirements of each and their operational temperature range.

Figure E.1 shows the streams where the A to F heat exchangers were placed in the power plant. These heat exchangers enabled the heat integration of the power plant. The heat exchangers A and B were used to heat the natural gas (NG) and steam entering the steam methane reformer (SMR), and C was used to provide heat in the SMR reaction. The heat exchangers D and E were used for cooling the syngas, before it entered the higher temperature shift (HTS) and the lower temperature shift (LTS) reactors, respectively. Heat exchanger F was used to recover the heat from the exhaust gas of the gas turbine (GT).

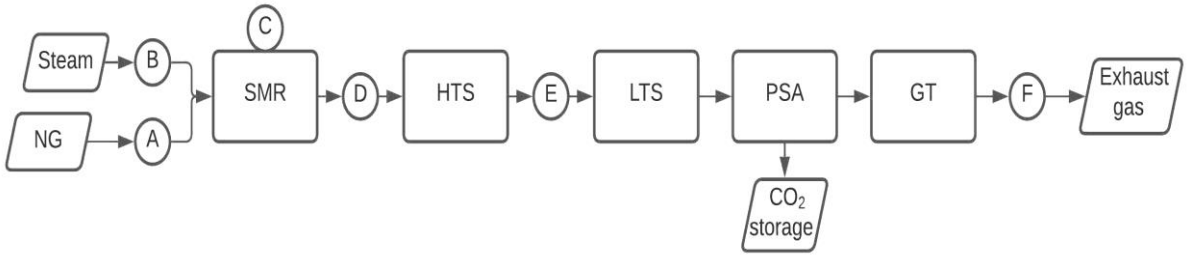

Figure E.1. Heat exchangers placement for heat integration in the NGCC power plant

The heat exchangers shown in Figure E.1 were used to provide heating or cooling to the cold and hot streams, respectively, shown in Table E.1. The flow rates of the streams, the initial and target temperatures, and the heat duty calculated by process simulation in gPROMS® ProcessBuilder are shown in this table. The heat duty values of the hot streams were negative due to heat release.

Table E.1. The hot and cold streams used for heat integration in the NGCC power plant

Heat exchanger	Stream type	Mass flow rate (kg/s)	Inlet temperature (K)	Target Temperature (K)	Heat duty (kw)
A	Cold	1.75	283	773	2630.7
B	Cold	4.82	283	773	16566.7
C	Cold	6.57	771	1073	28737.6
D	Hot	6.57	1073	680	-9964.0
E	Hot	6.57	832	473	-7347.7
F	Hot	20.69	763	300	-68865.0

The values in Table E.1 show that the maximum (T_{max}) and minimum (T_{min}) temperature requirements for hot streams were 1073 and 300 K, respectively, and 1073 and 283 K for the cold streams. The temperatures of the cold and hot streams were divided into ranges, from the maximum to the minimum process temperature. Tables E.2 and E.3 show the defined temperature intervals for the cold and hot streams, respectively. The heat exchangers that operate in each temperature interval are also included.

Table E.2. The temperature ranges of the cold streams for the pinch analysis in the NGCC power plant

Temperature interval	Maximum temperature of interval (K)	Minimum temperature of interval (K)	Heat exchangers
1	1073	832	D
2	832	763	D,E
3	763	680	D,E,F
4	680	473	E,F
5	473	300	F

Table E.3. The temperature ranges of the hot streams for the pinch analysis in the NGCC power plant

Temperature interval	Maximum temperature of interval (K)	Minimum temperature of interval (K)	Heat exchangers
1	1073	773	C
2	773	771	A,B,C
3	771	283	A,B

Once the temperature ranges were defined for the streams, the minimum temperature difference (dt_{min}) between the cold and hot streams was established as 10°C following the guidelines of Kemp (2011). In order to determine the pinch temperature, the hot and cold streams had to differ by at least dt_{min}, within each of the temperature ranges defined in Tables E.2 and E.3. Therefore, the hot streams' temperatures were decreased by half of the value of dt_{min} (5°C), and the temperatures of the cold streams were increased by that same value.

These shifted temperatures were used to determine the pinch point using the problem table approach, shown in Table E.4. This table shows the heat duties using the shift temperatures. The heat duties were determined using flowsheet-based simulation in gPROMS®, and then the heat cascade of the process was determined. The pinch point is shown with an asterisk in Table E.4, and it was located at the temperature where the heat cascade showed a deficit value. Above the pinch temperature value, heat could not be exchanged with the streams below the pinch temperature value. Therefore, 214.67 kw of external heating was required in the NGCC power plant, estimated from the deficit of the accumulated heat cascade.

Table E.4. The problem table and pinch point determination using the hot and cold streams of the NGCC power plant

Interval	Temperature (K)	Streams	Heat duty (kw)	Accumulated heat cascade (kw)	Heat cascade with pinch point (kw)
0	1078	C	N/A	-	214.67
1	1068	C	-214.67 (deficit)	-214.67* (deficit)	0 (Pinch)
2	827	C,D	379.68 (surplus)	165.01 (surplus)	379.68
3	778	C,D,E	1055.77 (surplus)	1220.78 (surplus)	1435.45
4	776	A,B,C,D,E	-26.69 (deficit)	1194.09 (surplus)	1408.76
5	758	A,B,D,E	401.67 (surplus)	1595.76 (surplus)	1810.43
6	675	A,B,D,E,F	882.89 (surplus)	2478.65 (surplus)	2693.32
7	468	A,B,E,F	-2478.26 (deficit)	0.398 (surplus)	215.06
8	295	A,B,F	175.40 (surplus)	175.80 (surplus)	390.47
9	288	A,B	-175.35 (surplus)	0.45 (surplus)	215.12

APPENDIX F – ECONOMIC ANALYSIS DATA

The economic analysis of the NGCC power plant was estimated for a reference plant with and without carbon capture. The economic analysis was divided into the estimation of (i) the total capital investment, and (ii) the annual total production cost. This appendix shows the purchased equipment cost values used to estimate the TCI, with contingencies and installation costs.

Section F.1 presents the value of these components for the reference NGCC power plant without carbon capture. This plant used natural gas directly provided from the pipeline, since there was no carbon dioxide capture process. Therefore, a syngas production plant was not required for this case. Section F.2 presents the PEC values for the plant with carbon capture using PSA. This plant also required a syngas production unit before PSA to capture the carbon dioxide, in order to maximize the carbon dioxide concentration in the inlet of the fixed-bed reactor unit.

F.1 The Purchase Equipment Cost (PEC) of the Plant without Carbon Capture

Table F.1. The purchase equipment cost and installation cost of the plant without carbon capture

Plant section	Unit	Quantity	PEC per unit ($/unit)	Total PEC ($)	PEC contingency ($)	PEC installation ($)
Power station	Gas Turbine	1	5,500,000	5,500,000	N/A	2,750,000
	Waste heat boiler	1	55,000	55,000	5,500	16,500
Gas and water supply/ circulation	Water supply and circulating pumps	3	7,000	21,000	4,410	6,300
	Steam compressor	1	593,700	593,700	124,677	237,480

F.2 The Purchase Equipment Cost (PEC) of the Plant with Carbon Capture using PSA

The values in Tables F.2 and F.3 are those obtained with the PSA process operating with four fixed-bed reactors. The cost analysis for the NGCC power plant cases with five and six fixed-bed reactors in the PSA process was obtained with the same procedure, multiplying the number of beds by the PEC per unit stated as the PSA fixed-bed reactor cost item. The hydrogen storage tank was included in the cost of the power plant when hydrogen co-production was considered in the plant (Section 6.2.3).

Table F.2. The purchase equipment cost and installation cost for the syngas production and carbon capture units in the plant with capture

Plant section	Unit	Quantity	PEC per unit ($/unit)	Total PEC ($)	PEC contingency ($)	PEC installation ($)
Syngas product	Steam methane reformer (SMR)	1	55,000	55,000	5,500	38,500
	Water gas shift (WGS) reactor	2	47,000	94,000	9,400	65,800
	Compressor to WGS	1	548,910	548,910	115,271	219,564
	SMR burner	1	56,356	56,356	5,635	16,907
	WGS to PSA cooler	1	30,000	30,000	3,000	9,000
Carbon capture	PSA fixed-bed reactor	4	40,000	160,000	16,000	112,000
	Carbon dioxide storage tank for recycling	1	30,000	30,000	3,000	9,000
	Hydrogen storage tank*	1	38,000	38,000	3,800	11,400

*Power plant units when including hydrogen co-production

Table F.3. The purchase equipment cost and installation cost for the carbon storage, power production and utilities supply units

Plant section	Unit	Quantity	PEC per unit ($/unit)	Total PEC ($)	PEC contingency ($)	PEC installation ($)
Carbon dioxide compression for storage	Compressor (36.7 bar)	1	192,700	192,700	40,467	77,080
	Compressor (80 bar)	1	94,900	94,900	19,929	37,960
	Pump (150 bar)	1	6,000	6,000	1,260	2,400
	Quench cooling	3	30,000	90,000	9,000	27,000
Power station and heat exchangers	Gas Turbine	1	5,500,000	5,500,000	N/A	2,750,000
	Waste heat boiler	1	55,000	55,000	5,500	16,500
	Shell and tube heat exchanger	5	55,000	275,000	27,500	82,500
Gas and water supply/ circulation	Water supply and circulating pumps	5	7,000	35,000	7,350	10,500
	Steam compressor	1	593,700	593,700	124,677	237,480

APPENDIX G – LIST OF PUBLICATIONS AND CONFERENCE PRESENTATIONS

G.1 List of Published Work

Azpiri Solares, R.A., Soares dos Santos, D., Ingram, A., Wood, J., 2019. Modelling and parameter estimation of breakthrough curves for amine-modified activated carbons under pre-combustion carbon capture conditions. Fuel 253, 1130–1139. doi:10.1016/j.fuel.2019.05.095

Azpiri Solares, R.A., Wood, J., 2020. A parametric study of process design and cycle configurations for pre-combustion PSA applied to NGCC power plants. Chemical Engineering Research and Design 160, 141-153. doi:10.1016/j.cherd.2020.04.039

G.2 Conference Presentations

Posters and oral presentations on this project have been shown at the following conferences and international visits:

-Poster Presentations at the Advanced Process Modelling (APM) Forums. London (UK), March 2017, 2018 and 2019.

-Oral and Poster Presentations at the Research Conference of the Centre for Doctoral Training in Carbon Capture and Storage and Cleaner Fossil Energy. The University of Nottingham (UK), February 2017 and 2018. The University of Sheffield (UK), February 2019.

-Oral and Poster Presentations at the European Conference on Fuel and Energy Research and its Applications (ECCRIA). Cardiff (UK), September 2018.

-Oral Presentation at the Illinois Sustainable Technology Center, as part of the international visit activities. Champaign (USA), September 2018.

-Poster Presentation at the Research Poster Conference. The University of Birmingham (UK), June 2019.

-Oral Presentation at the 69th Canadian Chemical Engineering Conference. Halifax (Canada), October 2019.

REFERENCES

Aaron, D. and Tsouris, C., 2005. Separation of CO_2 from flue gas: A review. Separation Science and Technology 40, 321–348. doi:10.1081/SS-200042244.

Abanades, J.C., Arias, B., Lyngfelt, A., Mattisson, T., Wiley, D.E., Li, H., Ho, M.T., Mangano, E. and Brandani, S., 2015. Emerging CO_2 capture systems. International Journal of Greenhouse Gas Control 40, 126–166. doi:10.1016/j.ijggc.2015.04.018.

Adams, T. and Mac Dowell, N., 2016. Off-design point modelling of a 420 MW CCGT power plant integrated with an amine-based post-combustion CO_2 capture and compression process. Applied Energy 178, 681–702. doi:10.1016/j.apenergy.2016.06.087.

Agarwal, A., Biegler, L.T. and Zitney, S.E., 2010. Superstructure-based optimal synthesis of pressure swing adsorption cycles for pre-combustion CO_2 capture. Industrial and Engineering Chemistry Research 49, 5066–5079. doi:10.1021/ie900873j.

Aguilera, P.G. and Gutiérrez Ortiz, F.J., 2016. Prediction of fixed-bed breakthrough curves for H_2S adsorption from biogas: Importance of axial dispersion for design. Chemical Engineering Journal 289, 93–98. doi:10.1016/j.cej.2015.12.075.

Alhajaj, A., Mac Dowell, N. and Shah, N., 2016. A techno-economic analysis of post-combustion CO_2 capture and compression applied to a combined cycle gas turbine: Part II. Identifying the cost-optimal control and design variables. International Journal of Greenhouse Gas Control 52, 331–343. doi:10.1016/j.ijggc.2016.07.008.

Anantharaman, R., Bolland, O., Booth, N., van Dorst, E., Ekstrom, C., Fernandes, E.S., Franco, F., Macchi, E., Manzolini, G., Nikolic, D. and Pfeffer, A., 2011. European best practice guidelines for assessment of CO_2 capture technologies. CAESAR Consortium, Petten (Netherlands).

Arenillas, A., Smith, K.M., Drage, T.C. and Snape, C.E., 2005. CO_2 capture using some fly ash-derived carbon materials. Fuel 84, 2204–2210. doi:10.1016/j.fuel.2005.04.003.

Aresta, M. and Tommasi, I., 1997. Carbon dioxide utilisation in the chemical industry. Energy Conversion and Management 38, 373–378. doi:10.1016/s0196-8904(96)00297-x.

Auroux, A., 2013. Calorimetry and Thermal Methods in Catalysis. Springer, Heidelberg (Germany). doi:10.1007/978-3-642-11954-5.

Ayawei, N., Ebelegi, A. N. and Wankasi, D., 2017. Modelling and interpretation of adsorption isotherms. Journal of Chemistry 2017, 1-11. doi:10.1155/2017/3039817.

Azpiri Solares, R.A., Soares dos Santos, D., Ingram, A. and Wood, J., 2019. Modelling and parameter estimation of breakthrough curves for amine-modified activated carbons

under pre-combustion carbon capture conditions. Fuel 253, 1130–1139. doi:10.1016/j.fuel.2019.05.095.

Azpiri Solares, R.A. and Wood, J., 2020. A parametric study of process design and cycle configurations for pre-combustion PSA applied to NGCC power plants. Chemical Engineering Research and Design 160, 141-153. doi:10.1016/j.cherd.2020.04.039.

Ben-Mansour, R., Habib, M.A., Bamidele, O.E., Basha, M., Qasem, N.A.A., Peedikakkal, A., Laoui, T. and Ali, M. 2016. Carbon capture by physical adsorption: Materials, experimental investigations and numerical modeling and simulations - A review. Applied Energy 161, 225–255. doi:10.1016/j.apenergy.2015.10.011.

Brandani, F. and Ruthven, D.M., 2004. The effect of water on the adsorption of CO_2 and C_3H_8 on type X zeolites. Industrial and Engineering Chemistry Research 43, 8339–8344. doi:10.1021/ie040183o.

Budinis, S., Krevor, S., Mac Dowell, N., Brandon, N. and Hawkes, A., 2018. An assessment of CCS costs, barriers and potential. Energy Strategy Reviews 22, 61–81. doi:10.1016/j.esr.2018.08.003.

Cappelletti, A. and Martelli, F., 2017. Investigation of a pure hydrogen fueled gas turbine burner. International Journal of Hydrogen Energy 42, 10513–10523. doi:10.1016/j.ijhydene.2017.02.104.

Carpenter, S.M. and Long, H.A., 2017. Integration of carbon capture in IGCC systems. Integrated Gasification Combined Cycle (IGCC) Technologies 2017, 445–463. doi:10.1016/B978-0-08-100167-7.00036-6.

Casas, N., Schell, J., Pini, R. and Mazzotti, M., 2012. Fixed bed adsorption of CO_2/H_2 mixtures on activated carbon: Experiments and modeling. Adsorption 18, 143–161. doi:10.1007/s10450-012-9389-z.

Casas, N., Schell, J., Joss, L. and Mazzotti, M., 2013a. A parametric study of a PSA process for pre-combustion CO_2 capture. Separation and Purification Technology 104, 183–192. doi:10.1016/j.seppur.2012.11.018.

Casas, N., Schell, J., Blom, R. and Mazzotti, M., 2013b. MOF and UiO-67/MCM-41 adsorbents for pre-combustion CO_2 capture by PSA: Breakthrough experiments and process design. Separation and Purification Technology 112, 34–48. doi:10.1016/j.seppur.2013.03.042.

Chen, Z., Deng, S., Wei, H., Wang, B., Huang, J. and Yu, G., 2013. Activated carbons and amine-modified materials for carbon dioxide capture -- A review. Frontiers of Environmental Science and Engineering 7, 326–340. doi:10.1007/s11783-013-0510-7.

Choi, S., Drese, J.H. and Jones, C.W, 2009. Adsorbent materials for carbon dioxide capture from large anthropogenic point sources. ChemSusChem 2, 796–854. doi:10.1002/cssc.200900036.

Cormos, C.C., 2016. Evaluation of reactive absorption and adsorption systems for post-combustion CO_2 capture applied to iron and steel industry. Applied Thermal Engineering 105, 56–64. doi:10.1016/j.applthermaleng.2016.05.149.

D'Alessandro, D.M., Smit, B., Long, J.R., 2010. Carbon dioxide capture: Prospects for new materials. Angewandte Chemie International Edition 49, 6058–6082. doi:10.1002/anie.201000431.

Dantas, T.L.P., Rodrigues, A.E. and Moreira, R.F.P.M., 2012. Separation of Carbon Dioxide from Flue Gas Using Adsorption on Porous Solids. Greenhouse Gases–Capturing, Utilization and Reduction, Books on Demand, 57–80. doi:10.13140/2.1.2092.6404.

Di Biase, E. and Sarkisov, L., 2015. Molecular simulation of multi-component adsorption processes related to carbon capture in a high surface area, disordered activated carbon. Carbon 94, 27–40. doi:10.1016/j.carbon.2015.06.056.

Di Lorenzo, G., Barbera, P., Ruggieri, G., Witton, J., Pilidis, P. and Probert, D., 2013. Pre-combustion carbon-capture technologies for power generation: An engineering-economic assessment. International Journal of Energy Research 37, 89–402. doi:10.1002/er.3029.

Dinda, S., 2013. Development of solid adsorbent for carbon dioxide capture from flue gas. Separation and Purification Technology 109, 64–71. doi:10.1016/j.seppur.2013.02.027.

Ding, Y. and Alpay, E., 2000. Equilibria and kinetics of CO_2 adsorption on hydrotalcite adsorbent. Chemical Engineering Science 55, 3461–3474. doi:10.1016/S0009-2509(99)00596-5.

Ditaranto, M., Li, H. and Løvås, T., 2015. Concept of hydrogen fired gas turbine cycle with exhaust gas recirculation: Assessment of combustion and emissions performance. International Journal of Greenhouse Gas Control 37, 377–383. doi:10.1016/j.ijggc.2015.04.004.

DOE, 2017. Carbon capture opportunities for natural gas fired power systems. Available at: https://www.energy.gov/sites/prod/files/2017/01/f34/Carbon%20Capture%20Opportunities%20for%20Natural%20Gas%20Fired%20Power%20Systems_0.pdf (Accessed: 29 April 2020).

DOE, 2020. Hydrogen resources. Available at: https://www.energy.gov/eere/fuelcells/hydrogen-resources#:~:text=Currently%2C%20most%20hydrogen%20is%20produced,currently%20used%20to%20produce%20hydrogen (Accessed: 7 September 2020).

Dowling, A.W., Vetukuri, S.R.R. and Biegler, L.T., 2012. Large-scale optimization strategies for pressure swing adsorption cycle synthesis. AIChE Journal 58, 3777–3791. doi:10.1002/aic.13928.

Ebner, A.D., Gray, M.L., Chisholm, N.G., Black, Q.T., Mumford, D.D., Nicholson, M.A. and
Ritter, J.A., 2011. Suitability of a solid amine sorbent for CO_2 capture by pressure swing adsorption. Industrial and Engineering Chemistry Research 50, 5634–5641. doi:10.1021/ie2000709.

Edrisi, A., Mansoori, Z. and Dabir, B., 2016. Urea synthesis using chemical looping process - Techno-economic evaluation of a novel plant configuration for a green production. International Journal of Greenhouse Gas Control 44, 42–51. doi:10.1016/j.ijggc.2015.10.020.

Effendy, S., Farooq, S. and Ruthven, D.M., 2017. A rigorous criterion for approach to cyclic steady-state in PSA simulations. Chemical Engineering Science 160, 313–320. doi:10.1016/j.ces.2016.11.041.

Ergun, S., 1952. Fluid Flow Through Packed Columns. Chemical Engineering Progress 48, 89-94.

Fałtynowicz, H., Kaczmarczyk, J. and Kułażyński, M., 2015. Preparation and characterization of activated carbons from biomass material-giant knotweed. Open Chemistry 13, 1150–1156. doi:10.1515/chem-2015-0128.

Farooq, S. and Ruthven, D.M., 1990. Heat effects in adsorption column dynamics. 2. Experimental validation of the one-dimensional model. Industrial & Engineering Chemistry Research 29, 1084–90. doi:10.1021/ie00102a020.

Franchi, R.S., Harlick, P.J.E. and Sayari, A., 2005. Applications of pore-expanded mesoporous silica. 2. Development of a high-capacity: water-tolerant adsorbent for CO_2. Industrial & Engineering Chemistry Research 44, 8007–8013. doi:10.1021/ie0504194.

Fuller, E.N., Schettler, P.D. and Giddings, J.C., 1966. New method for prediction of binary gas-phase diffusion coefficients. Industrial & Engineering Chemistry Research 58, 18-27. doi.org/10.1021/ie50677a007

García, S., Pis, J.J., Rubiera, F. and Pevida, C., 2013. Predicting mixed-gas adsorption equilibria on activated carbon for precombustion CO_2 capture. Langmuir 29, 6042–6052. doi:10.1021/la4004998.

Gas Adsorption Technology, 2016. Adsorption equilibrium. Available at: https://gasadsorptiontech.wordpress.com/tag/adsorption-isotherm-types/ (Accessed: 15 October 2020).

Gasworld, 2019. Carbon capture: In focus like never before, but are we doing enough? Available at: https://www.gasworld.com/carbon-capture-in-focus-like-never-before-but-are-we-doing-enough/2017994.article (Accessed: 26 November 2019).

Gibson, J.A., Mangano, E., Shiko, E., Greenaway, A.G., Gromov, A.V., Lozinska, M.M., Friedrich, D., Campbell, E.E., Wright, P.A. and Brandani, S., 2016. Adsorption materials

and processes for carbon capture from gas-Fired power plants: AMPGas. Industrial and Engineering Chemistry Research 55, 3840–3851. doi:10.1021/acs.iecr.5b05015.

Global CCS Institute, 2017. Paris climate change targets cannot be met without CCS: COP23, Bonn, Germany.

Goldmeer, J., 2018. Fuel Flexible Gas Turbines as Enablers for a Low or Reduced Carbon Energy Ecosystem. GE, Electrify Europe. Available at: https://www.ge.com/content/dam/gepower/global/en US/documents/fuel-flexibility/GEA33861%20-%20Fuel%20Flexible%20Gas%20Turbines%20as%20Enablers%20for%20a%20Low%20Carbon%20Energy%20Ecosystem.pdf (Accessed: 9 June 2019).

Grande, C.A., 2012. Advances in pressure swing adsorption for gas separation. Chemical Engineering, 1–13. doi:10.5402/2012/982934.

Grande, C.A., Roussanaly, S., Anantharaman, R., Lindqvist, K., Singh, P. and Kemper, J., 2017. CO_2 capture in natural gas production by adsorption processes. Energy Procedia 114, 2259-2264. doi:10.1016/j.egypro.2017.03.1363.

Guthrie, K.M., 1974. Process Plant Estimating, Evaluation, and Control. Craftsman Book Company of America, California (USA).

Haghpanah, R., Majumder, A., Nilam, R., Rajendran, A., Farooq, S., Karimi, I.A. and Amanullah, M., 2013. Multiobjective optimization of a four-step adsorption process for postcombustion CO_2 capture via finite volume simulation. Industrial & Engineering Chemistry Research 52, 4249–4265. doi:10.1021/ie302658y.

Hao, G.P., Li, W.C. and Lu, A.H., 2011. Novel porous solids for carbon dioxide capture. Journal of Materials Chemistry 21, 6447–6451. doi:10.1039/c0jm03564e.

Hao, W., Björkman, E., Lilliestråle, M. and Hedin, N., 2013. Activated carbons prepared from hydrothermally carbonized waste biomass used as adsorbents for CO_2. Applied Energy 112, 526–532. doi: 10.1016/j.apenergy.2013.02.028

Hao, P., Shi, Y., Li, S., Zhu, X. and Cai, N., 2018. Correlations between adsorbent characteristics and the performance of pressure swing adsorption separation process. Fuel 230, 9–17. doi:10.1016/j.fuel.2018.05.030.

Harlick, P.J.E. and Tezel, F.H., 2004. An experimental adsorbent screening study for CO_2 removal from N_2. Microporous and Mesoporous Materials 76, 71–79. doi: 10.1016/j.micromeso.2004.07.035

Harlick, P.J.E. and Sayari, A., 2006. Applications of pore-expanded mesoporous silicas. 3. Triamine silane grafting for enhanced CO_2 adsorption. Industrial & Engineering Chemistry Research 45, 3248–3255. doi:10.1021/ie051286p.

Hasan, M.F., Baliban, R.C., Elia, J.A. and Floudas, C.A., 2012. Modeling, simulation, and optimization of postcombustion CO_2 capture for variable feed concentration and flow

rate. 1. Chemical Absorption and Membrane Processes. Industrial & Engineering Chemistry Research 51, 15642–15664. doi:10.1021/ie301571d.

Heuberger, C.F., Staffell, I., Shah, N. and Mac Dowell, N., 2017. What is the value of CCS in the future energy system? Energy Procedia 114, 7564–7572. doi:10.1016/j.egypro.2017.03.1888.

Himeno, S., Komatsu, T. and Fujita, S., 2005. High-Pressure adsorption equilibria of methane and carbon dioxide on several activated carbons. Journal of Chemical & Engineering Data 50, 369–376. doi:10.1021/je049786x.

Ho, M.T., Allinson, G.W. and Wiley, D.E., 2008. Reducing the cost of CO_2 capture from flue gases using pressure swing adsorption. Industrial & Engineering Chemistry Research 47,
4883–4890. doi:10.1021/ie070831e.

Hu, Y., Gao, Y., Lv, H., Xu, G. and Dong, S., 2018. A New integration system for natural gas combined cycle power plants with CO_2 capture and heat supply. Energies 11, 3055. doi:10.3390/en11113055

Hussin, F. and Aroua, M.K., 2020. Recent trends in the development of adsorption technologies for carbon dioxide capture: A brief literature and patent reviews (2014–2018). Journal of Cleaner Production 253, 119707. doi.org/10.1016/j.jclepro.2019.119707.

IEA-GHG, 2009. Criteria for technical and economic assessment of plants with low CO_2 emissions. TR3/May 2009. Available at: https://ieaghg.org/docs/General_Docs/Reports/2009-TR3.pdf (Accessed: 12 July 2020).

International Energy Agency, 2019a. Exploring clean energy pathways. Available at: https://webstore.iea.org/exploring-clean-energy-pathways/ (Accessed: 4 March 2020).

International Energy Agency, 2019b. The future of hydrogen. Available at: https://www.iea.org/publications/reports/thefutureofhydrogen/ (Accessed: 5 March 2020).

International Energy Agency, 2019c. Electricity information: Overview. Available at: https://www.iea.org/publications/reports/globalevoutlook2019/ (Accessed: 6 March 2020).

International Energy Agency, 2019d. The role of CO_2 storage. Available at: https://www.iea.org/reports/the-role-of-co2-storage/ (Accessed: 6 May 2020).

International Energy Agency, 2020. CCUS in clean energy transitions. Available at: https://www.iea.org/reports/ccus-in-clean-energy-transitions/a-new-era-for-ccus#growing-ccus-momentum (Accessed: 20 October 2020).

IPCC, 2005. Special report on carbon dioxide capture and storage. Cambridge University Press, Cambridge, New York.

IPCC, 2014. Climate change 2014: Mitigation of climate change. Contribution of Working Group III to the Fifth Assessment Report of the Intergovernmental Panel on Climate Change. Cambridge University Press, Cambridge (UK).

Jain, S., Moharir, A.S., Li, P. and Wozny, G., 2003. Heuristic design of pressure swing adsorption: A preliminary study. Separation and Purification Technology 33, 25–43. doi:10.1016/S1383-5866(02)00208-3

Jansen, D., Gazzani, M., Manzolini, G., van Dijk, E. and Carbo, M., 2015.. Pre-combustion CO_2 capture. International Journal of Greenhouse Gas Control 40, 167–187. doi:10.1016/j.ijggc.2015.05.028.

Jordá-Beneyto, M., Suárez-García, F., Lozano-Castelló, D., Cazorla-Amorós, D. and Linares-Solano, A., 2007. Hydrogen storage on chemically activated carbons and carbon nanomaterials at high pressures. Carbon 45, 293–303. doi:10.1016/j.carbon.2006.09.022.

Kamarudin, K. S. N. and Alias, N. O. R. M. A., 2013. Adsorption performance of MCM-41 impregnated with amine for CO_2 removal. Fuel Processing Technology, 106, 332-337. doi:10.1016/j.fuproc.2012.08.017.

Kemp, I.C., 2011. Pinch Analysis and Process Integration: A User Guide on Process Integration for the Efficient Use of Energy. Elsevier, Oxford (UK).

Khurana, M. and Farooq, S., 2019. Integrated adsorbent process optimization for minimum cost of electricity including carbon capture by a VSA Process. AIChE Journal 65, 184–195. doi:10.1002/aic.16362.

Knowles, G.P., Graham, J.V., Delaney, S.W. and Chaffee, A.L., 2005. Aminopropyl-functionalized mesoporous silicas as CO_2 adsorbents. Fuel Processing Technology 86, 1435–1448.
doi:10.1016/j.fuproc.2005.01.014.

Knox, J.C., Ebner, A.D., LeVan, M.D., Coker, R.F. and Ritter, J.A., 2016. Limitations of breakthrough curve analysis in fixed-bed adsorption. Industrial and Engineering Chemistry Research 55, 4734–4748. doi:10.1021/acs.iecr.6b00516.

Ko, D., Siriwardane, R., Biegler, L.T., 2005. Optimization of pressure swing adsorption and fractionated vacuum pressure swing adsorption Processes for CO_2 Capture. Industrial & Engineering Chemistry Research 44, 8084-8094. doi:10.1021/ie0204540.

Kunze, C. and Spliethoff, H., 2012. Assessment of oxy-fuel, pre- and post-combustion-based carbon capture for future IGCC plants. Applied Energy 94, 109–116. doi:10.1016/j.apenergy.2012.01.013.

Kyzas, G.Z and Mitropoulus, A.C., 2019. Composite Nanoadsorbents. Elsevier, Amsterdam (Netherlands). doi:10.1016/C2017-0-00861-3.

Lee, J.C., Lee, H.H., Joo, Y.J., Lee, C.H. and Oh, M., 2014. Process simulation and thermodynamic analysis of an IGCC (integrated gasification combined cycle) plant with an entrained coal gasifier. Energy 64, 58–68. doi:10.1016/j.energy.2013.11.069.

Lee, S.Y. and Park, S.J., 2015. A review on solid adsorbents for carbon dioxide capture. Journal of Industrial and Engineering Chemistry 23, 1-11. doi:10.1016/j.jiec.2014.09.001.

Li, M., Rao, A.D. and Samuelsen, S.G., 2012. Performance and costs of advanced sustainable central power plants with CCS and H_2 co-production. Applied Energy 91, 43–50. doi:10.1016/j.apenergy.2011.09.009.

Lima, F. V., Daoutidis, P. and Tsapatsis, M., 2016. Modeling, optimization, and cost analysis of an IGCC plant with a membrane reactor for carbon capture. AIChE Journal 62, 1568–1580. doi:10.1002/aic.15153.

Liu, H., Liu, B., Lin, L.C., Chen, G., Wu, Y., Wang, J., Gao, X., Lv, Y., Pan, Y., Zhang, X. and Zhang, X., 2014. A hybrid absorption-adsorption method to efficiently capture carbon. Nature Communications 5, 1–7. doi:10.1038/ncomms6147.

Liu, J., Thallapally, P.K., McGrail, B.P., Brown, D.R. and Liu, J., 2012. Progress in adsorption-based CO_2 capture by metal-organic frameworks. Chemical Society Reviews 41, 2308–2322. doi:10.1039/C1CS15221A.

Liu, Z.L., Teng, Y., Zhang, K., Yan, C.A.O and Pan, W.P., 2013. CO_2 adsorption properties and thermal stability of different amine-impregnated MCM-41 materials. Journal of Fuel Chemistry and Technology 41, 469–476. doi:10.1016/s1872-5813(13)60025-0.

Lopes, F.V.S., Grande, C.A., Ribeiro, A.M., Oliveira, E.L.G. and Loureiro, M., 2009. Enhancing capacity of activated carbons for hydrogen purification. Industrial & Engineering Chemistry Research 48, 3978–3990. doi:10.1021/ie801132t.

Lopes, F.V.S., Grande, C.A. and Rodrigues, A.E., 2011. Activated carbon for hydrogen purification by pressure swing adsorption: Multicomponent breakthrough curves and PSA performance. Chemical Engineering Science 66, 303–317. doi:10.1016/j.ces.2010.10.034.

Lozinska, M.M., Mangano, E., Mowat, J.P.S., Shepherd, A.M., Howe, R.F., Thompson, S.P., Parker, J.E., Brandani, S. and Wright, P.A., 2012. Understanding carbon dioxide adsorption on univalent cation forms of the flexible zeolite Rho at conditions relevant to carbon capture from flue gases. Journal of the American Chemical Society 134, 17628–17642. doi:10.1021/ja3070864.

Lozinska, M.M., Mowat, J.P., Wright, P.A., Thompson, S.P., Jorda, J.L., Palomino, M., Valencia, S. and Rey, F., 2014. Cation gating and relocation during the highly selective "trapdoor" adsorption of CO_2 on univalent cation forms of zeolite Rho. Chemistry of Materials 26, 2052–2061. doi:10.1021/cm404028f.

Luberti, M., Friedrich, D., Brandani, S. and Ahn, H., 2014a. Design of a H_2 PSA for cogeneration of ultrapure hydrogen and power at an advanced integrated gasification combined cycle with pre-combustion capture. Adsorption 20, 511–524. doi:10.1007/s10450-013-9598-0.

Luberti, M., Friedrich, D., Ozcan, D.C., Brandani, S. and Ahn, H., 2014b. A novel strategy to produce ultrapure hydrogen from coal with pre-combustion carbon capture. Energy Procedia 63, 2023–2030. doi:10.1016/j.egypro.2014.11.217.

Mac Dowell, N. and Staffell, I., 2016. The role of flexible CCS in the UK's future energy system. International Journal of Greenhouse Gas Control 48, 327–344. doi:10.1016/j.ijggc.2016.01.043.

Manaf, N.A., Cousins, A., Feron, P. and Abbas, A., 2016. Dynamic modelling, identification and preliminary control analysis of an amine-based post-combustion CO_2 capture pilot plant. Journal of Cleaner Production 113, 635–653. doi:10.1016/j.jclepro.2015.11.054.

Mangano, E., Brandani, S., Ferrari, M.C., Ahn, H., Friedrich, D., Lozinska, M.L., Wright, P.A., Kahr, J., Morris, R., Croad, M. and McKeown, N., 2013. Efficient and rapid screening of novel adsorbents for carbon capture in the UK IGSCC project. Energy Procedia 37, 40–47. doi:10.1016/j.egypro.2013.05.083.

Matzen, M.J. and Demirel, Y., 2016. Methanol and dimethyl ether from renewable hydrogen and carbon dioxide: Alternative fuels production and life-cycle assessment. Journal of Cleaner Production 139, 1068-1077. doi:10.1016/j.jclepro.2016.08.163.

McGillivray, A., Saw, J.L., Lisbona, D., Wardman, M. and Bilio, M., 2014. A risk assessment methodology for high pressure CO_2 pipelines using integral consequence modelling. Process Safety and Environmental Protection 92, 17–26. doi:10.1016/j.psep.2013.09.002.

Mohamed, A.R., Mohammadi, M. and Darzi, G.N., 2010. Preparation of carbon molecular sieve from lignocellulosic biomass: A review. Renewable and Sustainable Energy Reviews 14, 1591–1599. doi:10.1016/j.rser.2010.01.024.

Moon, D.K., Lee, D.G. and Lee, C.H., 2016. H_2 pressure swing adsorption for high pressure syngas from an integrated gasification combined cycle with a carbon capture process. Applied Energy 183, 760–774. doi:10.1016/j.apenergy.2016.09.038.

Moon, D.K., Park, Y., Oh, H.T., Kim, S.H., Oh, M. and Lee, C.H., 2018. Performance analysis of an eight-layered bed PSA process for H_2 recovery from IGCC with pre-combustion carbon capture. Energy Conversion and Management 156, 202–214. doi:10.1016/j.enconman.2017.11.013.

Myers, A.L., 2003. Equation of state for adsorption of gases and their mixtures in porous materials. Adsorption 9, 9-16. doi:10.1023/A:1023807128914

Nikolaidis, G.N., Kikkinides, E.S. and Georgiadis, M.C., 2015. Modelling and simulation of pressure swing adsorption (PSA) processes for post-combustion carbon dioxide (CO_2) capture from flue gas. Computer Aided Chemical Engineering 37, 287-292. doi:10.1016/B978-0-444-63578-5.50043-8.

Nikolic, D., Giovanoglou, A., Georgiadis, M.C. and Kikkinides, E.S., 2008. Generic modeling framework for gas separations using multibed pressure swing adsorption

processes. Industrial and Engineering Chemistry Research 47, 3156–3169. doi:10.1021/ie0712582.

Ozturk, M. and Dincer, I., 2013. Thermodynamic analysis of a solar-based multi-generation system with hydrogen production. Applied Thermal Engineering 51, 1235-1244. doi:10.1016/j.applthermaleng.2012.11.042.

Peters, M.S., Timmerhaus, K.D. and West, R.E., 2003. Plant Design and Economics for Chemical Engineers. 3rd edition, McGraw-Hill Education, New York (USA).

Pirngruber, G.D., Cassiano-Gaspar, S., Louret, S., Chaumonnot, A. and Delfort, B., 2009. Amines immobilized on a solid support for postcombustion CO_2 capture-A preliminary analysis of the performance in a VSA or TSA process based on the adsorption isotherms and kinetic data. Energy Procedia 1, 1335–1342. doi:10.1016/j.egypro.2009.01.175.

Plaza, M., Pevida, C., Arias, B., Fermoso, J., Arenillas, A., Rubiera, F. and Pis, J., 2008. Application of thermogravimetric analysis to the evaluation of aminated solid sorbents for CO_2 capture. Journal of Thermal Analysis and Calorimetry 92, 601–606. doi:10.1007/s10973-007-8493-x.

Rackley, S.A., 2017. Carbon Capture and Storage. 2nd edition, Elsevier, Oxford (UK). doi:10.1016/B978-0-12-812041-5.00004-0.

Rampe, J.M. and Tiwow, V., 2018. Fabrication and Characterization of activated carbon from charcoal coconut shell Minahasa, Indonesia. Journal of Physics: Conference Series 1028, 12033. doi:10.1088/1742-6596/1028/1/012033.

Rase, H. F., 1990. Fixed-Bed Reactor Design and Diagnostics. Elsevier, Boston (USA). doi:10.1016/c2013-0-04268-5.

Redlich, O. and Kwong, J.N., 1949. On the thermodynamics of solutions. V. An equation of state. Fugacities of gaseous solutions. Chemical Reviews 44, 233-244. doi:10.1021/cr60137a013.

Reichl, A.E., Schneider, R., Ohligschläger, A., Rogalinski, T. and Hauke, S., 2014. Process development and scale-up for post combustion carbon capture - Validation with pilot plant operation. Energy Procedia 63, 6379–6392. doi:10.1016/j.egypro.2014.11.673.

Ribeiro, A.M., Grande, C.A., Lopes, F.V., Loureiro, J.M. and Rodrigues, A.E., 2008. A parametric study of layered bed PSA for hydrogen purification. Chemical Engineering Science 63, 5258–5273. doi:10.1016/j.ces.2008.07.017.

Riboldi, L., Bolland, O., Ngoy, J.M. and Wagner, N., 2014. Full-plant analysis of a PSA CO_2 capture unit integrated in coalfired power plants: Post- And pre-combustion scenarios. Energy Procedia, 63 (1876): 2289–2304. doi:10.1016/j.egypro.2014.11.248.

Riboldi, L. and Bolland, O., 2015a. Comprehensive analysis on the performance of an IGCC plant with a PSA process integrated for CO_2 capture. International Journal of Greenhouse Gas Control 43, 57–69. doi:10.1016/j.ijggc.2015.10.006.

Riboldi, L. and Bolland, O., 2015b. Evaluating Pressure Swing Adsorption as a CO_2 separation technique in coal-fired power plants. International Journal of Greenhouse Gas Control 39, 1–16. doi:10.1016/j.ijggc.2015.02.001.

Riboldi, L. and Bolland, O., 2016. Pressure swing adsorption for coproduction of power and ultrapure H_2 in an IGCC plant with CO_2 capture. International Journal of Hydrogen Energy 41, 10646–10660. doi:10.1016/j.ijhydene.2016.04.089.

Riboldi, L. and Bolland, O., 2017. Flexible operation of an IGCC plant coproducing power and H_2 with CO_2 capture through novel PSA-based process configurations. Energy Procedia 114, 2156–2165. doi:10.1016/j.egypro.2017.03.1351.

Rouquerol, F., Rouquerol, J., Sing, K.S., Llewellyn, P. and Maurin, G., 2014. Adsorption by Powders and Porous Solids: Principles, Methodology and Applications. 2nd edition, Elsevier, Oxford (UK). doi:10.1016/B978-0-08-097035-6.00001-2.

Ruthven, D.M., 1985. Physical Adsorption and the Characterization of Porous Adsorbents. Principles of Adsorption and Adsorption Processes. John Wiley and Sons, New York (USA). doi:10.1016/0255-2701(85)80013-1.

Ruthven, D.M., Douglas M., Farooq, S. and Knaebel, K.S., 1994. Pressure swing adsorption. VCH Publishers, New York (USA).

Samanta, A., Zhao, A., Shimizu, G.K., Sarkar, P. and Gupta, R., 2012. Post-combustion CO_2 capture using solid sorbents: A review. Industrial and Engineering Chemistry Research 51, 1438–1463. doi:10.1021/ie200686q.

Schell, J., Casas, N. and Mazzotti, M., 2009. Pre-combustion CO_2 capture for IGCC plants by an adsorption process. Energy Procedia 1, 655–660. doi:10.1016/j.egypro.2009.01.086.

Seader, J.D. and Henley, E.J., 2006. Separation Process Principles. 2nd edition, John Wiley and Sons, New York (USA).

Seyitoglu, S.S., Dincer, I. and Kilicarslan, A., 2016. Assessment of an IGCC based trigeneration system for power, hydrogen and synthesis fuel production. International Journal of Hydrogen Energy 41, 8168–8175. doi:10.1016/j.ijhydene.2015.10.093.

Shafeeyan, M.S., Daud, W.M.A.W., Shamiri, A. and Aghamohammadi, N., 2015. Modeling of carbon dioxide adsorption onto ammonia-modified activated carbon: kinetic analysis and breakthrough behavior. Energy and Fuels 29, 6565–6577. doi:10.1021/acs.energyfuels.5b00653.

Shafeeyan, M.S., Wan Daud, W.M.A. and Shamiri, A., 2014. A review of mathematical modeling of fixed-bed columns for carbon dioxide adsorption. Chemical Engineering Research and Design 92, 961–988. doi:10.1016/j.cherd.2013.08.018.

Sharma, I., Friedrich, D., Golden, T. and Brandani, S., 2019. Exploring the opportunities for carbon capture in modular, small-scale steam methane reforming: An energetic

perspective. International Journal of Hydrogen Energy 44, 14732-14743. doi:10.1016/j.ijhydene.2019.04.080.

Sie, M.-J., Lin, C.-H. and Wang, S.-L., 2016. Polyamine-cladded 18-ring-channel gallium phosphites with high-capacity hydrogen adsorption and carbon dioxide capture. Journal of the American Chemical Society 138, 6719–6722. doi:10.1021/jacs.6b03305.

Singh, V.K. and Kumar, E.A., 2016. Measurement and analysis of adsorption isotherms of CO_2 on activated carbon. Applied Thermal Engineering 97, 77–86. doi:10.1016/j.applthermaleng.2015.10.052.

Soares dos Santos, D., 2019. Impregnation of activated carbons for pre- and post-combustion CO_2 capture in a fixed bed pressure swing adsorption reactor: a modelling and experimental comparison. University of Birmingham, Ph.D thesis.

Soave, G., 1972. Equilibrium constants from a modified Redlich-Kwong equation of state. Chemical Engineering Science 27, 1197-1203. doi:10.1016/0009-2509(72)80096-4.

Sreenivasulu, B., Gayatri, D.V., Sreedhar, I. and Raghavan, K.V., 2015. A journey into the process and engineering aspects of carbon capture technologies. Renewable and Sustainable Energy Reviews 41, 1324–1350. doi:10.1016/j.rser.2014.09.029.

Styring, P., 2019. Carbon dioxide utilization as a mitigation tool. Managing Global Warming, 527-551. Elsevier, Oxford (UK). doi:10.1016/B978-0-12-814104-5.00018-1.

Sun, N., Sun, C., Liu, J., Liu, H., Snape, C.E., Li, K., Wei, W. and Sun, Y., 2015. Surface-modified spherical activated carbon materials for pre-combustion carbon dioxide capture. RSC Advances 5, 33681–33690. doi:10.1039/c5ra02665b.

Surblé, S., Millange, F., Serre, C., Düren, T., Latroche, M., Bourrelly, S., Llewellyn, P.L. and Férey, G., 2006. Synthesis of MIL-102, a chromium carboxylate metal−organic framework, with gas sorption analysis. Journal of the American Chemical Society 128, 14889–14896. doi:10.1021/ja064343u.

The Fourth Generation, 2020. Life cycle emissions of hydrogen. Available at: https://4thgeneration.energy/life-cycles-emissions-of-hydrogen/ (Accessed: 22 October 2020).

The Global CO_2 initiative, 2016. A roadmap for the global implementation of carbon utilization technologies: transforming CO_2 from a liability to an asset at significant market scale. Available at: http://www.globalco2initiative.org/webinar (Accessed: 15 March 2019).

The Global CO_2 initiative, 2017. Carbon Capture and Use: The Missing Link for Climate Change? Available at: from https://www.globalco2initiative.org/2017/03/19/carbon-capture-and-use-the-missing-link-for-climate-change/ (Accessed: 16 March 2019).

The Royal Society and National Academy of Science, 2014. Climate Change Evidence & Causes. Available at: https://royalsociety.org/-

/media/Royal_Society_Content/policy/projects/climate-evidence-causes/climate-change-evidence-causes.pdf/ (Accessed: 3 January 2020).

Tien, C., 2019. Introduction to Adsorption. Elsevier, Amsterdam (Netherlands). doi:10.1016/b978-0-12-816446-4.00005-1.

Tzabar, N. and ter Brake, H.J.M. 2016. Adsorption isotherms and Sips models of nitrogen, methane, ethane, and propane on commercial activated carbons and polyvinylidene chloride. Adsorption 22, 901–914. doi:10.1007/s10450-016-9794-9.

Unuabonah, E.I., Omorogie, M.O. and Oladoja, N.A., 2019. Modeling in adsorption: fundamentals and applications. Composite Nanoadsorbents, 85-118. Elsevier, Amsterdam (Netherlands). doi:10.1016/B978-0-12-814132-8.00005-8.

U.S. Energy Information Administration (EIA), 2019. International Energy Outlook 2019. Washington, DC, USA. Available at: https://www.eia.gov/outlooks/ieo/index.php (Accessed: 16 February 2020).

U.S. Energy Information Administration (EIA), 2020. Hydrogen Production: Natural Gas Reforming. Washington, DC, USA. Available at: https://www.energy.gov/eere/fuelcells/hydrogen-production-natural-gas-reforming#:~:text=Most%20hydrogen%20produced%20today%20in,source%2C%20such%20as%20natural%20gas.

Van Der Zwaan, B. and Smekens, K., 2007. CO_2 capture and storage with leakage in an energy-climate model. Environmental Modeling & Assessment 14, 135-148. doi:10.1007/s10666-007-9125-3.

Wakao, N. and Funazkri, T., 1978. Effect of fluid dispersion coefficients on particle-to-fluid mass transfer coefficients in packed beds. Correlation of Sherwood numbers. Chemical Engineering Science 33, 1375–1384. doi:10.1016/0009-2509(78)85120-3.

Wang, X., Zeng, W., Guo, Q., Geng, Q., Yan, Y. and Hu, X., 2018. The further activation and functionalization of semicoke for CO_2 capture from flue gases. RSC Advances 8, 35521–35527. doi:10.1039/c8ra07560c.

Wang, Y., Dowling, A.W., Krieft, C., Walther, A. and Biegler, L.T., 2015. Pressure swing adsorption optimization strategies for CO_2 capture. Computer Aided Chemical Engineering 36, 197–223. doi:10.1016/B978-0-444-63472-6.00008-2.

Webley, P.A., 2014. Adsorption technology for CO_2 separation and capture: A perspective. Adsorption 20, 225–231. doi:10.1007/s10450-014-9603-2.

Wiheeb, A.D., Helwani, Z., Kim, J. and Othman, M.R., 2016. Pressure swing adsorption technologies for carbon dioxide capture. Separation and Purification Reviews 45, 108–121. doi:10.1080/15422119.2015.1047958.

Worstell, J., 2014. Adiabatic Fixed-Bed Reactors. Elsevier, Waltham (USA). doi:10.1016/b978-0-12-801306-9.00005-4.

Xiao, J., Peng, Y., Bénard, P. and Chahine, R., 2016. Thermal effects on breakthrough curves of pressure swing adsorption for hydrogen purification. International Journal of Hydrogen Energy 41, 8236–8245. doi:10.1016/j.ijhydene.2015.11.126.

Yang, H., Xu, Z., Fan, M., Gupta, R., Slimane, R.B., Bland, A.E. and Wright, I., 2008. Progress in carbon dioxide separation and capture: A review. Journal of Environmental Sciences 20, 14–27. doi:10.1016/S1001-0742(08)60002-9.

Yang, R.T., 1987. Gas Separation by Adsorption Processes. Imperial College Press, London (UK).

Yazaydin, A.Ö., Snurr, R.Q., Park, T.-H., Koh, K., Liu, J., Levan, M.D., Benin, A.I., Jakubczak, P., Lanuza, M., Galloway, D.B., Low, J.J. and Willis, R.R., 2009. Screening of metal-organic frameworks for carbon dioxide capture from flue gas using a combined experimental and modeling approach. Journal of the American Chemical Society 131, 18198–18199. doi:10.1021/ja9057234.

Yu, C.H., Huang, C.H. and Tan, C.S., 2012. A review of CO_2 capture by absorption and adsorption. Aerosol and Air Quality Research 12, 745–769. doi:10.4209/aaqr.2012.05.0132.

Yuan, B., Wu, X., Chen, Y., Huang, J., Luo, H. and Deng, S., 2013. Adsorption of CO_2, CH_4, and N_2 on ordered mesoporous carbon: Approach for greenhouse gases capture and biogas upgrading. Environmental Science and Technology 47, 5474–5480. doi:10.1021/es4000643.

Zhang, J., Singh, R. and Webley, P.A., 2008. Alkali and alkaline-earth cation exchanged chabazite zeolites for adsorption based CO_2 capture. Microporous and Mesoporous Materials 111, 478–487. doi:10.1016/j.micromeso.2007.08.022.

Zhang, W., Liu, H., Sun, C., Drage, T.C. and Snape, C.E., 2014. Performance of polyethyleneimine–silica adsorbent for post-combustion CO_2 capture in a bubbling fluidized bed. Chemical Engineering Journal 251, 293–303. doi:10.1016/j.cej.2014.04.063.

Zhao, L., Bacsik, Z., Hedin, N., Wei, W., Sun, Y., Antonietti, M. and Titirici, M.M., 2010. Carbon dioxide capture on amine-rich carbonaceous materials derived from glucose. ChemSusChem 3, 840–845. doi:10.1002/cssc.201000044.

Zhu, B., Li, K., Liu, J., Liu, H., Sun, C., Snape, C.E. and Guo, Z., 2014. Nitrogen-enriched and hierarchically porous carbon macro-spheres-ideal for large-scale CO_2 capture. Journal of Materials Chemistry A 15, 5481–5489. doi:10.1039/c4ta00438h.